Contents

List of Figures

List of Tables

Introducción

El objetivo de este trabajo es la caracterización de los prototipos del calorímetro hadrónico del detector ATLAS en el acelerador SPS del CERN durante los años 1997 - 1998 a diferentes energías de haces de test y la búsqueda del Bosón de Higgs basada en los datos procedentes de programas de simulación del detector ATLAS en el colisionador LHC (pp) del CERN durante 3 años a baja luminosidad ($10^{34}\ cm^{-2}\ s^{-1}$) a una energía en centro de masas de $E_{cm} = 14$ TeV.

El colisionador LHC está diseñado para tener cada 25 ns 23 colisiones protón-protón. El detector ATLAS está en la fase de construcción con un estricto esquema de trabajo para producir las primeras colisiones en el LHC durante el verano del 2005. El detector ATLAS tiene diferentes subdetectores: El detector Interno, los Calorímetros electromagnéticos y hadrónicos y el Sistema de muones. Los calorímetros hadrónicos abarcan la región $|\eta| <4.9$. En la región $|\eta| <1.7$ nos encontramos con el calorímetro de tejas (hierro-centelleador) usadas para el barril y su extensión y con la zona "muerta" (ITC) situada entre ambos calorímetros y utilizada para depositar los cables y la electrónica de dichos detectores. En la región $1.5< |\eta| <4.9$ nos encontramos con los calorímetros de Argón Líquido, donde tenemos los tapones (HEC) que se extienden hasta $|\eta| <3.2$ y los calorímetros hacia adelante (FCAL) en el intervalo $3.1< |\eta| <4.9$.

El calorímetro de tejas (Tile - Cal) es un calorímetro de centelleo que utiliza hierro como absorbente y placas centelleadoreas como medio activo. La construcción de los módulos se hace por apilamiento repetitivo de placas de hierro siguendo un período de cuatro densidades. El calorímetro es un barril de radio interno 2.28 m y de radio externo 4.32 m. Se subdivide en un barril central de 5.64 m y dos dilatados de 2.65 m cada uno. Cada uno de los barriles representa 64 módulos (sectores) en azimutal (ρ). La innovación principal de esta tecnología es la orientación de las tejas centelleadoras que se colocan perpendicularmente a los haces de partículas en colisión. Esta orientación guiada por las simulaciones de Monte Carlo permite una construcción mecánica muy simple así como una lectura fácil de las tejas y suministra una buena homogeneidad de los datos cuando se coloque un calorímetro electromagnético delante del hadrónico con el fin de tener dos longitudes de interacción de los materiales activos.

Dentro del marco de la colaboración RD34, el equipo de Valencia trabaja sobre el concepto y el perfeccionamiento del calorímetro hadrónico de tejas centelleadoras. Los primeros test comenzaron en 1993 con tres módulos de 1 m de longitud y 1.80 m de profundidad. En 1994 y 1995, el prototipo ha pasado de 3 a 5 módulos de las mismas dimensiones que en 1993. En 1994 y 1996, se ha podido efectuar una serie de tets combinados entre un prototipo del calorímetro electromagnético de argón líquido y los 5 módulos. En septiembre de 1996, se efectuó un test de un prototipo de la parte del barril del calorímetro, llamandose módulo "0". En octubre de 1997, se ha realizado un test sobre dos prototipos de los tapones del barril "extended barrel module 0". Este test consisitió en dos tapones analizados conjuntamente con los 5 módulos anteriormente mencionados. En Julio de 1998, se volvió a hacer un test sobre el módulo "0" junto con los 5 módulos de 1 m de longitud. Uno de los principales objetivos sobre la realización de estos test con haces de partículas es la optimización del diseño para cumplir los requisitos físicos y mecánicos impuestos a la calorimetría hadrónica en el LHC, como por ejemplo:

- identificar los *jets* y medir sus energías y sus dirección,
- medir la energía transversal total perdida (E_T^{miss}),
- mejorar la capacidad de identificar las partículas.

Una resolución en energía de $\frac{\sigma}{E} = \frac{50\%}{\sqrt{E}} \oplus 3\%$, y una segmentación de $\Delta\eta \times \Delta\phi = 0.1 \times 0.1$ es la que deberá poseer el calorímetro para esperar los objetivos físicos marcados.

El Modelo Estándar de la Física de Partículas Elementales (SM) describe con un alto grado de precisión la materia y sus interacciones a las energías alcanzadas por los aceleradores actuales. Sin embargo, algunas cuestiones continúan todavía sin ser resueltas y existe la convicción entre los expertos de que este modelo no puede considerarse la teoria final. Una de las extensiones más prometedoras del Modelo Estándar es la Supersimetría (SUSY). Ésta asume la existencia de una simetría entre fermiones y bosones que da lugar a la predicción de nuevas partículas supersimétricas, compañeras de todas las partículas conocidas.

El modelo supersimétrico predice dos dobletes de Higgs y cinco estados físicos del bosón de Higgs a diferencia del SM que predice un doblete y un estado físico. Los estados físicos son, dos cargados ($H^{\pm}$) y tres neutros (h, H, A). El h y H son escalares y el A es pseudoescalar. Uno de los principales objetivos de investigación a estos niveles de altas energías (14 TeV) es la búsqueda de nuevas partículas, en especial, el bosón de Higgs y las partículas supersimétricas.

La búsqueda de los cinco estados físicos del bosón de Higgs ha sido realizada dentro del marco del Modelo Estándar Supersimétrico Mínimo (MSSM). Las masas y acoplamientos de estos estados pueden ser expresados en términos de dos parámetros como pueden ser m_A, la masa del bosón de Higgs pseudoescalar y tanβ, el valor esperado en el vacío del cociente entre los dos dobletes de Higgs. Además, se supone que las partículas supersimétricas no juegan un papel importante en la fenomenología de las desintegraciones del Higgs en el MSSM, debido a que se consideran suficientemente pesadas. Los canales más interesantes de desintegración del Higgs son: h $\rightarrow$ b$\bar{\text{b}}$, H $\rightarrow$ ZZ $\rightarrow$ 4l los cuales también son accesibles en el SM, con valores grandes de tanβ (20-50): H/A $\rightarrow \tau\tau$, H/A $\rightarrow \mu\mu$ y con valores pequeños de tanβ (1-3): H/A $\rightarrow$ t$\bar{\text{t}}$, A $\rightarrow$ Zh, H $\rightarrow$ hh.

En colisones protón-protón el descubriento del bosón de Higgs por el experimento ATLAS dentro de las regiones del espacio de parámetros, m_A = 50 - 500 GeV y tanβ = 1-50 deberia estar garantizado. Además más de un bosón de Higgs y/o más de un modo de desintegración será accesible en dichas regiones.

Este trabajo está estructurado en cinco capítulos. En el primero se introduce el concepto de Supersimetría y se mencionan las cuestiones no resueltas por el Modelo Estándar y que sugieren la búsqueda de teorías más generales más alla de este modelo. Seguidamente, se discuten las motivaciones para la Supersimetría y se presentan los conceptos básicos del Modelo Estándar Supersimétrico Mínimo. También se explican los mecanismos de ruptura de la Supersimetría y sus consecuencias fenomenológicas más importantes.

En el segundo capítulo se describe el dispositivo experimental. Se comienza con una introducción al acelerador LHC y su funcionamiento, seguida de la descripción del detector ATLAS. Las principales características de los subdetectores son también tratadas en este capítulo.

En el tercero se centra en la descripción de las principales características de la cascada electromagnética y hadrónica como sus diferencias. A continuación, se discute los efectos del cociente e/h sobre la construcción de un calorímetro y como afecta a la resolución energética del mismo. Finalmente, se describre el calorímetro hadrónico de tejas del detector ATLAS. Al final del capítulo se resumen todos los requisitos físicos y mecánicos del calorímetro hadrónico para conseguir los objetivos físicos marcados en el ambicioso programa del LHC.

En el capítulo cuatro se describe los test con haces de partículas de la parte del barril y de la extensión del barril del calorímetro hadrónico de tejas centelleadoras. En Octubre de 1997 se efectuó un test sobre dos extensiones ("extended barrel modules 0"), una fabricada en Barcelona (España) y la otra en Argonne (USA). Los módulos fueron analizados junto los cinco módulos viejos de 1 m de longitud, de tal forma que ambos "extended barrel modules 0", fueron situados en medio de los 5 módulos anteriormente mencionados disminuyendo de esta forma la pérdida de cascada transversal. En Julio de 1998 se realizó un test utilizando un prototipo del barril ("barrel module 0"). El módulo fué estudiado junto a los cinco módulos de 1 m de longitud como en el test de 1997.

El análisis realizado en este trabajo tiene como objetivo calcular la resolución energética hadrónica, la linealidad y el factor e/h del calorímetro de tejas para comprobar que están dentro de los requisitos exigidos para el calorímetro hadrónico de ATLAS. Para realizar este estudio se han utilizado haces de test de piones con energías entre 20 y 400 GeV para valores de η des -1.4 hasta -0.25. También se describen los cortes utilizados para la elección de los sucesos a ser analizados. Además, se mencionan los métodos utilizados para la reconstrucón de la energía de los piones ("Raw Data", "Benchmark", y "H1"), estudiándose la evolución de la linealidad y de la resolución energética hadrónica através de dichos métodos. Después, se proporcionan detalles acerca de la simulación y generación Monte Carlo de sucesos del prototipo del barril ("Barrel Module 0"), usando los mismos métodos para la reconstrución de la energía y el estudio de la linealidad y la resolución. Se comprueba que la linealidad y la resolución de los prototipos del calorímetro de tejas mejoran utilizando el método "H1". Además, los resultados son compatibles entre los diferentes módulos y valores de η. El método de "Benchmark" proporciona resultados idénticos respecto a la linealidad que los "Raw data", mejorandola un poco a altas energías. A continuación se muestra un análisis para extraer el valor e/h, que es el cociente entre la respuesta electromagnética y la no electromagnética (puramente hadrónica) de la cascada hadrónica en el calorímetro. Valores de e/h diferentes a 1 causan desviaciones en la linealidad de la respuesta hadrónica, empeorando la resolución energética e introduciendo colas en las distribuciones energéticas. En el caso del calorímetro de tejas, se espera que el valor del factor e/h sea mayor que uno, debido a la orientación perpendicular de las tejas repecto al haz incidente. Por último se hace un estudio comparativo entre los prototipos del barril y de las extensiones, poniendo de manifiesto que ambos prototipos cumplen con los requisitos exigidos a nivel de resolución, linealidad y e/h por la colaboración ATLAS.

En el capítulo cinco se describe la búsqueda del bosón de Higgs desintegrándose a quarks top dentro del marco del Modelo Estándar Supersimétrico Mínimo (MSSM) suponiendo que las partículas supersímetricas son muy pesadas, de tal forma que no juegan un papel importante en las desintegraciones del bosón de Higgs. Debido al fuerte acoplamiento del bosón de Higgs a bosones "gauge", la probabilidad de desintegración del $H \rightarrow t\bar{t}$ es muy pequeña del orden del 10%. Sin embargo, en el caso del MSSM la probabilidad de desintegración del $H \rightarrow t\bar{t}$ y $A \rightarrow t\bar{t}$ es muy próxima al 100% para masas del bosón de Higgs mayores que dos veces la masa del top y para valores de $\tan\beta$ próximos a 1. Las desintegraciones $H \rightarrow t\bar{t}$ y $A \rightarrow t\bar{t}$ no se pueden distinguir experimentalmente, debido a que ambos bosones están degenerados en masa en la región relevante del espacio de parámetros. En un segundo paso se proporcionan detalles acerca de la simulación del detector ATLAS y la generación de los sucesos usando dos Monte Carlos. El primero se llama ATLFAST, el cual es un programa de simulación intermedio entre un análisis simple a nivel de partones y una sofisticada simulación completa del detector. Este programa se utiliza para una rápida generación de sucesos de la señal y del fondo incluyendo los aspectos más relevantes del detector: reconstrución de "jets" en los calorímetros, reconstrución del momento y de la energía de los leptones y fotones, efectos de los campos magnéticos y evaluación de la energía perdida transversa. El segundo programa usado se llama SLUG-DICE-ATRECON, el cual proporciona una simulación sofisticada del detector y por lo tanto la generación de suecesos no es tan rápida como en el caso de ATLFAST. Una “Full simulation” del detector es siempre necesesaria para el estudio de los efectos del ruido, calibración e intercalibración de calorímetros, detallado desarrollo de la cascada, “pile-up”, “cracks” y además proporciona una parametrización para la “Fast simulation”.

La estrategia utlizada para la identificación de sucesos procedentes de las desintegraciones del H/A a quarks top se basa en la identificación de estados finales de la forma $\mathrm{WWb\bar{b}}$. Uno de los top se desintegra, $\mathrm{t} \rightarrow \mathrm{Wb}$, seguido de una desintegración semileptónica del bosón W, $\mathrm{W} \rightarrow \mathrm{l}\nu$, dando un lepton aislado utilizado para el “trigger”. El segundo bosón W se desintegra hadrónicamente, $\mathrm{W} \rightarrow \mathrm{jj}$. Por lo tanto, esta situación nos proporciona una topologia con un leptón aislado y cuatro “jets” en el estado final. En primer lugar se explican los cortes cinemáticos aplicados sobre los sucesos con el objetico de rechazar el fondo reducible (W + “jets”) con $\mathrm{W} \rightarrow \mathrm{l}\nu$ y disminuir el fondo irreducible ($\mathrm{t\bar{t}} \rightarrow \mathrm{bl}\nu\mathrm{bjj}$). Después, se estudian diferentes algoritmos para la reconstrución de la masa invariante $\mathrm{t\bar{t}}$, obteniendo la resolución de la señal, la relación señal/ruido y la significancia estadística para masas del Higgs entre 370 y 450 GeV. Además, se reproduce la forma y la magnitud del fondo combinatorial para el canal hadrónico ($\mathrm{t} \rightarrow \mathrm{bjj}$) y para el semileptónico ($\mathrm{t} \rightarrow \mathrm{bl}\nu$). A continuación se hace un estudio con intención de extraer la señal respecto al fondo, para el intervalo de masas mencionado anteriormente, teniendo en cuenta los errores sistemáticos procedentes de la normalización y de la forma del fondo. Se comprueba que la extración de la señal puede llegar a ser posible para masas del Higgs diferentes a 400 GeV debido a que el fondo irreducible forma un pico alrededor de esta masa. Para masas próximas a 400 GeV, únicamente un exceso de sucesos sobre el fondo irreducible nos llevaria a la observabilidad de la señal y si además se vencieran las incertidudes teóricas sobre la forma del fondo. Finalmente, una comparación entre los dos programas de simulación es llevada acabo, encontrandose un buen acuerdo entre las aceptancias de selección de los cortes cinemáticos y las resoluciones en masa del top y del Higgs. Al final del capítulo se resume el potencial del detector ATLAS para el descubrimiento del bosón de Higgs dentro del marco del Modelo Estándar o del Modelo Estándar Supersimétrio Mínimo, haciendo un repaso de todas las opciones de desintegración del Higgs.

Para finalizar, se dedican las últimas páginas a recoger las conclusiones más importantes derivadas de este trabajo.

Introduction

The goal of this work is the hadronic calorimeter prototipes characterization of the ATLAS detector at the SPS collider of CERN during the years 1997 - 1998 for several beam energies and the search for Higgs boson using the data sample of the Monte Carlo simulations of proton-proton collisions for the ATLAS detector at the LHC collider during three years at low luminosity (10^{34} cm^{-2} s^{-1}) and a centre-of-mass energies of E_{cm} = 14 TeV.

Beam crossings are 25 ns apart and at design luminosity there are 23 interactions per cossing. The ATLAS experiment has now entered the construction phase for many of its detector components, with a strict schedule to meet the first collisions at LHC in summer 2005. The ATLAS experiment has several subdetectors: Inner Detector, Electromagnetic and Hadron Calorimeters and the Muon system. The ATLAS hadronic calorimeters cover the range $|\eta|$ <4.9. Over the range $|\eta|$ <1.7, the iron scintillating-tile technique is used for the barrel and extended barrel tile calorimeters and for partially instrumenting the gap between them with the intermediate tile calorimeter (ITC). This gap provide space for cables and services from the innermoot detectors. Over the range 1.5< $|\eta|$ <4.9, Liquid Argon calorimeters were chosen: the hadronic end-cap calorimeter (HEC) extends to $|\eta|$ <3.2, while the range 3.1< $|\eta|$ <4.9 is covered by the high-density forward calorimeter (FCAL).

The tile calorimeter (Tile - Cal) is a sampling calorimeter using iron as the absorber and scintillating tiles as the active material. The tiles are placed radially and staggered in depth. The structure is periodic along z. The tile calorimeter is composed of one barrel of 5.46 m and two extended barrels of 2.65 m each one. Radially the tile calorimeter extends from an inner radius of 2.28 m to an outer radius of 4.32 m. Azimutally (ρ), the barrel and extended barrels are divided into 64 modules. The new feature of its design is the orientation of the scintillating tiles which are placed in planes perpendiculars to the colliding beams and are staggered in depth. A good sampling homogeneity is obtained when the calorimeter is placed behind an electromagnetic compartment and a coil equivalent to a total of about two interaction lengths of material. This has been verified with Monte Carlo simulation and has been proven by the test beam results.

In the framework of the RD34 project, the Valencia team works in an extensive program of beam tests demostrating the good performance of the calorimeter that fulfils the requirements for the ATLAS hadronic barrel calorimetry. The Tile Calorimeter test beam program was started in 1993 using three 1 m prototype modules. Between 1994 and 1995, the test beam was categorized to take data with a prototype stack of five 1 m modules. A first test of the electromagnetic and the five hadronic calorimeter prototypes in a combined setup was performed in 1994. Another run was performed in 1996. In 1996 September a full scale barrel sector (Module 0) was tested. In 1997 October two Extended Barrel Module 0 were been exposed to the calibration beams. The five originale one meter prototype modules were placed on either sides of Extended Barrel Modules 0, three on one side and two on the other. In 1998 July the Barrel Module 0 was tested with five one meter prototypes placed on either sides of module 0. The main goal of the test beam programs is the optimization of the design in order to reach the desired physics and mechanics requirements, for example:

- measurement of the energy and direction of jets,
- measurement of the missing transverse momentum of the event (E_T^{miss}),
- accurate measurement of the energy and position of electrons and photons.

The single particle hadronic energy resolution of $\frac{\sigma}{E} = \frac{50\%}{\sqrt{E}} \oplus 3\%$, and a granularity $\Delta\eta \times \Delta\phi = 0.1 \times 0.1$ is needed to reach the physics goals.

The Standard Model of Elementary Particle Physics (SM) describes with a very high precision matter and its interactions at the energies reached by the present accelerators. However, several questions remain still unanswered and there is a consensus among physicists that this model cannot be considered a final theory. One of the most promising extensions of the Standard Model is Supersymmetry (SUSY). It assumes a symmetry between fermions and bosons which leads to the prediction of new supersymmetric particles, partners of all known particles.

The Higgs supersymmetric sector requires two Higgs doublets and five physical states of the Higgs boson. The SM predicts one Higgs doublet and the existence of a Higgs boson. The physical states of the Higgs boson are two charged ($H^{\pm}$) and three neutral (h, H, A) physcial states. The h and H are the CP-odd scalars and A is the CP-even scalar. One of the main goals of this high energy (14 TeV) regime is the search for new particles, in particular, the search for the lightest Higgs boson and supersymmetric particles.

The search for the five physical states of the Higgs boson has been carried out in the framework of the Minimal Supersymmetric Standard Model (MSSM). At the three level, all Higgs-boson masses and couplings can be expressed in terms of two parameters only. They are usually chosen to be m_A, and tanβ, the ratio of the vacuum expectation values of the Higgs doublets. It is assumed that SUSY particles are suficiently heavy that they do not play an important role in the phenomenology of MSSM Higgs-boson decays. The interest was focused on the discovery potential of various decay modes accesible also in the case of the SM Higgs boson: $h \to b\bar{b}$, $H \to ZZ \to 4l$, and of modes strongly enhanced at large tanβ: $H/A \to \tau\tau$, $H/A \to \mu\mu$. Much attention was given also to other potentially interesting channels such as: $H/A \to t\bar{t}$, $A \to Zh$, $H \to hh$.

In proton-proton collisions in the complete region of parameter space, m_A = 50-500 GeV and tanβ = 1-50, should be accesible for Higgs-boson discovery by the ATLAS experiment. Over a large fraction of this parameter space, more than one Higgs boson and/or more than one decay mode would be accesible.

The work is presented in five chapter. In the first chapter a brief introduction of the Supersymmetry concepts is given and mention is made of several of the open questions in the Standard Model wich suggest that it is necessary to look for more general theories beyond this model. Later on in the chapter, the motivations of Supersymmetry and the basic concepts of the Minimal Supersymmetry Standard Model are discussed. The main supersymmetry breaking mechanisms and its phenomenological consequences are also summarised.

The experimental setup is described in the second chapter. A general description of the LHC accelerator system is given and its operation is summarised. On the other hand, the ATLAS detector and the main characteristics of its subdetectors are treated.

The third chapter is devoted to the main features of electromagnetic and hadronic showers and its differences. Then, how the e/h ratio affects the calorimeter performance and energy resolution are discussed. Finally, a description of the Tile Calorimeter as one of the sub-detectors of the ATLAS is shown. All the requirements on the detector specifications to reach the ambitious goals physics of the LHC are gathered at the end of the chapter.

The fourth chapter describes the test beam performance of the barrel and extended barrel Tile Calorimeter prototipes. In 1997 October two extended barrel modules 0 were built for the test, one in Barcelona (Spain), and the other at Argonne (USA). The modules were tested at CERN together with the five 1 meter old modules. In order to improve the transverse leakage for both, the two extended barrel modules were sandwiched between the 1 m prototype modules. In 1998 July the barrel module 0 was tested in the beam area using the same five 1 meter modules as for the test beam in 1997.

The analysis carried out in this work has as goal study the resolution, linearity and e/h ratio of the barrel and extended barrel to demonstrate the good performance of the calorimeter, which fulfils the requirements for the ATLAS barrel calorimetry. Test beam pion energies from 20 to 400 GeV along different values of η, from η = -1.4 to η = -0.25 have been used in this analysis. The cuts used in the choice of the events are also described. The methods followed in the pion energy reconstruction (Raw Data, Benchmark, and H1) are also mentioned. The evolution of the linearity and resolution parameters in the data reconstruction, from Raw Data to H1 weighting method going through the benchmark method is studied. Then, a comparison between the test beam data of the Tile Calorimeter prototype modules and the GCALOR full simulation Monte Carlo program has been done for the 1998 test beam. The linearity and resolution of the Tile Calorimeter prototypes improve using the H1 method. Also these results are compatible for the different modules and η values. Respect to the linearity, the benchmark approach gives aproximately the same results than the raw data, improving a little at high energies. The response obtained for electron and pions gives the possibility to extract the e/h value, that is the ratio of the calorimeter responses to the electromagnetic and non-electromagnetic (purely hadronic) components of hadron showers. An e/h value different from 1 causes deviation from linearity in the hadronic response versus energy, besides broadening the energy resolution and introducing tails in the energy distribution. In the case of the Tile Calorimeter this ratio is expected to be greater than 1 for the conventional orientation of tiles perpendicular to incident hadrons. Finally, a comparative study between the barrel and extended barrel prototipes is provided, showing the good agreement obtained with the ATLAS calorimetry requirements about resolution, linearity and e/h value.

The search for a Higgs boson via its decay to $t\bar{t}$ in a possible extension of the Standard Model, the MSSM is explained in detail in chapter five. It is assumed that SUSY particle masses are large, so that Higgs-boson decay to SUSY particles are kinematicaly forbidden. Due to the strong coupling of the SM Higgs boson to gauge-boson pairs, the $H \rightarrow t\bar{t}$ branching ratio is too small for this channel to be observable in the SM case. In the MSSM case, however, the $H \rightarrow t\bar{t}$ and $A \rightarrow t\bar{t}$ branching ratios are close to 100% for m_H, $m_A > 2m_t$ and for tan$\beta \sim 1$. The $H \rightarrow t\bar{t}$ and $A \rightarrow t\bar{t}$ decays cannot be distinguished experimentally from each other, since the H and A bosons are almost degenerate in mass in the relevant region of parameter space. Then, some details about the ATLAS simulation and the two Monte Carlo programs used to generate events are given. The first program, ATLFAST, is an intermediate step between a simple parton-level analysis and a very sophisticated full detector simulation. It can be used for fast simulation of signal and background processes, including the most crucial detector aspects: jet reconstruction in the calorimeters, momentum/energy smearing for leptons and photons, magnetic field effects and missing transverse energy evaluation. The second program, SLUG-DICE-ATRECON, is a sophisticated and high CPU-time intensive full detector simulation. It is always needed to study effects due to noise, calibration and intercalibration of calorimeters, detailed showers development, pile-up, cracks, and to provide parametrisation for fast simulation.

The strategy used to identify $t\bar{t}$ decays from H/A consists in searching for $WWb\bar{b}$ finale states. One top decay, $t \rightarrow Wb$, is required to be followed by the semileptonic decay of the W-boson, $W \rightarrow l\nu$, giving an isolated lepton to trigger the experiment. The secon W boson is required to decay hadronically, $W \rightarrow jj$. This final topology consists of one isolated lepton and four reconstructed jets. Firstly, the initial selection cuts on events used to reject events coming from the reducible (W + jets) and from the irreducible background ($t\bar{t} \rightarrow bl\nu bjj$) are explained. Then, several algorithms for reconstructing the invariant mass of the $t\bar{t}$ pair have been studied in order to obtain the signal resolution, the signal-to-background ratio and the statistical significance for a $m_A = 370$, 400 and 450 GeV. The shape and magnitude of the combinatorial background to the ($t \rightarrow bjj$) hadronic channel, and the ($t \rightarrow bl\nu$) semileptonic channel is reproduced. Later on in the chapter, the signal is extracted by fitting a superposition of a polynomial background and a Gaussian to the mass distribution taken into account the statistical error, the systematic error from overall normalisation and from the shape of the background. This is not posible for a mass of 400 GeV, since also the background peaks around this value. For masses close to 400 GeV only an excess of events above the continuum background would be observed. This excess would be statistically significant if the theoretical uncertainties on the continuum background shape were not larger than about a percent. Then, a comparison between full and fast simulation is described. A good agreement between the two simulation packages is found for the acceptance of the kinematic cuts and the top and Higgs mass resolutions. The performance of the ATLAS detector in search for a Standard Model or a Minimal Supersymmetric Standard Model Higgs boson is reviewed at the end of the chapter.

To end up, the most important conclusions extracted from this work are summarised.

Chapter 1

Theoretical motivation

In the first section of this chapter an overview of the most important theoretical and phenomenological aspects related to the Standard Model (SM) are given with the aim of explaining the spontaneous symmetry breaking. The Higgs mechanism and *the defects of the Standard Model are also examined.* The second section includes an introduction to the supersymmetry and explains its motivations by the gauge hierarchy problem. Section three is devoted to the supersymmetric extension of the SM (the Minimal Supersymmetric Standard Model).

1.1 The Standard Model

The Standard Model is the most successful yet developed model to explain the physics of the fundamental particles and their interactions. The aim of this model is to reveal the relationship between matter and forces in terms of particles and underlying symmetries [1].

The current Standard Model is built on the successes of three previous theories. The first is Quantum Electrodynamics (QED), the theory which describes the electromagnetic (EM) interaction in terms of underlying U(1) symmetry. The success of QED has led to its use as a model for the theories that have followed. The next theory in the Standard Model progression is the electroweak interaction theory, guided by $SU(2) \times U(1)$ symmetry, first proposed by Glashow, Weinberg and Salam in the late 1960's and referred to as the Glashow-Weinberg-Salam model [2] [3] [4]. This theory incorporates the successful QED model and provides a description of the weak force in terms of the exchange of massive vector bosons [5]. The fact that these vector boson masses were successfully predicted from the theory before the particles were discovered is considered one of the major triumphs of the model. In the Standard Model, the masses of these bosons are generated by the Higgs mechanism. The third theory which makes up the Standard Model is Quantum Chromodynamics (QCD), guided by SU(3) symmetry. This is the quantum field theory describing the interactions of quarks through the strong "colour" field [5].

The fact that the Standard Model is made up from three gauge theories means that it is built up from three gauge symmetries. These symmetries correspond to the three relevant fundamental forces in particle physics, namely the strong, the weak, and the electromagnetic force. The Standard Model gauge group is the product group $SU(3) \times SU(2) \times U(1)$, with *SU(3), SU(2)* and *U(1)* component groups being associated with the colour, weak and hypercharge symmetries. The corresponding gauge bosons are the massless gluons of QCD, the massive W^+, W^- and Z of the weak interaction, and the massless photon of electromagnetism.

The spin $\pm$ 1/2, or fermion content of the model is divided into two parts, both of which appear to come in three families. The two parts which make up the fermion content of the model are known as the quarks and the leptons. Leptons are fermions that interact only under electroweak interactions, while the quarks are fermions that also interact strongly [6]. The observed fermion content of the model (leptons and quarks) is listed below in Table 1.1.

Table 1.1: The fermions of the Standard Model.

	MASS (GeV/c^2)	Q	Family	Hypercharge
QUARKS				
d	0.008	-1/3	1	1/3
u	0.004	+2/3	1	1/3
s	0.15	-1/3	2	1/3
c	1.2	+2/3	2	1/3
b	4.7	-1/3	3	1/3
t	175	+2/3	3	1/3
LEPTONS				
e	0.0005	-1	1	0
ν_e	$<$ 0.000015, CL 90%	0	1	0
μ	0.105	-1	2	0
ν_μ	$<$ 0.00017, CL 90%	0	2	0
τ	1.8	-1	3	0
ν_τ	$<$ 0.0182, CL 95%	0	3	0

The predictions of the Standard Model have been tested and verified with unprecedented precision by experiments at the **L**arge **E**lectron **P**ositron Collider (LEP) [8], SLAC and many other laboratories. However, there are several incomplete aspects of the Standard Model which lack yet understanding, such as: the unverified origin of the mass, the interactions are not unified, an explanation for why there are only three families of particles does not exist; there are many (19) free parameters in the model [9]; gravitation is not included in the model; the mass scale is not "natural" (ie. radiative corrections to the Higgs mass suffer from large divergences requiring two quantities of the order $\sim 10^{32}$ which almost cancel to produce a result of 10^4, this fortuitous cancellation is considered "unnatural" [9] [10].); and it provides no dark matter candidate. These incomplete aspects of the model imply that the Standard Model can be considered only as an effective theory. That is, the Standard Model is a low energy approximation of a more general underlying theory.

One of the most important unanswered questions of the model is the origin of the masses. It is widely believed that this question can be answered by invoking the Higgs mechanism, which requires the onset of spontaneous symmetry breaking of the local gauge symmetry and provides a mass generation mechanism for both of the SU(2) weak gauge bosons and the observed massive quarks and leptons. It also predicts the existence of a massive scalar particle known as the Higgs boson. The best experimental verification of the existence of the Higgs Mechanism would be the discovery of its physically detectable manifestation, i.e. the existence of the Higgs boson.

1.1.1 Spontaneous Symmetry Breaking

Spontaneous symmetry breaking occurs when the Lagrangian of a system retains its invariance under the symmetry group, but the vacuum state (ground state of the system) does not exhibit the same invariance. The vacuum state breaks the symmetry [6]. To explain how this is achieved, we consider the case of a single complex scalar field, $\phi(x)$, and the *U(1)* invariant Lagrangian under phase rotations given by equation 1.1,

$$L(\phi, \phi^\dagger, \partial_\mu \phi, \partial_\mu \phi^\dagger) = \partial_\mu \phi^\dagger \partial^\mu \phi - V(\phi^\dagger \phi) \tag{1.1}$$

with $V(\phi^\dagger \phi) = \mu^2 |\phi|^2 + \Lambda |\phi|^4$. For this system, the Euler-Lagrange equation implies that the vacuum state must satisfy

$$\phi_0(\mu^2 + 2\Lambda |\phi_0|^2) = 0. \tag{1.2}$$

This condition offers two possibilities: either both μ^2 ($mass^2$) and Λ (coupling strength) are positive, or μ^2 is negative while Λ remains positive (Λ cannot be negative as the potential must has a lower bound). The former case implies that there is only one solution, that of conventional vacuum with $\phi_0 = 0$, while the latter case permits a second solution:

$$|\phi_0^2| = \frac{-\mu^2}{2\Lambda} \equiv \frac{v^2}{2} \tag{1.3}$$

$$\phi_0 \equiv \langle\phi\rangle \frac{1}{\sqrt{2}} v e^{i\zeta}. \tag{1.4}$$

The second solution implies that the true vacuum corresponds to a non-zero vacuum expectation value (VEV) for ϕ. The spontaneous symmetry breaking potential is the famous "Mexican Hat" potential, with an infinite number of VEV degenetared states of minimum energy ($\langle\phi\rangle$), laying in a circle of $\frac{v}{\sqrt{2}}$ radius and centred at the origin. Figure 1.1 shows a 2-D slice of the potential $V(\phi^\dagger\phi)$ for both solutions to the spontaneous symmetry breaking condition.

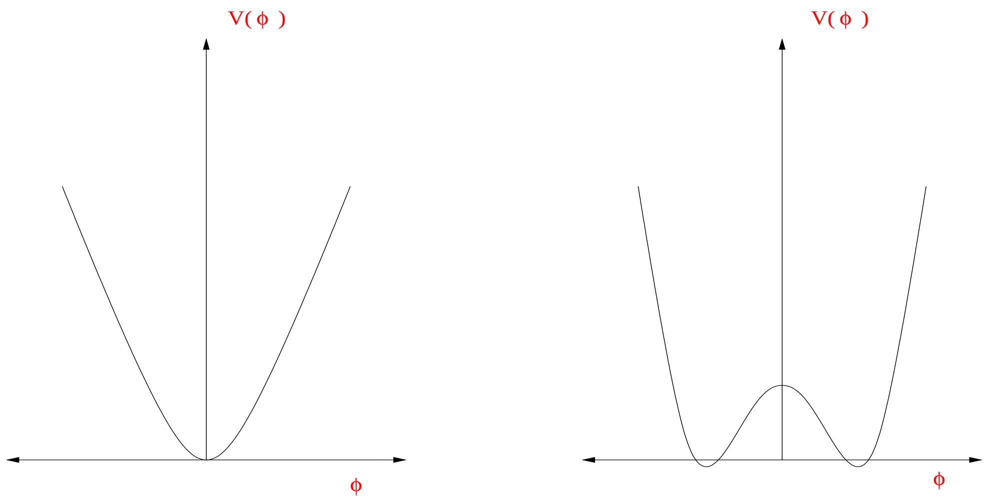

Figure 1.1: Two version of the simple U(1) invariant Higgs potentials: (a) The conventional vacuum Higgs potential with $\langle\phi\rangle = 0$, (b) a 2-d slice of the spontaneous symmetry breaking Higgs potential with $\langle\phi\rangle \neq 0$.

There is, however, a problem with the second solution of equation 1.1. The problem is that the scalar field has an unphysical negative solution for the mass. However, this situation can be remedied by means of a field redefinition of ϕ, where ϕ is expanded around its VEV. The form of this expansion is

$$\phi(x) = \frac{1}{\sqrt{2}}(\rho(x) + v)e^{i[g+\frac{\xi}{v}]} \tag{1.5}$$

with $\rho(x)$ and $\xi(x)$ being real fields. In this expansion, the introduction of $\rho(x)$ takes into account oscillations around the Mexican Hat minimum at $x = v/\sqrt{2}$, while $\xi(x)$ parametrises the motion around the minimum (ie. the minimum is really a flat circle). The effect on the Lagrangian of this field redefiniton is to cause an alteration of its form:

$$L = \frac{1}{2}\partial_\mu\rho\partial^\mu\rho + \frac{1}{2}\frac{(\rho+v)^2}{v^2}\partial_\mu\xi\partial^\mu\xi + \mu^2\rho^2 - \Lambda v\rho^3 - \frac{\Lambda}{4}\rho^4 - \frac{\mu^2 v^2}{4}. \tag{1.6}$$

The motivation for the field redefinition becomes now apparent. Equation 1.6 is the Lagrangian for two real scalar fields, one of which ($\rho(x)$) has a positive mass while the other ($\xi(x)$) is massless. Both are phisically acceptable fields. Further, this Lagrangian does not explicitly exhibit the original invarance under phase rotations (due to the expansion of ϕ around its VEV), nevertheless, by its pure construction, the Lagrangian still possesses the underlying internal symmetry of the gauge group. Because of this, the symmetry has been spontaneously broken, and is resulting in the appearance of a massles field (Nambu-Goldtone boson) which is free to move along the minima of the "Mexican Hat" potential.

1.1.2 The Higgs Mechanism

The exact mechanism by which the masses of the Standard Model vector bosons and fermions are generated remains unverified [10]. However, it is widely believed that the Higgs Mechanism is the key to explain this mass generation.

The Higgs mechanism is the application of the spontaneous symmetry breaking to a local gauge group. Again one considers the complex scalar field, but this time requires it to be invariant under local gauge transformation, as well as having the "Mexican Hat" potential. The Lagrangian of Equation 1.1 becomes

$$L = \frac{-1}{4}F_{\mu\nu}F^{\mu\nu} + (D_\mu\phi)^\dagger D^\mu\phi - \mu^2|\phi|^2 - \Lambda|\phi|^4, \tag{1.7}$$

where $F_{\mu\nu}$ is the field strength and D_μ the covariant derivative, D_μ given by

$$D_\mu \phi_i(x) = [\partial_\mu + igQ_i A_\mu(x)]\phi_i(x). \tag{1.8}$$

As before, we can develop ϕ around its vacuum expectation value in order to recover the physical scalar fields, but the expansion is a little more complicated due to the local nature of the required gauge invariance. In this case, the second term of the Lagragian written in Equation 1.7 becomes:

$$(D_\mu\phi)^\dagger D^\mu\phi = \frac{1}{2}\partial_\mu\rho\partial^\mu\rho + \frac{1}{2}\frac{(\rho+v)^2}{v^2}(\partial_\mu\xi)^\dagger\partial^\mu\xi \tag{1.9}$$
$$-g\frac{(\rho+v)^2}{v}A^\mu\partial_\mu\xi + \frac{1}{2}g^2(\rho+v)^2A^\mu A_\mu.$$

Again the field redefinition generates masses, but this time for a vector gauge field. An additional term, which does not correspond to a standard interaction, is also generated. However, this can be solved by means of a redefinition of the gauge field, allowing the introduction of a massive field $B_\mu(x)$ defined by

$$B_\mu(x) = A_\mu(x) + \frac{1}{gv}\partial_\mu\xi(x) \tag{1.10}$$

which restores the Lagrangian to the form:

$$L = \frac{-1}{4}B_{\mu\nu}B^{\mu\nu} + \frac{1}{2}m_B^2B^\mu B_\mu + \frac{\lambda^2}{2}(\rho^2+2\rho v)B^\mu B_\mu \tag{1.11}$$
$$+\frac{1}{2}\partial_\mu\rho\partial^\mu\rho - \frac{1}{2}m_\rho^2\rho^2 - \frac{\Lambda}{4}\rho^4 - \Lambda v\rho^3.$$

One of the physical fields introduced in the symmetry breaking process ($\xi(x)$) has disappeared. Once all traces of the Nambu-Goldstone boson field $\xi(x)$ have been removed, instead of a massless gauge field the theory contains a massive vector gauge field $B_\mu(x)$ with mass $m_B = gv$, as well as a massive scalar, $\rho(x)$ of mass $m_\rho = \sqrt{-2\mu^s}$. What has happened is that the spontaneous symmetry breaking originates the absorption of the Nambu-Golstone boson $\xi(x)$ by the original massless gauge field. Colloquially, the massless vector boson has "eaten" the scalar field $\xi(x)$, and by doing so has became the massive vector gauge field. This allows the calculation of the W and Z vector boson masses, given by the following formulae:

$$m_{W^\pm}^2 = \frac{g_2^2 v^2}{4},\ m_Z^0 = (g_1^2 + g_2^2)\frac{v^2}{4} = \frac{m_W^2}{cos^2\theta_W} \tag{1.12}$$

where g_1 and g_2 are coupling constants and θ_W is the Weinberg angle or weak mixing angle.

So, by means of spontaneous breaking of a local gauge symmetry (the Higgs mechanism), gauge bosons obtain their masses. In addition to give masses to the gauge bosons, the Higgs mechanism is remarkable because it can be simultaneously used to generate the fermions masses in the theory [10]. The introduction of this SU(2) Higgs doublet allows to write Yukawa-like terms of the form

$$\sqrt{\frac{1}{2}} g_f v(\overline{f_L} f_R + \overline{f_R} f_L) \tag{1.13}$$

with the mass of the fermion being given by $g_f v/\sqrt{2}$.

With this mechanism, the Standard Model predicts the existence of a Higgs boson (the physical manifestation of the Higgs mechanism) but does not predict its mass, because very little of what it has been measured on the Standard Model parameters depends directly of this mass. However, by imposing to the theory certain internal consistency requirements the range of possible values may be narrowed [6]. Two crucial requirements are triviality (a trivial theory would be non-interacting at low energies) and unitarity (the probability of scattering from a particular state to another one grows with energy and can be close to one) [10]. The mass upper bound obtained by imposing these constraints is of the order of 1 TeV/c^2.

Current experimental limits exclude the existence of the Higgs boson below $\sim$ 95 GeV (LEP II [7]). By the end of LEP II this limit could be extended to 110 GeV. Therefore it is crucial to have the facility of an accelerator for searching the Higgs up to at least 1 TeV/c^2. Either the Higgs will be produced or some other exotic particles signifying new physics will be discovered. The LHC will be the first accelerator in the world to explore this mass regime.

1.1.3 The Standard Model defects

It has been already said that there is not confirmed experimental evidence contradicting the Standard Model. Nevertheless, it seems obvious that the Standard Model is not a complete theory. Even if one accepts the rather bizarre set of group representations and hypercharges that it requires, the Standard Model contains at least 19 parameters: 3 gauge couplings $g_{1,2,3}$ and 1 CP-violating non-perturbative vacuum angle θ_3, 6 quarks and 3 charged-lepton masses with 3 charged weak mixing angles and 1 CP-violating phase δ, and 2 parameters: $(\mu,\ \lambda)$ or $(m_H,\ m_W)$ to characterize the Higgs sector. Moreover, many more parameters are required if one wishes to accommodate observations from non-accelerator experiments. For example, neutrino masses and mixing introduce at least 7 parameters: 3 masses, 3 mixing angles and 1 CP-violating phase, cosmological inflation introduces at least 1 new mass scale of the order 10^{16} GeV, the cosmological baryon asymmetry is not explicable within the Standard Model, so one or more additional parameters are needed, and the cosmological constant may be non-zero.

It is convenient to organize the questions raised by the Standard Model into three broad categories. One is the **Problem of Mass**: do particle masses really originate from a Higgs boson, and, if so, why are these masses not much closer to the Planck mass $m_P \sim 10^{19}$ GeV? Another question is the **Problem of Unification**: can all the particle interactions be unified in a simple gauge group, and, if so, does it predict new observable phenomena such as baryon decay and/or neutrino masses, and does it predict relations between parameters of the Standard Model such as gauge coupling or fermion masses? Also there is the **Problem of Flavour**: what is the origin of the six flavours of quarks and leptons, and what explains their weak charged mixing current and CP violation? Finally, one of the most important problems that the Standard Model cannot solve is the "hierarchy problem" [11]. This does not mean really a difficulty with the Standard Model itself, but rather a disturbing sensitivity of the Higgs potential to the new physics in almost any imaginable extension of the SM.

1.1.3.1 The hierarchy problem

From measurements of the properties of the weak interactions it is known that the squared Higgs mass is of the order $m_H^2 \sim -(100\ GeV)^2$. However, m_H^2 is affected by enormous corrections from the virtual effects of every particle which couples, directly or indirectly, to the Higgs field.

For example in Figure 1.2a we show a correction to m_H^2 from a loop containing a Dirac fermion f with mass m_f. If the Higgs field couples to f with a term in the Lagrangian $-\lambda_f H\overline{f}f$, then the Feyman diagram in Figure 1.2a yields a correction

$$\Delta m_H^2 = \frac{|\lambda_f|^2}{16\pi^2}[-2\Lambda_{UV}^2 + 6m_f^2 ln(\Lambda_{UV}/m_f) + ...]. \tag{1.14}$$

Here Λ_{UV} is an ultraviolet momentum cutoff used to regulate the loop integral; it should be interpreted as the energy scale at which new physics enters to alter the high-energy behaviour of the theory. The largest corrections come when f is the top quark with $\lambda \approx 1$. In this case if Λ_{UV} is of the order of M_P, say, then this quantum correction to m_H^2 is 30 orders of magnitude larger than the aimed-for value of $m_H^2 \sim -(100GeV)^2$.

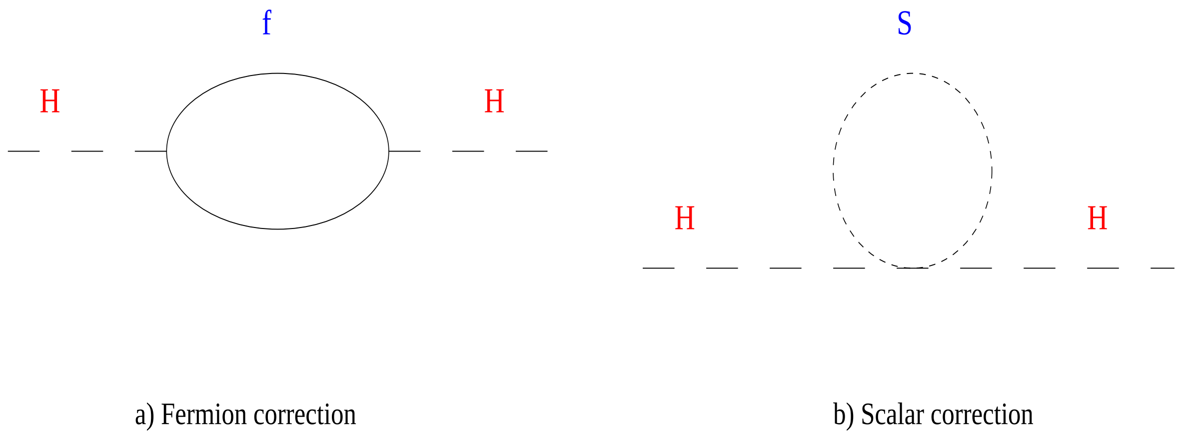

Figure 1.2: Correction to m_H^2 from: a) loop containing a Dirac fermion f with mass m_f, b) loop containing a heavy complex scalar particle S with mass m_S.

If the Higgs boson is a fundamental particle, either the assumption that it does not exist *any* heavy particle which couples (even indirectly or extremely weakly) to the Higgs scalar field has to be made, or some rather striking cancellation is needed between the various contributions to Δm_H^2. Fortunately, cancellation of all such contributions to scalar masses are not only possible, but are actually unavoidable once we merely assume that a symmetry relating fermions and bosons, called a *supersymmetry*, should exist.

1.2 Supersymmetry

Suppose there exists a heavy complex scalar particle S with mass m_S which couples to the Higgs with a lagrangian term $-\lambda_S|H|^2|S|^2$. Then the Feynman diagram in figure 1.2b gives a correction:

$$\Delta m_H^2 = \frac{|\lambda_S|^2}{16\pi^2}[\Lambda_{UV}^2 + 6m_S^2 ln(\Lambda_{UV}/m_S) + ...]. \tag{1.15}$$

The systematic cancellation of the dangerous contributions to Δm_H^2 can only be brought by the type of conspiracy which is better known to physicists as a symmetry. It is evident from comparing eqs. (1.14), (1.15) that the new symmetry ought to relate fermions and bosons, because of the relative minus sign between fermion loop and boson loop contributions to Δm_H^2. If each of the quarks and leptons of the Standard Model is accompanied by two complex scalars with $\lambda_S = |\lambda_f|^2$, then the Λ_{UV}^2 contributions of figures 1.2a and 1.2b will be neatly canceled (to explain this would go beyond the aims of this chapter, which is to give an introduction to supersymmetry).

A supersymmetry transformation turns a bosonic state into a fermionic state, and viceversa. The Q operator generating such transformations must be an anticommuting spinor, with

$$Q|Boson\rangle = |Fermion\rangle, \quad Q|Fermion\rangle = |Boson\rangle. \tag{1.16}$$

Spinors are intrinsically complex objects, so $Q^\dagger$ (the hermitian conjugate of Q) is also a symmetry generator. Because Q and $Q^\dagger$ are fermionic operators, they carry angular momentum of spin 1/2, so it is clear that sypersymmetry [12] must be a spacetime symmetry.

The single-particle states of a sypersymmetric theory fall naturally into irreducible representations of the supersymmetry algebra which are called *supermultiplets*. Each supermultiplet contains both fermion and boson states, which are commonly known as *superpartners* of each other. The $(mass)^2$ operator $-P^2$ commutes with the Q, $Q^\dagger$ operators, and with all spacetime rotation and translation operators, so it follows immediately that particles which inhabit the same irreducible supermultiplet must have equal eigenvalues of $-P^2$, and therefore equal masses.

The supersymmetry generators also commute with the generators of the gauge transformations. Therefore particles in the same supermultiplet must also be in the same representation of the gauge group, and so must have the same electric charges, weak isospin and color degrees of freedom.

Each supermultiplet contains an equal number of fermionic and bosonic degrees of freedom:

$$n_B = n_F. \tag{1.17}$$

The simplest possibility for a supermultiplet which is consistent with eq. (1.17) has:

- a single Weyl fermion (with two helicity states, so $n_F = 2$) and

• two real scalars (each with $n_B = 1$).

This combination of a two-componet Weyl fermion and a complex scalar field is called a *chiral or matter supermultiplet.*

The next simplest possibility for a supermultiplet contains:

• a spin-1 vector boson. A massless spin-1 boson has two helicity states, so the number of bosonic degrees of freedom is $n_B = 2$. Its superpartner is therefore a massless spin-1/2 Weyl fermion, again with two helicity states, so $n_F = 2$. Gauge bosons must transform as the adjoint representation of the gauge group, so their fermionic partners, called *gauginos*, must also.

Such a combination of spin-1/2 gauginos and spin-1 gauge bosons is called a *gauge or vector supermultiplet.*

The ordinary, non-extended, phenomenologically-viable type of supersymmetric model is sometimes called $N = 1$ supersymmetry, with N referring to the number of supersymmetries (the number of distinct copies of Q, $Q^\dagger$).

The names for the spin-0 partners of the quarks and leptons are constructed by prepending an "s", which is a short for scalar. Thus generically they are called *squarks* and *sleptons* (short for "scalar quark" and "scalar lepton"). The symbols for the squarks and sleptons are the same as for the corresponding fermions, but with a tilde used to denote the superpartner of a Standard Model particle.

The Higgs supersymmetry sector requires two Higgs doublets H_u, H_d with opposite hypercharges in order to give masses to all the matter fermions and to avoid gauge anomalies originated by the spin-1/2 higgsinos (this will be explain in the next section). H_u and H_d are the fields that appear in the Lagrangian, but the physical states of the Higgs boson, after electroweak symmetry breaking, are two charged ($H^\pm$) and three neutral (h, H, A) physical states. The h and H are the CP-odd scalars and A is the CP-even scalar.

1.3 The Minimal Supersymmetric Standard Model (MSSM)

This section explains the supersymmetric extension of the Standard Model (SM). Subsection 1.3.1 presents the SM particles and their superpartners. Subsection 1.3.2 discusses the superpotential and supersymmetric interactions of the MSSM. Subsection

1.3.3 presents the R-parity (also known as matter parity) and its consequences. Subsection 1.3.4 describes the soft supersymmetry breaking in the MSSM. Finally, the last subsection, 1.3.5, introduces the electroweak symmetry breaking and the Higgs bosons in the MSSM.

1.3.1 MSSM spectrum of particles

The chiral supermultiplets of a minimal phenomenologically viable extension of the Standard Model are summarized in Table 1.2, classified according to their transformation properties under the Standard Model gauge group $SU(3)_C \times SU(2)_L \times U(1)_Y$, which combines ($u_L$, d_L) and (ν, e_L) degrees of freedom into $SU(2)_L$ doublets. Here we have followed the standard convention that all chiral supermultiplets are defined in terms of left-handed Weyl spinors, so that the *conjugates* of the right-handed quarks and leptons (and their superpartners) appear in Table 1.2. Q stands for the $SU(2)_L$-doublet chiral supermultiplet containing $\widetilde{u}_L$, u_L (with weak isospin component $L_3 = 1/2$) and $\widetilde{d}_L$, d_L (with $L_3 = -1/2$), while $\overline{u}$ stands for the $SU(2)_L$-singlet supermultiplet containing $\widetilde{u}^*_R$, $u^\dagger_R$. There are three families for each of the quark and lepton supermultiplets, but we have used first-family representatives only. The superpartners of the left- and right-handed parts of the electron Dirac field are called left- and right-handed selectrons and they are denoted by $\widetilde{e}_L$ and $\widetilde{e}_R$. It is important to keep in mind that the "handedness" here does not refer to the helicity of the selectrons, since they are spin 0 particles, but to that of their superpartners. In the SM the neutrinos are always left-handed, so the sneutrinos are denoted generically by $\widetilde{\nu}$ with a subscript to indicate which lepton flavour they carry.

The two Higgs doublets (H_u, H_d) have hypercharge Y= +1/2 and -1/2 respectively. This is due to the structure of the supersymmetric theories: only a $Y = 1/2$ Higgs chiral supermultiplet can have the necessary Yukawa couplings to give masses to up-type quarks with charge +2/3, and only a $Y =$ -1/2 Higgs can give masses to down-type quarks with charge -1/3 and to charged leptons. The neutral scalar that corresponds to the physical SM Higgs boson is a linear combination of H^0_u and H^0_d. The fermionic partners of the Higgs scalars are called higgsinos. It is interesting to note that the Higgs chiral supermultiplet H_d has exactly the same Standard Model gauge quantum numbers as the left-handed sleptons and leptons L_i.

The electroweak gauge symmetry $SU(2)_L \times U(1)_Y$ has associated with it the spin-1 gauge bosons W^+, W^0, W^- and B^0, as well as the spin-1/2 superpartners $\widetilde{W}^+, \widetilde{W}^0, \widetilde{W}^-$ and $\widetilde{B}^0$, called *winos* and *bino*. After electroweak symmetry breaking, the W^0, B^0 gauge eigenstates mix to give mass eigenstates Z^0 and γ. The corresponding gaugino mixtures of $\widetilde{W}^0$ and $\widetilde{B}^0$ are called zino ($\widetilde{Z}^0$) and photino ($\widetilde{\gamma}$). Table 1.3 summarizes the gauge supermultiplets of a minimal supersymmetric extension of the Standard Model.

Table 1.2: Chiral supermultiplets in the Minimal Supersymmetric Standard Model. The hypercharge is computed using the equation $Q_{em} = L_3 + Y$ where L_3 is the third isospin component, Q_{em} is the electromagnetic charge and Y is the hypercharge.

Names		spin 0	spin 1/2	$SU(3)_C \times SU(2)_L \times U(1)_Y$
squarks, quarks	Q	$(\widetilde{u}_L, \widetilde{d}_L)$	(u_L, d_L)	(3,2,1/6)
(× 3 families)	$\overline{u}$	$\widetilde{u}^*_R$	$u^\dagger_R$	($\overline{3}$,1,-2/3)
	$\overline{d}$	$\widetilde{d}^*_R$	$d^\dagger_R$	($\overline{3}$,1,1/3)
sleptons, leptons	L	$(\widetilde{\nu}, \widetilde{e}_L)$	(ν, e_L)	(1,2, -1/2)
(× 3 families)	$\overline{e}$	$\widetilde{e}^*_R$	$e^\dagger_R$	(1,1,1)
Higgs, Higgsinos	H_u	(H^+_u, H^0_u)	$(\widetilde{H}^+_u, \widetilde{H}^0_u)$	(1,2,1/2)
	H_d	(H^0_d, H^-_d)	$(\widetilde{H}^0_d, \widetilde{H}^-_d)$	(1,2,-1/2)

Table 1.3: Gauge supermultiplets in the Minimal Supersymmetric Standard Model.

Names	spin 1/2	spin 1	$SU(3)_C \times SU(2)_L \times U(1)_Y$
gluino, gluon	$\widetilde{g}$	g	(8,1,0)
winos, W bosons	$\widetilde{W}^\pm$, $\widetilde{W}^0$	$W^\pm$, W^0	(1,3,0)
bino, B boson	$\widetilde{B}^0$	B^0	(1,1,0)

Higgsinos and electroweak gauginos mix with each other because of the effects of electroweak symmetry breaking. The neutral higgsinos $\widetilde{H}_u^0$ and $\widetilde{H}_d^0$, and the neutral gauginos $\widetilde{B}$ and $\widetilde{W}^0$ combine to form four neutral mass eigenstates called *neutralinos*, $\widetilde{X}_{i=1,2,3,4}^0$. The charged higgsinos $\widetilde{H}_u^{\pm}$ and $\widetilde{H}_d^{\pm}$, and the winos $\widetilde{W}^{\pm}$, mix to form two mass eigenstates with charge ± 1 called *charginos* $\widetilde{X}_{i=1,2,3,4}^{\pm}$.

1.3.2 The superpotential and supersymmetric interactions

The superpotential for the MSSM is given by:

$$W_{MSSM} = \overline{u} y_u Q H_u - \overline{d} y_d Q H_d - \overline{e} y_e L H_d + \mu H_u H_d \tag{1.18}$$

where H_u, H_d, Q, L, $\overline{u}$, $\overline{d}$, $\overline{e}$ are the chiral superfields corresponding to the chiral supermultiplets given in Table 1.2. The dimensionless Yukawa coupling parameters: y_u, y_d, y_e are 3×3 matrices in the familie space. The Yukawa matrices determine the masses and CKM (Cabibbo-Kobayashi-Maskawa) mixing angles of the ordinary quarks and leptons after the neutral scalar components of H_u and H_d get VEVs (Vacuum Expectation Value). The μ term is the supersymmetric version of the Higgs boson mass in the Standard Model.

Since the Yukawa interactions y^{ijk} in a general supersymmetric theory must be completely symmetric under interchange of i, j, k, we know that y_u, y_d and y_e imply not only Higgs-quark-quark and Higgs-lepton-lepton coupling as in the Standard Model, but also squark-Higgsino-quark and slepton-Higgsino-lepton interactions. To illustrate this, some of the interactions which involve the top-quark Yukawa coupling are shown in figure 1.3.

Figure 1.3a is the Standard Model-like coupling of the top quark to the neutral complex scalar Higgs boson. In figure 1.3b, it is shown the coupling of left-handed top squark $\widetilde{t}_L$ to the neutral higgsino field H_u^0 and right-handed top quark, while in figure 1.3c the right-handed top-squark field couples to $\widetilde{H}_u^0$ and t_L. For each of the three interactions, there is a similar one by changing $H_u^0 \to H_u^+$ and $t_L \to -b_L$ (with tildes where appropriate). All of these interactions are required by the supersymmetry to have the same strength y_t. This is also an incontrovertible prediction of softly-broken supersymmetry at tree-level.

There exist also scalar quartic interactions with strength proportional to y_t^2, as can be seen in figure 1.4. Three of them are shown in the figure, but there are nine more, which can be obtained by replacing $\widetilde{t}_L \to \widetilde{b}_L$ and/or $H_u^0 \to H_u^+$ in each vertex. This

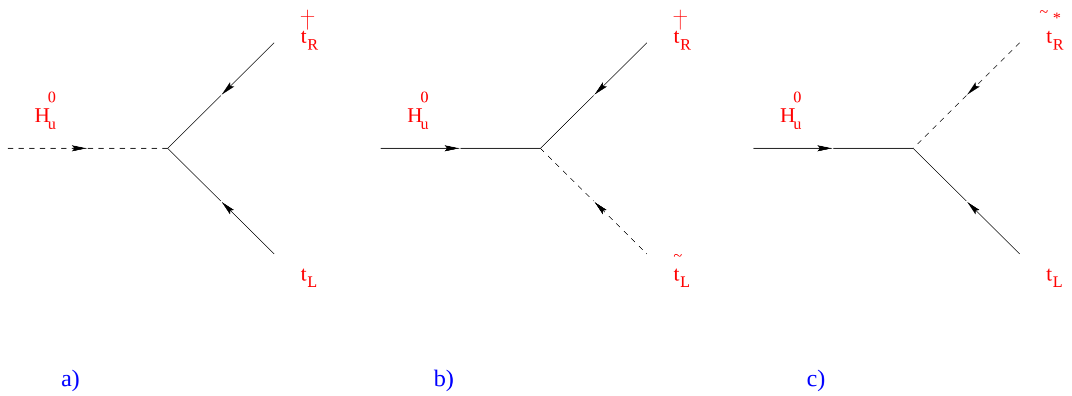

Figure 1.3: The top-quark Yukawa coupling (a) and its supersymmetrizations (b), (c), all of strength y_t.

illustrates the remarcable economy of supersymmetry; there are many interactions determined by only a single parameter! In a similar way, the existence of all other quark and lepton Yukawa couplings in the superpotential leads not only to the Higgs-quark-quark and Higgs-lepton-lepton in the lagrangian terms as in the ordinary Standard Model, but also to squark-higgsino-quark and slepton-higgsino-lepton terms, and scalar quartic coupling terms $[(squark)^4$, $(slepton)^4$, $(squark)^2(slepton)^2$, $(squark)^2(Higgs)^2$, and $(slepton)^2(Higgs)^2]$.

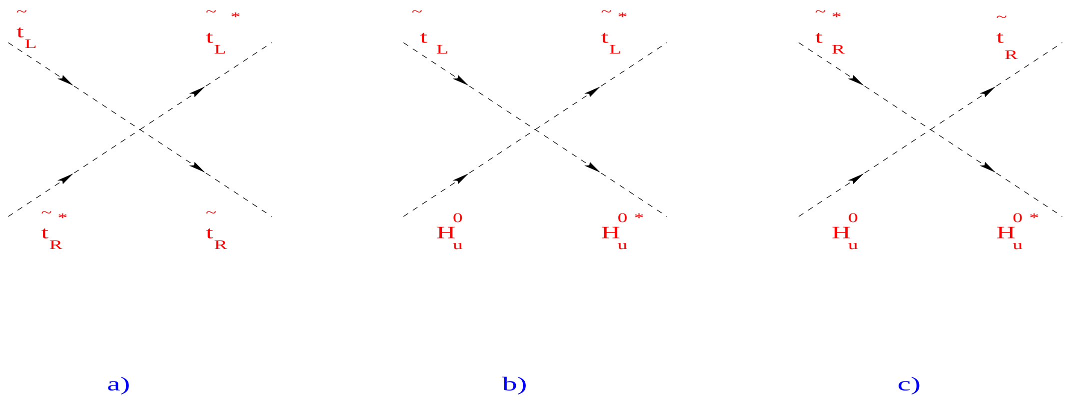

Figure 1.4: Some of the quartic interactions with strength proportional to y_t^2.

Decay and especially production processes for superpartners in the MSSM are typically dominated by the supersymmetric interactions of the gauge-coupling strength. The couplings of the Standard Model gauge bosons (photon, $W^\pm$, Z^0) to the MSSM particles are determined completely by the gauge invariance of the kinetic terms in the lagrangian. The gauginos also couple to (squark, quark), (slepton, lepton) and (Higgs, higgsino) pairs. The Feynman diagram for this interaction is shown in figure 1.5a.

Figure 1.5b,c shows in a similar way the coupling of (squark, quark), (lepton, slepton) and (Higgs, higgsino) pairs to the winos and bino, with strengths proportional to the electroweak gauge couplings g and g' respectiveley.

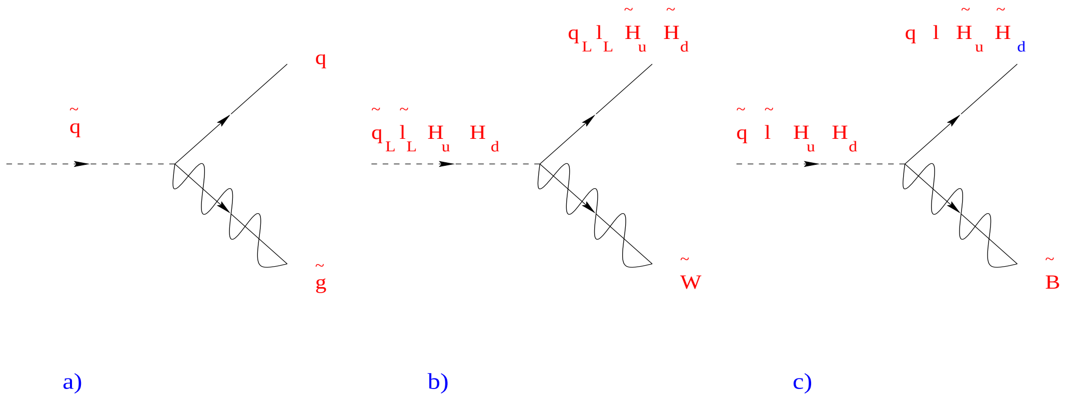

Figure 1.5: Coupling of the gluino, wino, and bino to MSSM (scalar, fermion) pairs.

The dimensionful terms in the supersymmetric part of the MSSM lagrangian are all dependent on μ. The μ-term and the Yukawa couplings in the superpotential, eq. (1.18), combine to yield $(scalar)^3$ of the form represented in figure 1.6 for the MSSM case. These couplings which are proportional to $\mu^* y_t$, $\mu^* y_b$, and $\mu^* y_\tau$, respectively, play an important role in determing the mixing of top squarks, bottom squarks, and tau sleptons.

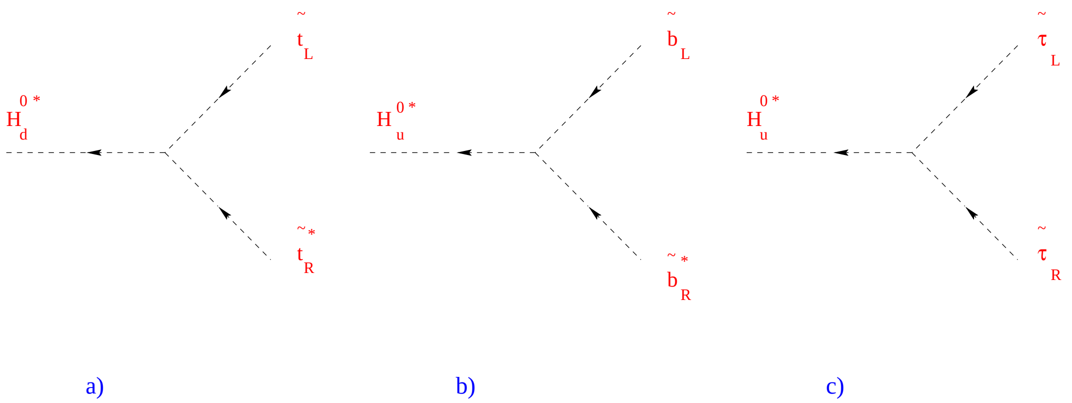

Figure 1.6: Some of the supersymmetric cubic couplings proportional to $\mu^* y_t$, $\mu^* y_b$, and $\mu^* y_\tau$.

1.3.3 R-parity and its consequences

In the MSSM one needs to add a new symmetry which has the effect of eliminating the possibility of baryon (B) and lepton (L) violating terms in the renormalizable superpotential. This new symmetry is called "R-parity" [13], also known as "matter parity", which is defined for each MSSM particle as:

$$P_R = (-1)^{3(B-L)+2s} \tag{1.19}$$

where B and L are the baryon and lepton quantum numbers and s is the spin of the particle.

The advantage of R-parity is that it can be in principle an *exact* and fundamental symmetry, while B and L themselves cannot, since they are known to be violated by non-perturbative electroweak effects. Even though with exact matter parity conservation in the MSSM, one expects that baryon number and total lepton number violation will occur in very tiny amounts, due to non-renormalizable terms in the Lagrangian.

The R-parity assignment is very useful for phenomenology because all of the Standard Model particles and the Higgs bosons have even R-parity ($P_R = +1$), while all of the squarks, sleptons, gauginos and higgsinos have odd R-parity ($P_R = -1$).

The odd R-parity particles are known as "supersymmetric particles" or "sparticles" for short, and they are distinguished by a tilde (see tables 1.2 and 1.3). If R-parity is exactly conserved, then there can be no mixing between the sparticles and the $P_R = +1$ particles. Furthermore, every interaction vertex in the theory contains an even number of $P_R = -1$ sparticles. This has three extremely important phenomenological consequences:

• The lightest sparticle with $P_R = -1$, called the "lightest supersymmetric particle" or LSP, must be absolutely stable. If the LSP is electrically neutral it interacts only weakly with ordinary matter, and therefore can be an attractive candidate [14] for the non-baryonic dark matter which seems to be required by cosmology.

• Each sparticle other than the LSP must eventually decay into a state which contains an odd number of LSPs (usually just one).

• In collider experiments, sparticles can only be produced in even numbers (usually two at a time).

1.3.4 Soft supersymmetry breaking in the MSSM

A realistic phenomenological model must contain supersymmetry breaking, because if supersymmetry were unbroken there would have to exist, for example, slectrons with the same mass as the electrons, and such particles would be very easy to detect, but they have not been discovered yet. From a theoretical perspective, we expect that supersymmetry, if it exists at all, should be an exact symmetry which is spontaneously broken. In other words, the ultimate model should have a lagrangian density which is invariant under supersymmetry, but a vacuum state which is not. Many models of the spontaneous symmetry breaking have indeed been proposed. They always involve the MSSM extending to include new particles and interactions at very high mass scales, and there is no consensus on exactly how this should be done. However, from a practical point of view, it is extremely useful to simply parametrize our ignorance of these issues by just introducing extra terms which break supersymmetry explicitly in the effective lagrangian. The extra supersymmetry-breaking coupling should be soft in order to be able to naturally maintain a hierarchy between the electroweak scale and the Planck mass scale. In the context of a general renormalizable theory, the possible soft supersymmetry-breaking terms in the lagrangian are:

$$\begin{aligned} L_{soft}^{MSSM} = & -\frac{1}{2}(M_3\widetilde{g}\widetilde{g} + M_2\widetilde{W}\widetilde{W} + M_1\widetilde{B}\widetilde{B}) + c.c. \\ & -(\widetilde{\overline{u}}\mathbf{a_u}\widetilde{Q}H_u - \widetilde{\overline{d}}\mathbf{a_d}\widetilde{Q}H_d - \widetilde{\overline{e}}\mathbf{a_e}\widetilde{\overline{L}}H_d) + c.c \\ & -\widetilde{Q}^\dagger\mathbf{m_Q^2}\widetilde{Q} - \widetilde{L}^\dagger\mathbf{m_L^2}\widetilde{L} - \widetilde{\overline{u}}\mathbf{m_{\overline{u}}^2}\widetilde{\overline{u}}^\dagger - \widetilde{\overline{d}}\mathbf{m_{\overline{d}}^2}\widetilde{\overline{d}}^\dagger - \widetilde{\overline{e}}\mathbf{m_{\overline{e}}^2}\widetilde{\overline{e}}^\dagger \\ & -m_{H_u}^2 H_u^* H_u - m_{H_d}^2 H_d^* H_d - (bH_uH_d + c.c.) \end{aligned} \tag{1.20}$$

where M_3, M_2 and M_1 are the gluino, wino, and bino mass terms. The second line in the lagrangian contains the cubic scalar couplings. Each of a_u, a_d, a_e is a complex 3×3 matrix in a family space, with mass dimensions. They are in one-to-one correspondence with the Yukawa coupling matrices in the superpotential. The third line consists of squarks and slepton mass terms, where m_Q^2, m_L^2, $m_{\overline{u}}^2$, $m_{\overline{d}}^2$, $m_{\overline{e}}^2$ are 3×3 matrix. Finally, in the last line we have supersymmetry-breaking contributions to the Higgs potential, being $m_{H_u}^2$, $m_{H_d}^2$ and b $(mass)^2$ terms.

L_{soft}^{MSSM} introduces many new parameters which were not present in the ordinary Standard Model. A careful counting reveals that there are 105 parameters: masses, phases and mixing angles in the MSSM lagrangian which cannot be rotated away by redefining the phases and basics flavours for the quark and lepton supermultiplets, and which have no counterpart in the ordinary Standard Model. Thus, in principle, supersymmetry appears to introduce a tremendous arbitrariness in the lagrangian.

Fortunately, there is already good experimental evidence that some sort of powerful "organizing principle" must govern the soft terms [12]. This is because most of the new parameters in eq. (1.20) involve flavour mixing or CP violation of the type which is already severely restricted by the experiments [15].

1.3.4.1 Electroweak symmetry breaking and the Higgs bosons

In the MSSM, the description of electroweak symmetry breaking is slightly complicated by the fact that there are two complex Higgs doublets: $H_u = (H_u^+, H_u^0)$ and $H_d = (H_d^+, H_d^0)$, rather than just one as in the ordinary Standard Model. The reason is the following: the features of the W superpotential (equation 1.18 in section 1.3.2), which determines the chiral interactions, do not allow to introduce complex conjugates. If complex conjugates are introduced in the superpotential, supersymmetry is automatically broken in an uncontrolled way. To avoid this problem, the complex conjugates are substituted by another Higgs doublet. As it has been explained in section 1.3.2, supersymmetry must be broken in a controlled way by introducing soft terms in the potential.

Having established the necessary conditions for H_u^0 and H_d^0 to get non-zero VEVs, we can now require that they are compatible with the observed phenomenology of electroweak symmetry breaking $SU(2)_L \times U(1)_Y \to U(1)_{EM}$. Being their VEVs: $\langle H_u^0 \rangle = v_u$ and $\langle H_d^0 \rangle = v_d$, at the minimum of the potential. These VEVs can be connected to the known mass of the Z^0 boson and the electroweak gauge couplings:

$$v_u^2 + v_d^2 = v^2 = 2m_Z^2/(g^2 + g'^2) \sim (174\ GeV)^2. \tag{1.21}$$

The ratio of the two VEVs is traditionally written as:

$$tan\beta = v_u/v_d \tag{1.22}$$

The $tan\beta$ value is not fixed, but it depends on the MSSM lagrangian parameters in a calculable way. Since $v_u = vsin\beta$ and $v_d = vcos\beta$ were taken to be real and positive, we have a requirement that $0 < \beta < \pi/2$.

The Higgs scalar fields in the MSSM consist of two complex $SU(2)_L$-doublets, or eight real scalar degrees of freedom. When the electroweak symmetry is broken, three of them are the would-be Nambu-Goldstone bonsons G^0 and $G^\pm$ which become the longitudinal modes of the Z^0 and $W^{\pm}$ massive vector bosons. The remaining five Higgs scalar mass eigenstates consist of one CP-odd neutral scalar A^0, a charge +1 scalar H^+ and its conjugate charge -1 scalar H^-, and two CP-even neutral scalars h^0 and H^0.

The masses of A^0, H^0 and $H^{\pm}$ can in principle be arbitrarily large, but the mass of h^0 is bounded from the requirements given above [12]:

$$m_{h^0} \leq 150\ GeV \tag{1.23}$$

that is assuming that none of the MSSM sparticles have masses exceeding 1 TeV and that all of the couplings in the theory remain perturbative up to the unification scale. The particles A^0, H^0 and $H^{\pm}$ are much heavier and nearly degenerate, forming an isospin doublet which decouples from sufficiently low-energy experiments.

In the MSSM the masses and CKM mixing angles of the quarks and leptons are determined by the Yukawa coupling of the superpotential and by the $tan\beta$ parameter. This is because the top, charm and up quarks get masses proportional to $v_u = vsin\beta$ and the bottom, strange, and down quarks as well as the charge leptons get masses proportional to $v_d = vcos\beta$.

There are good theoretical motivations to consider models with large $tan\beta$. For example: models based on the Grand Unification Theory (GUT) gauge group $SO(10)$ can unify the running top, bottom and tau Yukawa couplings at the unification scale; this requires $tan\beta$ to be roughly of the order of m_t/m_b [16].

Bibliography

[1] Hall, Nina, A Supercollider for Europe, New Scientist v.131, p. 35-9, July 27, 1991.

[2] Glashow, S.L., Nucl. Phys. 22, 579 (1961).

[3] Weinberg, S., Phys. Rev. Lett. 19, 1264 (1967).

[4] Salam, A., Elementary Particle Theory, N. Svartholm, ed.(Stockholm: Almquist and Wiksell, 1986).

[5] Coughlan, G.D. and Dodd, J.E., The Ideas of Particle Physics: An Introduction for Scientists, Cambridge University Press, Cambridge, 1991.

[6] Quigg, Chris., Gauge Theories of the Strong, Weak, and Electromagnetic Interactions, Addison-Wesley, Reading, Massachusetts, 1993.

[7] Ellis, J., Beyond the Standard Model for Hillwalkers, CERN-TH/98-329, 1998.

[8] Jenni, P. and White, H., Physics and Experimental Challenge of Future Hadron Colliders, Proceeding of a lectures series given at Eigth Lake Louisse Winter Institute, Lake Louise, Alberta, Canada, February, 1993.

[9] Gelmini, G., Beyond the Standard Model, Proceedings of the Eighth Lake Louisse Winter Institute, Lake Louise, Alberta. Canada, February, 1993.

[10] Gunion, J. et al., The Higgs Hunter's Guide, Addison-Wesley, Redwood City, California, 1990.

[11] Weinberg, S., Phys. Rev. D 13, 974 (1976); Phys. Rev. D 19, 1277 (1979); Susskind, L., Phys. Rev. D 20, 2619 (1979); Hooft, G. 't., in Recent development in gauge theories, Proceedings of the NATO Advanced Summer Institute, Cargese 1979, ed. Hooft, G. 't. et al. (Plenum, New York 1980).

[12] Martin S. P., A Supersymmetry Primer, hep-ph/9709356.

[13] Farrar, G. R. and Fayet, P., Phys. Lett. B 76, 575 (1978).

[14] Goldber, H., Phys. Rev. Lett. 50, 1419 (1983); Ellis, J., Hagelin, J., Nanopoulos, D.V., Olive, K., and Srednicki, M., Nucl. Phys. B238, 453 (1984).

[15] Gabbiani, F., Gabrielli, E., Masiero, A., and Silvestrini, L., Nucl. Phys. B477, 321 (1996) and references therein.

[16] Lopez, C., Phys. lett B 126, 54 (1983); Arason, H., et al., Phys. Rev. Lett. 67, 2933(1991); Barger, V., Berger, M.S., and Ohmann, P., Phys. Rev. D 47, 1093 (1993); Anderson, G. et al, Phys. Rev. D 49, 3660 (1994).

Chapter 2

The experimental setup

LEP (**L**arge **E**lectron **P**ositron collider) has provided unsurpassed measurements in quantity and quality which serve to test our best description of sub-atomic matter (The Standard Model), at the moment with a precision of 1% and soon one part in a thousand will be reached. By 1996, the energy per beam was doubled upto 100 GeV in the phase called LEPII, opening up an important new discovery domain. LEP data are so accurate that they are sensitive to phenomena that occur at energies beyond those of the machine itself; rather like delicate measurements of earthquake tremors far from an epicentre. This gives us a “preview” of exciting discoveries that may be made at higher energies, and allow us to calculate the parameters of a machine that can make those discoveries. All evidences indicate that new physics and answers to some of the most profound questions of our time lie at energies around 1 TeV.

To look for this new physics, the next research instrument in Europe’s particle physics armoury is the **L**arge **H**adron **C**ollider LHC. This accelerator will be operative at CERN (The European Laboratory for Particle Physics) in the 2005.

ATLAS is a general-purpose experiment that will exploit the full potential of the LHC p-p collision program. The design aspects of the ATLAS sub-detectors are described in this chapter, including performance results from the prototypes being built in the past years. Most of the information is taken from the recently published Technical Design Reports for all of the sub-systems of the experiment. In addition, some highlights of the LHC machine and its challenges are described at the beginning of the chapter.

2.1 The LHC Machine

The LHC is designed to share the 27-kilometre LEP tunnel, and be fed by existing particle sources and pre-accelerators (fig. 2.1). The LHC is a high-energy, high luminosity proton–proton collider to be built in the existing LEP tunnel at CERN [1]. It will collide beams of 7 TeV and its design luminosity is $10^{34}\ cm^{-2}\ s^{-1}$.

Before the particles are injected into the LHC ring they are accelerated up to a given energy by a chain of preaccelerators:

- the LINAC accelerates the protons up to 50 MeV, then the Booster up to 1 GeV;

- the Proton Synchrotron (PS) and Super Proton Synchrotron (SPS) increase the energy up to 26 GeV and 450 GeV respectively, for the final injection into LHC (fig. 2.1).

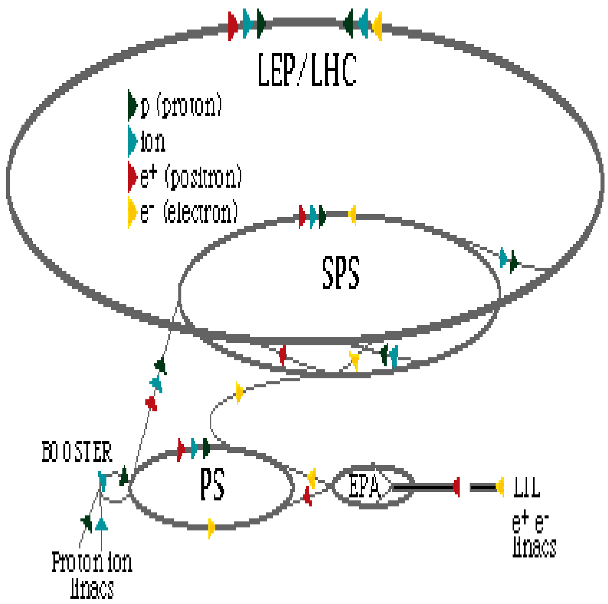

Figure 2.1: The LEP/LHC injector system.

Since in the LHC will collide particle beams of the same charge, two separate beam-lines are necessary in order to allow two proton beams to circulate in opposite directions. The direction of the magnetic field in one beam-line must be opposite to that of the other beam-line. CERN has decided to accomplish this by using a magnet design that combines the two guide fields into a single magnet design as shown in figure 2.2. This option was chosen over the one using two separate magnets due to space restrictions in the LEP tunnel. In order to meet the LHC energy requirements, 1296 superconducting magnets (cooled with superfluid Helium) with a length of 12.2 metres and a field strength of $\sim$ 8.6 Tesla will be installed. However, dipole bending magnets are not the only superconducting magnets needed for the LHC ring; 3.1 metre, 6.9 Tesla superconducting quadrupole magnets are also neeeded for beam focusing.

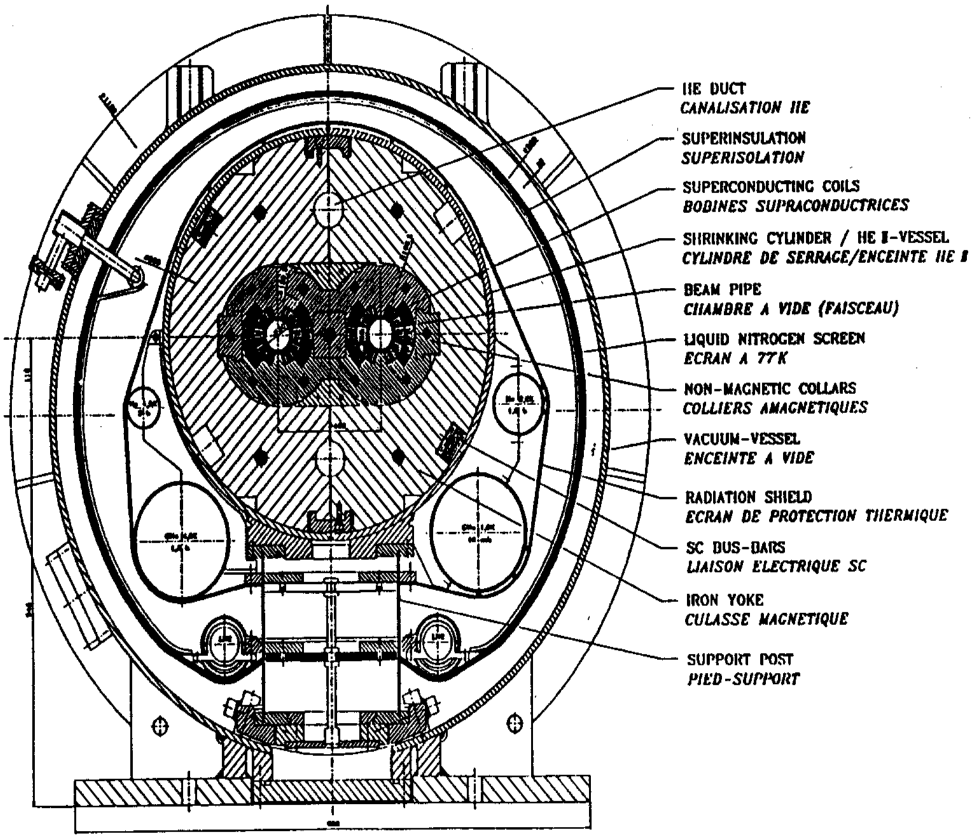

Figure 2.2: The cross-section of an standard LHC two-in-one dipole in its cryostat.

The primary purpose of the LHC is to search for and to study new physics. Although with the LEP results the Standard Model is tested sometimes to better than 1% level, some fundamental questions are still open. In particular, one hopes to understand the origin of electroweak symmetry breaking (masses of W and Z bosons) looking primarily for one or more Higgs bosons, for example. The LHC can also be used to search for Supersymmetric (SUSY) particles which -if exist- will be produced in some cases with large rates, since the cross-sections for producing squarks and gluinos are large. Some other possibilities for new physics that could be studied at LHC are: quark compositeness, leptoquarks and heavy vector bosons (W',Z'). And last but not least, with the new energy regime that opens, there is always room for the unexpected.

Experiments at LHC will be able to provide many measurements related to known physics, such as top decay properties, B-physics and numerous cross-section measurements (W,Z, γ and jet production, for example). The B-physics programme will include studies of CP violation which will allow testing of the Standard Model, in which CP violation is parametrised within the CKM matrix. It will also include the measurement of B_s^0 oscillations, the search for rare B decays such as $B_s^0 \to \mu^+ \mu^-(X)$ and the study of doubly-heavy hadrons such as B_c.

The LHC can also be used to collide beams of heavy ions (e.g. lead ions) with a centre-of-mass energy of about 6 TeV per nucleon, but with lower luminosity ($\sim 10^{27}$ cm^{-2} s^{-1}) and interaction rate of $\sim 10^4$ s^{-1}, to be compared with 10^9 s^{-1} for p-p collisions. The heavy-ion programme has as its primary objective the search for the quark-gluon plasma. One will try to investigate different stages in the production of the plasma before the formation of the normal hadronic matter: the initial conditions, the quark-gluon plasma, the phase transition and the hadronic matter. Finally, it would be possible to operate simultaneously the LHC and a rebuild LEP machine in order to produce e-p collisions, but this only if there are strong physics arguments in the future.

2.1.1 The experimental environment at LHC

In the LHC machine, bunches of protons in counter-rotating beam will be made to collide at the "interaction points". An important parameter of the machine is the 25 ns bunch spacing. The LHC will operate at very high luminosity 10^{34} cm^{-2} s^{-1}. The total inelastic, non-diffractive cross-section at LHC energies will be about 100 mb, corresponding to an interaction rate of 10^9 Hz. The task of the LHC experiments is to identify and select the interesting events on top of a high background. For example, in the case of the Higgs particle with mass 500 GeV, about 17 K events will be produced per year, compared to a total of 1.7×10^{16} events from the inelastic interactions! In addition, with a bunch-crossing rate of 40 MHz (period 25 ns), about 23 interactions will happen in each bunch crossing ("pile-up") resulting in about $\sim$ 10000 tracks in the detector within 100 ns, the typical duration of a pulse in the detectors. This situation impose stringent requirements to the design and performance of the LHC detectors: they must be rather fast, in order to integrate the signals from the pile-up events over many bunch crossings and highly granular in order to minimise the contribution of pile-up in a given detector cell.

The LHC performance parameters are shown in the table 2.1.

The basic layout of the machine (Figure 2.3) mirrors that of LEP, with eight straight sections, each approximately 528 m long, available for experimental insertions or utilities. The two high-luminosity insertions are located at diametrically opposite straight

Table 2.1: *LHC performance parameters.*

Machine performances	
Energy per beam	7 TeV
Dipole field	8.6 Tesla
Coil aperture	56 mm
Distance between apertures	194 mm
Luminosity	$10^{34}\ cm^{-2}\ s^{-1}$
Beam-beam parameter	0.0034
Injection energy	450 GeV
Circulating current/beam	0.54 A
Bunch spacing	25 ns
Particles per bunch	10^{11}
Stored beam energy	334 MJ
Normalized transverse emittance	3.75 μm rad
r.m.s bunch lenght	0.075 m
β-values at I.P. in collision	0.5 m
Full crossing angle	200 μ rad
Beam lifetime	22 h
Luminosity lifetime	10 h
Energy loss per turn	6.7 KeV
Critical photon energy	44.1 eV
Total radiated power per beam	3.6 kW

sections, at point 1 will be placed ATLAS (**A** **T**oroïdal **L**HC **A**pparatu**S**) and at point 5 CMS (**C**ompact **M**uon **S**olenoid). Two more experimental insertions are located at point 2 ALICE (**A** **L**arge **I**on **C**ollider **E**xperiment) and at point 8 LHC-B. These latter straight sections also contain the injection systems. The rings cross only at these four locations.

The high flux of particles from proton-proton interactions (and to a lesser extent from beam losses) places the detectors and associated electronics in a high-radiation environment. Only radiation resistant detectors and read-out electronics can be used.

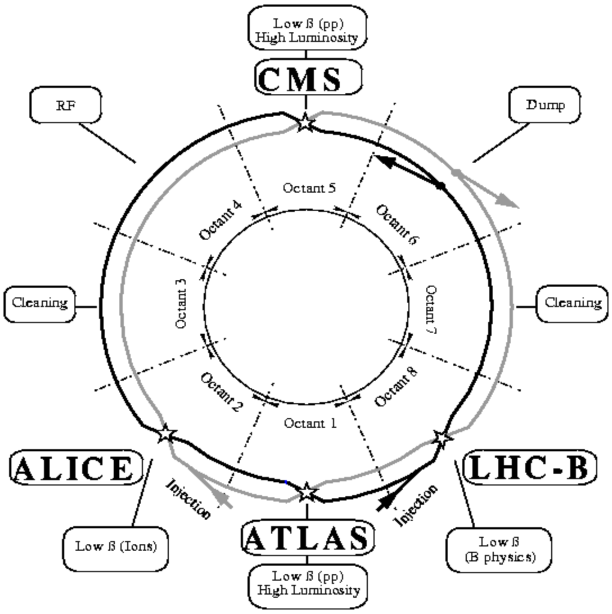

Figure 2.3: The Schematic layout of the LHC.

2.2 The ATLAS Detector

The four LHC experiments differ in their design depending on the physics goals each one would reach. ATLAS uses a large (∼20 m diameter) air-core toroid system for its muon spectrometer, as shown in Figure 2.4. The electromagnetic (EM) calorimetry uses the liquid-argon technique. In the barrel, an iron–scintillator hadronic calorimeter is used and in the endcap the hadronic calorimeter is of the liquid-argon type. In front of the EM barrel calorimeter, and integrated in the same cryostat, there is a superconducting-solenoid coil that provides a 2 T field. The inner-tracking system consists of semiconductor detectors in the innermost part and straw-tubes in the outer part.

The basic design considerations for the ATLAS detector can be summarised as follows: very good EM-calorimetry for e, γ identification and measurement; hermetic jet and E_T^{miss} calorimetry; efficient tracking at high luminosity for lepton measurement, b-quark tagging and enhanced e, γ identification; τ and heavy flavour vertexing and reconstruction capability of some B decays (low luminosity running); low p_T thresholds for the trigger. The detector is expected to be operational in the middle of 2005, when the start-up of the LHC machine is planned.

The ATLAS detector concept was first presented in the Letter of Intent (LoI) [2] and later in the Technical Proposal [3]. Since then, the design has evolved guided by detailed physics performance studies, experience from a rigorous and broad R&D programme, and the necessity to stay within cost-effective technologies. The ATLAS experiment is designed, constructed and operated by a world-wide collaboration of scientists and engineers (~1800 members) from 146 institutions of 33 countries. Spain is contributing with three Institutes and about 4.1% of the ATLAS members.

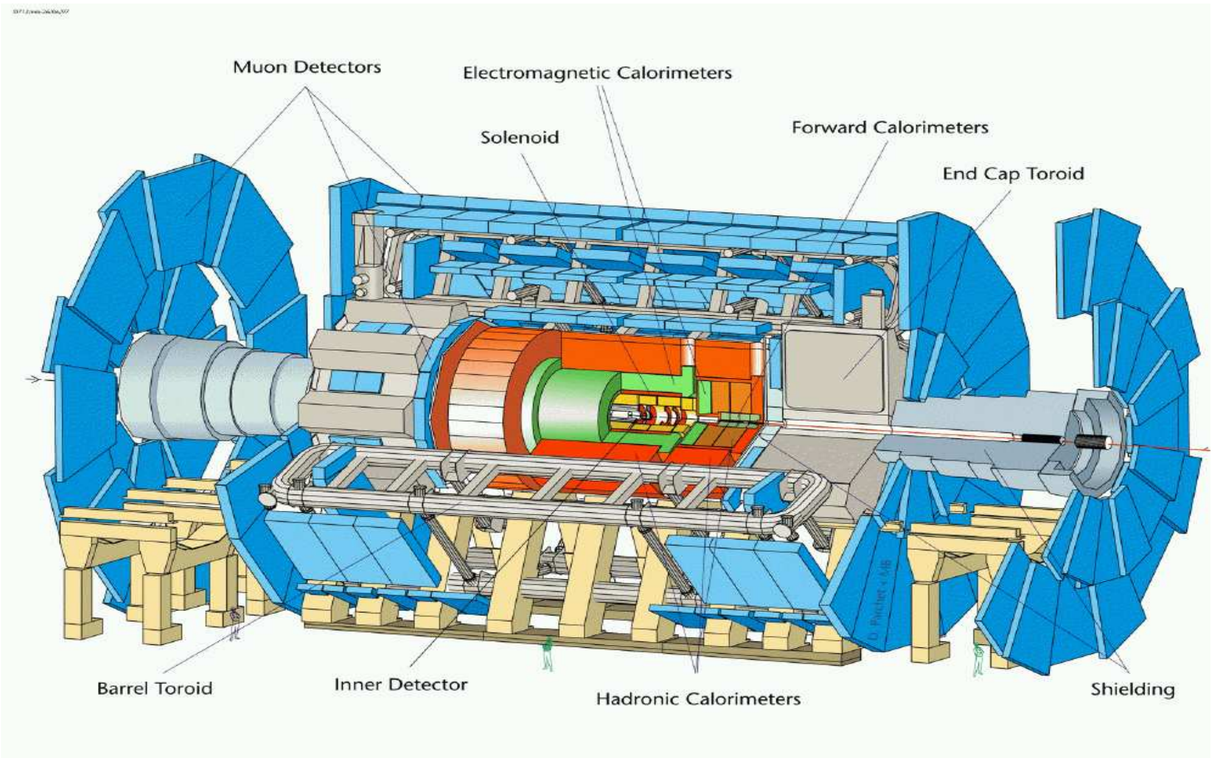

Figure 2.4: The ATLAS detector.

During 1996 to 1998, Technical Design Reports for all the major sub-systems of the experiment were published (except for the Computing, the Higher Level Trigger and

DAQ systems, which are scheduled for later in order to gain the most from technological developments) and presented to the LHC Committee. Since then, following the positive recommendations from the committee, the collaboration entered in a new phase, that of production, which is now starting for many systems. A set of milestones for the project and a complete scheme for regular progress reviews is defined for each system. Such major progress reviews took place in 1998 for the calorimetry, the muon, the inner detector and the magnet systems, with positive results.

Apart from the various sub-detectors of the experiment which will be described in detail in the following subsections, major components are the so called "common projects", which include the magnet system with its inner tracker solenoid and the outer air core toroids for the muon spectrometer, the three cryostats housing the Liquid Argon Calorimeter, and the supports. Substantial progress has been made in these areas and prototype modules for the coils are under construction along with a large test area [4]. The activity in this area as well as the overall experimental hall is in the hands of the Technical Coordination of the experiment which has recently published its Technical Design Report.

A brief description of the experiment sub-detectors is given in the following subsections, putting emphasis in their Module-0 program. The status and major milestones for each system are given as well.

2.2.1 The Inner Detector

The Inner Detector (ID) task is to reconstruct the event tracks and vertices with high efficiency and to contribute with the calorimeter and muon systems to the electron, photon and muon measurement, providing the signature for short-lived particle decay vertices. Its acceptance covers the range $|\eta| \leq 2.5$ (the η is defined as $-log(tan(\theta/2))$, where θ is the polar angle between the beam axis and the particle direction), matching that of the rest of the ATLAS systems for precision measurements [5].

The detectors that constitute the ID at LHC have to meet very stringent requirements such as: be very fast, resistent to hard radiation, have high granularity and good momentum resolution. In addition, the amount of material should be kept as small as possible, otherwise the momentum resolution in the tracker itself will be degraded due to the multiple scattering, and consequently the photon and electron identification as well as energy measurement in the calorimeters will be spoiled. ATLAS has chosen semiconductor detectors for the innermost part of the tracker. A three dimensional cut-away view of the layout of the ID is shown in Figure 2.5. The outer radius of the tracker cavity is 115 cm and the total length is 7 m. Mechanically, the ID consists of three units: a barrel part extending over 2×80 cm and two identical end-caps covering the rest of the cylindrical cavity. In the barrel ($|\eta| \leq 1$), the high-precision detector layers are arranged on concentric cylinders around the beam axis, while the end-cap detectors are mounted on perpendicular disks to the beam axis.

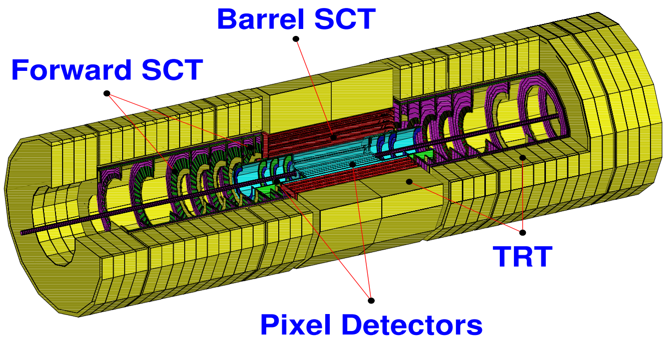

Figure 2.5: Three dimensional cut-away view of the ATLAS Inner Detector.

Starting from the beam pipe, in the range from 4 to 22 cm in radius, pixel detectors providing up to 3 space points per track are used. Following that, and up to 56 cm in radius, a set of Si-strip detectors provide four space points per track. To improve momentum reconstruction, pattern recognition and electron identification a straw-tube Transition Radiation Tracker (TRT) is placed, which provides 36 points per track (> 7 points/track for *electron-identification*). The basic design parameters and resolutions for the space-point measurements are summarised in Table 2.2.

Althoug the straw hits have lower precision than the ones from the silicon layers, their large number and the fact that they come from larger average radius compensate for that, therefore the overall momentum resolution is improved and no single measurement dominates. This means that the overall performance is robust, even in the case that a single system would not perform its full specification. The full momentum resolution, combining the information from the discrete precision points and the large number of drift-time measurements of the TRT in a global fit through the realistic solenoid field map, is shown in Figure 2.6.

The innermost silicon layer of the pixel detector, located at about 4 cm from the interaction point, also called “the B-layer”, has a substantial contribution to the sec-

Table 2.2: The main parameters for the Inner Detector. The quoted resolution are typical values (the actual resolution in each detector depends on $|\eta|$).

Position	**Area** (m^2)	**Resolution** σ (μm)	**Channels** (10^6)	**Coverage** en $\lvert\eta\rvert$
		Pixel Detector		
1 replay barrel layer	0.2	$R\phi = 12 \quad z = 66$	16	± 2.5
2 barrel layers	1.4	$R\phi = 12 \quad z = 66$	81	± 1.7
5 disks/side	0.7	$R\phi = 12 \quad z = 66$	43	1.7-2.5
		SCT Detector		
4 barrel layers	34.4	$R\phi = 16 \quad z = 580$	3.2	± 1.4
9 wheels/side	26.7	$R\phi = 16 \quad z = 580$	3.0	1.4-2.5
		TRT Detector		
axial barrel straws		170/straw	0.1	0.7
radial straws		170/straw	0.32	0.7-2.5

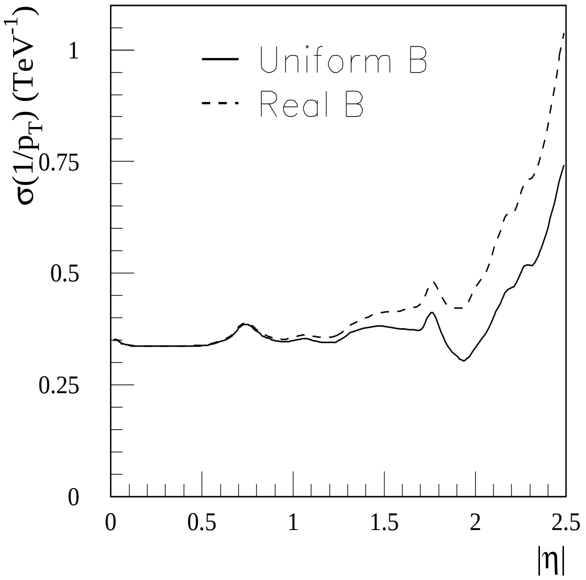

Figure 2.6: Expected momentum resolution from the ID system.

ondary vertex measurement performance during the initial low luminosity running of LHC, and in particular for the B physics sector. Due to the hostile environment at this position, in terms or radiation, this layer is designed to be replaceable during the high luminosity running, since recent physics studies have demonstrated the need for good b-tagging performance during all phases of the LHC, to achieve Higgs and supersymmetry searches. The impact parameter resolution, shown in Figure 2.7, can be parametrised in $r\phi$ as $\sigma(d_0) = 11 + 60/p_T sinv$ and in z as $\sigma(z_0) = 70 + 100/p_T(sinv)^3$ (both in μm) when the dedicated B-physics layer is present. Here d_0 and z_0 are the transversal and logitudinal impact parameters and v is the polar angle.

A big effort has been done to keep the material in the tracking volume to a minimum, by carefull design of the active detectors and by the use of low-Z materials such as aluminium for the power cables, and carbon-fibre reinforced plastic for the support structures (Figure 2.8).

The ATLAS **Pixel Detector** is composed of modular units. Read out integrated circuits are mounted on a detector substrate to form barrel and disk modules. The detector substrate is silicon, and the current baseline is an $n^+ - n$ bulk sensor, with a pixel granularity of 50 $\mu m \times 300$ μm. The read out integrated circuits are mounted on the silicon sensor using bonding techniques. An additional integrated circuit for control and clock distribution and data compression is mounted on each module, and flexible cables connect each module to data transmission/control circuitry located within the detector volume. Prototype detector modules (Figure 2.9) have been built and tested

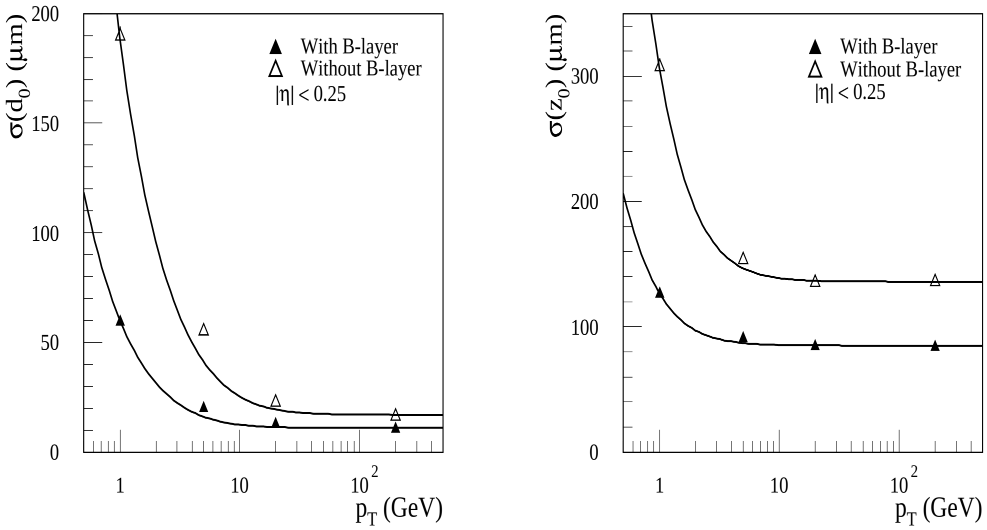

Figure 2.7: The impact parameter resolution: (left) transverse, (right) longitudinal.

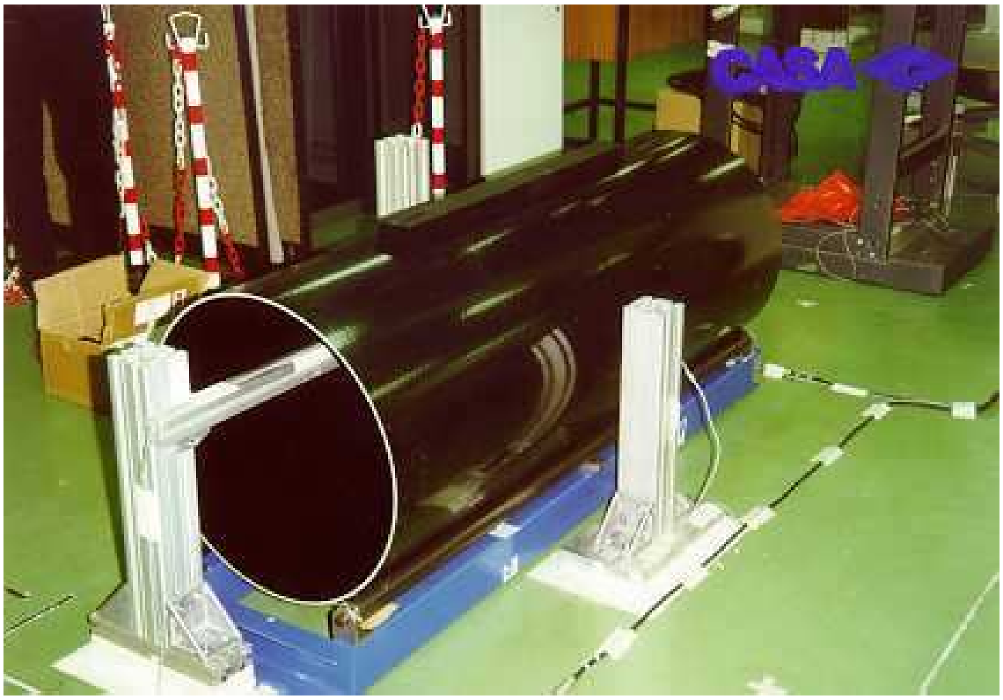

Figure 2.8: Prototype of the SCT detector support cylinder constructed in Spain.

with a particle beam. The modules are overlapped on the support structure in order to give hermetic coverage. There are about 1500 identical barrel modules and about 700 disk modules for the system. Both the barrel and disk modules are mounted on special supporting structures and the resulting mechanical structure is very stable and provides the cooling capability to maintain the silicon temperature at $\leq$ -6° C, even with the large heat load from the electronics. Special attention has been put to the radiation hardness of the detectors, since they have to withstand over 300 KGy of ionising radiation and over 5×10^{14} neutrons per cm^2 in ten years of operation.

The ATLAS **Semiconductor Tracker (SCT)** system is an order of magnitude larger in surface area than previous generations of silicon microstrip detectors and in addition it must face radiation levels which will alter the fundamental characteristics of the silicon wafers themselves. The barrel SCT uses four layers of silicon microstrip detectors to provide precision points in the $r\phi$ and z coordinates, with a small stereo angle to obtain the z measurement. Each silicon detector is 6.36×6.40 cm^2 with 768 read-out strips each with 80 μm pitch. The detector contains 61 m^2 of silicon detectors, with 6.2 million read-out channels. Solutions have been found to the critical issues in the system, and prototype modules have been successfully tested with beams in a magnetic field, showing the required performances in resolution, signal-to-noise ratio and speed. Modules containing both: front-end electronics and detectors, irradiated to the level expected for 10 years of LHC operation have shown to operate within the specifiactions (Figure 2.9).

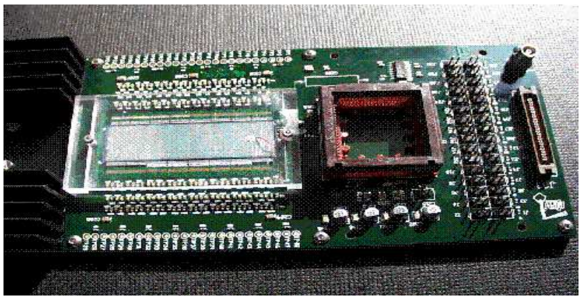

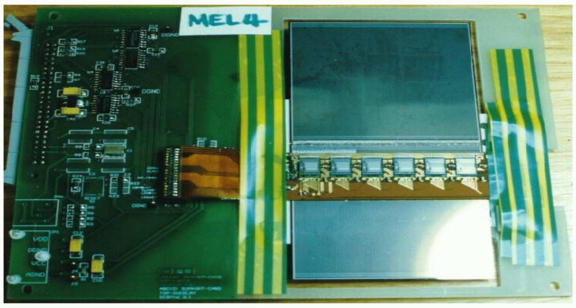

Figure 2.9: Prototype module for the pixel detector (left). View of an assembled SCT module (right).

The **Transition Radiation Tracker** is based on the use of straw detectors, which can operate at the very high rates needed, by virtue of their small diameter and the isolation of the sense wires within individual gas envelopes. Electron identification capability is added by employing Xenon gas to detect transition-radiation photons created in a radiator between the straws. Each straw is 4 mm in diameter, giving a fast response and good mechanical properties for a maximum straw length of 150 cm. The barrel contains about 50000 straws, each divided in two at its centre in order to reduce the occupancy and read out at each end. The end-caps contain 320000 radial straws, with the read-out at the outer radius. The total number of electronic channels is 420000. Each channel provides a drift-time measurement, giving a spatial resolution of 170 μm per straw, and two independent thresholds. These allow the detector to discriminate between tracking hits, which pass the lower threshold, and transition-radiation hits, which pass the higher.

2.2.2 Calorimetry

The calorimeter system will play a crucial role at the LHC. The detectors are required to measure the energy and direction of photons, electrons, isolated hadrons and jets, as well as the missing transverse energy. At the LHC, calorimeters will be the leading detectors for many measurements in physics channels of prime interest. Combined with the inner tracker, calorimeter measurements are used for electron and photon identification. Fast detector response (< 50 ns) and fine granularity are required to minimise the impact of the pile-up on the physics performance. High radiation resistance is also needed, given the high particle fluxes expected over an operation period of at least ten years.

The ATLAS calorimetry covers the range $|\eta| \leq 5$ using different techniques as best suited to the different requirements and radiation environment. A view of the ATLAS calorimetry is shown in Figure 2.10. The rapidity coverage and basic granularity of the calorimeters is summarised in Table 2.3. The EM calorimeter system is contained in a cylinder of outer radius 2.25 m and a total length of 6.65 m along the beam axis. The hadronic calorimeter barrel system has an outer radius of 4.23 m and a total lenght of $\sim$ 12 m. The total weight of the calorimeter system is about 4000 T. The Electromagnetic end-cap, Hadronic and Forward calorimeters are housed in the same cryostat.

The **Electromagnetic Calorimeter** is a Lead Liquid-Argon (LAr) detector with accordion geometry [6]. The principle of the calorimeter is seen in Figure 2.11. In the pseudorapidity range $|\eta| \leq 1.8$ it is preceded by a presampler detector, installed immediately behind the cryostat cold wall and used to correct the lost of energy in the material (inner detector, cryostats, coil) upstream the calorimeter. Its total thickness is $\sim 25\ X_0$ in the barrel and $\sim 26\ X_0$ in the end-caps, being X_0 the radiation length. The total number of channels is about 200000.

During 1998 full size detector modules were constructed and tested with beams (figure 2.12). The energy resolution for electrons is in agreement with the values obtained from the prototype program, with a sampling term of (9.90-10.4)%, a local constant

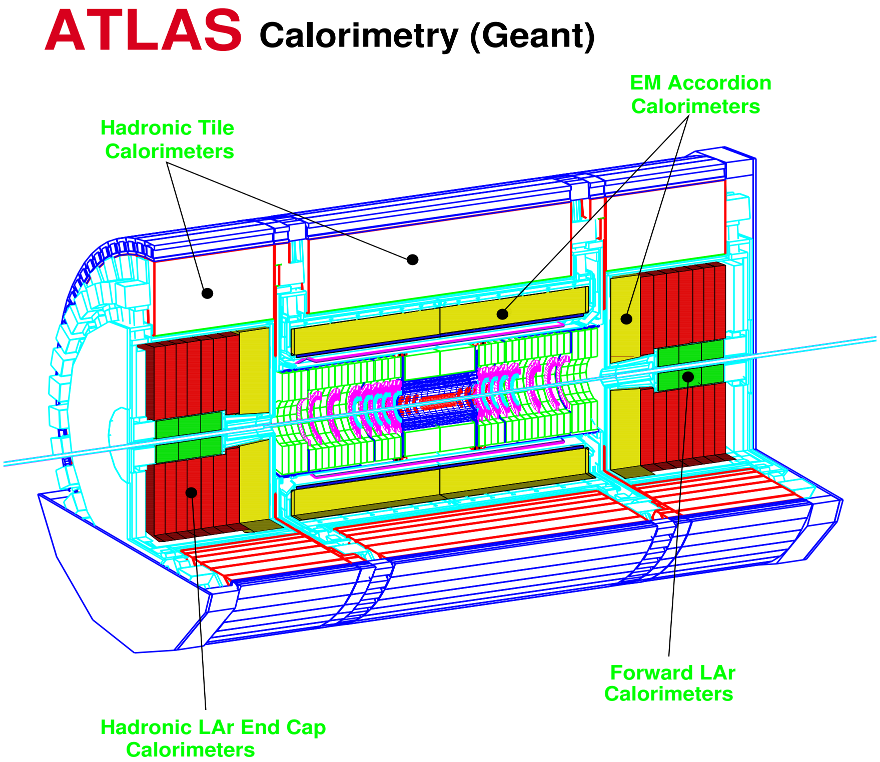

Figure 2.10: View of the ATLAS calorimetry.

Table 2.3: The ATLAS calorimeter system.

System	$\|\eta\|$ **coverage**	**Granularity** ($\Delta\eta \times \Delta\phi$)
EM barrel	$\|\eta\| \leq 1.475$	$0.03 \times 0.1(s1)$ $0.025 \times 0.025(s2)$ $0.05 \times 0.025(s3)$
Presampler	$\|\eta\| \leq 1.8$	0.025×0.1
Hadronic barrel	$\|\eta\| \leq 1.8$	0.1×0.1
Hadronic endcap	$1.5 \leq \|\eta\| \leq 2.5$ $2.5 \leq \|\eta\| \leq 3.2$	0.1×0.1 0.2×0.2
FWD Calo	$3.2 \leq \|\eta\| \leq 4.9$	-0.1×0.2

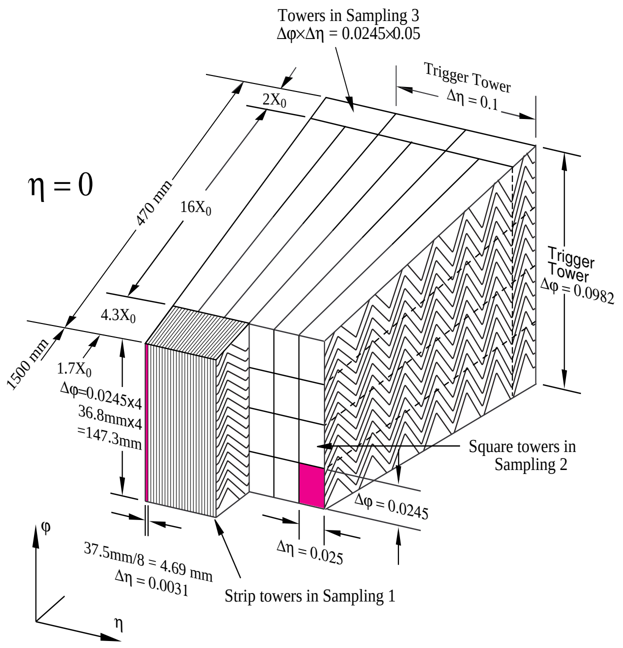

Figure 2.11: Sketch of the accordion structure of the electromagnetic calorimeter.

term of (0.27-0.35)% and a noise term of (280-520) MeV over the full $|\eta|$ range. The overall constant term (which dominates at high energies, therefore very important for LHC) is 0.7% which puts stringent requirements on: the detector construction, the dead material in front of it and the calibration precision.

Apart from the energy measurement, the *EM* calorimeter will provide, thanks to its high granularity, powerful electron/photon identification and rejection of the jet background. The thin strips in the first sampling are the most important feature of this calorimeter. They allow π^0 rejection by a factor larger than 3 at 50 GeV of E_T. In total, the jet rejection, at 20 GeV or above, is expected to be about 5000. Such a rejection is required to eliminate the huge QCD background to the $H \to \gamma\gamma$ channel. The narrow strips contribute also to the photon angular measurement in the $|\eta|$ direction, with an accuracy of about 50 mrad/$\sqrt{E}$, an essential information in the reconstruction of the channel mentioned above. The *EM* calorimeter also serves in identifying τ decays into hadrons. Combined with the tracker, a rejection of about 400 against jets is possible with about 30% efficiency, allowing to improve significantly the signal to background ratio in the search for MSSM Higgs bosons (A/H) decaying into $\tau\tau$ [7].

The **Tile Hadronic Calorimeter** covers the range $|\eta| \leq 1.6$ and it consists of a central barrel and two extended barrel cylinders [8]. The hadronic barrel calorimeter is a cylinder with an inner radius of 2.28 m and an outer radius of 4.23 m. It is based on a sampling technique with plastic scintillator plates (tiles) embedded in an iron absorber

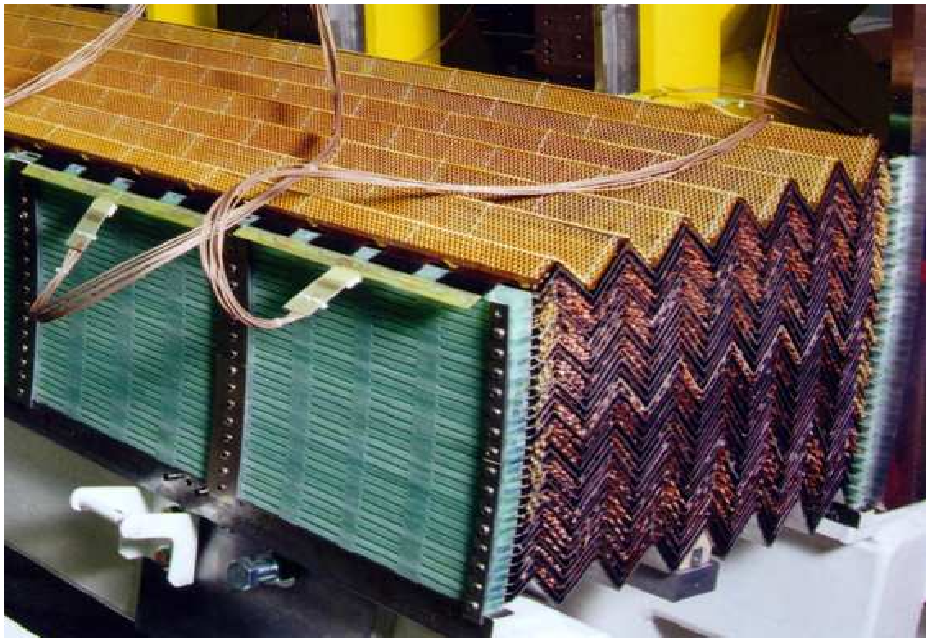

Figure 2.12: EM barrel calorimeter full size module.

matrix; the read out is performed by wave length shifting fibres. The tiles are placed in the perpendicular plane to the beam axis and staggered in depth, simplifying the mechanical construction and the fibre routing. In Figure 2.13 a full size extended barrel calorimeter module is shown during construction.

The calorimeter is segmented in three layers, approximately 1.4, 4.0 and 1.8 λ_{abs} thick at η=0. Azimuthally, the barrel and extended barrels are divided into 64 modules. Read-out cells are built by grouping the optical fibres and routing them to the photomultipliers; this gives the possibility to define pseudo-projective towers in the η direction pointing to the interaction region. The total number of channels is 10000. The tile calorimeter is placed behind the *EM* calorimeter ($\sim 1.2\ \lambda_{abs}$) and the solenoid coil, resulting in a total active calorimeter thickness (*EM* + Tile) of 9.2 λ_{abs} at $\eta = 0$ and a total amount of material in front of the muon system, including the support structure of the Tile calorimeter, of 11 λ_{abs} also at $\eta = 0$.

The required energy resolution is governed by jets measurement, *i.e* $\Delta(E)/E = 50\%/\sqrt{E} \oplus 3\%$, $|\eta| \leq 3$ [8]. The pion resolution obtained from the test beam runs with EM and hadronic prototype modules is $\Delta(E)/E = (38.3 \pm 4.6)\%/\sqrt{E} \oplus (1.62 \pm 0.29)\% \oplus (3.06 \pm 0.18)/E$, in agreement with the ATLAS specifications.

The **Liquid Argon Hadronic Calorimeter** covers the range $1.5 \leq |\eta| \leq 4.9$. The end-cap hadronic calorimeter extends to $|\eta| = 3.2$ while the range $3.1 \leq |\eta| \leq 4.9$ is

Figure 2.13: A Tile Calorimeter extended barrel module constructed in Spain.

covered by the high-density forward calorimeter. Both the hadronic end-cap and the forward calorimeter are integrated in the same cryostat, housing also the EM end-caps. Each hadronic end-cap calorimeter consists of two, equal diameter, independent wheels. The first wheel is built out of 25 mm copper plates, while the second one uses 50 mm plates; in both wheels the gap between consecutive copper plates is 8.5 mm, and is equipped with 3 electrodes that split it in 4 drift spaces of $\sim$ 1.8 mm each one. The wheels are divided in two longitudinal read-out segments. The read-out cells are fully pointing in ϕ direction but only "pseudo pointing" in η. The thickness of the active part of the end-cap calorimeter is $\sim 12\ \lambda_{abs}$.

In ATLAS the **Forward Calorimeter** is integrated in the end-cap cryostat, with the front face at about 5 meters from the interaction point. This makes the forward calorimeter a particular detector due to the high level of radiation. However, a clear benefit in terms of coverage continuity is obtained, because the effects of the crack in the transition region around $|\eta| = 3.1$ are reduced to the minimum, with advantages to the forward efficiency jet tagging and the reduction of the tails in the E_T^{miss} distribution. The forward calorimeter has to accommodate at least 9 λ_{abs} of active detector in a rather short longitudinal space. Thus it is a high density detector, consisting of three longitudinal sections, the first one made of copper, and the other two of tungsten. Each of them consists of a metal matrix with regularly spaced longitudinal channels filled with quartz rods. The sensitive medium is Liquid Argon and fills the gap between the quartz rod and copper matrix. The gaps are 250 microns wide in the first section and 375 (500) microns in the second (last) one. In the forward calorimeter region the electronic noise for E_T in a jet cone of $\Delta R = 0.5$ is ~ 1 GeV at $\eta = 3.2$ and drops quickly to 0.1 GeV at $\eta = 4.6$. The expected jet resolution in the full rapidity range combining the information from the various calorimeters is shown in Figure 2.14 and is adequate for the measurements to be performed.

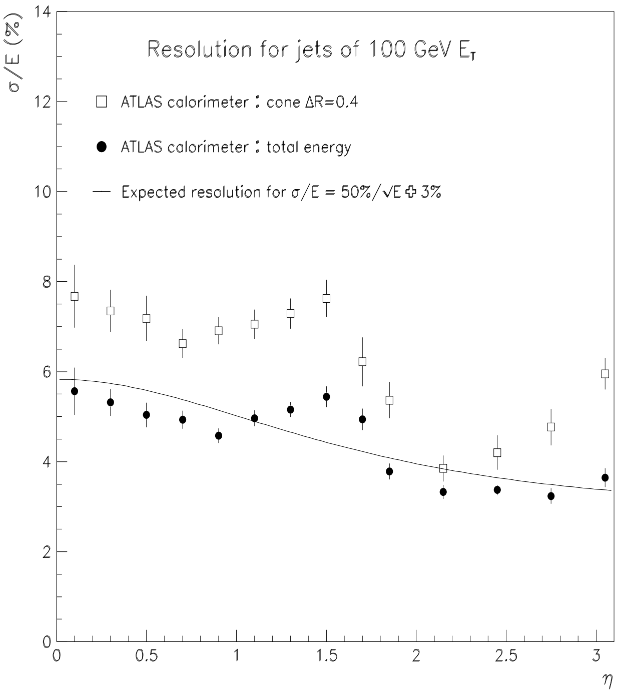

Figure 2.14: The expected jet resolution in ATLAS for the full rapidity range.

2.2.3 The Muon Spectrometer

High-momentun final-state muons are among the signatures of LHC physics the most promising and robust. The discovery potential of the spectrometer has been optimised on the basis of selected benchmark processes, in particular Standard Model and supersymmetric Higgs decays and new vector bosons. The performance of the apparatus for low transverse momentum particles detection which are interesting for beauty physics and CP violation has also been studied. Important parameters that need to be optimised for maximum physics aims are: resolution, second-coordinate measurement, rapidity coverage of track reconstruction, trigger selectivity, trigger coverage and bunch-crossing identification. To exploit this potential, the ATLAS collaboration has designed a high-resolution muon spectrometer with stand-alone triggering and momentum measurement capability covering a wide range of transverse momentum, pseudorapidity and azimuthal angle [9]. The view of the muon spectrometer is shown in Figure 2.15.

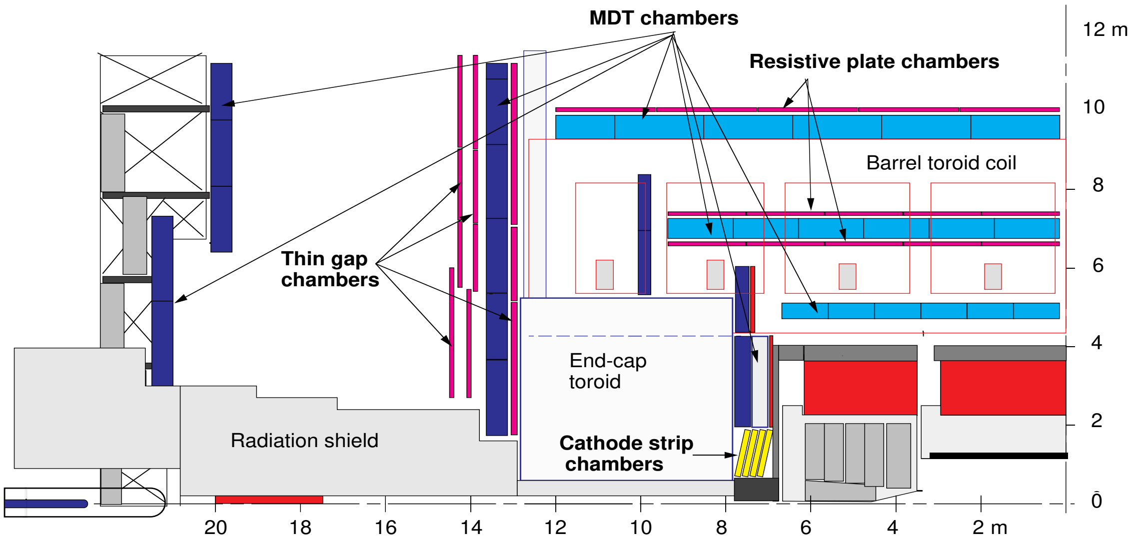

Figure 2.15: View of the ATLAS muon spectrometer.

The muon spectrometer exploits the magnetic deflection of muon tracks in a system of three large superconducting air-core toroid magnets (one barrel and two end-caps) instrumented with separate-function trigger and high-precision tracking chambers. In the pseudorapidity range $|\eta| \leq 1$, magnetic bending is provided by a large barrel magnet consisting of eight coils surrounding the hadron calorimeter. For $\sim 1.4 \leq |\eta| \leq 2.7$, muon tracks are bent in two smaller end-cap magnets inserted into both ends of the barrel toroid. In the interval $1.0 \leq |\eta| \leq 1.4$, referred to as transition region, magnetic deflection is provided by a combination of barrel and end-cap fields. This magnet configuration provides a field that is mostly orthogonal to the muon trajectories, and this minimizes the degradation of resolution due to multiple scattering.

The different contributions to the barrel momentum resolution are shown in Figure 2.16; the behaviour observed is typical for an open-geometry magnetic spectrometer. The resolution is limited by energy loss fluctuations at small momentum and by detector resolution at high momentum, whereas the multiple scattering effect is approximately momentum-independent. The momentum resolution is typically 2-3 % over most of the kinematic range apart from very high momenta, where it increases to ~ 10 % at $p_T = 1$ TeV. Its dependence with $|\eta|$ is also shown in Figure 2.17, for $p_T = 100$ GeV muons. The resolution is largely constant over the η range of the spectrometer, with

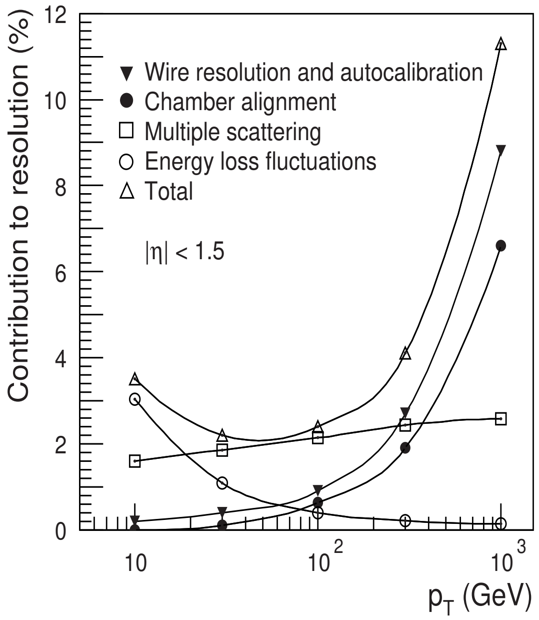

Figure 2.16: Contributions to the momentum resolution of the muon spectrometer, averaged over $|\eta| \leq 1$ and azimuthal angle, in a standard sector.

the exception of some spikes at pseudorapidities obstructed by barrel magnet elements and a degradation around $\eta = 1.5$ owing to a less bending power in the transition region between barrel and end-cap magnets.

Over most of the pseudorapidity range, a precise measurement of the track coordinates in the principal bending direction of the magnetic field is provided by **Monitored Drift Tubes (MDT)**. The basic detection elements are aluminium tubes of 30 mm diameter and 400 μm wall thickness, with a 50 μm diameter central W-Re wire. The tubes are operated with a non-flammable $ArCO_2$ mixture at 3 bar absolute pressure. The envisaged working point provides a non-linear spacetime relation with a maximum drift time of $\sim$ 700 ns, a small Lorentz angle and good ageing properties due to small gas amplification. The single-wire resolution is typically 80 μm. To improve the resolution of a chamber beyond the single wire limit and to achieve adequate redundancy for pattern recognition, the MDT chambers are constructed from 2×4 monolayers of drift tubes for the inner and 2×3 monolayers for the middle and outer stations. The tubes are arranged in multilayers of three or four monolayers, respectively, on either side of a rigid support structure. The construction of prototypes has demonstrated that they can be built with the required mechanical accuracy of $\sim 30\ \mu m$. Full size prototype modules have been built and tested in the beam, showing good performance within the specifications for ATLAS.

Cathode Strip Chambers (CSC) are used in the first station of the end-cap region and for pseudorapidity $|\eta| \geq 2$ to provide the finer granularity which is required

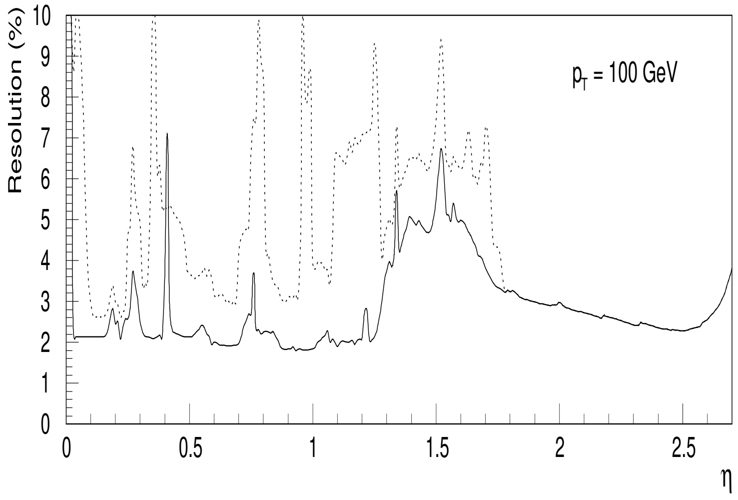

Figure 2.17: Momentum resolution for $p_T = 100$ GeV as a function of η averaged over all azimuthal angles. The solid curve applies to a standard sector; the dotted curve corresponds to one of the bottom sectors, where barrel toroid coils are placed inside the support structure for the inner parts of the detector.

to cope with the demanding rate and background conditions. The CSC are multiwire proportional chambers with cathode strip read-out and with a symmetric cell in which the anode-cathode spacing is equal to the anode wire pitch. The precision coordinate is obtained by measuring the charge induced on the segmented cathode by the avalanche formed on the anode wire. The anode wire pitch is 2.54 mm and the cathode read-out pitch is 5.08 mm; r.m.s. resolutions better than 60 μm have been measured in several prototypes. Other important characteristics are: small electron drift times (30 ns), good time resolution (7 ns), good two-track resolution and low neutron sensitivity. The CSC are arranged in 2×4 layers. The design uses low-mass construction materials to minimize multiple scattering and detector weight.

The **Trigger Chambers** for the ATLAS muon spectrometer serve a threefold purpose:

- Bunch crossing identification, requiring a time resolution better than the LHC bunch spacing of 25 ns.

- A trigger with well-defined p_T cut-off in moderate magnetic fields, requiring a granularity of the order of 1 cm.

- Measurement of the second coordinate in a direction orthogonal to the one measured in the precision chambers with a typical resolution of 5-10 mm.

The proposed system employs two different types of detectors, **Resistive Plate Chambers (RPC)** in the barrel ($|\eta| \leq 1.4$) and **Thin Gap Chambers (TGC)** in the end-cap region. The trigger chambers cover a total area of about 3650 m^2 in the barrel and 2900 m^2 in the end-cap region, each chamber containing at least two detector layers. The total number of channels is about 350000 for the barrel and 440000 in the end-caps.

The RPC is a gaseous detector providing a typical space-time resolution of 1 cm $\times$ 1 ns with digital read-out. The basic RPC unit is a narrow gas gap formed by two parallel resistive bakelite plates, separated by insulating spacers. The TGC chambers are designed in a way similar to multiwire proportional chambers, with the difference that the anode wire pitch is larger than the cathode-anode distance. Signals from the anode wires, arranged parallel to the MDT wires, provide the trigger information together with read-out strips arranged orthogonal to the wires. The read-out strips also serve to measure the second coordinate.

2.2.4 Trigger/DAQ and Physics Performance

The high interaction rate of the LHC puts stringent requirements to the trigger and data-acquisition systems. Only a tiny fraction of the interactions can be recorded for off-line analysis, requiring a trigger selectivity of about one interaction in 10^7. Furthermore, massive amounts of data have to be transmitted to and stored in buffer memories while the trigger system performs its calculations. Note that, since it is impossible to make a trigger decision within the 25 ns between bunch crossings, the so-called "pipelined readout" has to be used, typically with electronics mounted on the detector. The scheme of the pipelined readout along with the general architecture of the Trigger and DAQ system is illustrated in Figure 2.18.

After having described all the components of the ATLAS detector, the proof that they perform as a whole can only be demonstrated by the expected results for some interesting physics issues at LHC. One of those is the search for the Higgs, which implies stringent requirements on all detector parts in order to cover a broad mass spectrum with discovery capability in the relevant decay channels. Figure 2.19 (left) shows that this is achievable over the whole mass range. Another case is the search for Supersymmetry, where it seems clear that -if it exists- it can be discovered through the decay chains of squarks and gluinos to LSP. The real issue will be to extract measurements for well-chosen points in the SUGRA parameter space. If characteristic deviations from the SM appear and they point to some class of models indicating the rough mass scale, then typical kinematic features of the events (such as a sharp cut in the dilepton mass as shown in Figure 2.19 (right)) could further help exploiting constraint fits to a large number of hypotheses.

Concerning the B-physics studies, a very interesting scenario for the initial low lu-

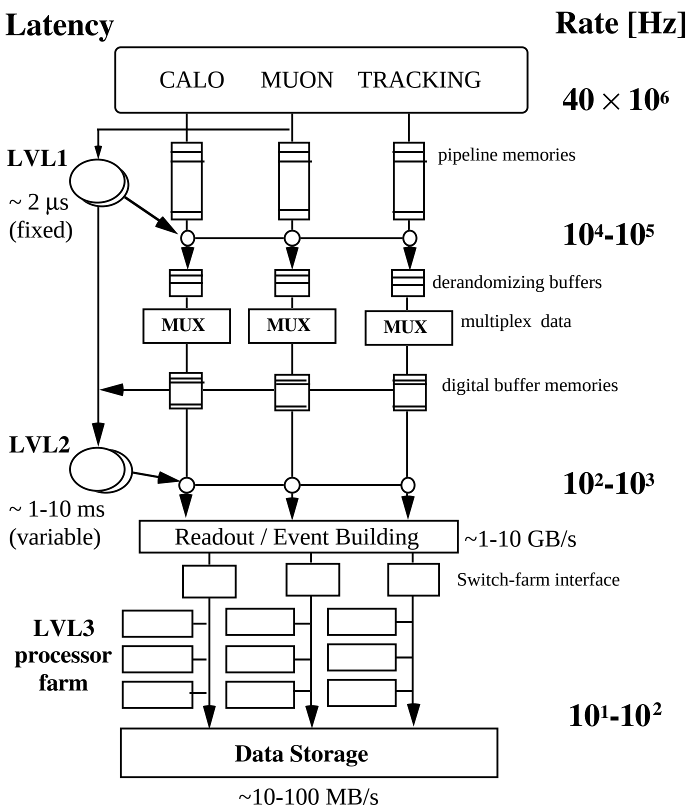

Figure 2.18: View of the pipelined readout architecture of the ATLAS LHC detector.

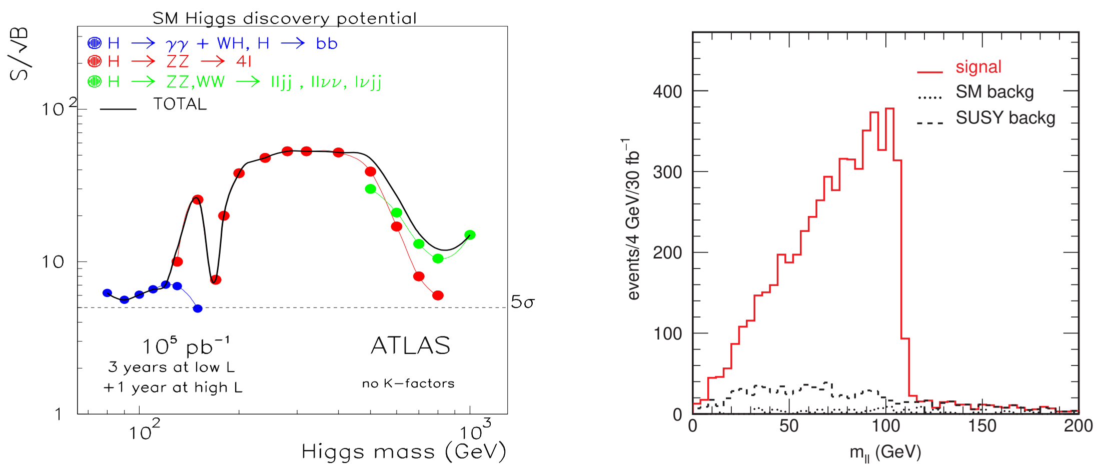

Figure 2.19: a) Higgs particle discovery potential for ATLAS. b) Dilepton signal for SUGRA point 5 (solid) background from other SUSY sources (dashed) and sum of SM backgrounds (dotted).

minosity period, it has been shown that the angles of the unitarity triangle can be measured through asymmetries in the relevant B-decays. With the achievable precision in sin2β and sin2α of ± 0.01 and ± 0.05 respectively, it will be possible to establish direct CP violation and to perform various Standard Model measurements. As an example, the errors on the W and the top masses which are expected to be in ATLAS 0.02 GeV and 2 GeV respectively, put significant constraints on the Higgs mass.

2.2.5 Physics and detector simulation

This point presents the software tools used throughout this thesis to evaluate in a consistent way the detailed performance of the various detector systems, both individually and combined, as well as the corresponding physics performances over a wide variety of different topics.

The requirements from these two aspects of the work (detector performance and physics performance) are sometimes conflicting:

• the detector simulation (Inner Detector, LAr, Tile Calorimeters and Muon System) and combined-performance (b-tagging, electrons/photons, jets/E_T^{miss}/τ-leptons, muons and trigger) working groups in ATLAS have been, in most cases, the promoters of detailed simulations using the GEANT package (version 3.21) [1]. These simulations have to be performed in an environment containing many interactions per beam-crossing (in the case of the Inner Detector and calorimeters) and high rates of background noise from low-energy neutrons (in the case of the Muon System). These groups have also performed detailed studies requiring the full data samples reconstruction of individual particles or of complete physics events;

• in contrast, the physics-simulation working groups (Higgs bosons, supersymmetry, B-physics and top physics) have been concentrated generally on fast simulation of high-statistics signal and background samples of complete physics events. Whenever is necessary results from full simulation and reconstruction have been used to improve, refine and enrich the fast-simulation program, *e.g.* when studying invariant masses of reconstructed final-state objects originated from the decay of a narrow resonance.

The software tools and their technical and performance aspects have been developed over the past decade or so, but are now quite complete, from the tools devoted to accurate Monte Carlo generation of complex physics processes, to interactive graphics tools dedicated to dynamically display and modify the results of the reconstruction programs, and finally to the tools devoted to interactive physics analysis of very large datasets. They meet in many areas the requirements needed for the final ATLAS software and will have to be maintained active, as a reference, over the next years, while the new software (OO/C++) for the experiments is designed and produced.

2.2.5.1 Full simulation of the ATLAS response

The complexity of the physics events to be analysed at the LHC and the diversity of the detectors to be integrated into ATLAS make it an absolute necessity to provide an accurate detector simulation program, with which the detector and physics performance can be evaluated in detail. Such a program must be extremely flexible in all its components, in order to meet the wide variety of requirements, which appear throughout the development phase of the experiment. These requirements are very stringent, especially for the detector geometry modules, which must be very powerful and versatile, in order to describe the very complicated experimental setup foreseen for ATLAS, while at the same time maintaining the possibility of changing or replacing parts of the detector in a simple and reproducible way.

The detector simulation program must solve as efficiently and as realistically as possible how to reproduce faithfully the harsh experimental conditions to be encountered during operation at the LHC. Given the huge complexity of the detector geometry which the simulation program must deal with, one simply cannot afford to simulate complete bunch crossings (which involve 23 inelastic interactions on average at the LHC design luminosity) for different values of the instantaneous luminosity. The same is true for the noise in the detector, which in many cases depends crucially on the luminosity and which must be introduced after the GEANT simulation has been performed.

The ATLAS simulation program (normally referred to as DICE [12], Detector Integration for a Collider Experiment) has been developed continuously since 1990, as a tool to cope with the most important deadlines of the collaboration. The third (and current) version of DICE contains an even more specialised version of the geometry representation, where only small adjustments are possible, to take into account detector layout modifications, and to deal with the increased complexity of the geometry description. Utility libraries for building the geometry in a standardised way have been provided, together with a macro-based language which gives definite advantages in terms of description uniformity and bank manipulation.

The ATLAS simulation program can be logically divided into three separate modules:

- event generation;
- detector simulation;
- digitisation.

These three parts communicate through a set of ZEBRA [22] banks and can be run separately or in sequence. The framework for the simulation program is provided by a package called SLUG (Simulation for LHC Using GEANT). SLUG provides the basic infrastructure for handling ZEBRA banks. It also provides a set of facilities for dealing with event generation, detector geometry and simulation, event merging for pile-up studies, together with stubs for user-defined routines to gain access to every step in the simulation process and tools for managing histograms and n-tuples. The program flow is controlled via an extensive set of pre-defined command procedures, which the user can control and execute through FFREAD datacards.

The event-generation phase is normally run separately in order to have a consistent input stream which can be used many times. Event generation facilities are implemented within SLUG by using the GENZ package, which provides a common interface between the most widely used event generators (PYTHIA [23], HERWIG [24], ISAJET [25]) and GEANT via the standard HEPEVT common block and ZEBRA banks.

The detector-simulation part is the most critical and time consuming; it can be run with different initial conditions (*e.g.* geometrical setup) on the same set of physics events in order to understand the impact on the physics of a change in the detector performance.

The digitisation step is a second level phase of detector simulation, placed just at the interface with the reconstruction program, where the physical information registered within the HITS bank is collected, re-processed in order to simulate the detector output and eventually written out (in the GEANT DIGI structure) to be then used by the reconstruction programs. The output from the digitisation is obtained in a similar form to that which might be expected from the readout electronics in the real experiment.

2.2.5.2 Reconstruction

The reconstruction of particles and other physics objects in the ATLAS detector has been developed over many years, and is implemented in a single program named ATRECON, based on the SLUG framework. ATRECON is mostly written in Fortran77, using ZEBRA as memory manager, although some parts have already been rewritten in C++, but not with a fully object-oriented design. This software will be replaced over the coming years by new OO software [11], which will use the existing software and its performance as a reference benchmark and will be built from the algorithms and experience gained in developing ATRECON. ATRECON runs on fully simulated GEANT 3.21 data and does not handle raw data nor calibration/alignment constants.

The reconstruction proceeds in two stages (in addition to initialisation). First, data from each detector is reconstructed in a stand-alone mode. Second, the information from all detectors is combined to get the most accurate measurements and identification of the final objects used in the analysis: photons, electrons, muons, τ-leptons, K_s^0, jets, b-jets, E_T^{miss}, primary vertex, etc..

2.2.5.3 Fast simulation and reconstruction

Fast particle-level simulation and reconstruction is an intermediate step between simple parton-level analysis of the event topology, which in general yields too much optimistic results for physics processes at hadron colliders, and very sophisticated and CPU-consuming full detector simulation and reconstruction. This kind of approach is needed for quick and approximate estimates of signal and background rates for specific channels. In addition, fast simulation and reconstruction is the only practical tool for high-statistics studies of complex background processes.

A complete package for fast detector simulation and physics analysis has been implemented recently and exists in two implementations:

- ATLFAST, the FORTRAN implementation of the algorithm [17], interfaced to PAW;

- ATLFAST++, the OO/C++ implementation of the same algorithm [18] , interfaced to ROOT [19].

Only the first version have been used for the results presented in this thesis.

ATLFAST can be used for fast simulation of signal and background processes, including the most crucial detector aspects: jet reconstruction in the calorimeters, momentum/energy smearing for leptons and photons, magnetic field effects and missing transverse energy. It provides, starting from the list of particles in the events, a list of reconstructed jets, isolated leptons and photons, the expected missing tranverse energy and reconstructed charged tracks. Values for the rejections against non-b jets and non τ jets are also provided as a function of the efficiencies for identifying b-jets and τ-jets. In most cases, the detector-dependent parameters are tuned to what is expected for the performance of the ATLAS detector from full simulation and reconstruction.

The ATLFAST package aims to reproduce as well as possible the expected detector performance in terms of resolution and particle-identification for important physics signals. It does not attempt, at present, to reproduce accurately the expected efficiencies for lepton and photon isolation. In the case of hadronic jets, the jet reconstruction (and veto) efficiency is often dominated by physics effects, which are straightforward to model in the fast simulation. For any specific channel the predictions from ATLFAST, in terms of resolution and reconstruction efficiency, should always be confirmed with full-simulation results. The acceptances, jet reconstruction efficiencies, jet-veto efficiencies and mass resolutions have shown good agreement between fast and full simulations.

Not all the detector effects can be readily parametrised in the fast simulation and only the basic information of the detector geometry is used in the package. This basic information is for example: the η-coverage for precision physics and for the calorimetry, the size of the barrel/end-cap transition region for the EM Calorimeter, and the granularity of the hadronic calorimeters. No effects related to the detailed shapes of particle showers in the calorimeters, the charged track multiplicity in jets, etc., are taken into account. In particular, energy isolation of leptons is only simulated in a crude way.

For practical reasons, the package has been divided into two parts: the main package, ATLFAST, executed on the generated events, and a supplementary package, ATLFAST-B, which can be executed on the filtered n-tuples during user analysis. The main features of ATLFAST and their relationship with the full simulation and reconstruction results are described in the chapter 5.

Bibliography

[1] The Large Hadron Collider, CERN/AC/95–05.

[2] ATLAS Letter of Intent for a General-Purpose pp Experiment at the Large Hadron-Collider at CERN, CERN/LHCC/92–4, LHCC/I2 (1992).

[3] The ATLAS Technical Proposal for a General Purpose pp Experiment at the Large Hadron Collider at CERN, CERN/LHCC/94-43 (1994).

[4] ATLAS Magnet System Technical Design Report, CERN/LHCC 97-18,97-19,97-20 (1997).

[5] ATLAS Inner Detector Technical Design Report, CERN/LHCC 97-16,97-17 (1997).

[6] ATLAS Liquid Argon Calorimeter Technical Design Report, CERN/LHCC 96-41 (1996).

[7] ATLAS Calorimeter Performance Technical Design Report, CERN/LHCC 96-40 (1996).

[8] ATLAS Tile Calorimeter Technical Design Report, CERN/LHCC 96-42 (1996).

[9] ATLAS Muon Spectrometer Technical Design Report, CERN/LHCC 97-22 (1997).

[10] R. Brun et al., GEANT3, CERN/DD/EE/84-1 (1996).

[11] ATLAS Collaboration Computing Technical Proposal, CERN/LHCC 96-43 (1996).

[12] DICE manual Version 0.10, CERN, Switzerland, Feb. 1995.

[13] J. Shiers et al., ZEBRA System, CERN Program Library entries Q100 and Q101, Febuary 1995.

[14] T. Sjostrand, High-Energy-Physics Event Generation with PYTHIA 5.7 and JET-SET 7.4, CERN preprint CERN-TH.7111/93 and CERN-TH.7112/93.

[15] G. Marchesini et al., Comput. Phys. Communication, 67 (1992) 465.

[16] F. E. Paige and S. D. Protopopescu, Manual ISAJET 7.13.

[17] E. Richter-Was, D. Froidevaux and L. Poggioli, "ATLFAST 1.0 A package for particle-level analysis", ATLAS Internal Notes ATL-PHYS-96-079 (1996) and ATL-PHYS-98-131 (1998).

[18] R. Brun and E. Richter-Was, "Getting started with ATLFAST++", http://atlasinfo.cern.ch/Atlas/GROUPS/PHYSICS/HIGGS/ATLFAST-www/OOimplementation.html.

[19] R. Brun et al., http:/root.cern.ch.

Chapter 3

Calorimetry in High-Energy physics

The name calorimeters refers to the detectors that measure the energy and position of the particles by means of their total absorption or destruction in such detectors. The absorption process always takes place through the secondary particle generation that interact as well with the detector in their sine.

Conceptually, a calorimeter consists of a matter block that serves to intercept primary particles, and has sufficient thickness so that all the energy of the radiation, originated by the primary particle and the created ones in the subsequent cascade, is deposited in its interior. The energy of a particle is degraded to the level of detectable atomic ionizations and excitations. Calorimeters are used to measure not only the energy, but also the spatial position, the direction and, in some cases, the nature of the primary particle. Some fraction of the deposited energy could be detected as a usefull signal (e.g. scintillation light, Cherenkov light or ionization charge), which should be proportional to the initial energy.

Calorimeters offer many atractive capabilities, supplementing or replacing the information obtained with magnetic spectrometers:

- They are sensitive to charged and neutral particles.

- The energy degradation through the development of the particle shower is a statistical process, and the average number $\langle N \rangle$ of secondary particles is proportional to the energy of the incident particle.

- The length of the detector increases logarithmically with the particle energy E.

- With segmented detectors, the information on the shower development allows precise measurements of the incident particle coordinates.

• The different response to electrons, muons and hadrons can be exploited for particle identification.

• Their fast time response allows the operation with high particle rates, and the pattern of the energy deposition can be used for fast on-line event selection.

According to the detected type of particle and the generated cascades, the calorimeters are classified:

• *Electromagnetic calorimeters.* The photons and the electrons interact electromagnetically with the absorber material through the following processes:

i) bremsstrahlung

ii) pair production

iii) Compton scattering

iv) photo-electric effect.

The cross-section of these processes and the multiplicity of the particles that take place in the cascade determine the characteristics of these instruments. The typical electromagnetic calorimeters scale is about 10 times the radiation length X_0.

• *Hadronic calorimeters.* The hadrons interact strongly with the absorber material. The absorption length λ of hadrons in the material is the appropriate scale to have an idea of its size ($\lambda >> X_0$).

In this chapter we comment on the main features of electromagnetic showers (section 3.1) and hadronic showers (section 3.2). In section 3.3 we will discuss how the e/h ratio affects the calorimeter performance. Section 3.4 is devoted to the description of the principle and physics requirements of the Tile Calorimeter as one of the sub-detectors of the ATLAS spectrometer.

3.1 Electromagnetic showers

The electromagnetic interaction can be manifested through:

a) Scintillation light produced by de-excitations of atoms and molecules excited by charged radiation,

b) Cherenkov light originated by electrons when the medium has a refraction index $n > 1$,

c) bremsstrahlung radiation, with photon emission and the subsequent pair production (basic processes in the electromagnetic showers development),

d) nuclear reactions with fragmentation of the target nucleus and production of secondary hadrons with a very low cross-section.

The behaviour of photons in matter is different from that of charged particles, the main interactions which can undergo are:

- Photo-electric effect.
- Compton scattering.
- Pair production.

The contribution of the various energy loss mechanisms as a function of the particle energy are given in figure 3.1, for electrons and positrons, and in figure 3.2 for photons [1]. Above approximately 1 GeV the principal processes (bremsstrahlung for electrons and positrons, and pair production for photons) become energy independent. It is through a succession of these energy loss mechanisms that the electromagnetic cascade (EMC) is propagated, until the energy of the charged secondaries has been degraded to the regime dominated by ionization loss. Within this description, the combined energy loss of the cascade particles in the detector equals the energy of the incident electron or photon.

The measurable signal (excitation or ionization of the medium) can be considered as the sum of the signals from the track segments of the positrons and electrons. The quantity which is usually introduced to represent the spatial development of the shower is the differential distribution of the *track length* T, defined as the sum of the tracks of all the charged particles in the shower.

The electromagnetic shower is fully described by quantum electrodynamics (QED)[2], and depends essentially on the density of electrons in the absorber medium. For this reason it is possible to describe the characteristic longitudinal dimensions of the high-energy EMC (E > 1 GeV) in a material-independent way, using the *radiation length* X_0. The energy loss ΔE due only to radiation in a distance Δx can then be written as:

$$(\Delta E)_{radiation} = -E(\Delta x/X_0) \tag{3.1}$$

and the X_0 numerical value is well approximated by the following expression:

$$X_0\ [g/cm^2] \sim 180A/Z^2\ (to\ better\ than\ 20\%\ for\ \sim\ Z > 13). \tag{3.2}$$

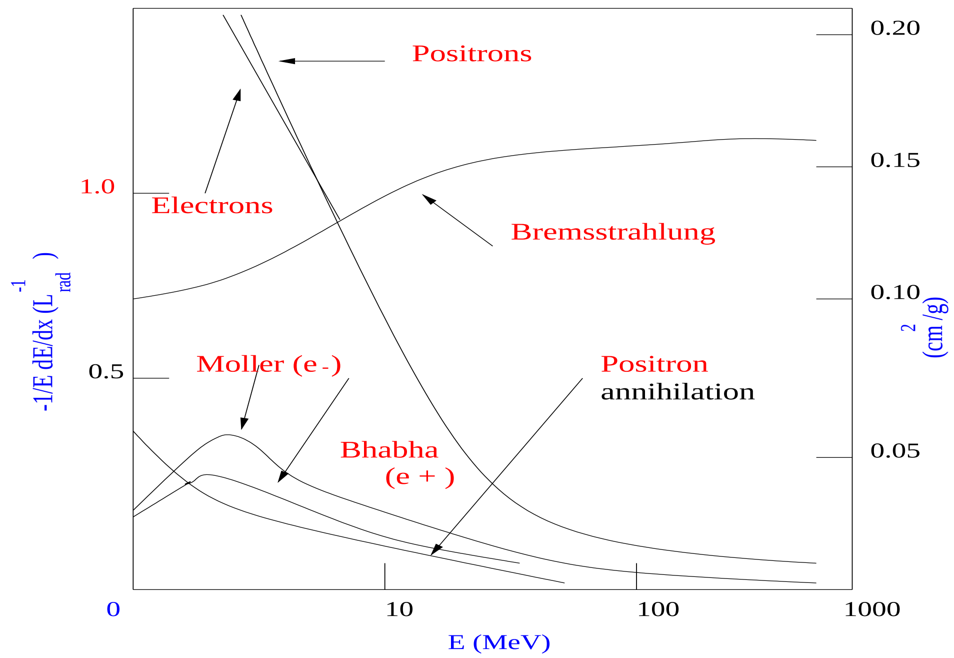

Figure 3.1: Fractional energy loss per radiation length (left ordinate) and per g/cm^2 (right ordinate) in lead as a function of electron or positron energy.

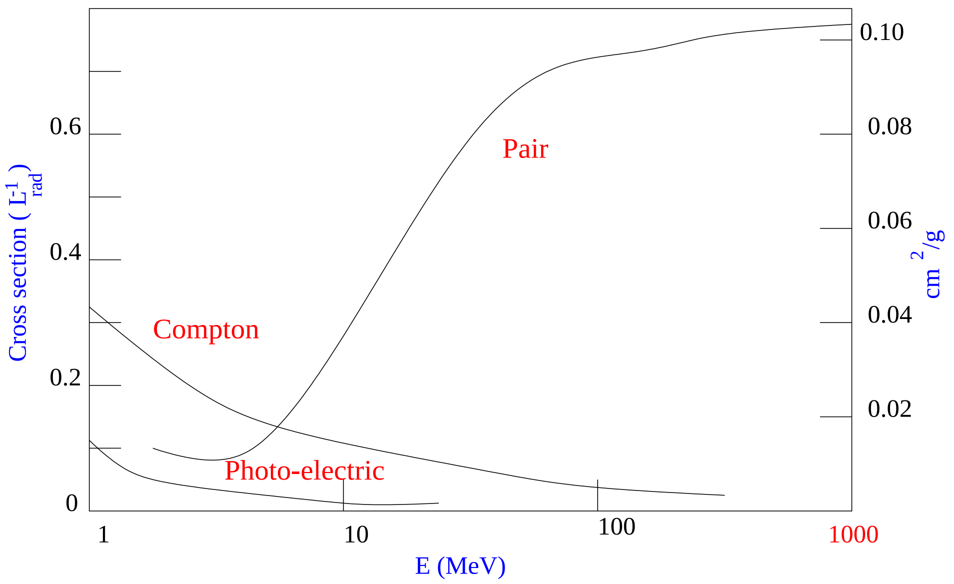

Figure 3.2: Photon cross-section σ in lead as a function of the photon energy. The intensity of photons can be expressed as $I = I_0 exp(-\sigma x)$, where x is the path distance in radiation length units.

Whilst the high-energy part of the EMC is governed by the value of X_0, the low-energy tail of the shower is characterized by the *critical energy* ϵ of the medium. It is defined as the energy loss by *collisions* of electrons or positrons of energy ϵ in the medium in one radiation length, i.e:

$$(dE)_{collision} = -\epsilon(dx/X_0) \tag{3.3}$$

where ϵ (MeV) is approximately $550 \times Z^{-1}$ (accurate to better than 10% for $Z > 13$). This value of ϵ coincides with the value of the electron energy below which the ionization energy loss starts to dominate the energy loss by bremsstrahlung.

The characteristic longitudinal EMC profile is shown in figure 3.3, for four very different materials, and demonstrates the *longitudinal scaling in radiation length.* A convenient analytical description of the profiles has been given in the form [3]:

$$dE/dt = E_0 b^{\alpha+1}/\Gamma(\alpha+1)t^{\alpha}e^{-bt} \tag{3.4}$$

where $t = x/X_0$, $\alpha = bt_{max}$ and $b \sim 0.5$.

The transverse shower properties can also be easily understood qualitatively. At the beginning, where is the most energetic part of the cascade, the lateral spread is characterized by both the typical angle for bremsstrahlung, $\theta_{brems} \sim p_e/m_e$, and the multiple scattering in the absorber. This latter process produces an increasment of the lateral spread when the energy of the shower particles decreases and consequently causes a gradual widening of the shower. For the purpose of total energy measurement, the EMC occupies a cylinder of radius R:

$$R \approx 2\rho_M; \qquad \rho_M = 21X_0/\epsilon \approx 7A/Z \ [g\ cm^{-2}], \tag{3.5}$$

ρ_M being the *Molière Radius*, which describes the average lateral deflection of electrons of energy ϵ after traversing one radiation length.

3.1.1 Rossi-Heitler model

This is a simple but useful model of the development of the electromagnetic shower from the energetic point of vue.

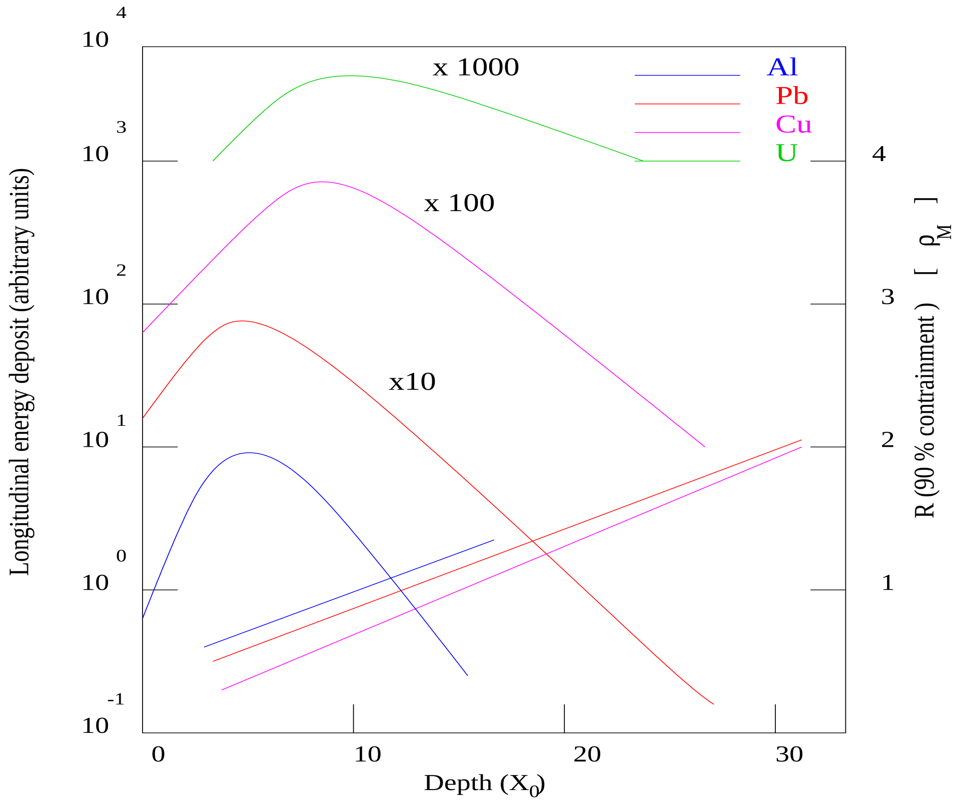

Figure 3.3: Longitudinal shower development (left ordinate) of 6 GeV/c electrons in four very different materials, showing the scaling in units of radiation length X_0. On the right ordinate the shower radius for 90% containment of the shower is given as a function of the shower depth. In the later development of the cascade, the radial shower dimensions scale with the Molière radius $\rho_M \sim 7A/Z$.

The development of the electromagnetic cascade can be parametrized in a simple form, if we follow the hypotheses of Rossi:

• After crossing a radiation length X_0, the electrons radiate by bremsstrahlung a photon, being the photon and electron energies: $E_\gamma = E_{in}/2 = E_e$.

• Moreover, after crossing a radiation length X_0 the energetic photons should be materialized in a pair e^+ e^- with symmetrical distribution of energy: $E_{e^+} = E_\gamma/2 = E_{e^-}$.

• The Compton effect and the electron energy loss by ionization or excitation are not considered for $E_e > \epsilon$, being ϵ the critical energy.

• The shower development stops when $E_e = \epsilon$.

The simple image of the model can be observed in the figure 3.4.

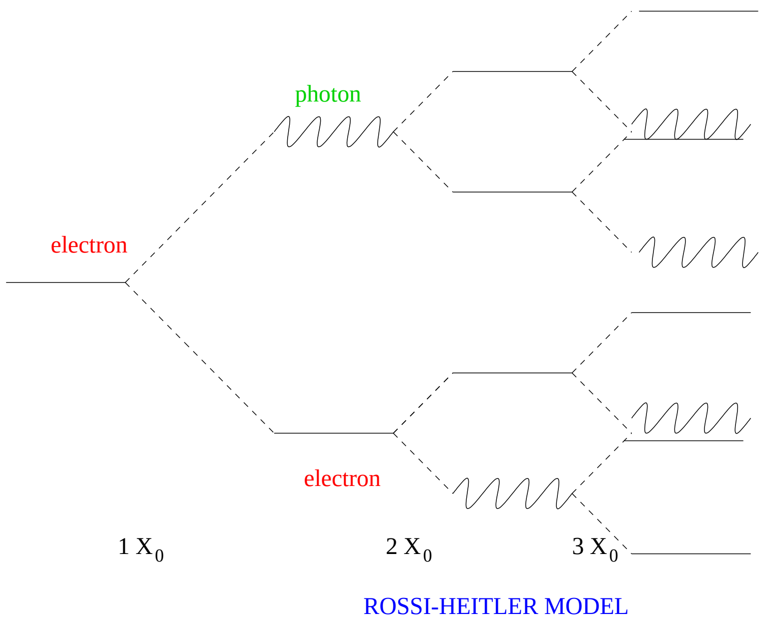

Figure 3.4: Schematic representation of the development of an electromagnetic shower according to the Rossi-Heitler model. X_0 is the radiation length.

An inmediate conclusion of the model is that after t radiation lengths, the number of particles that will be in the shower is:

$$N = 2^t \tag{3.6}$$

and the energy of each particle will be:

$$E = E_{in}/2^t. \tag{3.7}$$

The number of particles with an energy greater than E is growing exponentially with t, from $t = 0$ to $t = t_{max}$, where:

$$t_{max} = \frac{ln(E_0/\epsilon)}{ln2} \tag{3.8}$$

$$N_{max} = E_0/\epsilon$$

Although the Rossi model is quite simple it can reproduce interesting properties of electromagnetic showers:

- Concept of the maximum development of the shower, t_{max}.
- Linearity between E_{in} and the number of particles generated in the shower.
- Logarithmic growth of the longitudinal development of the shower with the incident energy E_{in}.

The number of particles with energy greater than a prefixed value E' can be calculated like:

$$N(E > E') = \int_0^{t(E')} N(t)dt \sim \frac{1}{ln2}\frac{E_0}{E'}, \tag{3.9}$$

where $N(t) = 2^t$; for this reason the energetic espectrum of the shower decreases like $1/E^2$.

In the same way, the total length of charged tracks in the shower is proportional to the incidente energy:

$$L = \frac{2}{3}\int_0^{t_{max}} N(t)dt \sim \frac{E_0}{\epsilon}. \tag{3.10}$$

The 2/3 factor is the fraction of charged tracks.

3.1.2 Classification of the electromagnetic calorimeters

Conceptually there exist two types of different detectors for the identification and measurement of the energy and position of the $e^{\pm}$, γ based on the formation of the electromagnetic showers:

• *Homogeneous calorimeters*: These calorimeters combine in a single material the active and passive functions. The medium acts at the same time as the absorber in which the multiplication of the secondary particles takes place and therefore the shower development (passive function), and is where the energy deposited by the secondary particles is converted in a detectable signal (active function).

Some examples of these calorimeters are the INa(Tl), BGO crystals and the lead glass counters.

• *Heterogeneous calorimeters*: For these detectors the materials for the active and passive functions are different. The method allows the optimal selection of both materials (high Z for the absorber and low Z for the active medium).

Traditionally these detectors are constituted by an alternate succession of absorber (generally Pb) and active material layers (scintillator, liquid argon, etc.).

3.1.3 Limits on Energy Resolution for Electromagnetic Calorimeters

The resolution of the measured energy is determined by the fluctuations in the shower propagation. The intrinsic component of the resolution is caused by the fluctuations in T_d (the *detectable* track length). This represents the lower bound on the energy resolution. In practical detectors, usually a number of additional components must be considered, which may affect the resolution. One important instrumental contribution to the energy resolution comes from the incomplete containment of the showers (*energy leakage*). The longitudinal containment of the shower can be parametrized, on average, as:

$$L(98\%)_{av} \approx t_{max} + 4\lambda_{att} \tag{3.11}$$

where $L(98\%)$ gives the length for the 98% longitudinal containment. The quantity λ_{att} characterizes the slow exponential decay of the shower after the shower maximum (see figure 3.3). The values of λ_{att} are found to be rather energy independent, but material dependent and close in value to the mean free path of photons that have minimum attenuation in a given material. The effect of the longitudinal leakage on the energy resolution is consistent with the parametrization:

$$\sigma(E)/E \approx [\sigma(E)/E]_{f=0} \times [1 + 2\sqrt{E(GeV)} \times f] \tag{3.12}$$

being f the fractional energy loss through leakage. For values of $f < 0.2$ and $E < 100\ GeV$, one notes that the longitudinal leakage is more critical than the transverse leakage due to the fact that the fluctuations around the average longitudinal loss are much larger than for transverse leakage.

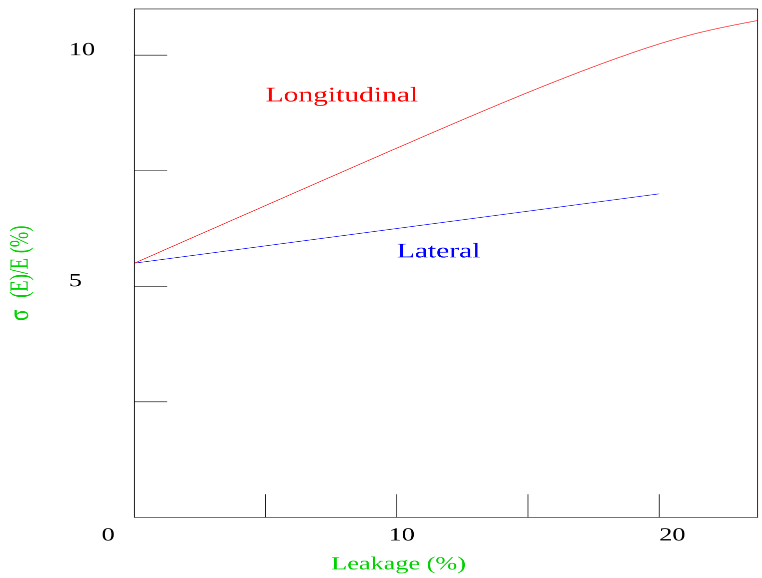

Figure 3.5: Effects of longitudinal and lateral losses on the energy resolution as measured for electrons in the CHARM neutrino calorimeter [4].

3.1.4 Energy resolution in "Sampling" calorimeters

Sampling calorimeters are devices in which the functions of energy degradation and energy measurement are separated in alternating layers of different substances. The choice of a *pasive* absorber (typically plates made of Fe, Cu, or Pb, each ranging in thickness from a fraction of X_0 to a few X_0) makes possible to build rather compact devices and permits optimization for a specific experimental requirement such as electron/pion discrimination or position measurement. The disadvantage is that only a fraction of the total shower energy is *sampled* in the active planes, resulting in additional fluctuations of the energy determination. Today we know that the energy resolution depends on the characteristics of both the passive and active medium (in particular, thickness and density) and because that several effects contribute to the *total* sampling fluctuations.

The *intrinsic sampling* fluctuations express the statistical fluctuations in the number of e^+e^- pairs traversing the active signal planes. The number N_x of crossings is:

$$N_x = T\ (total\ track\ length)/d\ (distance\ between\ active\ plates) \tag{3.13}$$

where $T = E/\epsilon$ and hence $N_x = E/\epsilon d = E/\Delta E$, ΔE being the energy loss per unit cell. The contribution to the energy resolution is:

$$\sigma(E)/E_{sampling} = \sigma(N_x)/N_x = 1/\sqrt{N_x} = 3.2\%\ [\Delta E\ (MeV)/E\ (GeV)]^{1/2} \tag{3.14}$$

This expression has to be regarded as a lower bound on the sampling fluctuations, due to the following reasons:

• tracks originate from pair-produced particles and therefore the number of independent gap crossings would be only $N_x/2$ for totally correlated production;

• it ignores multiple scattering, which increases the effective distance d to $d\ =\ d\ /\ \langle\cos\theta\rangle$, where the characteristic multiple scattering angle θ is given by 21 $(MeV)/\epsilon\pi$ [5].

The energy resolution seems to be rather well described by these estimates, provided that instrumental effects (such as calibration errors, photon statistics, leakage, etc.) do not dominate.

3.2 Hadronic showers

Hadronic calorimeters are detectors whose objective is to measure the energy of the particles that are not completely absorbed in the electromagnetic calorimeters and therefore are normally located behind those electromagnetic devices. Usually the electromagnetic calorimeters suppose up to a few interaction lengths λ of the hadronic calorimeter, and consequently the first part of the hadronic shower is gathered in the electromagnetic calorimeter, this is the reason why the studies of combined calorimetry are becoming more and more popular.

The development of the hadronic shower in matter is so complicated that simplified analytical treatments are not available. Conceptually, the energy measurement of hadronic showers is analogous to that of EMCs, but the much greater variety and complexity of the hadronic processes propagating the hadronic shower (HC) complicate the detailed understanding.

Typical of the hadronic interactions is the multiple particle production with transverse momentum $\langle p_t \rangle \cong 0.35$ GeV/c, for which about half of the available energy is consumed (the inelasticity $K \cong 0.5$). The remaining energy is carried by fast forward-going (leading) particles. The secondaries are mostly pions and nucleons, and their multiplicity is only weakly energy-dependent. The characteristic stages in the HC development are summarized in Table 3.1. Two specific features have been identified as the principal physical limitations to the energy resolution of hadronic calorimeters:

• A considerable part of the secondaries are π^0, which will propagate electromagnetically without any further nuclear interactions. The size of the π^0 component is largely determined by their production in the first interactions, and therefore, event-by-event fluctuations around the average value are important.

• A sizeable amount of the available energy is converted into excitation or break-up of the nuclei, of which only a fraction will result in detectable (*visible*) energy.

The two processes, intimately correlated, may lead for a given entering hadron, to a very different shower composition, which has a very different detectable response. They impose the intrinsic limitation on the performance of the hadronic calorimeters. Neutral pions amount is on average 1/3 of the produced pions and their energy is dissipated in the form of electromagnetic showers. The fraction of the total energy which is dissipated in ionizations by electrons and charged hadrons fluctuates from event to event and is the main contribution to the energy resolution in hadron calorimetry, because while the electromagnetic energy and the energy of the charged hadrons are well sampled, a large fraction of the remaining energy is not seen.

Table 3.1 gives some indications of the relative importance of these competing processes. Considerable knowledge has been gained from very detailed Monte Carlo calculations, which in their most ambitious form aim to simulate the full nuclear and particle physics aspects of the hadronic cascade based on the measured cross-section of the elementary processes [6]. Examples showing the energy dependence of the principal effects are given in figure 3.6. It should be noticed that these various processes contribute in varying degrees to the visible energy of the HC, and that a considerable fraction (such as nuclear binding energy, muons, and neutrinos) will be lost in the form of *invisible* or undetectable energy.

The longitudinal average and the transverse distributions are useful estimates of

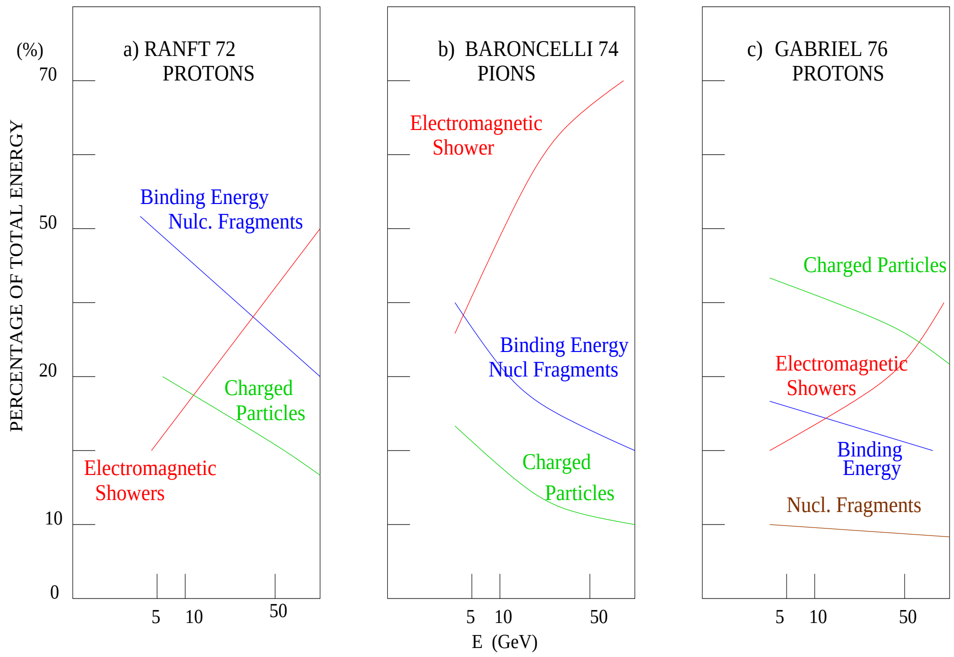

Figure 3.6: Relative contributions of the most important processes to the energy dissipated by hadronic showers in iron. The Monte Carlo calculations are by Ranft, Baroncelli and Gabriel [6].

Table 3.1: Properties of the phenomena which determine the development of hadronic showers.

Reaction	Properties	Influence on energy resolution	Charac. time (s)	Charac. length (g/cm^2)
Hadron production	Multiplicity $\cong A^{0.1}$ ln s Inelasticity $\cong 1/2$	π^0/π^+ ratio Binding energy loss	10^{-22}	Abs. length $\lambda \cong 35A^{1/3}$
Nuclear deexcitation	Evaporation energy $\cong$ 10% Binding energy $\cong$ 10% Fast neutrons $\cong$ 40% Fast protons $\cong$ 40%	Binding energy loss Poor or different response to n, charged particles, and $\gamma' s$	$10^{-18} - 10^{-13}$	Fast neutrons $\lambda_n \cong 100$ Fast protons $\lambda_p \cong 20$
Pion and muon decays	Fractional energy of $\mu' s$ and $\nu' s \cong 5\%$	Loss of $\nu' s$	$10^{-8} - 10^{-6}$	$\gg \lambda$
Decay of c, b particles produced in multi- TeV cascades	Fractional energy of $\mu' s$ and $\nu' s$ at percent level	Loss of $\nu' s$ Tails in resolution function	$10^{-12} - 10^{-10}$	$\ll \lambda$

the characteristic dimension for near-complete shower containment. The average longitudinal distribution exhibit *scaling in units of absorption length* λ. The transverse distribution depends (as in the case of EMCs) on the longitudinal depth: the core of the shower is rather narrow (FWHM from 0.1 to 0.5λ), increasing with the shower depth.

Experimental data are consistent with the following parametrization:

- The shower maximum, measured from the face of the calorimeter, is given by

$$t_{max}(\lambda) \sim 0.2\ lnE\ (GeV) + 0.7 \tag{3.15}$$

and it occurs at a smaller depth in high-Z materials due to the smaller ratio of X_0/λ.

- The longitudinal dimension required for almost full containment is approximated by

$$L_{0.95}(\lambda) \cong t_{max} + 2.5\lambda_{att} \tag{3.16}$$

again measured from the face of the calorimeter. The quantity λ_{att} describes the exponential decay of the shower beyond t_{max} and increases with the energy approximately as $\lambda_{att} \cong \lambda\ [E\ (GeV)]^{0.13}$, with an indication of a weaker energy dependence for high-Z absorbers. The expression for $L_{0.95}$ describes the available data in the energy range from a few GeV to a few hundred GeV within 10%.

• The transverse radius R of the 95% containment cylinder is approximately $R_{0.95} \leq 1\ \lambda$; it does not scale with λ and is smaller in high-Z substances.

• A useful parametrization of the longitudinal shower development is

$$dE/ds = K[wt^a e^{-bt} + (1 - W)l^c e^{-dl}], \tag{3.17}$$

where $dE\ /\ ds$ is the longitudinal energy deposited, t is the depth, starting from the shower origin, in radiation lengths, and l is the same depth in units of absorption lengths. The parameters $a,\ b,\ c,\ d$ are obtained from a fit to the data and they show a logarithmic energy dependence.

3.2.1 Intrinsic energy resolution

The principal limitations to the hadron energy resolution are due to the fluctuations originated by the vastly different detection mechanisms for different particles (from π^0's to slow neutrons, muons, and neutrinos). These fluctuations have been found to be larger (of the order of 50% at 1 GeV) in strong contrast with the measurement of electromagnetic calorimeters, where the *intrinsic* fluctuations of the visible track length are less than 1% at 1 GeV. The dominant influence of the nuclear processes manifests itself also in the shape of the response function (figure 3.7) and is corroborated by detailed Monte Carlo estimates. Available experimental evidence indicates that the intrisic hadronic energy resolution is:

$$\frac{\sigma}{E} = \frac{45 - 50\%}{\sqrt{E}} \oplus b\%, \tag{3.18}$$

where the first term is atributed to shower fluctuations. It is sizeable because, about one fourth of the hadron energy E is not sampled and the fluctuations on the missing 25% are very large. The second term has the typical dependence of the energy resolution for electromagnetic showers, which is appoximately the fraction of the total energy dissipated in ionizations by electrons, positrons and charged hadrons.

The level of these nuclear effects and, more generally, the level of *invisible* energy is sensitively measured by comparing the calorimeter response for electrons and hadrons at the same *available* energy, which is the kinetic energy of electrons and nucleons, the total energy for mesons, and the total energy plus the rest mass for antinucleons.

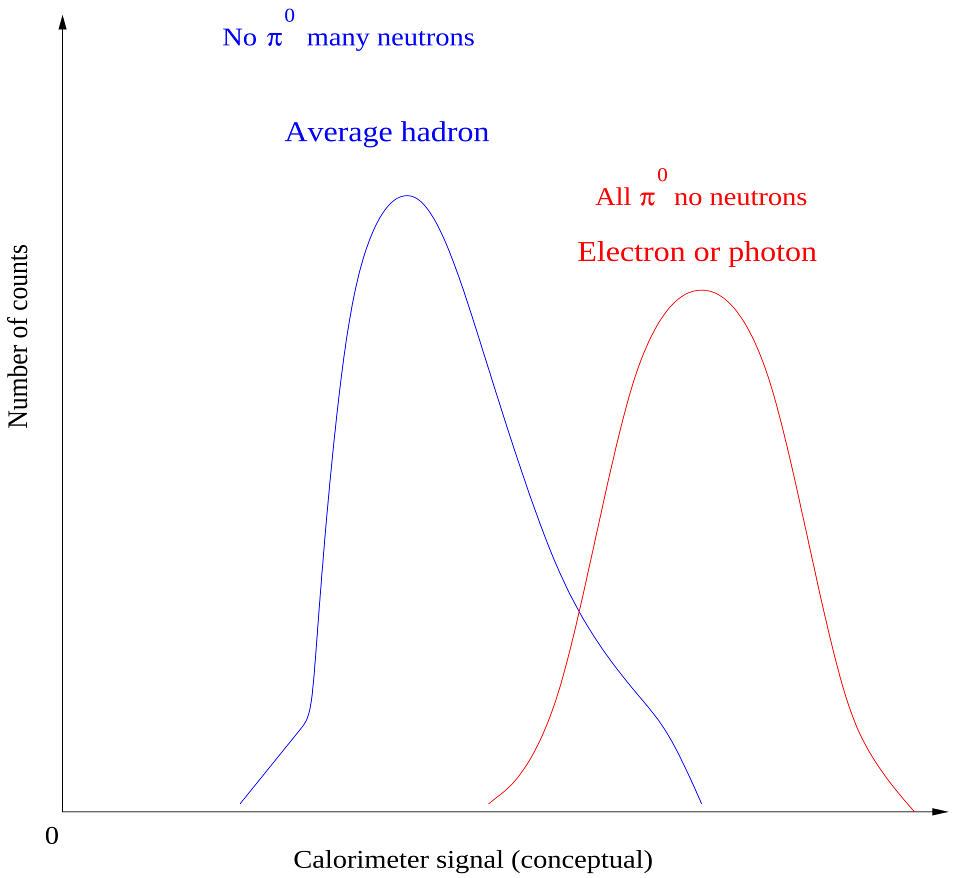

Figure 3.7: Calorimeter response for 10 GeV/c pions. The fluctuations are dominated by the nature of the first inelastic interaction. On average, a certain number of π^0's, charged pions, nuclear fragments, and slow protons and neutrons will be produced. At the other extreme the reaction products are mostly π^0's, and the energy deposit will be very similar to that of electrons or photons of equivalent energy.

All calorimeters except those made from uranium show a visible energy of approximately 70% relative to electrons (for uranium especially designed calorimeters, the nuclear losses are effectively compensated, leading to a response that is nearly equal for charged and neutral pions), which slowly increases owing to the rise in the electromagnetic component at higher energies. At low-energy limit all calorimeters, including those using uranium as a degrader, are expected to give similar responses. This interpretation is confirmed by the fact that in this limit the relative resolution improves.

In summary, the response of hadrons relative to electrons in a calorimeter is a sensitive probe of the level of nuclear effects. The intrinsic resolution of hadron calorimeters is limited to $\frac{\sigma}{E} = \frac{45-50\%}{\sqrt{E}} \oplus b\%$. The material and energy dependence of the limiting resolution is the most important open problem in hadron calorimetry.

3.2.2 Compensating fluctuations (Methods to reduce the effects of fluctuations)

We have emphasized that the relative response between electrons and pions is a sensitive measure of the level of nuclear interactions. An improvement in the energy resolution would be expected if the response of the electromagnetic cascade were identical compared with the purely hadronic one.

Several suggestions have been made for monitoring the level of the electromagnetic componet measured event-by-event. One suggestion was to use, as an indicator, the Cherenkov light from relativistic particles mainly produced by e^+e^- pairs [7], but Monte Carlo estimates for practical devices suggest that it is difficult to obtain a very useful correlation and to improve the resolution significantly. Another suggestion was to monitor the level of the nuclear component by associating heavily ionizing particles with the *late* component of the hadronic shower [8]. The most successful attempt was done by a weighting algorithm applied to the individual longitudinal measurements relative to the total energy measured. In figure 3.8 the unweighted and weighted results for the energy resolution are presented. Firstly, it can be seen that the raw results show a marked deviation from the expected $E^{-1/2}$ dependence. Secondly, the weighting algorithm improves the resolution, particularly at the highest energies, to a level that would be expected from extrapolating the low-energy resolution according to an $E^{-1/2}$ law.

The more direct cure for these fluctuations is the uranium hadronic calorimeter to compensate the fluctuations due to the missing energy with the nuclear fissions produced by neutrons in uranium. With an argon-uranium calorimeter of these characteristics the hadron resolution is $\sim 30\%\sqrt{E}$, definitely much better than the resolution obtained with iron calorimeters. The improved resolution goes together with an increase of the ratio between the visible energies for pions and electrons from $\pi/e \sim 0.70$ in argon-iron to $\pi/e \sim 1.05$ in argon-uranium.

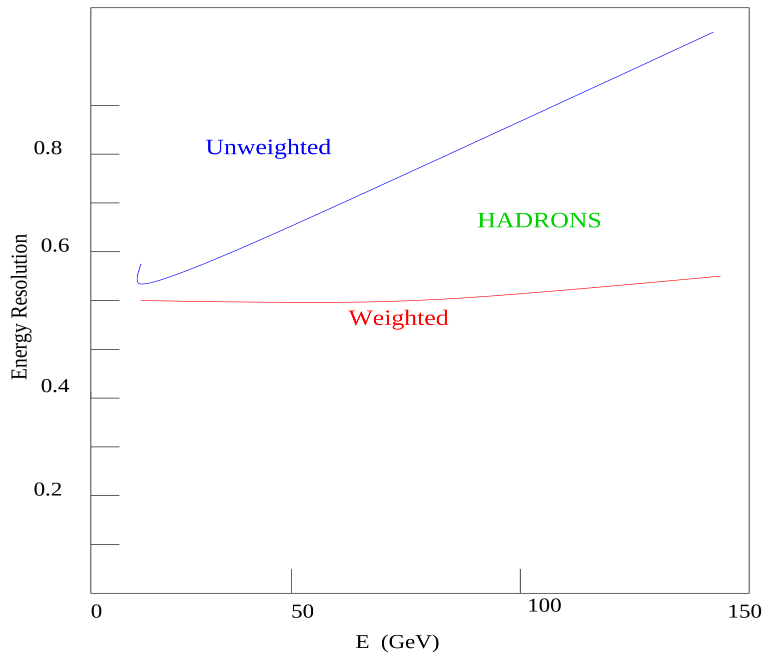

Figure 3.8: Energy resolution measured in the CDHS neutrino calorimeter versus the energy of the incident particle. With a weighting procedure to reduce the large fluctuation due to the electromagnetic component the resolution is improved, and is consistent with the $1/\sqrt{E}$ behaviour up to the highest energies measured [9].

3.2.3 Instrumental effects on the Energy resolution

Most hadronic calorimeters are *sampling* detectors, mainly using rather dense passive absorbers to reduce the linear dimensions of the instrument. Therefore, sampling fluctuations of statistical origin analogous to the case of electromagnetic ones should contribute to the energy resolution, although, for the sampling of the HC we do not have a similar and simple detailed description. Available measurements are consistent with a parametrization of the form:

$$\sigma(E)/E/hadron - sampling \cong 0.09\ [\Delta E\ (MeV)/E\ (GeV)]^{1/2}. \tag{3.19}$$

The quantity ΔE expresses the energy loss per unit sampling cell for minimum ionizing particles.

Energy leakage due to partial shower containment will not only degrade the energy resolution, but will also give rise to very asymmetric resolution functions with low-energy tails. Longitudinal fluctuations are larger than transverse fluctuations and hence longitudinal leakage is more critical to the performance.

3.2.4 Differences between the hadronic and electromagnetic showers

The dimensions and scale properties of both shower types are quite different:

- $\lambda_{inte} \sim A^{1/3}$.
- $X_0 \sim A/Z^2$.

The separation and identification of e, γ, π^0 versus hadrons works very well for a material of elevated Z in which the relation λ_{int}/X_0 reaches values of the order of 30.

The *invisible* energy generates peculiarities in the Hadronic Calorimeters. This energy comes from muons and neutrinos escaping out of the detector and the fraction of the incident energy devoted to break the targets with no *visible* mechanism. Several studies reveal that the *invisible* energy can reach the 40 % of the non-electromagnetic energy.

The range of signals to detect in a channel of a Hadronic Calorimeter is wider than in an electromagnetic calorimeter and in addition there appear strongly ionizing particles. Consequently they can show effects of saturation or effects of recombination. Therefore it appears a suppression of the detector signal, until a factor 5, with effects on the linearity (the calorimeter gives nonlinear response).

A crucial difference between the electromagnetic and hadronic showers is that in the last ones the neutrons (of several MeV) transport a considerable fraction of the incident energy, coming from the nuclear evaporation.

3.3 Effects of the e/h ratio on the calorimeter performance

We define as e the calorimeter response to the energy deposited through a purely electromagnetic process and h the response to the purely hadronic process, that means the response to a hadron substracted the electromagnetic part.

The ratio e/h is the relation between both responses. This ratio should be equal to 1.0 for optimal performace [10].

The sampling fluctuations and the fluctuations in the fraction of the energy deposited in the form of ionizing particles, mentioned before, have consequences for calorimetric hadron detection. Firstly, the signal distribution for hadrons of energy E will be broader than for electromagnetic showers at the same energy. Secondly, the average response (signal per unit of energy) will have a different value for electromagnetic and hadronic showers ($e/h \neq 1$). The latter will in general be smaller ($e/h > 1$).

In the development of a shower generated by a high-energy hadron some fraction (f_{em}) of the energy is usually spent on the production of π^0's and ν's. A hadron shower, therefore, has in general an electromagnetic (em) and a non-electromagnetic component (see figure 3.7). The fact that the ratio $e/h \neq 1$ has the following consequences for the calorimeter performance:

- The fluctuations in f_{em} give an additional contribution to the energy resolution.

- Because of the non-Gaussian nature of the fluctuations in f_{em} the energy resolution σ/E will not improve as $E^{-1/2}$ with increasing energy.

- The calorimeter signal is not proportional to the hadron energy (alinearity).

- The measured e/h ratio is energy dependent.

All these effects have been experimentally observed. This is ilustrated in figure 3.9, which shows experimental data on calorimetric hadron detection with and iron/plastic-scintillator ($e/h = 1.4$) calorimeter [14], and with uranium/plastic-scintillator [1] ($e/h = 1$). The calorimeter response for iron rises with energy, and consequently the e/h signal ratio decreases as the energy increases. This effect is absent for uranium, once the right ratio between active and passive layers has been chosen.

To avoid the confusion caused by the latter effect, we prefer to use the energy-independent quantity e/h^{intr}, which is an intrisic characteristic of a non-compensated calorimeter, given by the ratio of the mean values of the two curves in figure 3.7. The relation between the e/h^{intr} and e/h ratios is given by:

$$e/h\ (E) = \frac{e/h^{intr}}{1 - \langle f_{em}(E)\rangle[1 - e/h^{intr}]} \tag{3.20}$$

where

$$\langle f_{em}(E)\rangle = 0.1\ ln\ E\ (GeV) \tag{3.21}$$

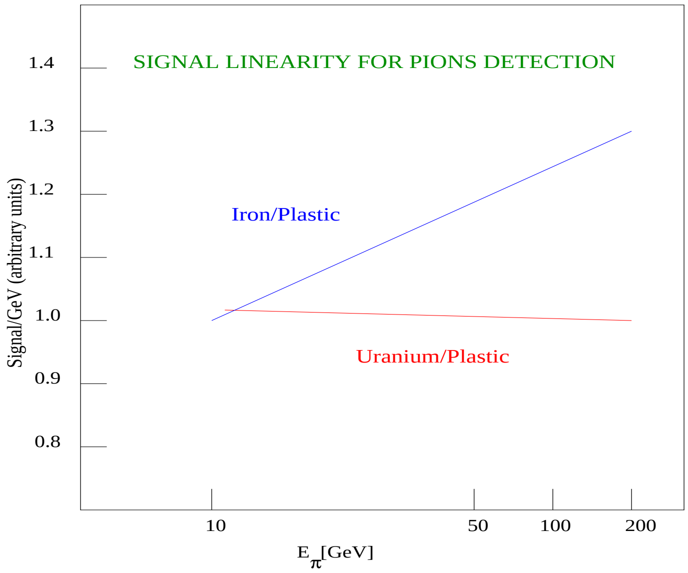

Figure 3.9: Linearity as a function of the energy from experimental data obtained with an iron/plastic-scintillator calorimeter, and with uranium/plastic-scintillator.

The figure 3.10 shows in a very clear way that, in particular at high energies, the value of e/h^{intr} is crucial for the energy resolution that can be obtained. For calorimeters with $e/h = 1.36$ at 10 GeV, the resolution σ/E does not become better than $\sim 7\%$, even at the highest energies. For calorimeters with $e/h^{intr} = 1$, the energy resolution will continue to improve with increasing energy, until limitations due to instrumental effects become important.

3.3.1 The e/h signal ratio

The e/h ratio depends on a large number of factors, of which we can emphasize:

- The Z of the active and passive media.
- The hydrogen content of the active medium.
- The saturation properties of the active medium.
- The nuclear level structure of the absorber.
- The size of the detector.
- The cross section for thermal neutron capture in the absorber.

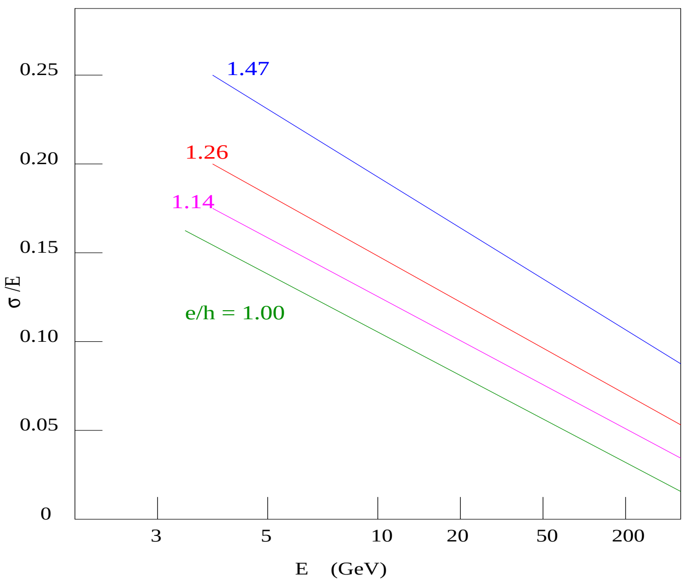

Figure 3.10: Monte Carlo simulation of the $e/h \neq 1$ effects on the energy resolution for hadron calorimeters.

- The signal integration time.
- The thickness of the active and passive layers.
- The sampling fraction.

The e/h ratio can therefore be tuned through the sampling fraction, and for the hydrogenous material (various plastic scintillators, TMP) an ideal sampling fraction ($e/h = 1$) exists.

The sensitivy of the e/h ratio with the sampling fraction depends on two factors:

- The fraction of hydrogen atoms in the active medium.
- The saturation of the active medium. Less saturation causes a larger sensitivity and consequentely leads to a larger optimal sampling fraction.

For calorimeters with nonhydrogenous active layers (e.g. LAr, Si), the effect of the sampling fraction on the relative contribution of neutrons to the calorimeter signal is absent. It turned out that the e/h ratio depends quite sensitively on the contribution of captured neutrons to the hadronic calorimeter signal, which can be tuned through the signal integration time.

In the nonelectromagnetic shower part inevitable losses that cannot be compensated will occur, e.g., the binding energy required to release protons or nucleons aggregates from their nuclear environment. Therefore, the e/h^{intr} signal ratio has always to be larger than 1.0 for such devices.

3.4 The Hadronic Tile Calorimeter of ATLAS

The Tile Calorimeter is one of the ATLAS sub-detectors. ATLAS is one of the general purpose pp detectors designed for the Large Hadron Collider (LHC) to be built at CERN. It is a large hadronic sampling calorimeter which makes use of iron as the absorber material and scintillating plates, read out by wavelength shifting (WLS) fibres, as the active medium. The new feature of its desing is the orientation of the scintillating tiles which are placed in planes perpendicular to the colliding beams and are staggered in depth. A good sampling homogeneity is obtained when the calorimeter is placed behind an electromagnetic compartment and a magnetic coil equivalent to a total of about two interaction lengths (λ) of material. This has been verified with Monte Carlo simulation and has been proved by the test beam results [13].

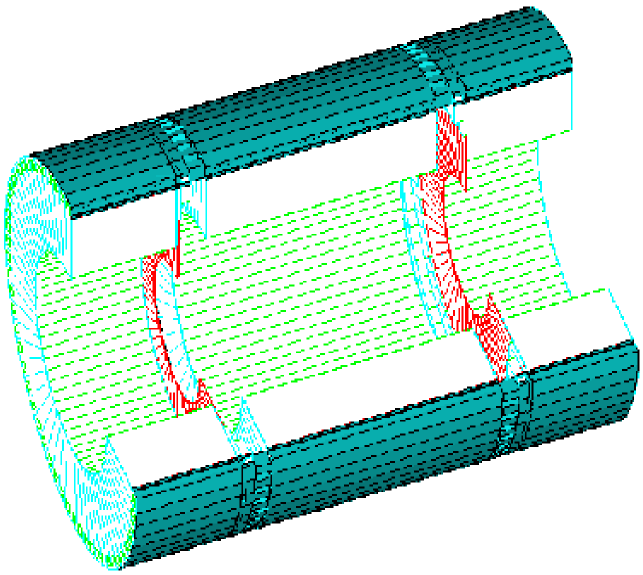

Figure 3.11: Layout view of the Tile Calorimeter barrel and extended barrels.

The Tile Calorimeter consist of a cylindrical structure with an inner radius of 2280 mm and an outer radius of 4230 mm. It is subdivided into a 5640 mm long central barrel and two 2910 mm extended barrels as shown in figure 3.11. The scintillating tiles lie in the $r-\phi$ plane and span the width of the module in the ϕ direction. WLS fibres running radially collect the light from the tiles along their two open edges. Readout cells are then defined by grouping together a set of fibres into a photomultipler (PMT), to obtain a three dimensional segmentation. Radially, the calorimeter is segmented into three layers, approximately 1.4, 3.9 and 1.8 interaction lengths thick at $\eta = 0$; the $\Delta\eta \times \Delta\phi$ segmentation is 0.1×0.1 (0.2×0.1 in the last radial layer). This calorimeter layout has been successfully proved with large-sized prototypes in the test beam area as a part of the RD34 project [14].

At the LHC, calorimeters will be the leading detectors in many measurements for the reconstruction of prime interest physics channels. In the region between the sensitivity limit of LEP2 ($\sim$ 98 GeV) and $m_H = 130$ GeV, the Higgs would most likely be observed in the $H \to \gamma\gamma$ channel, which will be reconstructed in the electromagnetic (EM) calorimeter. In the region $130 < m_H < 600$ GeV, the cleanest decay mode would be $H \to ZZ \to 4l$, and the reconstruction of final states containing two or four electrons will be mainly based on the EM calorimeter information. In the region $m_H > 600$ GeV, two decay channels are expected to be observable above the background: $H \to ZZ \to ll\nu\nu$, which requires excellent measurement of the missing transverse energy (E_T^{miss}) in the calorimeters to reduce the potentially large instrumental background, and $H \to WW \to l\ \nu\ jet\ jet$, which can only be detected above the background if the $W \to jet\ jet$ invariant mass can be accurately reconstructed in the calorimeters and the two forward jets, produced in association with the Higgs, can be tagged efficiently in the forward calorimeters.

3.4.1 The principle of the Detector

The tiles are placed radially and staggered in depth. The structure is periodic in z. The tiles are 3 mm thick and the total thickness of the iron plates in one period is 14 mm. The highly periodic structure of the system allows the construction of a large detector by assembling smaller sub-modules together. Since the mechanical assembly is completely independent from the optical instrumentation, the design becomes simple and cost effective. Simplicity has been the guideline for the light collection scheme: fibres are coupled radially to the tiles along the outside faces of each module; the laminated structure of the absorber allows the coupling of the fibres. The use of fibre read-out allows to define a logical cell structure, creating a projective geometry for triggering and energy reconstruction (see figure 3.12). A compact electronics system is housed in the girder of each module. Finally, the read-out of the two sides of each of the scintillating tiles into two separate photon detectors (in our case photomultipliers, PMTs) guarantees a sufficient light yield and provides a redundancy which might be needed during the long expected period of operation of the ATLAS experiment.

The Tile Calorimeter is designed as one barrel and two extended barrel hadron

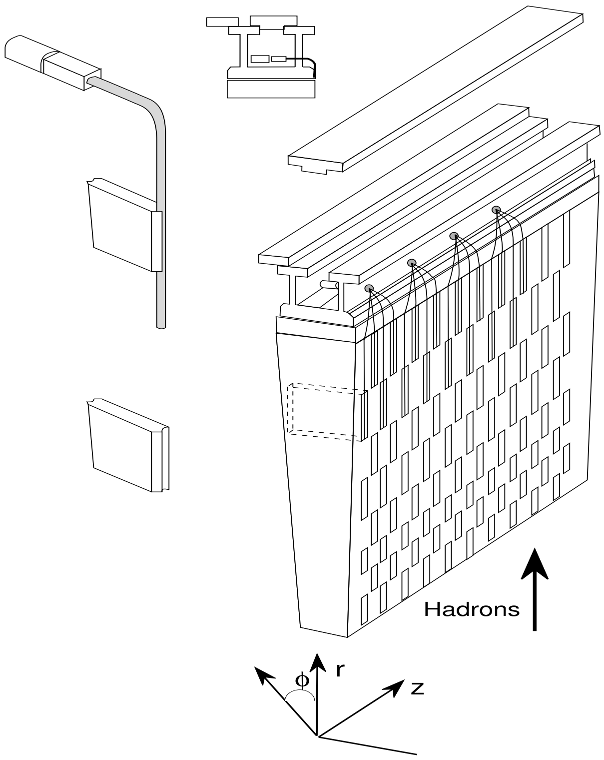

Figure 3.12: The principle of the Tile Calorimeter design.

parts with cylindrical structure. Each detector cylinder is built of 64 independent wedges along the azimuthal direction. Between the barrel and the extended barrels there is a gap of about 600 mm (see figure 3.13), which is needed for the Inner Detector and the Liquid Argon cables, electronics and services. The barrel covers the region $-1.0 < |\eta| < 1.0$, and the extended barrels cover the region $0.8 < |\eta| < 1.7$.

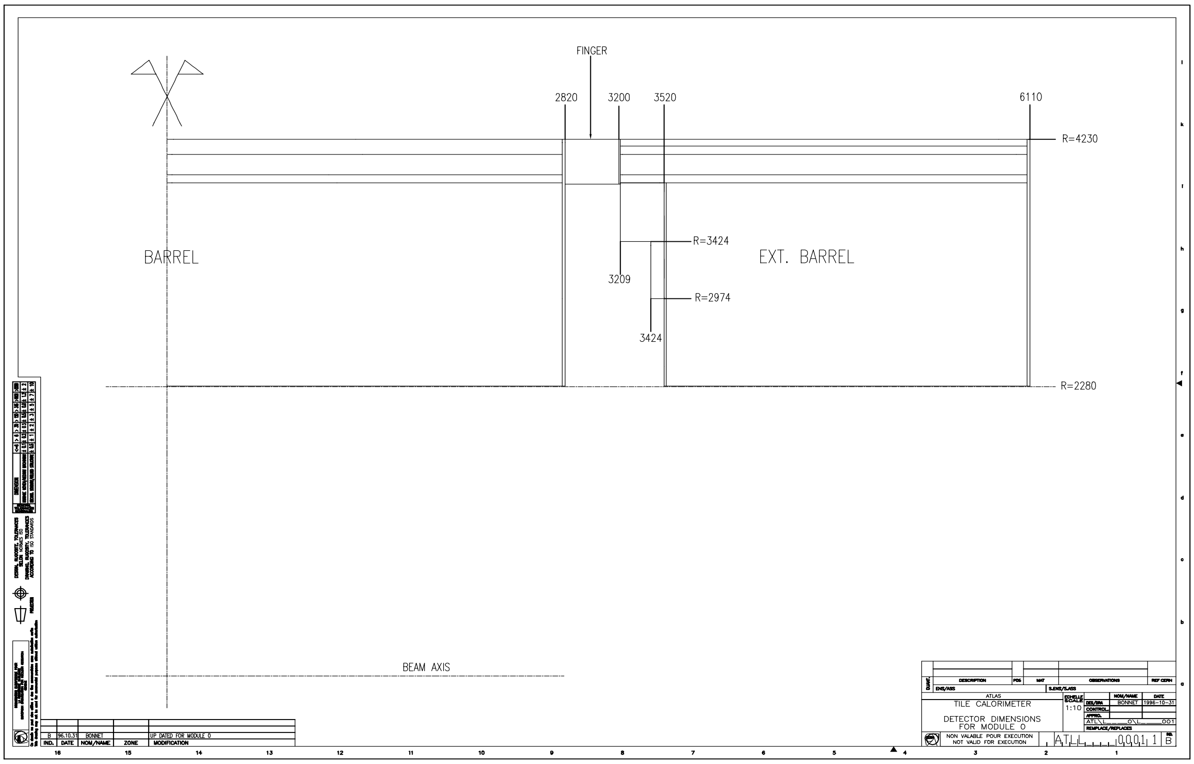

Figure 3.13: Overall schematic view of the Tile Calorimeter detector dimensions.

Part of the gap contains an extension of the extended barrel: the Intermediate Tile Calorimeter (ITC), which is a structure stepped in order to maximize the volume of the active material in this region, leaving still room for the services and cables. The ITC consists of a calorimeter pluged between the region $0.8 < |\eta| < 1.0$ and, due to severe space constraints, only scintillator between $1.0 < |\eta| < 1.6$. The scintillators in the region $1.0 < |\eta| < 1.2$ are called *gap scintillators*, and the scintillators between $1.2 < |\eta| < 1.6$ are called *crack scintillators*. These last ones extended down to the region in between the barrel and the end-cap cryostats. While the plug and the gap scintillators primarily provide hadronic shower sampling, the crack scintillator plays a critical role in sampling electromagnetic showers, where the normal sampling is comprised by the dead material of the cryostat walls and the inner detector cables.

The Tile Calorimeter forms the shell of the inner part of the ATLAS detector. Within its volume, once the barrel and the extended barrels are assembled, all the sub-detectors except the muon system will be placed. The massive iron structure is rigid enough to support their weight, with the most important components being the full Liquid Argon cryostat and the solenoid. The structure of the Tile Calorimeter as well as the corresponding to all the other sub-detectors inside it is self-supporting and has no mechanical connection with the outside muon system.

3.4.1.1 Detector environment: Radiation and Magnetic field

As mentioned above, the Tile Calorimeter sorrounds the Inner Detector and the Liquid Argon Calorimeter. Due to its position, the detector has to face three basic problems which have implications for its final performance: the level of radiation, the presence of the two magnetic fields from the inner solenoid and the outer toroids, and finally the amount and the $|\eta|$ distribution of the dead material in front of the calorimeter itself.

The dominant source of radiation in the ATLAS detector comes from the pp interaction rate, which is of the order of 10^9 interactions per second and per collision point. Other sources of radiation such as beam losses or beam gas interactions are expected to be at least two orders of magnitude smaller.

When the high energy particles produced at the interaction point enter in the detector material, they begin to develop the shower. If the material is thick (as is the case of a calorimeter) the shower will develop until most of the charged particles are absorbed and only neutrons and associated photons remain and most likely escape from the calorimeter volume. In figure 3.14 the isodose map of the inner detector and the calorimeters is shown. For most of the Tile Calorimeter volume the annual dose rates are below the 20 $Gy\ yr^{-1}$ line, with a maximum annual dose expected of $\sim 36\ Gy$, at $\eta = 1.2$. These radiation levels can affect the performance of the calorimeter over the long period of running due to the degradation in the light production and/or transmission in the scintillators and fibres.

A large program of irradiation test has been performed for the active components of the detector. Different tile/fibre setups have been irradiated with doses from 650 Gy to 10 kGy, at rates from 15 kGy/h down to 5.5 Gy/h. For 10 years of high luminosity running at LHC, a light loss of no more than 5% is expected in the tiles of the first longitudinal sampling, and even less for the others. Using those results and assuming no radiation damage for the Liquid Argon Calorimeter, the energy resolution and jet signal degradation is negligible.

The Tile Calorimeter is the return path for the flux of the solenoid, 70% of which passes through the girder structure, 25% through the active parts of the calorimeter return, and about 2% through the front-plates. A 3D simulation program has been

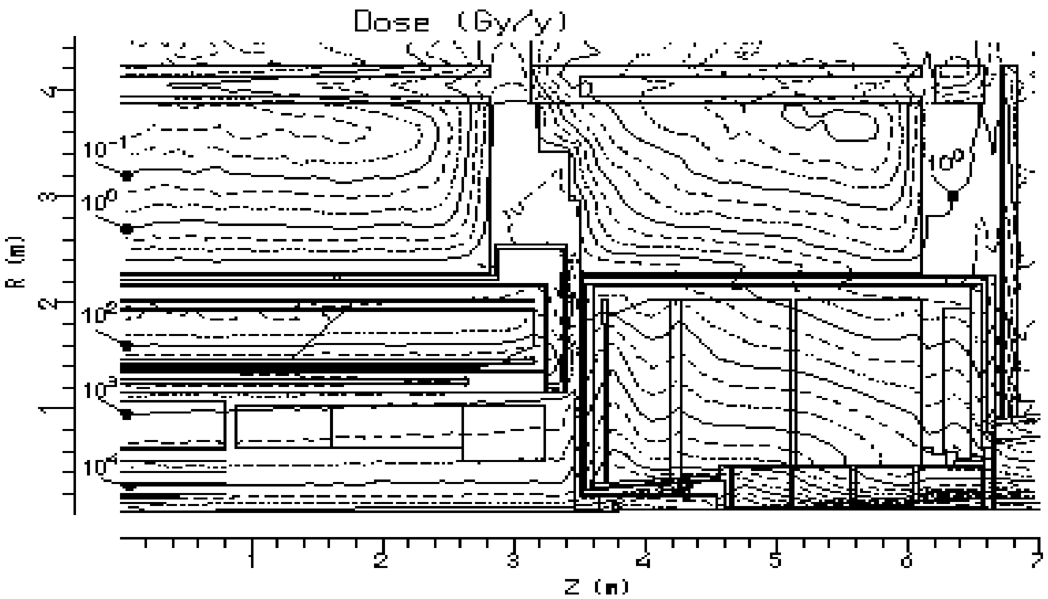

Figure 3.14: Yearly integrated dose ($Gy\,yr^{-1}$) in the inner detector and the calorimeters.

used to calculate the magnetic field at each point of the detector [15]. The highest field regions are at the outer edges of the barrel and extended barrels, with the maximum value, due to the toroid stray field of ~ 1.5 T, located at the outer girder radius. The maximum value in the scintillator does not exceed 6 ± 2 mT. Inside the girder region, the maximum varies from 80 mT at $R = 38$ m to 200 mT at $R = 4.2$ m. The influence of the magentic field on the scintillator light yield has been studied: the light output will increase by about $\sim 1\%$ as a consequence of the expected magnetic field. This value is well within the accuracy of the cell-to-cell intercalibration.

3.4.2 Physics requirements

The tasks of the calorimeters at hadron colliders are:

- accurate measurement of the energy and position of electrons and photons;

- measurement of the energy and direction of jets, and of the missing transverse momentum of the event;

- particle identification, for instance separation of electrons and photons from hadrons and jets, and of τ hadronic decays from jets;

• event selection at the trigger level.

The Standard Model (SM, [16]) Higgs search imposes specific requirements to the hadronic calorimetry. The $W \to jet - jet$ mass reconstruction and the forward jet tagging are crucial for discovering a high mass Higgs boson, and the $H \to b\bar{b}$ mass reconstruction using jet spectroscopy is important for the low mass Higgs search. Both jet identification and jet spectroscopy are clearly mandatory for studying top physics. In the Minimal Supersymmetric Standard Model (MSSM, [17]) a large region of the parameter space is covered by the detection of A^0/H^0 decays into $\tau\tau$ pairs; the $\tau\tau$ mass reconstruction is critically dependent of good p_T^{miss} resolution. In supersymmetric (SUSY, [18]) models, the need to detect the presence of non-interacting particles sets stringent limits on the hermeticity of the calorimeters. The study of quark compositness requires good measurement of very high-p_T jets and good linearity of response, as its effects would be observable as deviation from the QCD expectations in the high-p_T region of the jet cross-section. This set of examples, together with the SM Higgs is used for illustrating the physics requirements on hadronic calorimetry both in the inital low-luminosity phase and in the subsequent high-luminosity running, but it is by no means complete of all the physical issues that will be covered by ATLAS.

The ambitious physics programme of the LHC and the difficult experimental environment set stringent and challenging requirements on the detector specifications; all these will be discussed in the next section.

3.4.2.1 Hadronic calorimeter requirements

The general features of the hadronic calorimetry in terms of rapidity coverage, granularity, energy resolution, energy linearity, total thickness, noise, time of response, are:

• Rapidity Coverage: The main calorimeter task is the reconstruction of jets and the measurement of the event p_T missing. The jet detection has to extend to $|\eta| = 5$ for allowing an efficient tagging of the forward jets associated to the production of heavy Higgs, and the same η coverage is needed for a good missing p_T resolution.

• Granularity: The most stringent transverse granularity requirement comes from the $W \to jet - jet$ decay at high-p_T and applies for $|\eta| < 3$, where a granularity $\Delta\eta \times \Delta\phi = 0.1 \times 0.1$ is needed.

• Energy resolution: For the hadronic calorimeter the guidelines for the energy resolution performances are set requiring a jet energy resolution at different levels in different η regions

$$\frac{\sigma}{E} = \frac{\mathbf{50\%}}{\sqrt{E}} \oplus \mathbf{3\%} \tag{3.22}$$

for $|\eta| < 3$ and

$$\frac{\sigma}{E} = \frac{\mathbf{100\%}}{\sqrt{E}} \oplus \mathbf{10\%} \tag{3.23}$$

for $3 < |\eta| < 5$

Such resolutions are adequate to the tasks of providing jet reconstruction and jet-jet mass reconstruction as well as missing p_T measurement for physical processes of interest.

• Energy linearity: The most stringent linearity requirements for the hadronic calorimeter come from the study of quark compositness, where the jet energy scale has to be linear within 2% up to a transverse energy of 4 TeV [19].

• Total thickness: A total calorimeter (EM and hadronic) thickness of about 10 interaction lengths (λ) is required for shower containment, both for energy resolution reasons and for reducing the background in the muon chambers.

• Noise: The electronic noise level in the hadronic calorimeter is relevant at low luminosity for the quality of low energy jet reconstruction, but for this, as well as for the missing E_T reconstruction the dominant effects come from the EM calorimeter due to its high number of channels.

• Speed of response: A signal peaking time of $\sim$ 40 nanoseconds is required for minimizing the total noise (electronic and pile-up) at high luminosity.

A hadronic calorimeter with the above features is adequate for coping with the physics requirements listed in Section 3.4.2, because it is thus able to perform the critical tasks required. A short list of these tasks is given here:

• Jet identification and measurement: The jet performances are given as a function of η, taking into account the effects intrisically related to the quality of the calorimetry and the ones that would exist even with a perfect calorimeter, due to the energy carried away by neutrinos and muons or lost outside of the angular region used for the jet reconstruction and to pile-up.

The accuracy of the absolute jet calibration scale is a stringent requirement, e.g. for a precise measurement of the top quark mass and for the search of compositness.

• Jet-jet mass reconstruction: At low luminosity the aim is to approach a 1% error on the top quark mass reconstruction. At high luminosity the goal is the detection of a heavy SM Higgs boson decaying into a high-p_T $W \to jet - jet$, where the jet-jet mass reconstruction is the crucial point.

• Forward jet tagging: The acceptance region for the high-mass Higgs search with forward jet tagging is $2 < \eta < 5$. A smooth transition (at $\eta \sim 3.1$) to the forward-calorimetry region and a good performance of the forward calorimeter are key issues in this domain.

• E_T^{miss} reconstruction: The E_T^{miss} plays an essential role from two different points of view. First, the achievement of a good resolution is mandatory for the $\tau\tau$ mass reconstruction, and second, a very good control of the tails of the E_T^{miss} distribution is required for keeping low the level of the fake E_T^{miss} background. This background affects the search for SUSY particles, coming mainly from multijet events, and the search for $H \to ZZ \to ll\nu\nu$, coming mainly from Z+jets events. For the control of E_T^{miss} tails the critical regions are of course the cracks in the calorimeters.

All the requirements mentioned above can be summarized in table 3.2.

Table 3.2: *Physical hadronic calorimeter requirements.*

Hadronic calorimeter performances	
Rapidity Coverage	$\lvert\eta\rvert < \sim 5$
Granularity	$\Delta\eta \times \Delta\phi = 0.1 \times 0.1$ for $\lvert\eta\rvert \leq 3$
	$\Delta\eta \times \Delta\phi = 0.2 \times 0.2$ for $\lvert\eta\rvert > 3$
Energy resolution	$\frac{50\%}{\sqrt{E}} \oplus 3\%$ for $\lvert\eta\rvert \leq 3$
	$\frac{100\%}{\sqrt{E}} \oplus 10\%$ for $3 < \lvert\eta\rvert < 5$
Energy linearity	2 % up to a transverse energy of 4 TeV
Total thickness	10 interaction lengths (λ)
Noise	less than the 5 GeV (low energy jet)
Speed of response	40 nanoseconds
Jet identification	1% accuracy
Jet-jet mass reconstruction	1 % error on the top mass
Forward jet tagging	acceptance region $2 < \lvert\eta\rvert < 5$
$E_T^{miss} reconstruction$	good resolution for the $\tau\tau$ mass

Bibliography

[1] H. Messel and D. F. Crawfird, Electron-photon shower distribution: Function tables for lead, copper and air absorbers, Pergamon Press, London (1970).

[2] Y. S. Tsai, Rev. Mod. Phys. 46:815 (1974).

[3] E. Longo and I. Sestili, Nucl. Instrum. Methods 128:283 (1975).

[4] A. N. Diddens et al., Nucl. Instrum. Methods 178:27 (1980).

[5] U. Amaldi, Phys. Scripta 23:409 (1981).

[6] J. Ranft, Particle Accelerators 3:129 (1972); A. Baroncelli, Nucl. Instrum. Methods 118:445 (1974); T. A. Gabriel et al., Nucl. Instrum. Methods 134:271 (1976).

[7] Amendikua, S. R. et al., report Pisa 80-4 (29 May 1980), Contribution to the Conference on Experimentation at LEP, Uppsala, June 1980.

[8] W. Hofmann et al., Nucl. Instr. and Methods 163, 77 (1979).

[9] E. Gabathuler et al., Nucl. Instr. and Methods 120, 391 (1974).

[10] C. W. Fabjan and W. J. Willis, in: Proc. Calorimeter Workshop, ed., M. Atac, Batavia Illinois (1975) p. l.

[11] H. Abramowicz et al., Nulc. Instr. and Meth. 180 (1981) 429.

[12] T. Akesson et al., Performance of the Uranium/Plastic Scintilator Calorimeter for the HELIOS Experiment at CERN, CERN-EP/87-111.

[13] ATLAS Tile Calorimeter Technical Design Report, CERN/LHCC/96-42 (1996).

[14] E. Berger et al., (RD34 Collaboration), Construction and Performance of an Iron-scintillator Hadron Calorimeter with Longitudinal Tile Calorimeter Configuration. CERN/LHCC 95-44,CERN, Geneva, Switzerland.

[15] Preliminary results on the ATLAS solenoid magnetic field calculations in presence of hadronic tile calorimeter. V. Klyuklin and B. Klochkov, 31-01-1994; Calculation of the ATLAS magnetic field. F. Bergsma, 16-08-1995.

[16] S.L. Glashow, Nucl. Phys. 22, 579 (1961). S. Weinberg, Phys. Rev. Lett. 19, 1264 (1967). A. Salma, Elementary Particle Theory, H. Svartholm, ed. (Stockholm: Almquist and Wiksell, 1986).

[17] Z. Kunszt and F. Zwirner, Nucl. Phys. B385, 3 (1992).

[18] S. P. Martin, A Supersymmetry Primer, hep-ph/9709356.

[19] ATLAS Collaboration, Technical Proposal, CERN/LHCC/94-43, LHCC/P2.

Chapter 4

Test beam performance of the TileCal prototipes

The Tile Calorimeter test beam program started in 1993 with a standalone setup. The reduced hadron calorimeter prototype consisted of an azimuthal stack of five modules. Each module covering $2\pi/64$ in azimuth and 1 m length along the z direction.

The five prototypes were exposed to high-energy pion, electron and muon beams at the CERN SPS. The energy resolution for pions was studied in the energy range from 20 to 300 GeV and for incident angles from $\theta = 0^o$ to 45^o. Uniformity was studied with pions of 40 and 80 GeV at $\theta = 10^o$. The calorimeter response to muons was investigated using 225 GeV muons at various incident angles.

The results from this test beam data can be summarized as follows:

• The hadronic energy resolution was compatible with the design goal of $\frac{\sigma}{E} = \frac{50\%}{\sqrt{E}} \oplus 3\%$.

• Linearity between 20 and 300 GeV of the order of a few percent can be achieved with the Tile Calorimeter alone.

• The e/π ratio for the Tile Calorimeter prototype was found to be between 1.1 and 1.2, a relatively small deviation from the ideal compensation.

Recent test beam results related to the hadron response for prototypes and modules zero of the barrel and extended barrel are presented in this Chapter. The energy resolution, linearity and e/π ratio are also given. Up to date, we can categorize the test beam setups as follows:

• 1997 test beam with two Extended Barrel Modules 0.

• 1998 test beam with a full scale barrel sector (Module 0).

Early measurements were performed in the H8 beam line at the SPS at CERN. The beam lines were instrumented in a standard fashion with one threshold Cherenkov counter used for π/e separation for $E \leq 20$ GeV, a pair of delay-line wire chambers for both x and y coordinates, and a set of scintillators to define the trigger beam. The scintillators could define a beam spot of around 2-3 cm, while the chambers allowed the reconstruction of the impact point on the calorimeter face to better than ± 1 mm. Data were taken with muons, pions and electrons between 10 and 400 GeV.

For the needs of the Tile Calorimeter a full simulation package based on the GEANT program [1] has been developed, which describes in full detail the detector prototypes that have been used for the test beam runs. A comparison between the test beam data of the Tile Calorimeter prototype modules and the GCALOR [2] package in the framework of the GEANT program has been done for the 1998 test beam.

This program of test beam data taking has been carried out demonstrating the good performance of the calorimeter, which fulfils the requirements for the ATLAS hadronic barrel calorimetry.

4.1 The 1997 test beam

The extended barrel modules of Tilecal are smaller than the barrel ones, with a front face area of $259 \times 22\ cm^2$. The sizes of the barrel and extended barrel tiles are the same, but a different fiber configuration allows a different radial segmentation to adapt the modules to the higher η values where they will be located.

Two extended barrel modules 0 were built for the test, one in Barcelona (BCN), Spain, and the other at Argonne (ANL), USA. The cell structure of the modules is shown in figure 4.1, where two different routing of the fibers have been used, resulting in different fibre lengths in the modules. We used two different routing because the USA group insisted to make a different one, where the routing has a more clean path. The fibres used to equip the modules were the Kuraray multi-clad Y11(200)MS, dopped with 600 ppm of UV Absorber. Both modules were equipped with white fibre profiles. The modules have 3 segments in depth, corresponding to 1.37, 2.48 and 3.14 interaction lengths at $\eta = 0$. A semi-projective cell geometry is defined as it will be in ATLAS.

The modules were tested at CERN in October 1997 together with the five 1 meter old modules. In order to improve the transverse leakage for both, the two extended barrel modules were sandwiched between the 1 m prototype modules, as it is shown in figure 4.2. The ANL module was located on the top of the BCN module. The readout of the

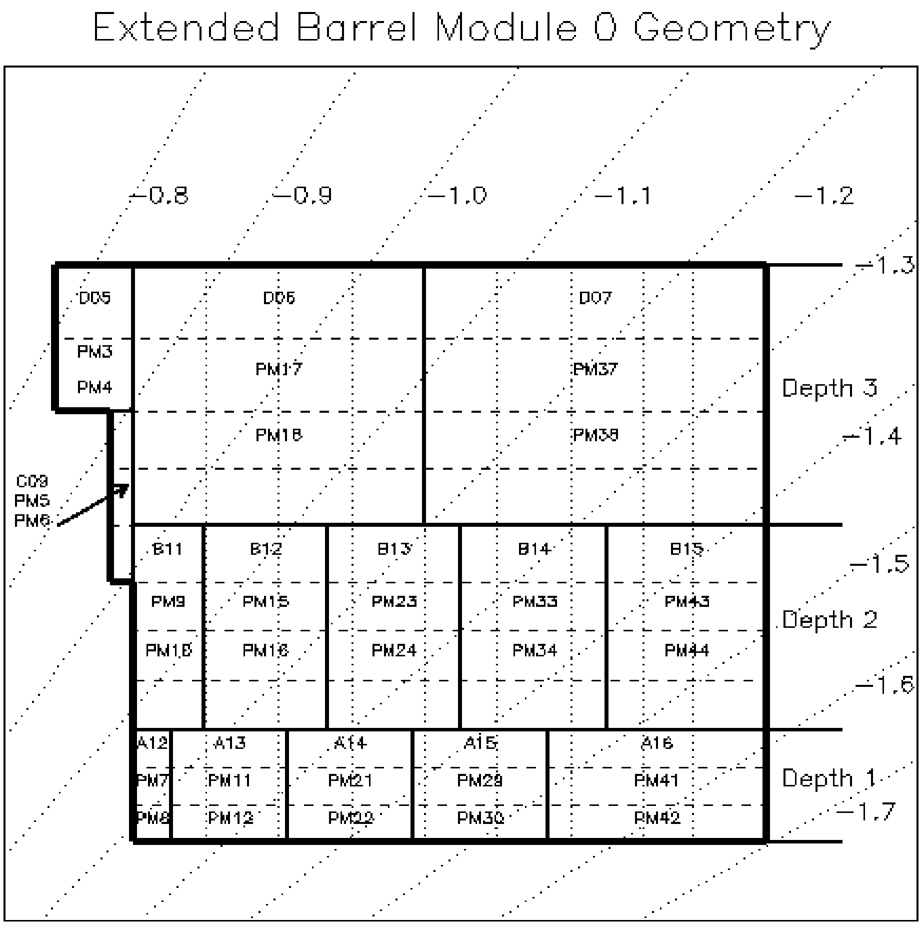

Figure 4.1: Configuration of the Extended Barrel Module 0 built in Barcelona.

ANL module used the Fermi system (1 ADC) [3], while part of the Barcelona module was equipped with a bi-gain 12 bit ADC readout. The photomultipliers (PMT's) were the Hamamatsu 8-stage R5900.

The calorimeter modules were installed on a table that moves horizontally and perpendiculary to the beam line (z direction). They can also be rotated around its vertical axis, allowing to change the θ angle, accesing the towers of different η values. The table can also be rotated around a horizontal axis, allowing to scan in the azimuthal incidence angle (ϕ).

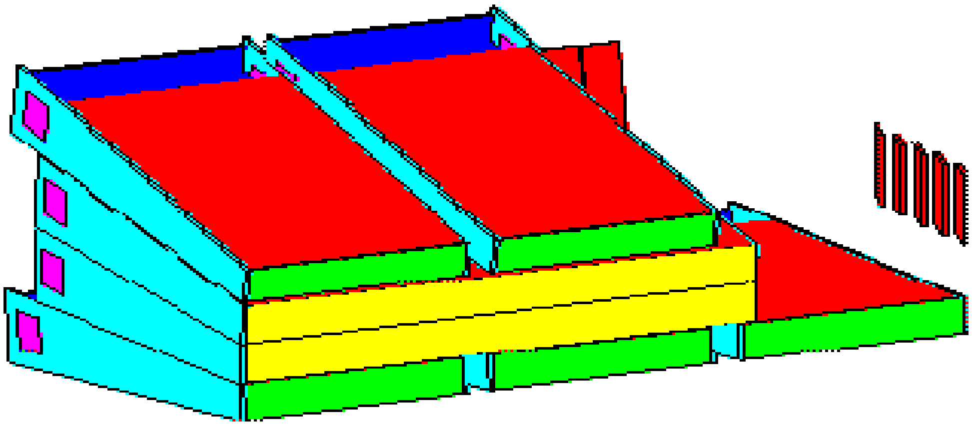

Figure 4.2: Extended barrel modules 0 in the test beam.

Test beam energies (20, 40, 50, 80, 100, 180, 300 and 400 GeV) along different values of η, from $\eta = -0.8$ up to $\eta = -1.4$ have been used in this analysis. On average, about ten thousand events are available for each energy. Cuts were applied on the beam chambers data to eliminate the beam halo and events with simultaneous particles in the scintillator chambers; finally 60% of the events were removed including pedestal events supression. The cut on the beam chamber coordinates remove around 10-20% of the sample data, whilst the scintillator chambers remove 15%. All the applied cuts have been taken from reference [4]. The cuts were applied with the agreement of the colaboration members.

Figures 4.3 and 4.4 show examples of the applied cuts effects.

This test beam experience has revealed the cross-talk effect. The high trasparency

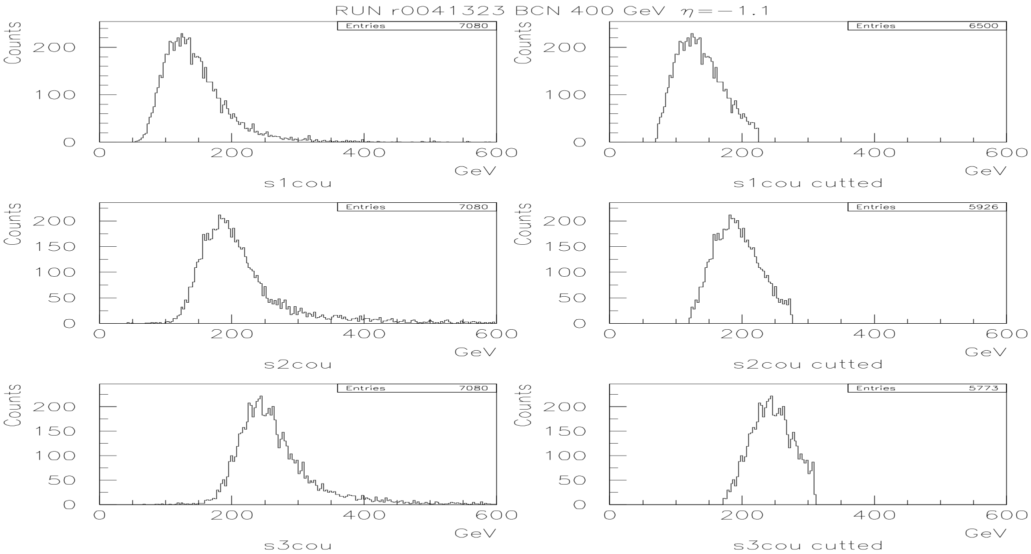

Figure 4.3: *Effects of the cuts in the scintillator chambers.*

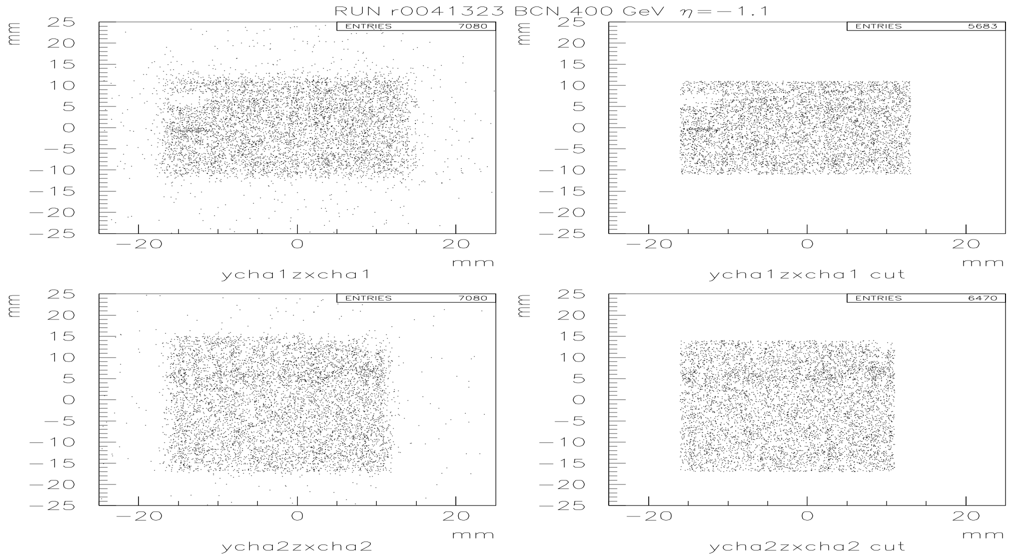

Figure 4.4: *Effects of the cuts in the beam chambers.*

of the plastic profiles used to group the fibres and stick them in the proper grooves, induced that the light produced in a given calorimeter cell from the third or second depth was transported by the same group of fibres to the first or second depth.

Let be E_i, $i = 1, 2, 3$, the energy measured in the i depth and ϵ_i the true energy deposited in the i depth. Because of the cross-talk between the depth 1 and the depths 2 and 3, and of the cross-talk between the depth 2 and 3, we can write:

$$E_1 = \epsilon_1 + x_{21}\epsilon_2 + x_{31}\epsilon_3 \tag{4.1}$$

$$E_2 = \epsilon_2 + x_{32}\epsilon_3$$

$$E_3 = \epsilon_3$$

where x_{ij} is the fraction of the energy measured in the j-th depth, due to a particle passing through the i-th depth.

In terms of measured energy:

$$\epsilon_1 = E_1 - x_{21}(E_2 - x_{32}E_3) - x_{31}E_3 \tag{4.2}$$

$$\epsilon_2 = E_2 - x_{32}E_3$$

$$\epsilon_3 = E_3$$

The total energy E_{total} can be written as:

$$E_{tot} = \epsilon_1 + \epsilon_2 + \epsilon_3 = E_1 + (1 - x_{21})E_2 + (1 - x_{31} - x_{32} + x_{21}x_{32})E_3 \tag{4.3}$$

the values of x_{ij} are between 0.2/0.3 as calculated from the muon and electron data, and the Cs calibration analysis [5]. We can then write:

$$E_{tot} = E_1 + \alpha E_2 + \beta E_3 \tag{4.4}$$

where the α and β coefficients are:

$$\alpha \cong 0.75, \quad \beta \cong 0.6 \tag{4.5}$$

4.2 Analysis of the 1997 pion data for the Extended Barrel Modules 0

The different energy values of the pion data taken with the setup described in the last section were reconstructed with two algorithms which are explained in detail in reference [6]. In this Section, we will briefly describe the two algorithms and will present a new method to reconstruct the pion energy; we will compare our strategy and results with previous approaches.

Before going into the energy reconstruction of the pion data, we will briefly discuss a crucial phenomenon for the understanding of the different techniques that will be explained. This concept is the so-called *non-compensation* (see chapter 3) in hadron calorimetry and is the main physical motivation for the algorithms applied in the reconstruction of the extended barrels and barrel pion data.

A high energy hadron which enters a calorimeter interacts inelastically with the nuclei of the calorimeter and develops a shower of particles that can be grouped as follows:

• High-energy secondaries, such as π^+, π^-, $\pi^0 \rightarrow \gamma\gamma$, p, n,... Note that the hadronically produced π^0's will immediately decay into $\gamma\gamma$ and develop an electromagnetic shower.

• Low-energy fragments emitted from the excited target nucleus, such as photons with energy in the range $\sim$ 1 - 10 MeV, neutrons and protons (*boil off* particles) with energy between $\sim$ 1 and 10 MeV. The binding energy to boil off these nucleons is *robbed* from the energy of the cascade and in most cases will not contribute to a measurable (*visible*) energy.

The picture of the hadronic cascade suggests to qualitatively distinguish between an electromagnetic component (mostly due to the π^0 production) and a purely hadronic component, which will invert a considerable fraction ($\sim$ 15-20% at 10 GeV incident energy) of its energy to overcome the binding energy of nucleons.

In order to study the performance of the calorimeters (see Section 3.4), it is very useful to compare the visible energy released by electrons with the signal released by pions of equal incident energy; this ratio is usually named e/π in calorimetry and allows us to introduce the concept of non-compensation: $e/\pi \neq 1$.

In most sampling calorimeters $e/\pi > 1$; this is mostly caused by the energy loss to overcome the binding energy of the excited nucleus in the hadronic shower development; the low-energy products produced in the boiling-off of nucleus will in general be registered very differently at the read-out level compared with the energetic cascade component.

Nevertheless, it is possible to achieve compensation. Two different strategies have been adopted, which may result in $e/\pi \cong 1$:

• designing an intrisically compensated calorimeter (U, Pb, etc.).

• achieving compensation in off-line analysis using different weights for the electromagnetic and hadronic components of the shower.

The previous approaches applied to the extended barrel data and our new approach use just the latter method in trying to achieve compensation. We will further see the characteristics of the different techniques and the results obtained in resolution and linearity.

In the next section we study in three steps the evolution of the linearity and resolution parameters in the data reconstruction, from raw data to H1 weighting method going through the benchmark method. The e/h ratio is determined from these data using the response obtained for electrons and pions.

4.2.1 Raw data

The first step in the linearity and resolution study was the direct analysis of the raw data. The three components of the total raw energy are the energy detected in the BCN, ANL and in the five 1 m modules. The energy in BCN and ANL modules has been corrected for the cross-talk problem [4], and the conversion factors from pC to GeV were calculated to be 1.26 GeV/pC for extended barrels (this electromagnetic scale is determined using electron data) and 0.1613 GeV/pC for old modules (it was determined several times in the past using electron runs of the test beam prototype modules). So finally:

$$E_{Raw} = E_{ANL}^{corr} + E_{BCN}^{corr} + E_{old} \tag{4.6}$$

According to this expresion we present the results of the mean reconstructed energy (μ), σ and resolution (σ/μ) in table 4.1. Also the plots of linearity, defined as E/E_{beam} and energy resolution can be seen in figures 4.5 and 4.6.

The linearity presents the typical shape of a non-compensated calorimeter, the slope is due to the increase of the electromagnetic component in the shower produced by a pion. The *rms* is around 4.3% for both modules and both values of η, which is one of the characteristics to improve.

Table 4.1: *Nominal energy, mean reconstructed energy, σ and resolution at various beam energies at two different η for BCN and ANL modules obtained from raw data.*

BCN	η=-1.1		
Beam Energy (GeV)	μ (GeV)	σ (GeV)	σ/μ(%)
20	16.55±0.04	2.03±0.03	12.2±0.2
40	34.17±0.10	3.30±0.08	9.6±0.2
50	42.25±0.10	3.37±0.09	7.97±0.21
80	69.01±0.11	5.32±0.09	7.71±0.13
100	86.24±0.12	5.94±0.10	6.89±0.12
180	160.6±0.3	9.16±0.23	5.71±0.14
300	275.5±0.3	16.8±0.3	6.09±0.10
400	373.8±0.4	23.5±0.4	6.28±0.11
ANL	η=-1.1		
Beam Energy (GeV)	μ (GeV)	σ (GeV)	σ/μ(%)
20	15.80±0.04	2.06±0.03	13.0±0.2
40	33.19±0.09	3.17±0.08	9.56±0.23
50	42.09±0.11	3.61±0.09	8.57±0.21
80	68.22±0.11	5.18±0.10	7.59±0.14
100	85.47±0.12	6.1±0.1	7.09±0.12
180	158.7±0.2	9.9±0.2	6.25±0.11
300	268.4±0.3	15.4±0.3	5.74±0.10
400	364.7±0.4	22.2±0.4	6.07±0.11
BCN	η=-1.2		
Beam Energy (GeV)	μ (GeV)	σ (GeV)	σ/μ(%)
20	16.11±0.05	2.23±0.02	13.9±0.2
40	33.72±0.08	3.30±0.08	9.8±0.2
50	44.74±0.13	4.09±0.08	9.15±0.21
80	72.20±0.13	5.90±0.09	8.17±0.15
100	90.98±0.15	6.98±0.11	7.67±0.12
180	168.5±0.3	11.7±0.2	6.94±0.11
300	282.3±0.4	19.6±0.3	6.95±0.10
400	380.0±0.5	24.9±0.3	6.55±0.10
ANL	η=-1.2		
Beam Energy (GeV)	μ (GeV)	σ (GeV)	σ/μ(%)
20	16.58±0.04	1.98±0.02	11.9±0.2
40	34.00±0.09	3.29±0.08	9.7±0.2
50	42.4±0.1	3.33±0.08	7.9±0.2
80	69.2±0.1	4.75±0.08	6.87±0.15
100	86.3±0.1	5.38±0.10	6.24±0.11
180	160.6±0.2	8.7±0.2	5.44±0.11
300	276.5±0.3	15.3±0.3	5.54±0.10
400	373.8±0.4	23.5±0.4	6.28±0.10

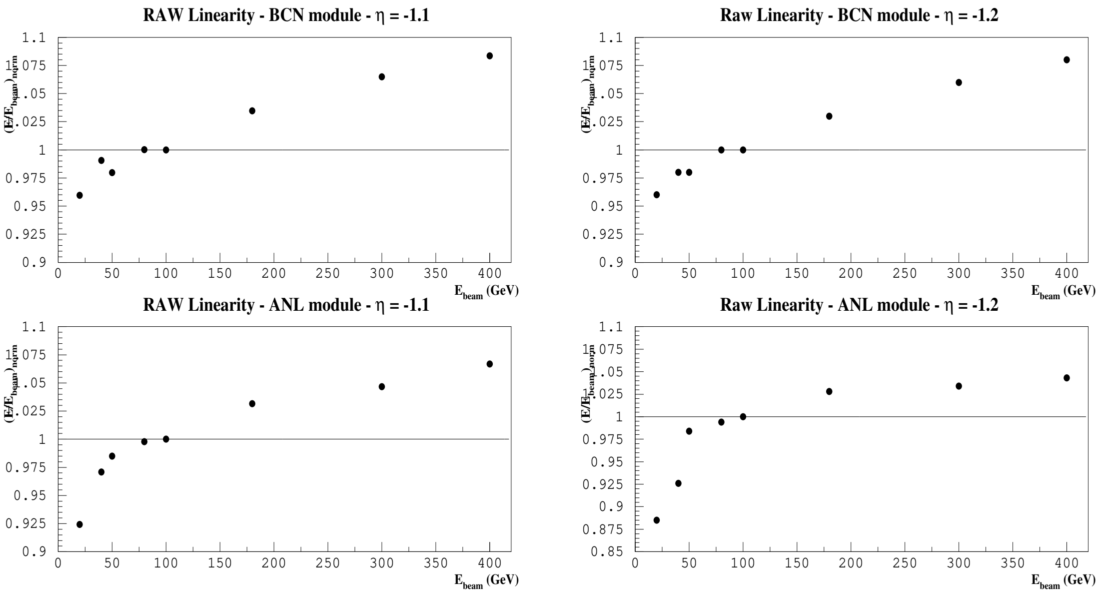

Figure 4.5: *Lineatiry of raw data. Left: for η=-1.1 BCN (top) and ANL (bottom) modules. Right: for η=-1.2 BCN and ANL respectivily.*

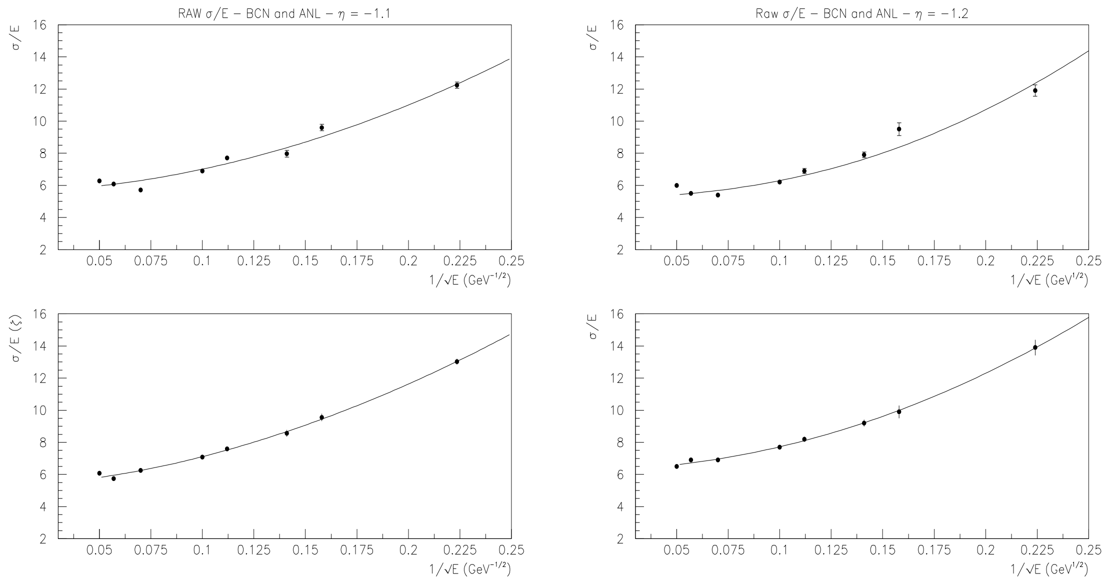

Figure 4.6: *Energy resolution of raw data. Left: for η=-1.1 BCN (top) and ANL (bottom) modules. Right: for η=-1.2 BCN and ANL respectively.*

A fit of the data is performed in the way:

$$\frac{\sigma}{E} = \frac{\mathbf{a}\%}{\sqrt{E}} \oplus \mathbf{b}\% \oplus \frac{\mathbf{c}}{E} \tag{4.7}$$

where **a** represents the statistical fluctuations in the shower development, **b** is the constant term dominant at high energies and **c** is the noise term. E is given in GeV and the $\oplus$ symbol indicates sum in quadrature.

The fit results for BCN and ANL modules at η = -1.1 and -1.2 are presented in the table 4.2.

Table 4.2: *Statistical (a), constant (b), and noise (c) terms at two different η for the BCN and ANL modules obtained from raw data.*

η	BCN			ANL		
	a (%)	b (%)	c	a (%)	b (%)	c
-1.1	40.88	5.61	1.26	45.01	5.35	1.27
-1.2	31.10	5.17	1.74	43.30	6.24	1.56

The **c** parameter in the expresison 4.7 takes into account the different noise contributions in the detector. It can be measured independently of the resolution studies and has been estimated from noise *rms* which mean value is around 0.06 GeV (figure 4.12) [8].

If we fit this expresison with the three parameters free, then the **c** parameter can take no representative values, it is due to the characteristics of the experimental data. These values affect directly to the **a** values as it can be seen in figure 4.7, impeding to compare the **a** parameters obtained from different methods.

In figure 4.7 is shown the strong relation between the two parameters **a** and **c** when we do the fit of the typical resolution expression.

In this analysis all the resolution fits have been done fixing $\mathbf{c}$ = 0.06 GeV (according to the mean in figure 4.12) and fitting with **a** and **b** free in order to obtain less aleatory results in the **a** value and to compare with other fits. In figure 4.7 it can be seen that at $\mathbf{c}$ = 0.06 GeV the **a** value reach a *plateau*.

The figure 4.8 shows the same data but fitted with this new consideration.

The results taking into account this idea are presented in the table 4.3. About the resolution, we can conclude that in general the requirement is reached. Moreover it can be seen that BCN module has better resolution than ANL.

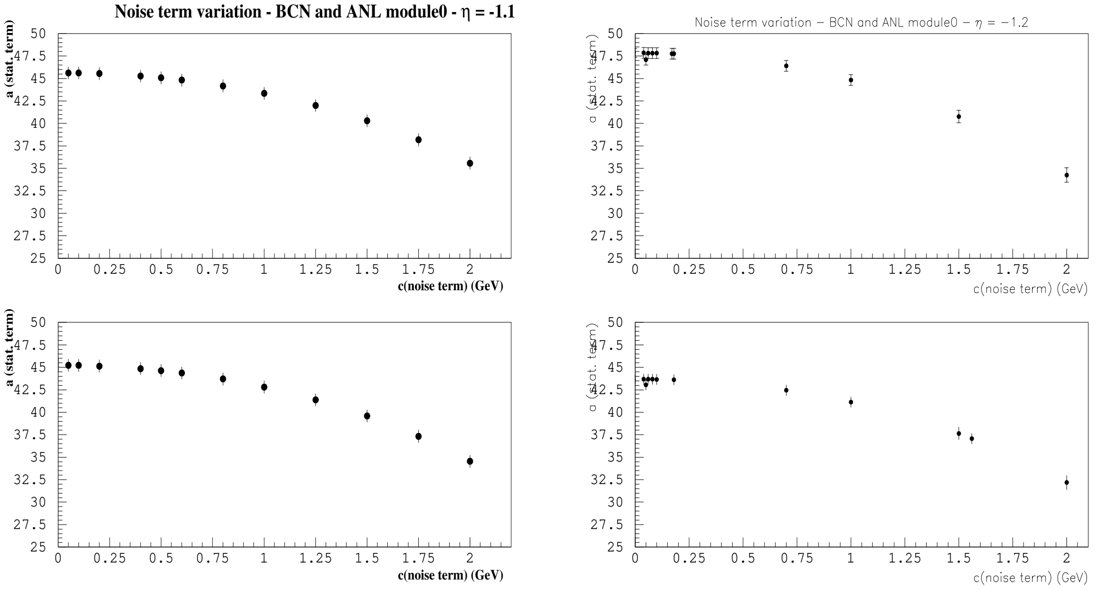

Figure 4.7: *Variation of parameter* **a** *as a function of* **c**.

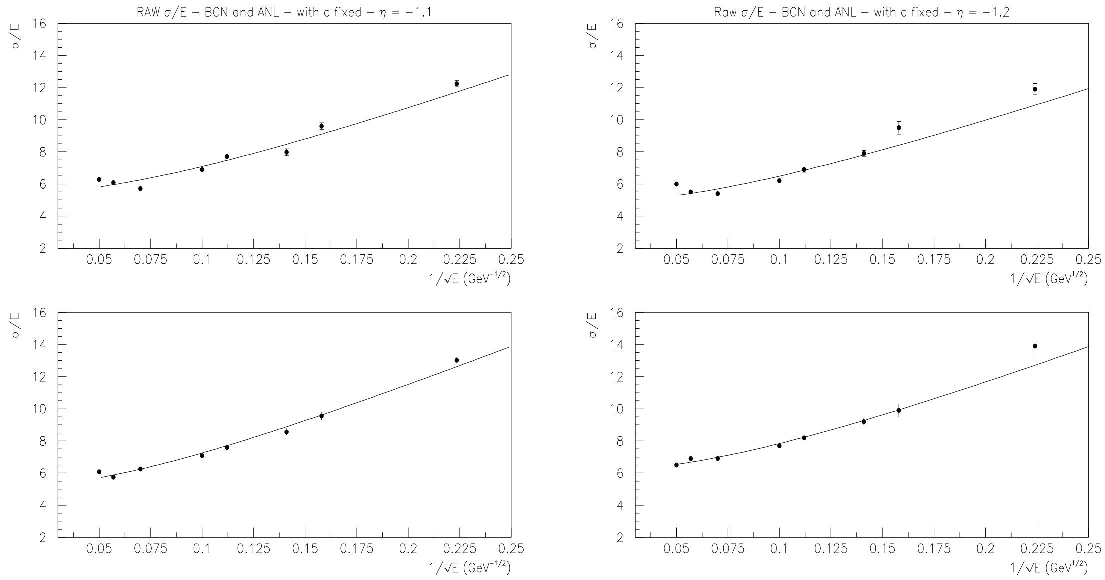

Figure 4.8: *Energy resolution of raw data with parameter* **c** *fixed at 0.06 GeV. Left: for* η*=-1.1 BCN (top) and ANL (botton) modules. Right: for* η*=-1.2 BCN and ANL respectively.*

Table 4.3: *Statistical (a), constant (b), and noise (c) terms at two different η for the BCN and ANL modules obtained from raw data fixing the* **c** *parameter.*

η	BCN			ANL		
	a (%)	b (%)	c	a (%)	b (%)	c
-1.1	46.70	5.34	0.06	51.71	5.09	0.06
-1.2	43.71	4.80	0.06	49.90	6.04	0.06

4.2.2 A Benchmark approach

In the *benchmark* algorithm, a one step procedure is adopted to reconstruct the nominal beam energy: the energy of the particle is obtained as the sum of several terms, and the involved parameters are optimized by minimizing the fractional energy resolution σ/E.

This method tries to correct the effect of the lateral and longitudinal leakage in the prototype [4].

The used algorithm is:

$$E_{TOT} = X[E_{tot}^{ANL} + E_{tot}^{BCN} + (A-1)(E_{S3}^{ANL} + E_{S3}^{BCN})] + BE_{old} \tag{4.8}$$

where E_{tot}^{ANL}, E_{tot}^{BCN} are the energy values corrected by cross-talk (in pC) detected in the ANL and BCN modules, and E_{S3}^{ANL}, E_{S3}^{BCN} are the energies detected in sample three of ANL and BCN modules. Finally E_{old} is the energy detected in the five 1 meter modules.

X =1.26 GeV/pC is the conversion factor from pC to GeV for the extended barrel.

(*A-1*) is the parameter that corrects the energy losses due to the longitudinal leakage of the shower. It is calculated looking at the dependence of the total energy with the energy deposited in sample three. It is logic to assume that the longitudinal leakage is proportional to the energy deposited in the last sample.

Finally, B takes into account the transversal leakage of the shower. The transversal losses are proportional to the energy deposited in the old modules due to the set up of the experiment. To obtain this parameter, the total energy is plotted as a function of the energy in the old modules. Moreover in this factor we included the conversion factor 0.1613 GeV/pC for the 1 meter modules. An example of this representation is shown in figure 4.9.

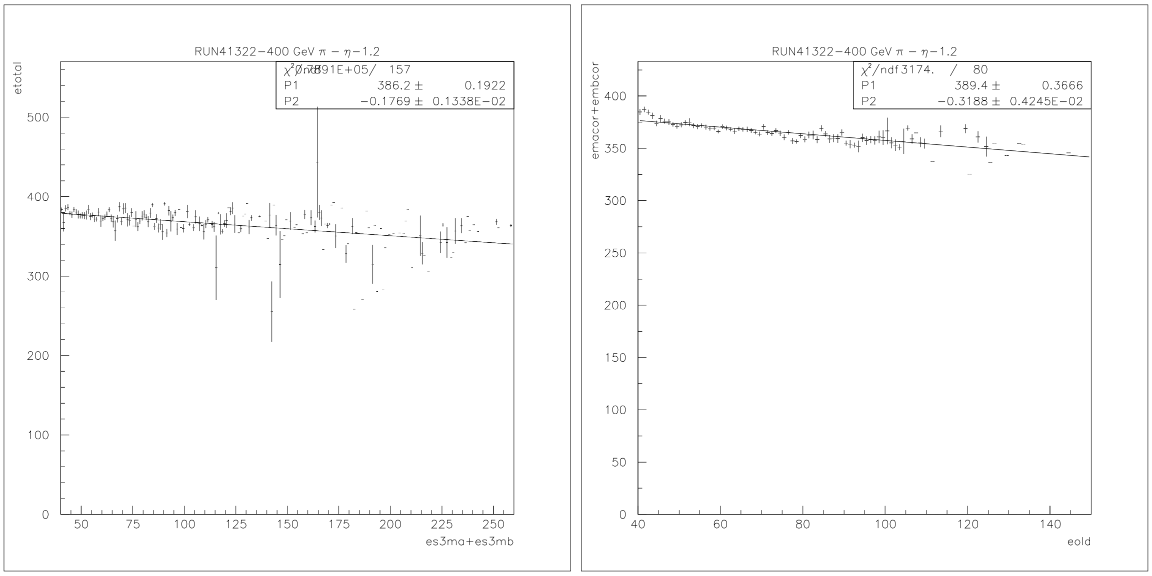

Figure 4.9: *Left: Total energy as a function of the deposited energy in the last samples. Right: Total energy as a function of the energy deposited in the old modules.*

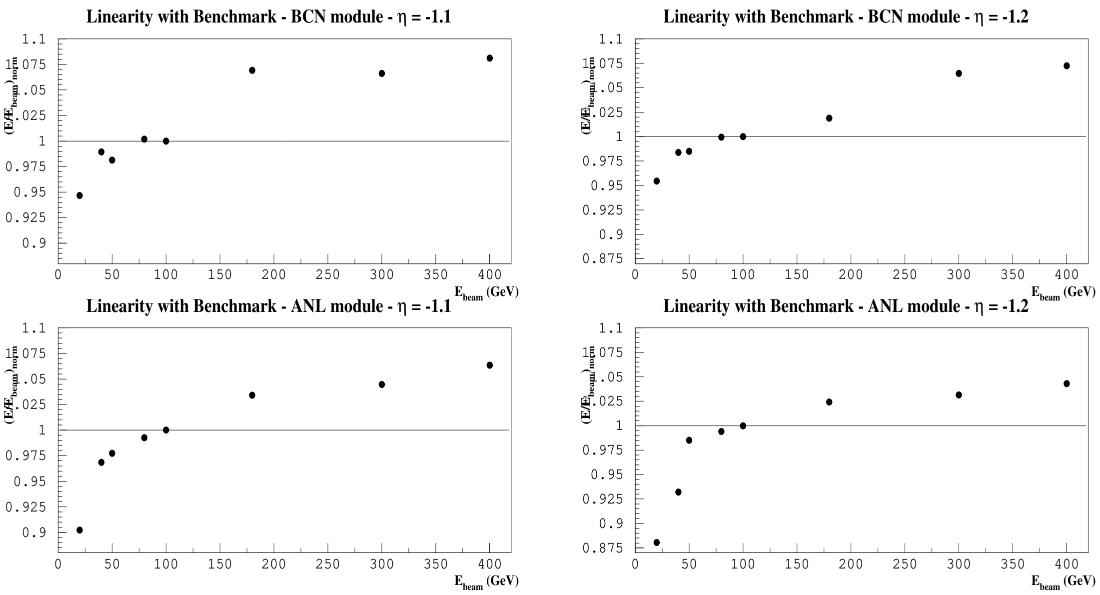

Figure 4.10: *Linearity plots obtained with the benchmark method. Left: for η=-1.1 BCN (top) and ANL (bottom) modules. Right: for η=-1.2, BCN and ANL modules, respectively.*

Table 4.4: *Nominal energy, mean reconstructed energy, σ and resolution at various beam energies and two different η for BCN and ANL modules obtained from benchmark method.*

BCN	η=-1.1		
Beam Energy (GeV)	μ (GeV)	σ (GeV)	σ/μ(%)
20	17.69±0.05	2.40±0.05	13.6±0.3
40	36.97±0.08	3.54±0.06	9.58±0.22
50	45.84±0.10	3.70±0.09	8.07±0.21
80	74.88±0.12	5.52±0.09	7.37±0.15
100	93.42±0.11	6.22±0.11	6.66±0.14
180	179.80±0.16	10.3±0.2	5.74±0.11
300	298.8±0.2	15.5±0.3	5.18±0.10
400	404.0±0.2	19.8±0.4	4.9±0.1
ANL	η=-1.1		
Beam Energy (GeV)	μ (GeV)	σ (GeV)	σ/μ(%)
20	16.73±0.05	2.5±0.03	15.0±0.3
40	35.92±0.04	3.5±0.07	10.0±0.3
50	45.31±0.12	3.9±0.09	8.7±0.3
80	73.62±0.12	5.7±0.10	7.7±0.2
100	92.72±0.13	6.3±0.11	6.79±0.15
180	172.6±0.3	10.3±0.2	5.99±0.15
300	290.6±0.3	17.6±0.3	6.07±0.11
400	394.4±0.4	18.1±0.4	4.60±0.15
BCN	η=-1.2		
Beam Energy (GeV)	μ (GeV)	σ (GeV)	σ/μ(%)
20	17.26±0.05	2.37±0.05	13.8±0.3
40	35.57±0.09	3.46±0.11	9.7±0.3
50	44.52±0.11	3.47±0.10	7.8±0.2
80	72.27±0.09	4.71±0.07	6.52±0.10
100	90.40±0.11	5.21±0.09	5.76±0.10
180	167.4±0.2	7.65±0.17	4.57±0.10
300	288.7±0.2	12.44±0.17	4.31±0.06
400	387.8±0.2	15.90±0.23	4.10±0.06
ANL	η=-1.2		
Energy	μ (GeV)	σ (GeV)	σ/μ(%)
20	16.68±0.05	2.53±0.05	15.2±0.3
40	35.32±0.05	3.52±0.07	9.96±0.19
50	46.65±0.12	4.05±0.10	8.7±0.2
80	75.34±0.12	5.63±0.09	7.48±0.12
100	94.72±0.13	6.60±0.10	6.97±0.12
180	174.6±0.3	9.6±0.3	5.48±0.16
300	293.1±0.3	16.7±0.3	5.7±0.1
400	345.2±0.4	19.3±0.3	5.6±0.1

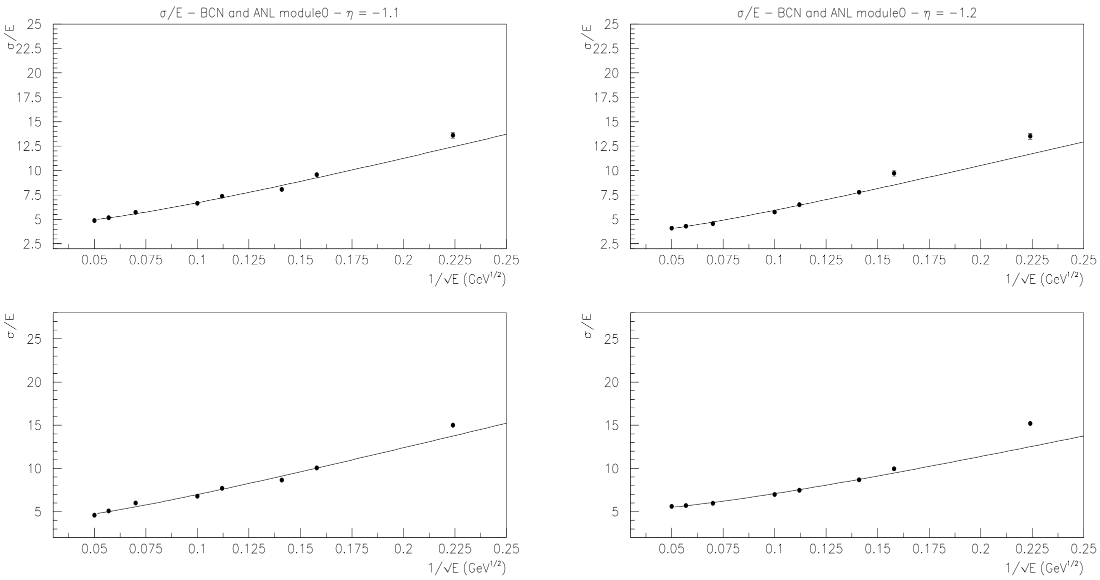

Figure 4.11: *Energy resolution plots obtained with the benchmark method. Left: for η = -1.1 BCN (top) and ANL (bottom) modules. Right: for η=-1.2, BCN and ANL modules, respectively. The* **c** *parameter has been fixed.*

In table 4.4 are shown the results obtained with the present method.

A similar behaviour as for direct raw data is obtained for linearity (figure 4.10). The *rms* changes from 4.3% to 4.5% in this analysis. This is logic if we consider that the benchmarck method does not correct the non-compensation of the detector. A short improvement can be seen in the linearity of points at high energies.

The fit results (figure 4.11) for BCN and ANL modules at η = -1.1 and -1.2 are presented in the table 4.5. There is a clear improvement in **b**, the dominant parameter at high energies, where the Benchmark method corrects the leakage.

Table 4.5: *Statistical (a), constant (b), and noise (c) terms at two different η for the BCN and ANL modules obtained from the Bechmark method.*

η	BCN			ANL		
	a (%)	b (%)	c	a (%)	b (%)	c
-1.1	50.10	3.10	0.06	51.50	4.87	0.06
-1.2	52.21	4.21	0.06	59.10	3.71	0.06

Applying the cell-by-cell cross-talk correction and the benchmark techniques to correct for the longitudinal and lateral behaviour of the hadronic shower, we have obtained an improvement in σ/E. The next step is the application of a weighting technique that could improve the poor linearity results obtained so far.

4.2.3 A new energy reconstruction of the pion energy (H1 method)

As it has been pointed out, the previous results were not quite satisfactory: after applying a benchmark technique an improvement in the **b** parameter of the resolution was obtained but the linearity is still quite poor.

We then decided to try an independent approach inspired in the H1 collaboration [9]. The correction strategy chosen in previous calorimeter studies [7] was to adjust *downwards* the response of read-out cells with a large signal to compensate for the response to large EM energy clusters, typically due to π^0 production. This method is based in correcting *upwards* the energy of the cells instead of *downwards* as the weighting techniqued applied to TILECAL standalone [10].

As a preliminary step, the signal in every calorimeter cell (ANL, BCN and five 1 meter modules) is expressed in GeV, using the signal-to-energy conversion constant obtained from electron runs [4].

The energy in each cell, E_{cell}, is corrected multiplying its value by a parameter a_i [9] which depends on the energy of the cell:

$$E_{Cell}^{Cor} = a_i \times E_{Cell} \tag{4.9}$$

As a first step, a simple minimization technique [11] is used to obtain a set of n correction parameters a_i (i = 1.,,,.n) for each beam energy. As second step the a_i are expressed as a function of the cell and beam energies.

In this analysis a noise cut has been applied to the energy of the cells; this helps in parametrizing the a_i because of their unstable behaviour in the noise region. The cut applied is the following:

$$|E_{cells}| > 0.056\ GeV/Cell \tag{4.10}$$

The reason for making a symmetric cut is that the electronic noise with its "zero suppression" appears as symmetric around zero. This sign-symmetric noise cut [12] has the advantage of statistically cancelling the noise signals beyond the cut; the bias introduced on the signal, inevitable with any cut, will in general be smaller than with an asymmetric cut.

The cut value was chosen from the plot shown in figure 4.12; the criteria are the *RMS* of the pedestal noise in the two modules.

4.2.3.1 Obtaining sets of a_i at each energy

For each beam energy the cell energy spectrum is divided into n intervals and a correction paramater a_i is calculated for each interval.

To obtain stable results it is useful to have about the same number of entries per interval. Also, in view of the subsequent a_i parametrization it is useful to develop a simple interval definition algorithm that can be applied at all beam energies.

The algorithm is based on selecting equal area intervals on an exponential cell energy distribution, as schematically is shown in figure 4.13, for the 20 GeV data.

The limits of the intervals are defined from the 20 GeV data and are unchanged at all other beam energies; hence the number of intervals is invariant, but the mean value of the cell energy in each interval changes somewhat with the energy.

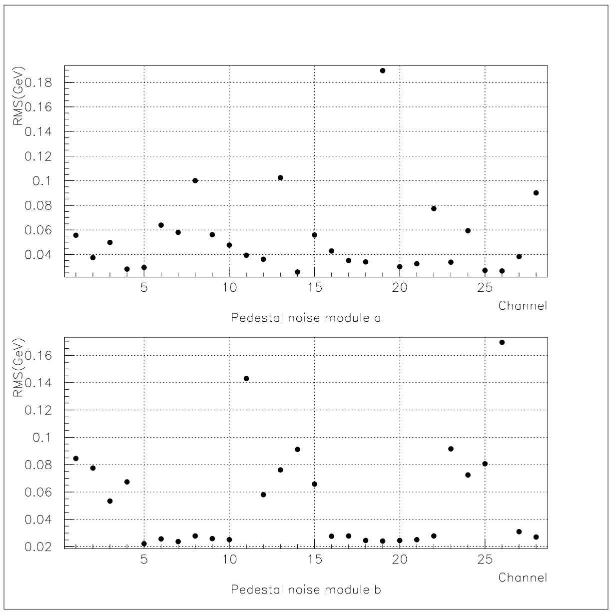

Figure 4.12: *RMS study of the pedestal noise for the ANL module (top) using only compressors and for the BCN module using compressors and bigain (bottom) [8].*

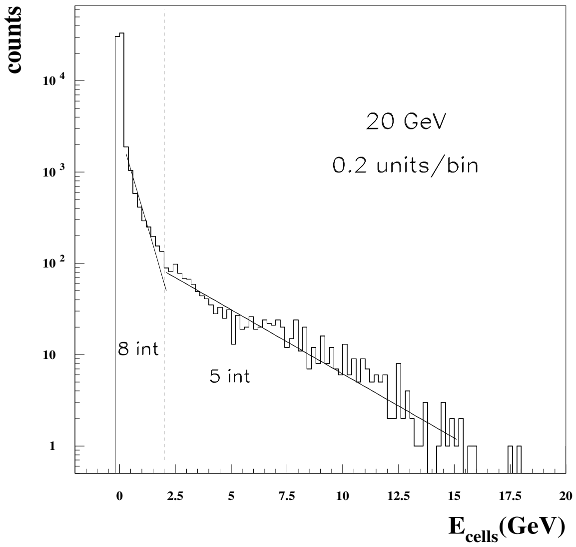

Figure 4.13: *Cell energy spectrum of the Tile calorimeter for 20 GeV pions. Two region are shown with the corresponding number of chosen intervals in each zone.*

A total of 13 intervals were defined at first. Two sets of parameters are calculated for the ANL and BCN module, respectively.

The a_i are obtained from de data at each energy, writing the corrected energy of the k event as

$$E^K_{cor} = a_1\ E^K_1 + ... + a_n\ E^K_n + B\ E_{old} \tag{4.11}$$

In this expression:

- E^K_i is the energy sum of all the cells within i interval, i.e.

$$E^K_i = \sum_{cells \in i} E_{Cell} \tag{4.12}$$

- E_{old} is the energy released in the old modules.

The set of correction parameters a_i is determined from the data by minimizing the expression

$$N\ \sigma^2 = \sum_{K=1,N} (E^K_{cor} - E_{Beam})^2 + \lambda \sum_{K=1,N} (E^K_{cor} - E_{Beam}) \tag{4.13}$$

in which the constraint that the mean reconstructed energy has to reproduce the nominal beam energy is introduced by means of a Lagrange multiplier.

The corrected total energy spectra were fitted with Gaussian distributions over a $\pm 2\sigma$ range. From the mean values of the fits we obtain plots of the deviation from a linear response. Such *linearity plots*, are shown in figure 4.14, left η=-1.1 and right -1.2, respectively. The improvement when including the *energy conservation* constraint is very clear; with this constraint, the *rms* deviation from linearity is 0.34% and 0.12% for ANL module at η=-1.1 and -1.2, respectively. For BCN module the *rms* is 0.4% for both η values.

The energy resolution (σ/E *vs.* the beam energy) is given in figure 4.15. The resolution obtained here can be parametrized for the BCN and ANL modules as shows the table 4.6.

The results of the fits to the reconstructed pion energies are given in table 4.7.

Before moving we can remark some observations:

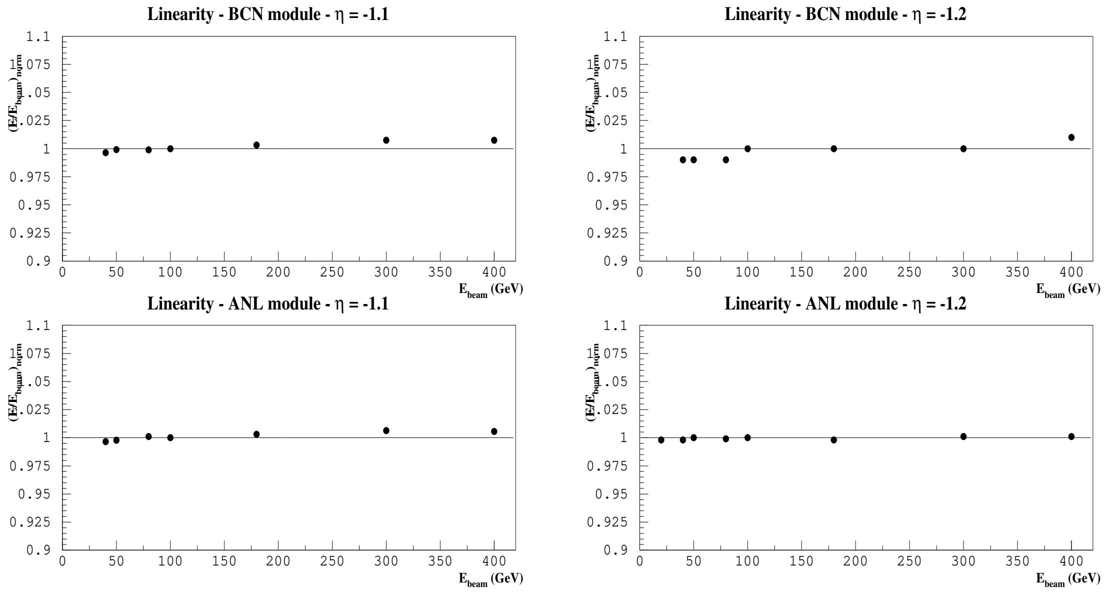

Figure 4.14: *Linearity plot minimizing the functional with the Lagrange multiplier. Left: η=-1.1, (top) BCN module and (bottom) ANL module. Right: η=-1.2, (top) BCN module and (bottom) ANL module. The points are obtained normalizing the mean reconstructed energy values from the Gaussian fits to the value of 100 GeV.*

Table 4.6: *Statistical (a), constant (b), and noise (c) terms at two different η for the BCN and ANL modules obtained with the constraint to the beam energy.*

η	BCN			ANL		
	a (%)	b (%)	c	a (%)	b (%)	c
-1.1	36.90	3.90	0.06	40.50	3.90	0.06
-1.2	40.51	3.21	0.06	36.30	4.91	0.06

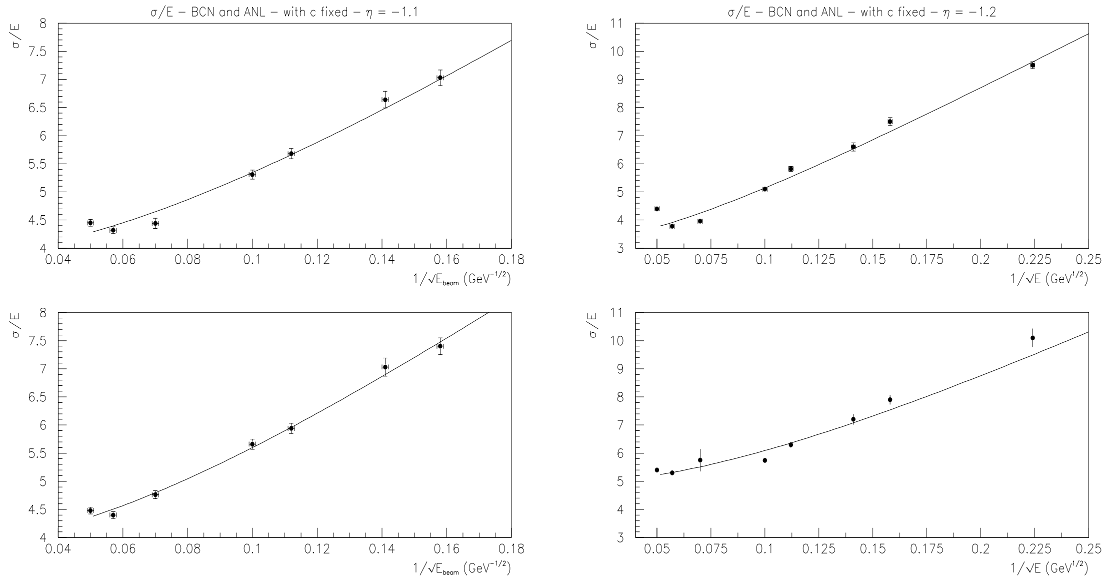

Figure 4.15: *Resolution plot minimizing the functional with the Lagrange multiplier. Left: η =-1.1, (top) BCN module and (bottom) ANL module. Right: η =-1.2, (top) BCN module and (bottom) ANL module.*

Table 4.7: *Nominal energy, mean reconstructed energy, σ and resolution at various beam energies at two different η for BCN and ANL modules obtained with the constraint to the beam energy.*

BCN	η=-1.1		
Beam energy (GeV)	μ (GeV)	σ (GeV)	σ/μ(%)
40	39.98 ± 0.07	2.81 ± 0.06	7.03 ± 0.14
50	50.11 ± 0.10	3.33 ± 0.07	6.64 ± 0.15
80	80.14 ± 0.09	4.55 ± 0.07	5.68 ± 0.09
100	100.3 ± 0.11	5.32 ± 0.08	5.31 ± 0.08
180	179.6 ± 0.64	7.13 ± 0.72	4.44 ± 0.09
300	303.2 ± 0.22	13.09 ± 0.20	4.32 ± 0.06
400	404.2 ± 0.23	15.00± 0.25	4.45 ± 0.06
ANL	η=-1.1		
Beam energy (GeV)	μ (GeV)	σ (GeV)	σ/μ(%)
40	39.98 ± 0.07	2.96 ± 0.06	7.40 ± 0.15
50	50.04 ± 0.11	3.52 ± 0.08	7.03 ± 0.16
80	80.34 ± 0.10	4.77 ± 0.07	5.94 ± 0.09
100	100.30 ±0.11	5.68 ± 0.09	5.66 ± 0.09
180	182.1 ± 0.10	10.21 ± 0.09	4.76 ± 0.07
300	302.8 ± 0.22	13.31 ± 0.20	4.40 ± 0.06
400	403.5 ± 0.23	15.05 ± 0.25	4.48 ± 0.06
BCN	η=-1.2		
Beam energy (GeV)	μ (GeV)	σ (GeV)	σ/μ(%)
20	19.95 ± 0.06	2.01 ± 0.06	9.5 ± 0.1
40	39.95 ± 0.07	3.01 ± 0.06	7.5 ± 0.1
50	49.93 ± 0.09	3.29 ± 0.08	6.6 ± 0.2
80	79.99 ± 0.09	4.65 ± 0.08	5.82 ± 0.09
100	100.1 ± 0.09	5.11 ± 0.08	5.1 ± 0.1
180	180.3 ± 0.15	7.15 ± 0.12	3.96 ± 0.06
300	300.5 ± 0.13	11.36 ± 0.10	3.78 ± 0.04
400	404.2 ± 0.23	18.01 ± 0.21	4.4 ± 0.06
ANL	η=-1.2		
Beam energy (GeV)	μ (GeV)	σ (GeV)	σ/μ(%)
20	19.97 ± 0.06	2.02 ± 0.05	10.1 ± 0.3
40	39.92 ± 0.08	3.15 ± 0.07	7.9 ± 0.2
50	50.01 ± 0.11	5.04 ± 0.09	7.2 ± 0.2
80	79.98 ± 0.10	5.74 ± 0.09	6.3 ± 0.1
100	100.00 ± 0.11	10.33± 0.09	5.74 ± 0.09
180	179.70 ± 0.87	3.59 ± 0.38	5.75 ± 0.11
300	300.50 ± 0.26	15.90 ± 0.24	5.30 ± 0.06
400	400.30 ± 0.34	21.65 ± 0.32	5.40 ± 0.07

• The improvement in resolution and linearity with respect to other weighting techniques is not surprising. The two terms of eq. 4.13 and the large number of parameters practically guarantee this result.

However, the good news is that the a_i vary smoothly with cell energy, and do not vary too much with E_{beam}. This simplifies the parametrizations which are described further in this work.

• The individual cell energies can be corrected using this method with a variety of similar algorithms: for instance, the a_i parameters can be defined by a distribution of volume energy density E_{cell}/V_{cell}. This latter approach was found to give significantly worse resolutions. Other approaches (such as normalizing the cell energies to the total energy) were tried; the choice of correcting the cell energies as a function only of the cell energy gives the best results and was chosen for this analysis.

4.2.3.2 Parametrizing the a_i

A total of 112 parameters are used to reconstruct the pion energy in the Tile Calorimenter: (13 + 1) at each of the 8 beam energies. To reduce the number of parameters we proceed as follows:

• The a_i are parametrized as a function of the cell energy in the way: $y = p_1 + p_2/E_{cell}$ (with different values p_1, p_2 for the BCN and ANL modules). The results are shown in figures 4.16, 4.17, 4.18 and 4.19 for various beam energies at η=-1.1 and -1.2, respectively.

The errors on the a_i shown in the figures are the *rms* values of ten independent sets of a_i obtained by classifing the data in 10 independent subsamples at each energy and solving the minimization equations for each set.

The corrected energy of the K event is expressed as:

$$E^K_{cor} = \sum_{cells} (p_1 + \frac{p_2}{E_{cell}}) E^K_{cell} + BE_{old} \tag{4.14}$$

• Next, the parameters p_1, p_2 and B (the old modules parameter) are expressed as a function of the beam energy using two parameter dependence for p_1 and B (i.e., $p'_1 + p'_2 \times E_{beam}$) and three parameter for p_2 (i.e., $p'_1 + p'_2 \times E_{beam} + p'_3 \times E^2_{beam}$). This is shown in figures 4.20, 4.21 and 4.22; for ANL and BCN modules at η=-1.1 and -1.2.

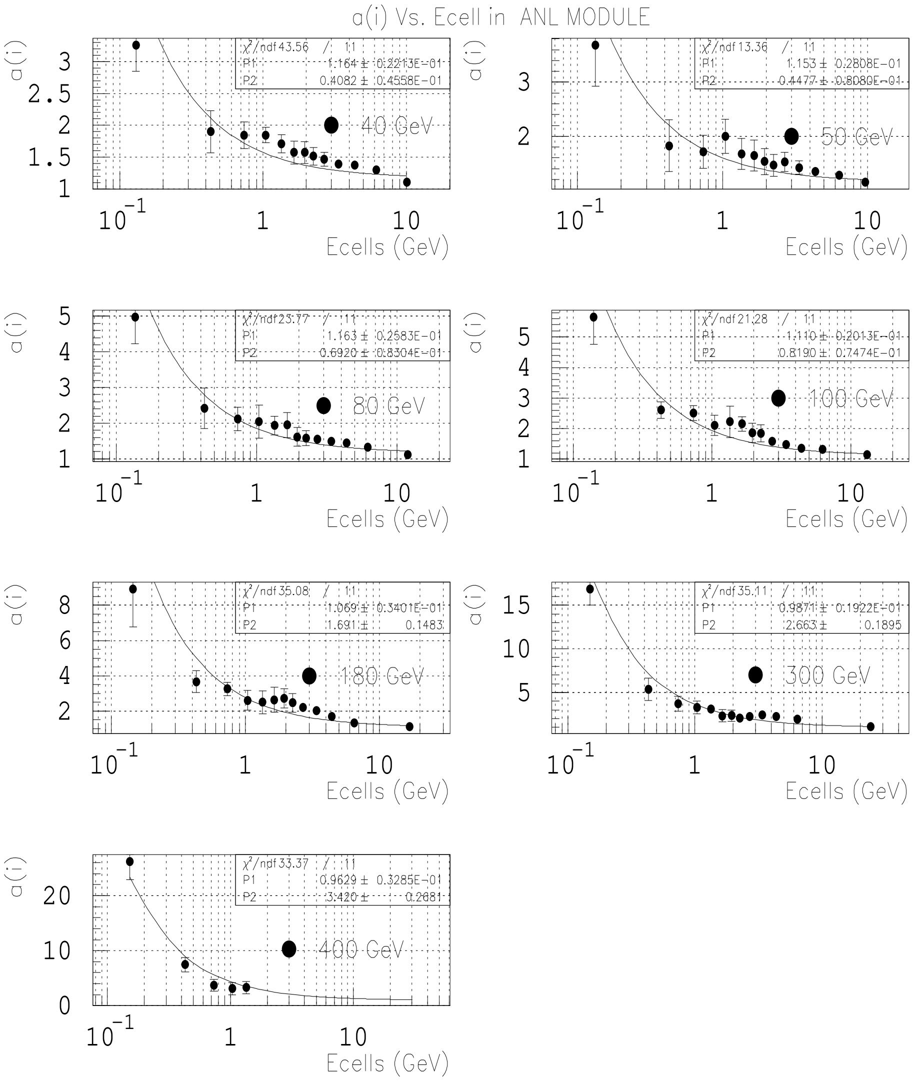

Figure 4.16: *Fits for the a_i parameters (ANL module) at various beam energies and η=-1.1. The parameters p_1 and p_2 obtained for ANL are also shown on the plots.*

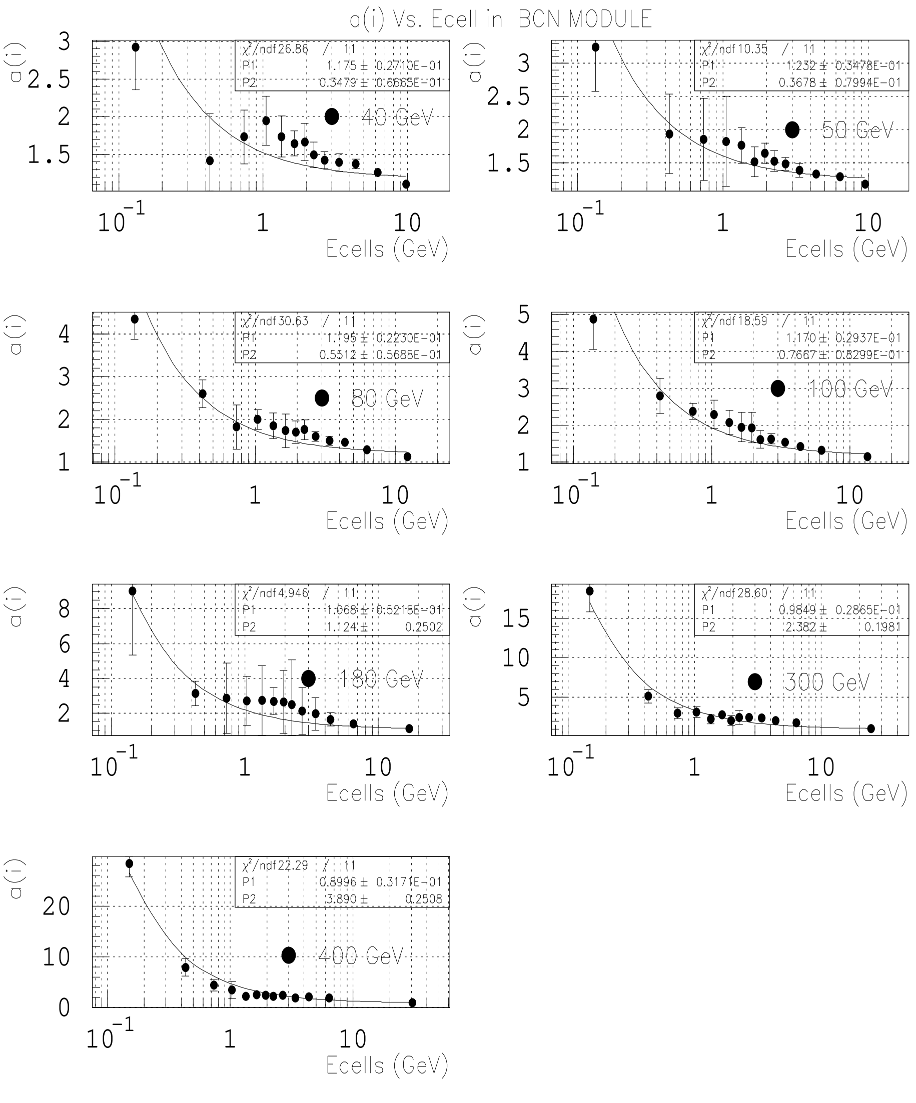

Figure 4.17: *Fits for the a_i parameters (BCN module) at various beam energies and η=-1.1. The parameters p_1 and p_2 obtained for BCN are also shown on the plots.*

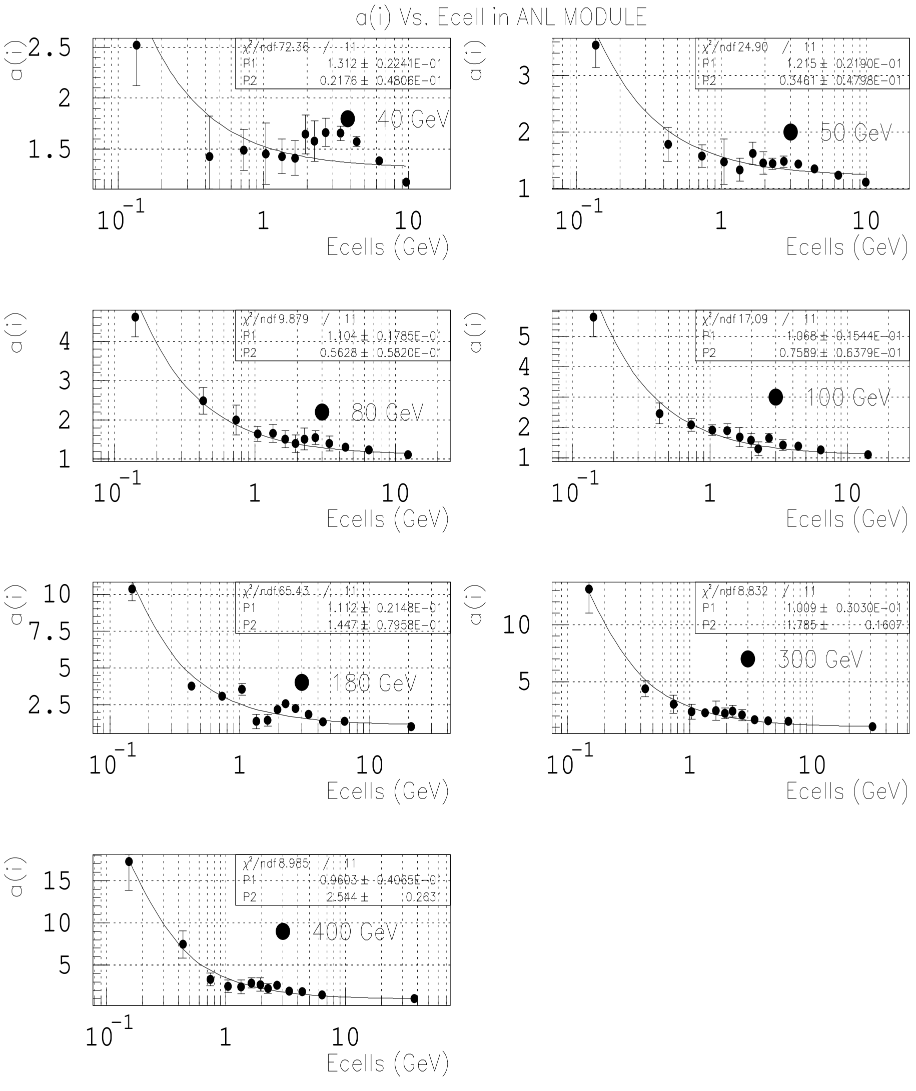

Figure 4.18: *Fits for the a_i parameters (ANL module) at various beam energies and η=-1.2. The parameters p_1 and p_2 obtained for ANL are also shown on the plots.*

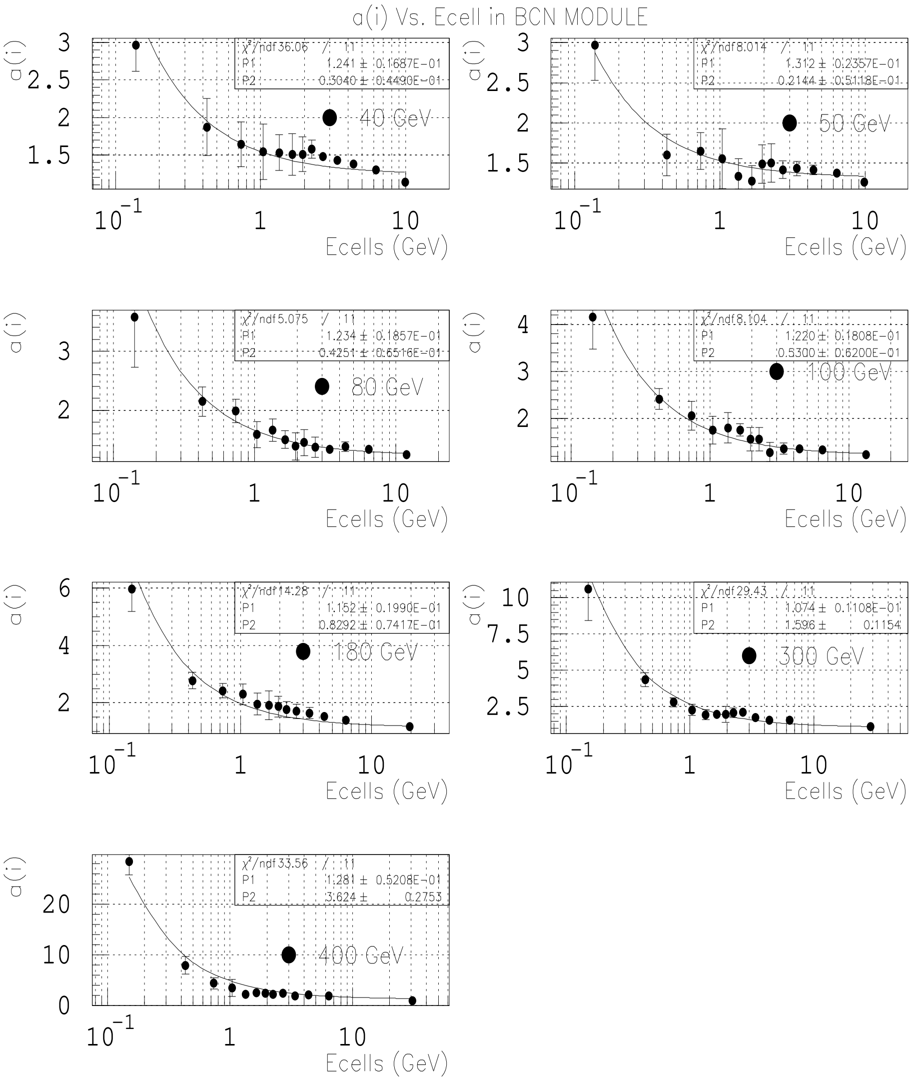

Figure 4.19: *Fits for the a_i parameters (BCN module) at various beam energies and η=-1.2. The parameters p_1 and p_2 obtained for BCN are also shown on the plots.*

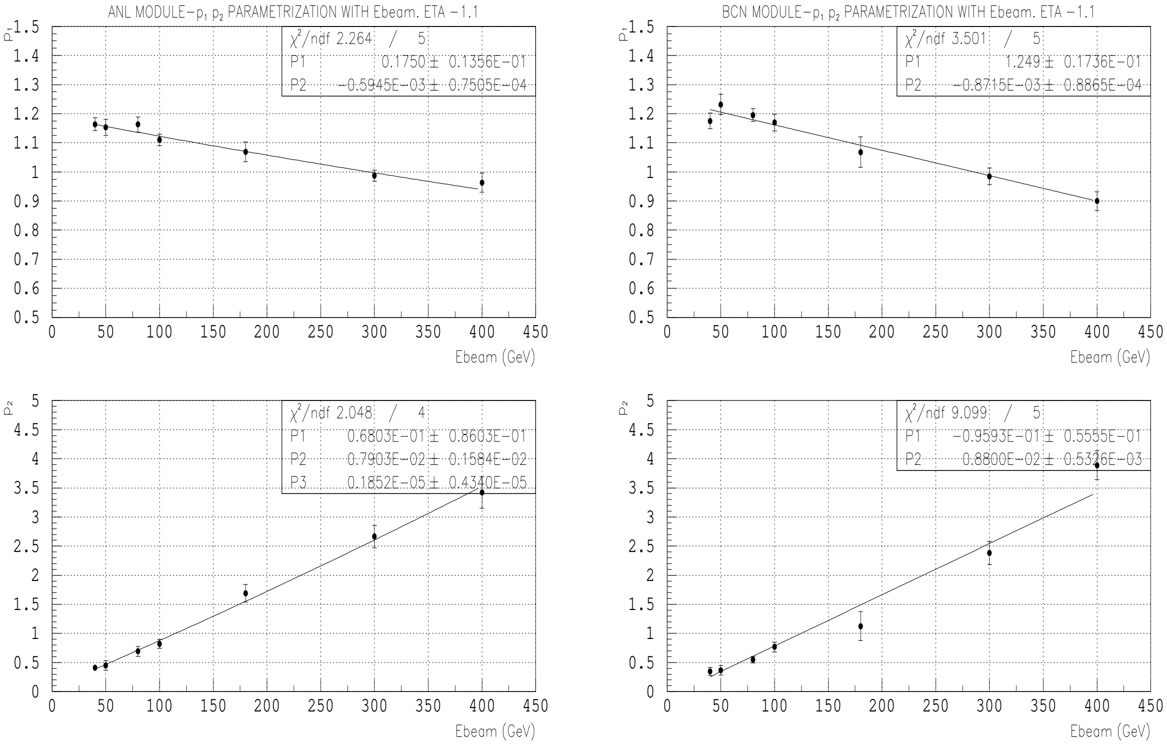

Figure 4.20: *For η=-1.1, the top plots show the parametrization with the beam energy of p_1 for the ANL (left) and BCN (right) modules; the bottom plots shown the same for the p_2. The values of the parameters p_1', p_2' and p_3' from the fits are also presented on the plots.*

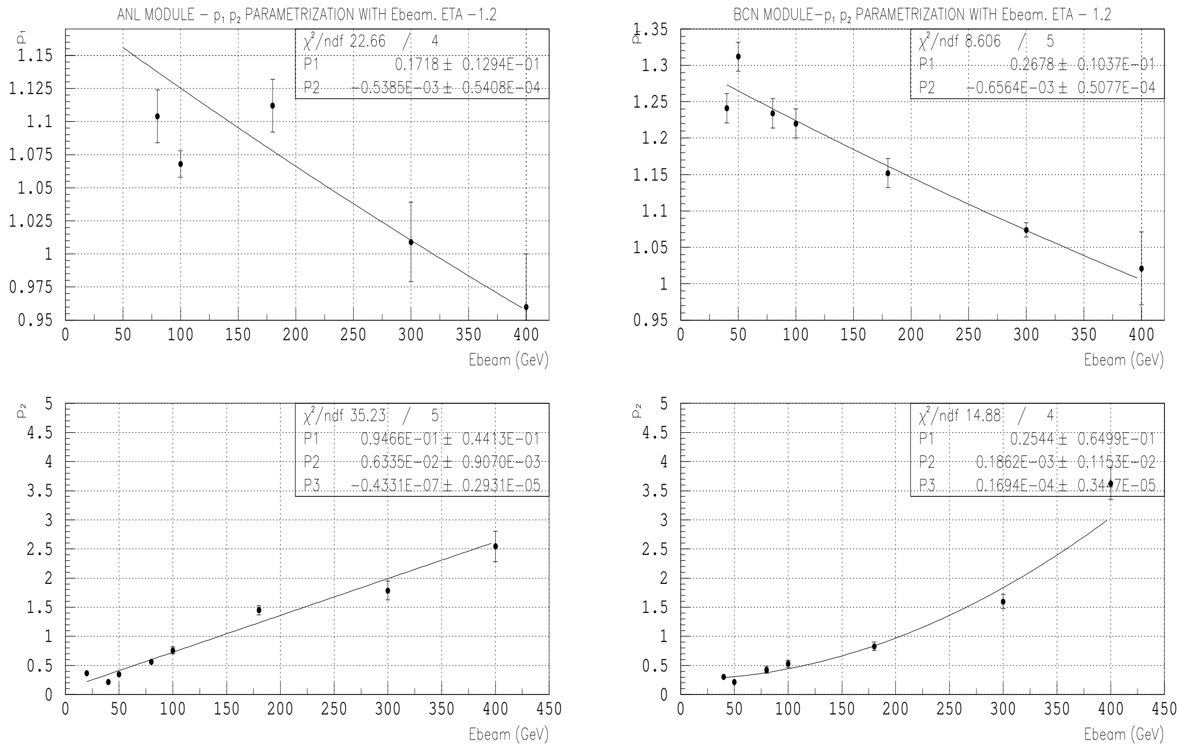

Figure 4.21: *For η=-1.2, the top plots show the parametrization with the beam energy of p_1 for the ANL (left) and BCN (right) modules; the bottom plots show the same for p_2. The values of the parameters p'_1, p'_2 and p'_3 from the fits are also presented on the plots.*

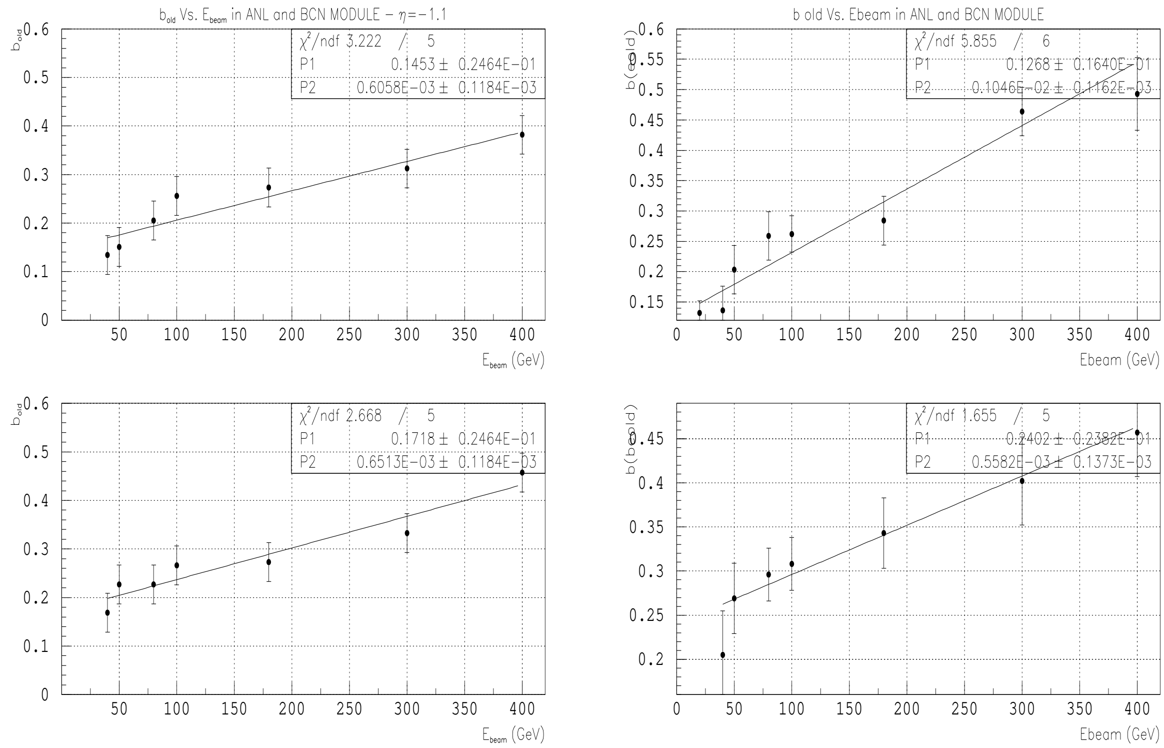

Figure 4.22: *The top plot show the parametrization with the beam energy of B for the ANL module; the bottom plots show the same for the BCN module. On the left η=-1.1 and on the right η=-1.2. The values of the parameters p_1' and p_2' from the fits are also presented on the plots.*

Following theses parametrizations, we have expressed the entire set of corrections by two sets of simple functions, containing only a total of seven parameters. The aim now is to check whether the reconstructed energies with 7 rather than 112 parameters are less precise. The mean, σ and resolution values obtained from this a_i parametrization are given in the table 4.8; the linearity and resolution plots are in figures 4.23 and 4.24. Comparing to the results previously obtained with 112 parameters (see table 4.6) it is seen that despite the dramatic reduction of correction parameters the resolution is negligibly worse and the linearity has degraded because the energy reconstruction is not good enough at low energies (discussed in subsection 4.2.3.4). Quantitatively, the *rms* deviation from linearity is now σ = 2.9% and 3.0% for ANL and BCN modules, respectively, at η=-1.2 instead of 0.12% and 0.4%. For η=-1.1 we get σ = 2.1% and 2.8% instead of 0.34% and 0.4%.

The resolution is now parametrized for the BCN and ANL modules as shows the table 4.9. Comparing with the results previously obtained in table 4.6 the statistical term has worsed but is less than 50% and the constant term has improved, being around 3%.

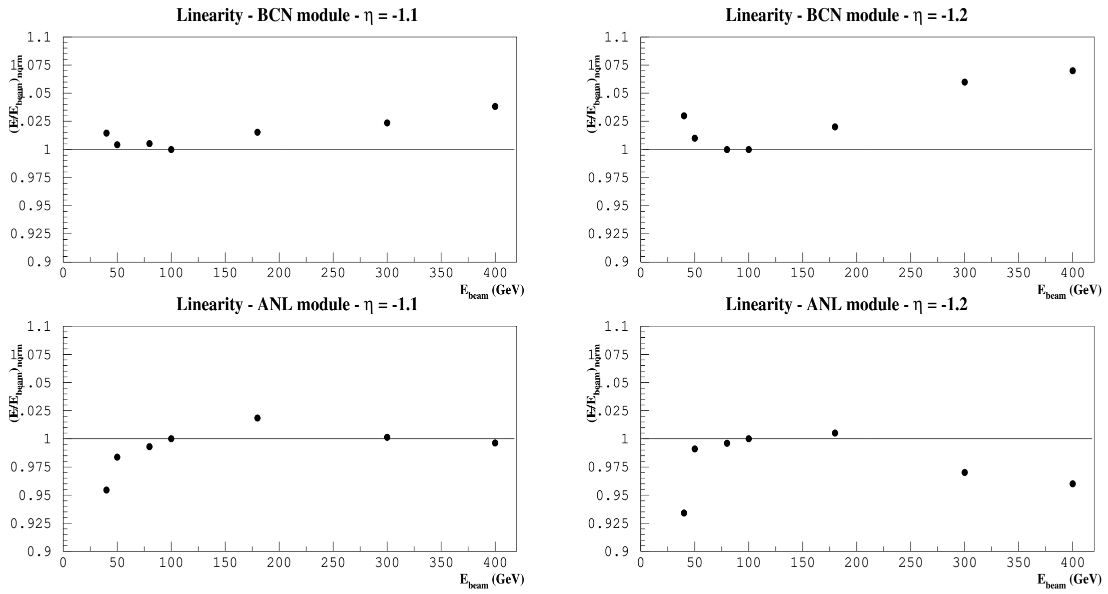

Figure 4.23: *Linearity with the beam energy after the parametrization. Left: For η= -1.1, BCN (Top) and ANL (Bottom) modules. Right: For η= -1.2, BCN (Top) and ANL (Bottom) modules.*

Table 4.8: *Nominal energy, mean reconstructed energy, σ and resolution at various beam energies at two different η for BCN and ANL modules obtained after the parametrization.*

BCN	η=-1.1		
Beam energy (GeV)	μ (GeV)	σ (GeV)	σ/μ(%)
40	40.30 $\pm$ 0.07	3.11 $\pm$ 0.06	7.61 $\pm$ 0.17
50	49.88 $\pm$ 0.11	3.44$\pm$ 0.08	6.73$\pm$ 0.16
80	79.93 $\pm$ 0.09	4.73$\pm$ 0.07	5.83 $\pm$ 0.09
100	99.23$\pm$ 0.11	5.24$\pm$ 0.08	5.26$\pm$ 0.09
180	181.90 $\pm$ 0.22	7.47$\pm$ 0.17	4.13 $\pm$ 0.10
300	306.40 $\pm$ 0.14	11.10 $\pm$ 0.15	3.54 $\pm$ 0.05
400	417.7 $\pm$ 0.19	15.59 $\pm$ 0.21	3.63$\pm$ 0.05
ANL	η=-1.1		
Beam energy (GeV)	μ (GeV)	σ (GeV)	σ/μ(%)
40	40.30$\pm$0.08	3.11$\pm$ 0.06	7.66$\pm$ 0.15
50	49.88$\pm$0.11	3.45$\pm$ 0.08	6.89$\pm$ 0.16
80	79.93 $\pm$0.09	4.73 $\pm$ 0.07	6.05$\pm$ 0.11
100	99.23$\pm$ 0.11	5.24 $\pm$ 0.08	5.43$\pm$ 0.08
180	181.9$\pm$ 0.22	7.47$\pm$ 0.17	4.52$\pm$ 0.07
300	306.4 $\pm$ 0.14	11.10$\pm$ 0.15	3.92$\pm$ 0.05
400	415.5 $\pm$ 0.19	15.69 $\pm$0.22	3.72$\pm$ 0.05
BCN	η=-1.2		
Beam energy (GeV)	μ (GeV)	σ (GeV)	σ/μ(%)
20	20.47 $\pm$ 0.06	2.05 $\pm$ 0.05	10.0 $\pm$ 0.3
40	38.60 $\pm$ 0.08	3.25 $\pm$ 0.06	8.4 $\pm$ 0.2
50	48.58 $\pm$ 0.09	3.29 $\pm$ 0.08	6.9 $\pm$ 0.2
80	76.62 $\pm$ 0.09	4.39 $\pm$ 0.08	5.81 $\pm$ 0.09
100	95.62 $\pm$ 0.09	4.80 $\pm$ 0.08	5.13 $\pm$ 0.07
180	175.6 $\pm$ 0.13	6.76 $\pm$ 0.12	3.92 $\pm$ 0.06
300	298.9 $\pm$ 0.17	10.70 $\pm$ 0.15	3.58 $\pm$ 0.04
400	402.3 $\pm$ 0.26	14.28 $\pm$ 0.25	3.55 $\pm$ 0.05
ANL	η=-1.2		
Beam energy (GeV)	μ (GeV)	σ (GeV)	σ/μ(%)
20	19.46 $\pm$ 0.07	2.34 $\pm$ 0.05	12.1 $\pm$ 0.5
40	39.50 $\pm$ 0.08	3.37 $\pm$ 0.07	8.6 $\pm$ 0.4
50	52.01 $\pm$ 0.12	3.78 $\pm$ 0.10	7.5 $\pm$ 0.2
80	79.40 $\pm$ 0.11	5.30 $\pm$ 0.09	6.4 $\pm$ 0.1
100	100.60 $\pm$ 0.12	5.89 $\pm$ 0.10	5.57 $\pm$ 0.09
180	186.90 $\pm$ 0.21	8.34 $\pm$ 0.19	5.10 $\pm$ 0.11
300	302.37 $\pm$ 0.23	14.50 $\pm$ 0.21	4.65 $\pm$ 0.06
400	403.50 $\pm$ 0.33	18.74 $\pm$ 0.31	4.60 $\pm$ 0.07

Table 4.9: *Statistical (a), constant (b), and noise (c) terms at two different η for the BCN and ANL modules obtained after the parametrization.*

η	BCN			ANL		
	a (%)	b (%)	c	a (%)	b (%)	c
-1.1	45.10	2.70	0.06	45.41	3.00	0.06
-1.2	45.20	2.60	0.06	47.50	3.70	0.06

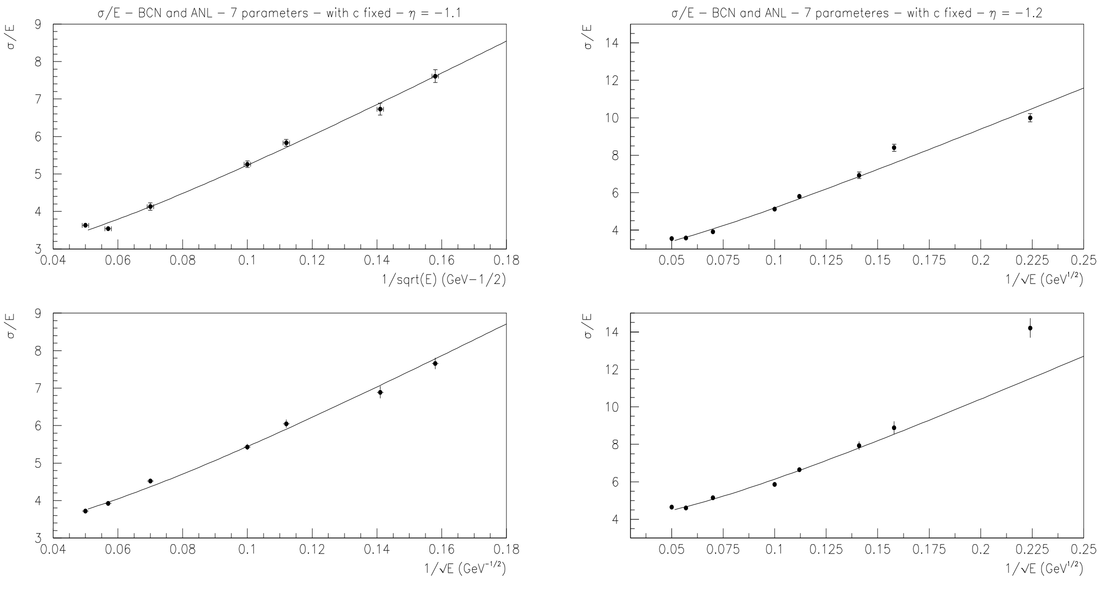

Figure 4.24: *Resolution as a function of the beam energy after the parametrization. Left: For η= -1.1, BCN (Top) and ANL (Bottom) modules. Right: For η= -1.2, BCN (Top) and ANL (Bottom) modules.*

4.2.3.3 Realistic energy reconstruction assuming no knowledge of the beam energy

The method described above cannot be used just *as it is* because the particle energy (needed to calculate the correction parameters) is unknown in a real life experiment. The aim of this section is to reconstruct the pion energy assuming no knowledge of the beam energy.

A more realistic energy reconstruction can be done by obtaining an initial estimate of the particle energy from the raw data and using this estimate as a first approximation of the true energy; the procedure may be iterated until it converges.

Two different algorithms have been considered to obtain the initial estimate of the particle energy:

The first one assumes that the sum of the cell energies (plus the old modules correction) follows a linear behaviour [13]:

$$E_{initial} = \frac{E^{ANL} + E^{BCN} + \alpha}{\beta} + \gamma\ E_{old} \tag{4.15}$$

where α, β and γ are 2.45, 0.88 and 0.31. The two first factors represent the electromagnetic scale determined using the 100 GeV electrons data at 90°, while the last has been determined several times in the past using electron runs of the protype modules test beams

The second uses the raw signal value as the initial estimated particle energy.

Both algorithms converge practically to the same total energy value after 3 or 4 iterations. The first was used for η=-1.2 and the second for η=-1.1.

The mean, σ and resolution of the reconstructed energies are presented in table 4.10. In figure 4.25 the linearity obtained by the *realistic* method is shown; the linearity remains as good as before. For ANL module the non-linearity ranges from 1.8% to 2.2% for η=-1.1 and from 2.9% to 3.4% for η = -1.2. For BCN module it goes from 1.2% to 2% and 3.0% to 3.5% for η=-1.1 and -1.2 respectively.

The resolutions obtained with the realistic algorithm, as we see in figure 4.26 present a slight degradation with respect to the values given in the preceding parametrization that uses the nominal beam energy. This result is unavoidable due to event-to-event fluctuations of hadronic showers. The figure shows that the degradation of the resolution is more pronounced at low energy, as expected from the energy dependence of σ/E.

Table 4.10: *Nominal energy, mean reconstructed energy, σ and resolution at various beam energies at two different η for BCN and ANL modules obtained assuming no knowledge of the beam energy.*

BCN	η=-1.1		
Beam energy (GeV)	μ (GeV)	σ (GeV)	σ/μ(%)
40	40.32±0.08	3.07 ±0.06	7.71 ± 0.15
50	49.89±0.11	3.56 ±0.07	6.93± 0.16
80	79.91±0.09	4.66± 0.07	5.92± 0.09
100	99.36±0.11	5.23± 0.08	5.27± 0.08
180	181.60±0.21	7.50± 0.18	4.11± 0.09
300	305.10±0.14	10.80± 0.15	3.62± 0.05
400	412.60±0.27	14.98± 0.23	3.76± 0.06
ANL	η=-1.1		
Beam energy (GeV)	μ (GeV)	σ (GeV)	σ/μ(%)
40	38.71± 0.07	2.99± 0.06	7.49±0.15
50	49.87± 0.11	3.45± 0.07	7.14± 0.11
80	80.56± 0.10	4.86± 0.08	6.07± 0.10
100	101.4 ± 0.10	5.47± 0.08	5.50± 0.09
180	185.9± 0.17	8.27± 0.13	4.57± 0.07
300	304.6± 0.15	11.93± 0.16	4.00± 0.06
400	404.1± 0.16	14.95± 0.22	3.78± 0.06
BCN	η=-1.2		
Beam energy (GeV)	μ (GeV)	σ (GeV)	σ/μ(%)
20	19.34 ± 0.06	2.08 ± 0.05	10.8 ± 0.3
40	37.97 ± 0.09	3.37 ± 0.06	8.9 ± 0.2
50	47.11 ± 0.10	3.27 ± 0.08	6.96 ± 0.21
80	75.79 ± 0.09	4.47 ± 0.08	5.91 ± 0.09
100	94.44 ± 0.09	4.95 ± 0.08	5.24 ± 0.07
180	175.3 ± 0.14	6.94 ± 0.12	3.96 ± 0.06
300	306.6 ± 0.13	10.70 ± 0.11	3.49 ± 0.04
400	410.6 ± 0.27	14.13 ± 0.25	3.40 ± 0.05
ANL	η=-1.2		
Beam energy (GeV)	μ (GeV)	σ (GeV)	σ/μ(%)
20	19.41 ± 0.07	2.31 ± 0.05	11.9 ± 0.5
40	39.40 ± 0.08	3.31 ± 0.07	8.4 ± 0.4
50	52.85 ± 0.12	3.89 ± 0.10	7.4 ± 0.2
80	85.16 ± 0.12	5.40 ± 0.09	6.34 ± 0.11
100	105.60 ± 0.12	6.02 ± 0.10	5.63 ± 0.09
180	193.20 ± 0.20	9.70 ± 0.18	4.98 ± 0.11
300	309.86 ± 0.23	14.19 ± 0.21	4.58 ± 0.06
400	404.73 ± 0.33	18.69 ± 0.30	4.62 ± 0.07

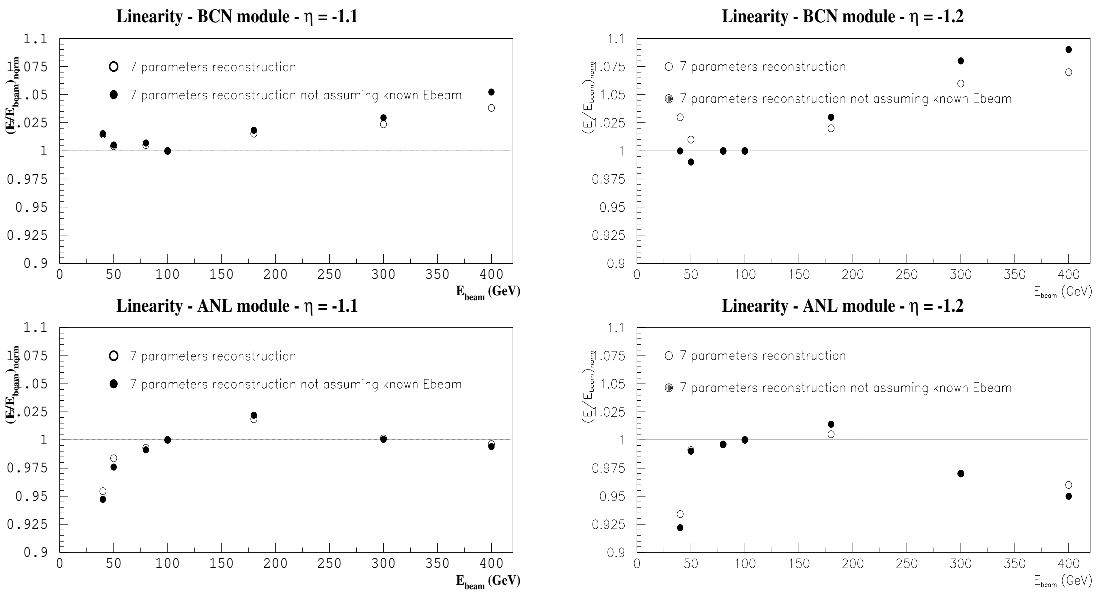

Figure 4.25: *Linearity plot comparing the method which does not use the beam energy with the one which does. Left: For η=-1.1 BCN, (Top) and ANL (Bottom) modules. Right: For η=-1.2, BCN (Top) and ANL (Bottom) modules.*

Table 4.11: *Statistical (a), constant (b), and noise (c) terms at two different η for the BCN and ANL modules obtained assuming no knowledge of the beam energy.*

η	BCN			ANL		
	a (%)	b (%)	c	a (%)	b (%)	c
-1.1	45.60	2.70	0.06	45.20	3.10	0.06
-1.2	47.80	2.60	0.06	44.50	3.90	0.06

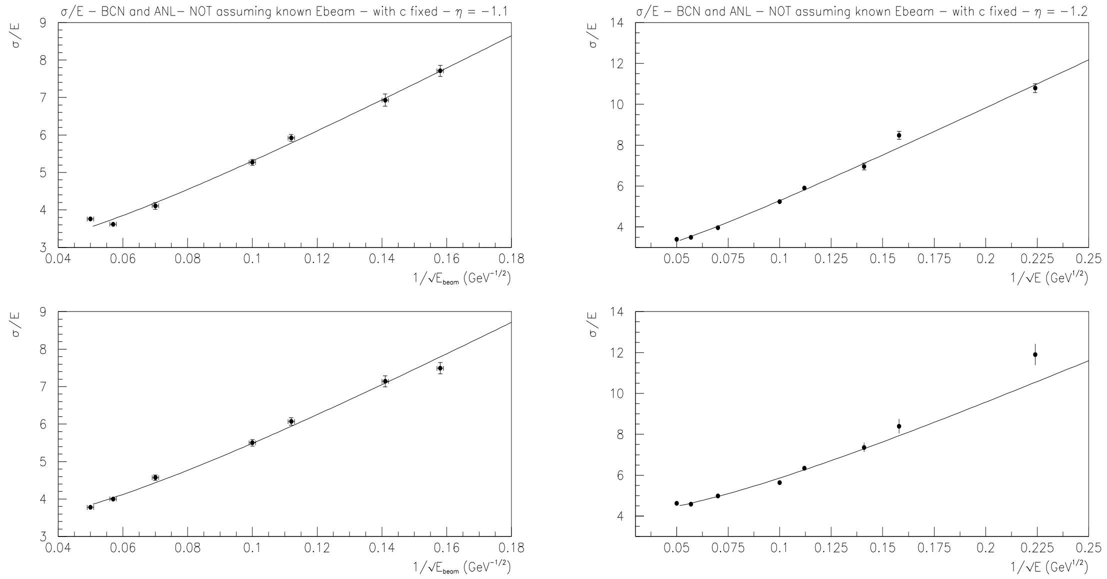

Figure 4.26: *Resolution plots without using the beam energy. Left: For η=-1.1, BCN (Top) and ANL (Bottom) modules. Right: For η=-1.2, BCN (Top) and ANL (Bottom) modules.*

The final results for the BCN and ANL modules are shown in the table 4.11

In this study we have proved that the linearity and resolution of the Tile Calorimeter prototypes improve using the H1 method. Also these results are compatible for the two modules used in the 1997 test beam and at two different values of η.

Respect to the linearity, the benchmark approach gives aproximately the same *rms* than the raw data, improving a little at high energies due to the leakage corrections. Using Lagrange multipliers we found a very linear response over the range of energies studied, because 112 weights have been used for each module. With the parametrization of these weights using a total of 7 constants and assuming no knowledge of the particle energy the linearity is degraded appreciably. This degradation is not seen in the 1994 [17] combined test analysis and it is caused by the difficulty in the parametrization, due to the bad quality of data; however it is still better than with the benchmark method.

For the resolution, figure 4.27 shows that the use of all those weights improves significantly the resolution respect to the raw data algorithm. As expected, the resolution degrades somewhat when no knowledge of the particle energy is assumed, been better than the obtained with the other methods.

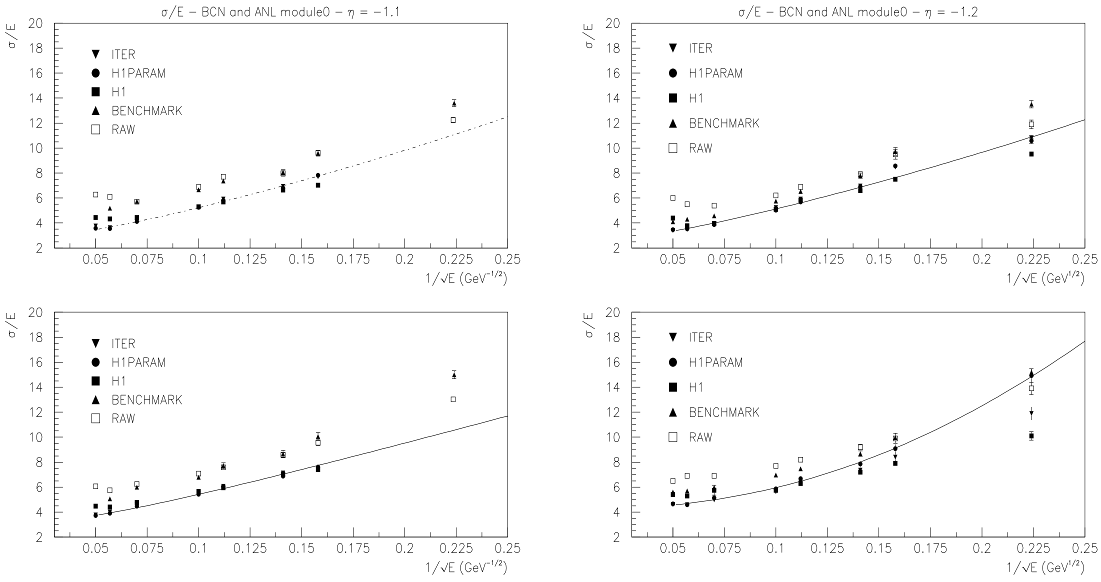

Figure 4.27: *Resolution plots applying all the described methods. Left: For η=-1.1, BCN (Top) and ANL (Bottom) modules. Right: For η=-1.2, BCN (Top) and ANL (Bottom) modules.*

4.2.3.4 Treatment of the low beam energy region

At low beam energies (below 50 GeV) the resolution deteriorates appreciably, as observed with all the reconstruction methods. This confirms that the problem is intrinsic to the data set. We describe here the results obtained for the linearity and resolution if we only consider energies greater than 40 GeV and the energy is reconstructed as in point 4.2.3.2.

The resolution is now parametrized as shows the table 4.12.

Table 4.12: *Statistical (a), constant (b), and noise (c) terms at two different η for the BCN and ANL modules obtained using beam energies greater than 40 GeV.*

η	BCN			ANL		
	a (%)	b (%)	c	a (%)	b (%)	c
-1.1	45.70	2.70	0.06	47.20	3.00	0.06
-1.2	44.30	2.50	0.06	41.10	4.10	0.06

The mean, σ and resolution values obtained are given in the table 4.13; the linearity and resolution plots are in figure 4.28 and 4.29. Comparing to the results previously obtained with beam energies below 50 GeV it is seen that the resolution is practically the same and the linearity has improved. Quantitatively, the *rms* deviation from linearity is now 2.0% and 0.6% instead of 2.12% and 2.8% for η=-1.1 and ANL and BCN modules respectively. For η=-1.2 the *rms* is now 2.0% and 1.5% instead of 2.9% and 3% for ANL and BCN modules.

4.2.4 e/π response

The Tile Calorimeter has not been designed to have a good electron performance, since it will have in front of it an electromagnetic compartment. However, it is important to understand the electron response, namely to study the e/π ratio. When studying the Tile Calorimeter response to electrons, the hadronic calorimeter can be considered as a set of different calorimeters, with variable absorber and scintillator thicknesses: from $t_{Fe} = 81$ to 28 mm, and from $t_{Scin} = 17$ to 6 mm for a θ angle between 10 and 30 degree, where t_{Fe} and t_{Scin} are the effective thicknesses of the absorber and the scintillator plates respectively [14]. Therefore, the electron response is a rather complicated function of E_{beam} and η.

Table 4.13: *Nominal energy, mean reconstructed energy, σ and resolution at various beam energies at two different η for BCN and ANL modules obtained with beam energies greater than 40 GeV.*

BCN	η=-1.1		
Beam energy (GeV)	μ (GeV)	σ (GeV)	σ/μ(%)
50	50.63±0.11	3.47±0.07	6.86±0.16
80	80.90 ± 0.09	4.74±0.07	5.86± 0.09
100	100.50 ± 0.11	5.33 ± 0.08	5.31 ± 0.08
180	182.60 ± 0.21	7.48± 0.16	4.09± 0.09
300	304.60 ± 0.19	11.02± 0.16	3.62± 0.05
400	409.70 ± 0.19	15.00± 0.20	3.66± 0.06
ANL	η=-1.1		
Beam energy (GeV)	μ (GeV)	σ (GeV)	σ/μ(%)
50	48.67 ±0.11	3.52 ± 0.07	7.22 ±0.15
80	80.17 ± 0.10	4.87± 0.08	6.07± 0.10
100	101.50 ± 0.11	5.62± 0.08	5.53± 0.09
180	187.40± 0.17	8.57± 0.14	4.57± 0.07
300	305.50 ± 0.32	12.11± 0.19	3.96 ±0.06
400	402.20 ± 0.20	15.11± 0.22	3.76± 0.06
BCN	η=-1.2		
Beam energy (GeV)	μ (GeV)	σ (GeV)	σ/μ(%)
50	49.81 ± 0.10	3.41 ± 0.08	6.85 ± 0.18
80	80.85 ± 0.09	4.57 ± 0.08	5.66 ± 0.09
100	100.9 ± 0.09	5.07 ± 0.08	5.03 ± 0.07
180	182.8 ± 0.14	6.94 ± 0.12	3.91 ± 0.06
300	299.6 ± 0.11	10.43 ± 0.09	3.48 ± 0.04
400	385.6 ± 0.17	13.31 ± 0.15	3.47 ± 0.05
ANL	η=-1.2		
Beam energy (GeV)	μ (GeV)	σ (GeV)	σ/μ(%)
50	49.76 ± 0.11	3.68 ± 0.09	7.4 ± 0.2
80	82.29 ± 0.11	5.16 ± 0.09	6.27 ± 0.14
100	104.3 ± 0.12	5.70 ± 0.10	5.47 ± 0.09
180	193.1 ± 0.21	9.56 ± 0.18	4.95 ± 0.07
300	309.0 ± 0.23	14.12 ± 0.21	4.57 ± 0.06
400	401.1 ± 0.26	18.77 ± 0.23	4.68 ± 0.07

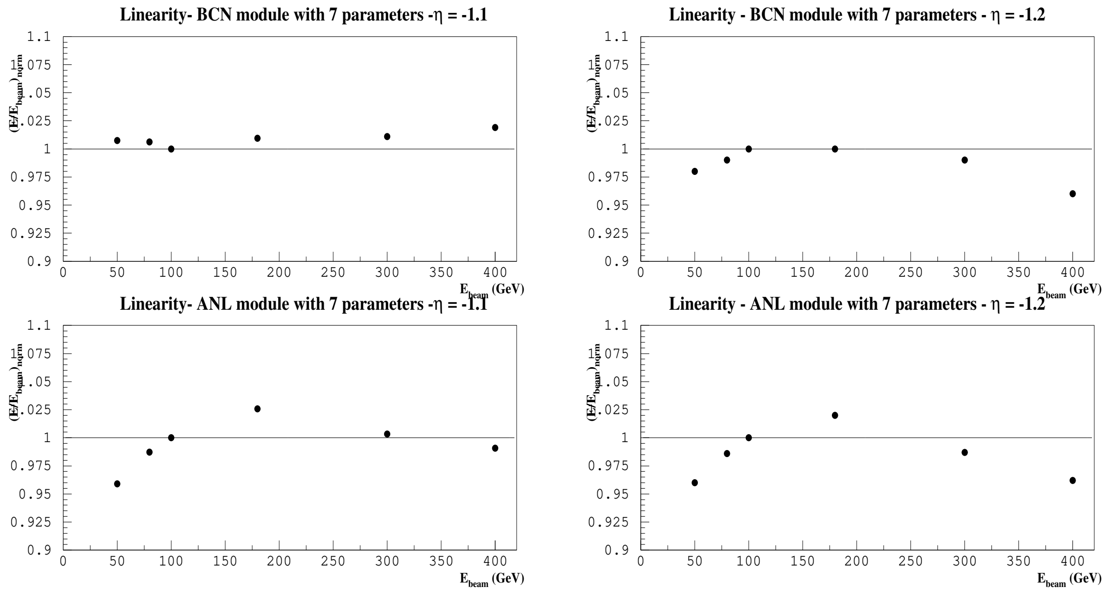

Figure 4.28: *Linearity plot minimising the functional with the Lagrange multiplier and beam energies greater than 40 GeV. Left: For η=-1.1, BCN (Top) and ANL (Bottom) modules. Right: For η=-1.2, BCN (Top) and ANL (Bottom) modules.*

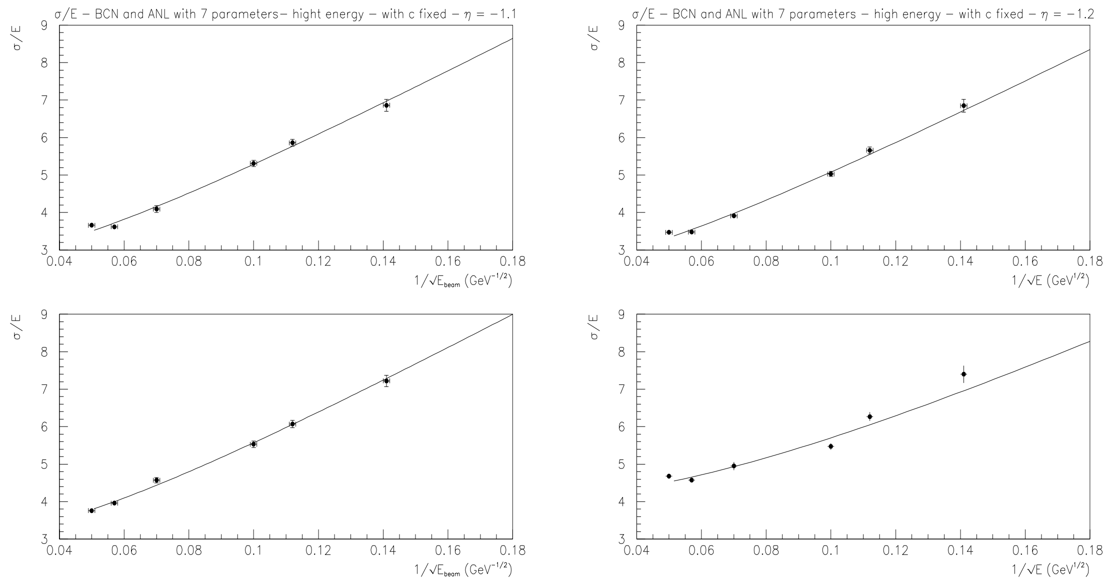

Figure 4.29: *Resolution plots minimizing the functional with the Lagrange multiplier and beam energies greater than 40 GeV. Left: For η=-1.1, BCN (Top) and ANL (Bottom) modules. Right: For η=-1.2, BCN (Top) and ANL (Bottom) modules.*

The response obtained for electrons and pions gives the possibility to extract the e/h value, that is the ratio of the calorimeter responses to the electromagnetic and non-electromagnetic (purely hadronic) components of hadron showers. An e/h value different from 1 causes deviation from linearity in the hadronic response versus energy, besides broadening the energy resolution and introducing tails in the energy distribution [15]. The value of the e/h ratio depends on a number of factors such as the thickness of the passive and active layers, and the sampling fraction. The e/h ratio of a sampling calorimeter with an iron-scintillator ratio less than 20 (in the case of the Tile Calorimeter this ratio is 4.7) is expected to be > 1 for the conventional orientation of tiles perpendicular to incident hadrons [16]. The Tile Calorimeter structure does not favour a simple relation, but rather a function such as $e/\pi = f(E, \eta)$.

The present study corresponds to the data taken in 1997 for the Extended Barrel Module 0 built in Barcelona (BCN), Spain.

The e/h ratio was extracted from the data by fitting the expression:

$$e/\pi = \frac{e/h}{1 + (e/h - 1) \times 0.11 \times ln(E)} \tag{4.16}$$

where $0.11 \times ln(E)$ is the average fraction of the incident hadron energy into π^0 production [15].

Figure 4.30 shows the e/π ratio as a function of the beam energy for BCN Extended Barrel module at four different η values. The response to pions relative to electrons is seen to increase with energy as expected, because the fraction of electromagnetic energy in a pion shower increases logarithmically with energy.

From the data we got four values for the e/h ratio; the results are presented in table 4.14. The table shows the results (e/h) as a function of η. The e/h value increases as the η increases, this is because the shower is better contained for $\eta = -1.1$ than for $\eta = -1.4$. Deviations from $e/h = 1$ contribute to the constant term in the energy resolution (see equation 4.7). This constant term is about 3% for the BCN Extended Barrel module.

The value $e/h = 1.38$ corresponding to η = -1.1 is in good agreement with the 1.36 obtained from previous precise studies and reported in the TDR [17].

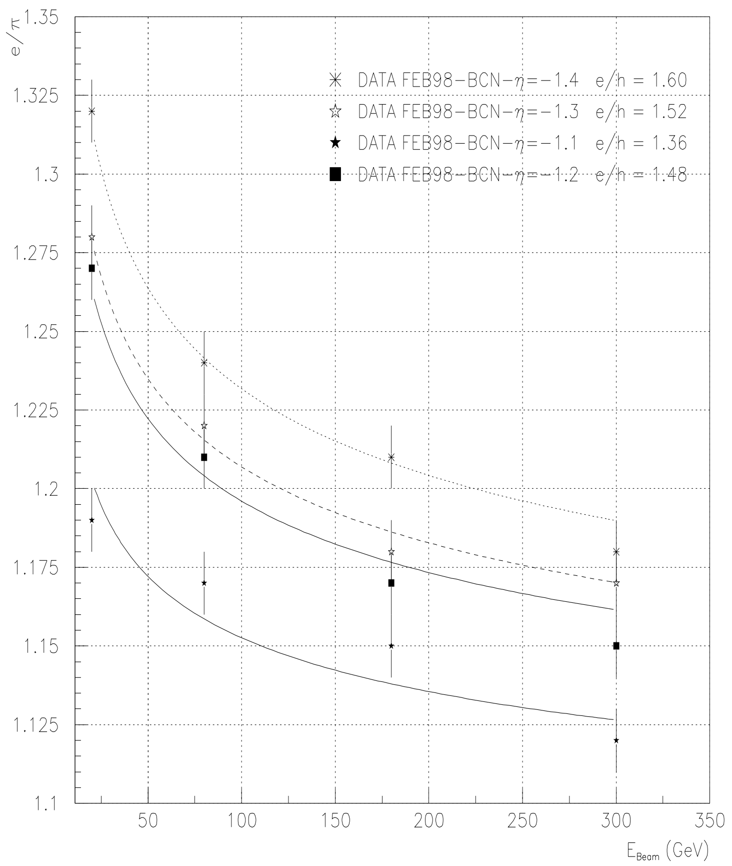

Figure 4.30: *The e/π ratio as a function of the beam energy for the BCN Extended Barrel module tested in the 1997 test beam at four differents η's. The lines are the fits of the equation (4.16).*

Table 4.14: *The values of the e/h ratio for the BCN Extended Barrel module at four differents η's using the equation (4.16).*

Module	η	e/h
BCN	-1.1	1.38 $\pm$0.013
BCN	-1.2	1.48 $\pm$0.014
BCN	-1.3	1.52 $\pm$0.015
BCN	-1.4	1.60 $\pm$0.016

4.3 The 1998 test beam

The Barrel Module 0 was tested in the beam area in 1998 using the same scanning table as for the test beam in 1997. In order to improve the transverse leakage for the Barrel Module 0, the five original one meter prototype modules (Old modules) were placed on either sides (in ϕ) of Module 0, three on one side and two on the other as shown in figure 4.31. Unlike the 1 m prototype modules, which had non-projective tower read-out, Module 0 had fibre routing in such a way that the scintillating tiles were grouped in a projective way with towers forming a minimun of granularity 0.1 in η. This is shown in figure 4.32. This projective tower structure defined by the fibre routing in Module 0 will most likely be the projective geometry used in ATLAS. For the test beam run, only half of the module was equipped with read-out electronics (η = 0 on the figure was actually the physical center of the structure).

The Tilecal modules have three segmentations in depth and the showers are sampled with 11 tiles varying their size in depth from 97 to 187 mm. The iron structure of the barrel Module 0 consists of 305 repeated periods sandwiched between two iron end plates of 20 mm thickness. Each period consists of four layers. The first and third layers are formed by 5 mm thick trapezoidal steel plates, spanning the full radial dimension of the module (master plates, 152 cm long). In the second and fourth layer, smaller trapezoidal steel plates and scintillator tiles alternate along the radial dimension. The front face area of the barrel modules is 560 $\times$ 22 cm^2. The granularity in $\Delta\eta \times \Delta\phi$ is 0.1 $\times$ 0.1 for the first two samplings and 0.2 $\times$ 0.1 for the last sampling. The thickness of the module at $\eta = 0$ is 1.5 λ in the first sampling which groups the 3 smallest tiles, 4.2 λ in the second which groups 6 tiles, and 1.9 λ in the third which is composed by the 2 largest tiles.

The negative η side of the module was equipped with Bicron multi-clad fibres. The cells of the sampling A (inner sampling) were equipped with fibers BCF99-28 dopped with 60 ppm of UV Absorber, and the other cells with fibres BCF91A without UV Absorber. The positive η side of the module was equipped with Pol.Hi.Tech multi-clad

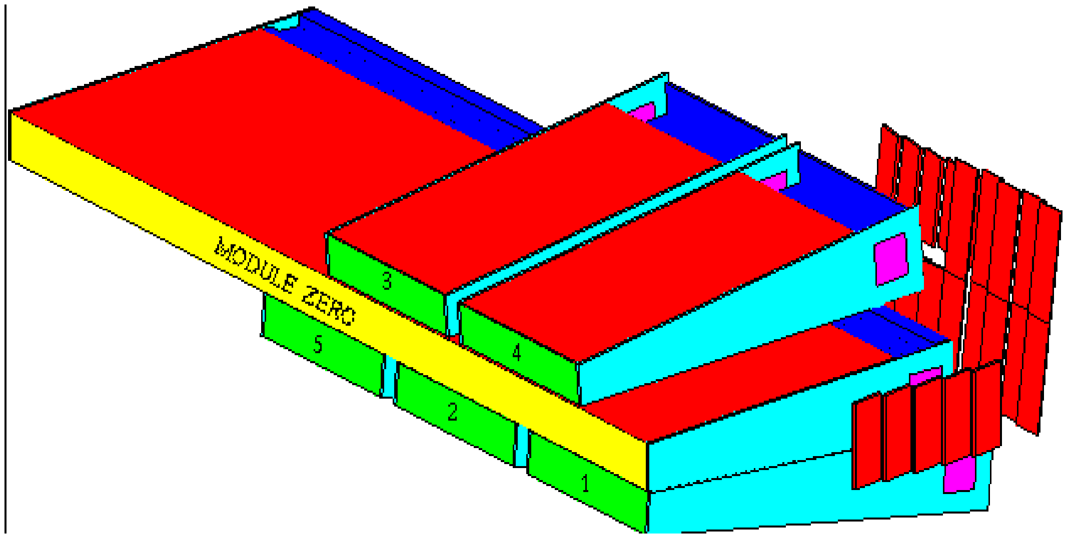

Figure 4.31: Barrel module 0 in the 1998 test beam.

S250-100 fibres dopped with UV Absorber. The full module was equipped with black fibre profiles (and a few gray near the ends) which were painted white in the face that ensures the tile-fibre optical coupling. The reason to use white painting is because a large fraction of the light is going to the fiber profiles and if they are white the light gets reflected back inside the fibers.

The PMT's used are the Hamamatsu 8-stage R5900. In the 1998 test an improved version of these PMT's was used in the positive η side of the module.

The phototube signals were sampled at 40 MHz with the FERMI system and the drawers were equipped with bi-gain 3-in-1 readout cards into FERMI ADC modules. Each drawer is equipped with 45 PMTs.

Pion calibration beams of different energies (20, 50, 80, 100, 150, 180, 300 and 400 GeV) at η = -0.25, -0.35, -0.45 and -0.55 have been analysed from the test beam data. On average, about ten thousand events are available for each energy. Cuts were applied in the beam chambers to eliminate the beam halo and events with simultaneous particle in the scintillator chambers (the same idea that in 1997 test beam); finally 60% of the events were removed including pedestal events supression.

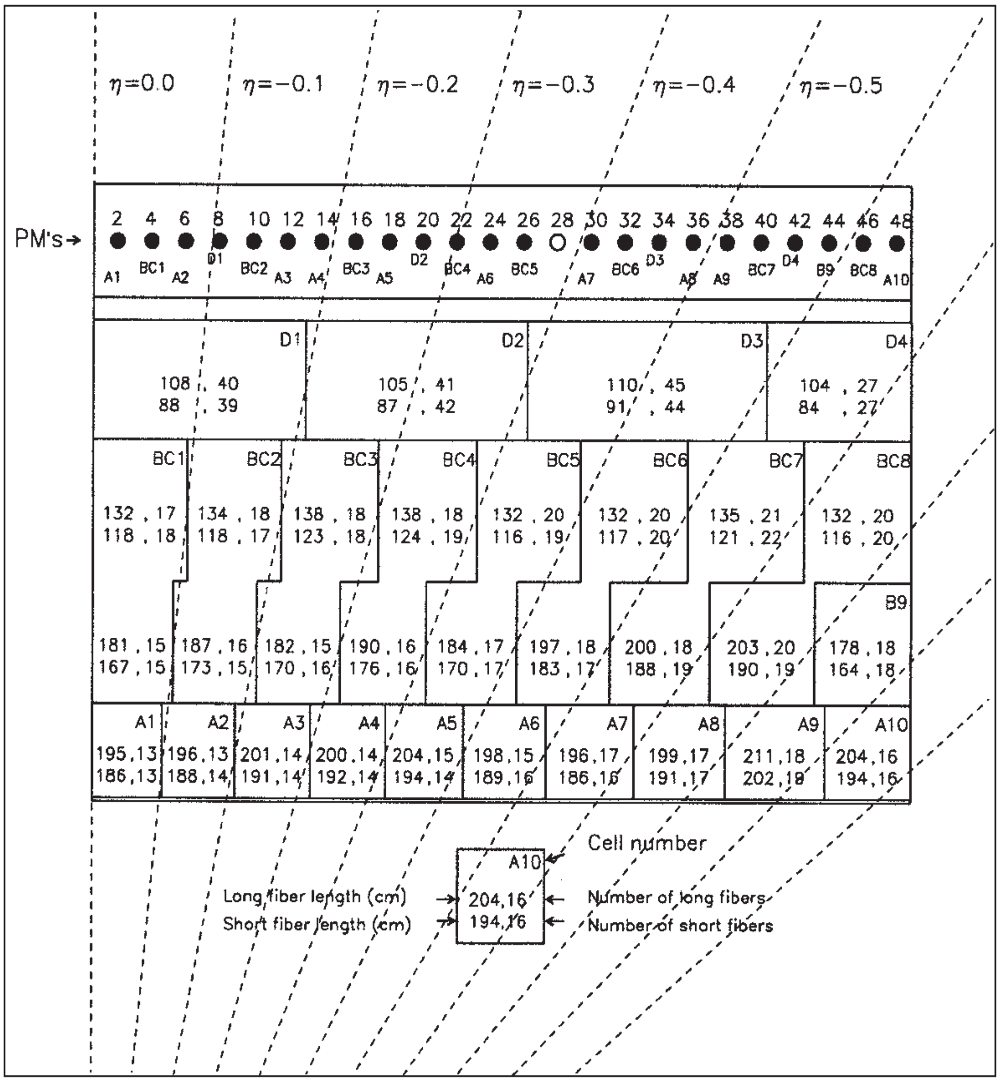

Figure 4.32: Cell geometry of the barrel module 0 tested in 1998.

4.4 Monte Carlo simulation

The data obtained in the test beam has been compared with Monte Carlo simulation. The test beam setup was simulated in the framework of GEANT3.21 [1] using DICE [18], [19] to simulate the geometry. The GCALOR [2] package was used to simulate the hadronic interactions.

The GEANT package has been used to simulate in detail the detector characteristics and performance. Version 3.21 is the best one suited for describing some of the very complex aspects of the detector geometry, while still providing a reasonable performance in terms of accuracy of the simulation and of CPU time needed to track particles through the complete detector. In addition to describing the detector geometry and tracking particles through it, the GEANT framework is used to describe the materials constituting the detector, to visualise the detector components, and to simulate and record the response of the sensitive elements of the various systems.

The DICE package contains general-purpose routines, which control the simulation flow, together with detector geometry modules, digitisation routines, and dedicated routines.

The final choice for the hadronic model was to use the GEANT interface to the CALOR package (GCALOR) because, although still far from an optimal fit to the data, it reproduces better than other procedures (FLUKA and GEISHA packages [20]) the experimental results. A cut set at 1 MeV for most of the hadronic processes has been used for event production, again as trade-off for performance.

The description of the Module 0 geometry in GEANT is probably the most critical issue for the detector-simulation program, since it must represent the right compromise between accuracy and performance. To simplify this procedure, a FORTRAN-based macro-language [21] has been used to set up detector-description banks, to implement the detector geometry, and to define HITS and DIGI structures associated with it. The advantage of this approach for the user is the possibility of having a generic interface to ZEBRA [22], while still maintaining a high level of flexibility.

The event-generation phase is normally run separately in order to have a consistent input stream which can be used many times. Event generation facilities are implemented within SLUG by using GENZ package, which provides a common interface between the most widely used event generators (PYTHIA [23], HERWIG [24], ISAJET [25]) and GEANT via the standard HEPEVT common block and ZEBRA banks.

We have simulated samples of two thousand pion events for different energy values in the range from 20 to 400 GeV and at different η values.

The simulation program is not complete and many features of the module 0 are not yet implemented in the simulation source code, namely:

- The fluctuations on the response of the fibres and tiles, including tile-to-tile and fibre-to-fibre fluctuations;

- The electronic of the read-out system, including the photostatistic effect and the electronic noise effect in the response of the module 0 to the particle beams.

4.5 Analysis of the 1998 pion data for the Barrel Module 0

When a particle develops a shower in a block of matter such a sampling calorimeter, some fraction of its energy is transformed into a measurable signal, usually a pulse of electrical charge. This pulse is the result of all the charged particles generated in the shower development which traverse and ionise the active layers of the detector. The energy resolution for detecting the original particle is determined by the fluctuations occuring in this process. This has consequences for calorimetric hadron detection (see chapter 3). Firstly, the signal distribution for hadrons of energy E will be broader than for electromagnetic showers at the same energy. Secondly, the average response (signal per unit of energy) will have a different value for electromagnetic and hadronic showers $e/h > 1$.

For hadrons the resolution and linearity of a non-compensated calorimeter ($e/h \neq 1$) are degraded by the different response to the electromagnetic and hadronic components of the hadronic shower [26]. The dependence of the e/h value with the energy affects the linearity, whereas the presence of the electromagnetic component in the shower generated by a hadron worses the resolution. All together, to these physical effects, which are limiting the intrinsic resolution of the detector, it has to be added the always experimental contributions, basically the losses due to leakage.

The purpose of weighting techniques is to compensate for this difference and to perform the energy reconstruction optimizing the linearity and resolution [30]. In the next subsections, the evolution of the linearity and resolution parameters with the data reconstruction is studied in two steps: from raw data to H1 weighting method. The benchmark approach is not used in this analysis, because the H1 method gives better results respect to the linearity and the resolution. The next point explains how to parametrize the leakage in order to improve the resolution. The e/h ratio is determined from the data taken in 1998 for Barrel Module 0. Finally, a comparison between Extended Barrel and Barrel Module 0 is presented.

4.5.1 Raw Data

The first step in the linearity and resolution study was the direct analysis of the test beam and Monte Carlo simulation raw data. The two components of the total raw energy are the energy detected in the barrel Module 0 and the energy measured in the five 1 m modules (old modules). The conversion factors from pC to GeV were calculated to be 1.26 and 36.1 for the barrel and 0.1613 and 29.2 for old modules, for the test beam data and Monte Carlo simulation respectively. So finally:

$$E_{Raw} = E_{M0}^{corr} + E_{old} \tag{4.17}$$

Using this formula we can reconstruct the beam energy as shown in Figure 4.33. The mean value is similar (for the test beam data is 65.7 GeV and for the Monte Carlo simulation 65.41 GeV) but the sigma parameter is bigger in the test beam data (6.3 GeV) than in the Monte Carlo simulation (5.2 GeV). This is because the simulation program does not have into account the fluctuations in the response of the fibres and tiles, and because of the limited knowledge of the hadronic showers development.

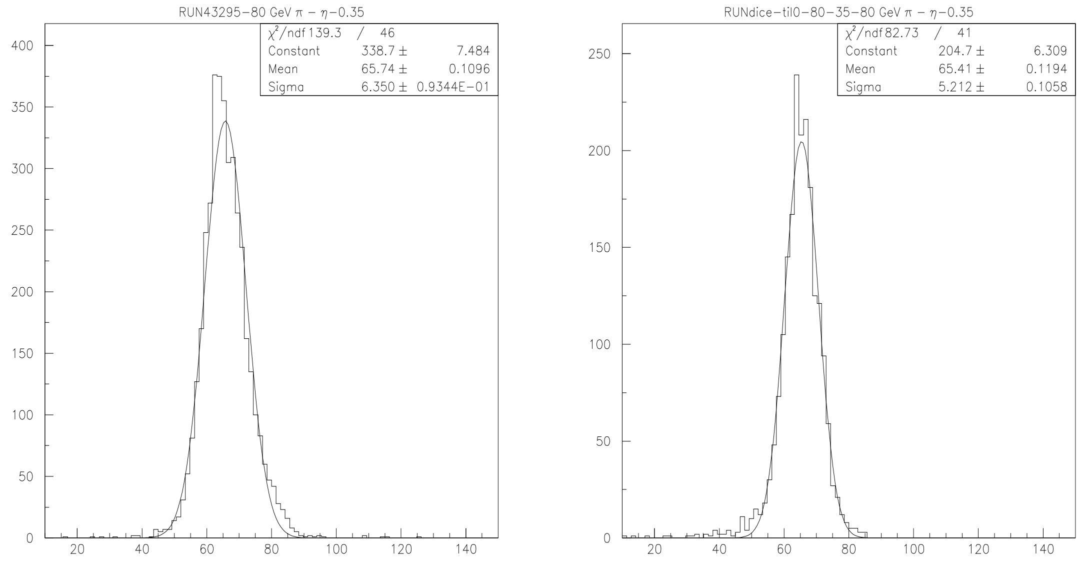

Figure 4.33: *Raw energy reconstruction for pions at 80 GeV and η=-0.35. Left: test beam data. Right: Monte Carlo simulation.*

According with the expresion (4.17) we present in table 4.15 the results of μ and σ for pion beams at η=-0.35 and in table 4.16 σ/μ for four different η values, obtained from the test beam data and from Monte Carlo simulation. Also the plots of linearity and energy resolution can be seen in figures 4.34 and 4.35, respectively.

Table 4.15: *Nominal energy, mean reconstructed energy and σ for pions at various beam energies at η=-0.35 for test beam data and Monte Carlo simulation obtained from raw data.*

η=-0.35	Test Beam data		MC simulation	
N. E. (GeV)	μ (GeV)	σ (GeV)	μ (GeV)	σ (GeV)
20	15.58±0.03	2.30±0.02	15.96±0.04	1.99±0.03
50	41.05±0.07	4.09±0.06	40.75±0.08	3.68±0.06
80	65.74±0.10	6.35±0.09	65.41±0.12	5.21±0.10
100	81.49±0.14	7.12±0.10	82.18±0.13	5.68±0.11
150	123.3±0.3	9.57±0.21	123.8±0.2	8.29±0.17
180	148.2±0.2	11.64±0.15	149.1±0.2	9.11±0.21
300	251.5±0.3	19.29±0.25	248.7±0.3	14.58±0.39
400	326.9±0.4	25.36±0.31	332.1±0.5	19.30±0.48

The linearity presents the typical shape of a non-compensated calorimeter, the slope is due to the increase of electromagnetic energy (π^0) with the incident pion energy in the shower. The big difference between the test beam data and the Monte Carlo simulation is found at high energies. The *rms* for the test beam data is greater (2% for all η's) than for the simulation (1.3%). This is mainly due to the data points at high energies, because the hadronic showers development knowledge is limited in the simulation program.

A fit of the data is performed using the expression (4.7). The study presented in the previous section 4.2.3 shows a strong correlation between parameters **a** and **c**, so that we have decided to fix the **c** value at 0.06 GeV in order to obtain less aleatory results in the **a** value and to compare with other fits.

The fit results for the test beam data and Monte Carlo simulation are presented in the table 4.17.

We obtain better resolution in the simulation than in the data. The figure 4.33 shows that in the Monte Carlo simulation the sigma parameter is lower than for the data, therefore as the mean value is similar for both, the resolution is better in the simulation.

Table 4.16: *Nominal energy and resolution for pions at various beam energies at four different η for test beam data and Monte Carlo simulation obtained from raw data.*

η=-0.25	Test Beam data	MC simulation
N. E. (GeV)	$\sigma/\mu(\%)$	$\sigma/\mu(\%)$
20	14.27±0.13	12.33±0.22
50	9.77±0.13	9.24±0.21
80	8.72±0.12	8.04±0.18
100	8.06±0.14	7.99±0.17
150	6.83±0.17	7.40±0.18
180	7.19±0.10	6.74±0.16
300	5.73±0.09	6.83±0.19
400	7.07±0.11	6.48±0.18
η=-0.35	Test Beam data	MC simulation
N. E. (GeV)	$\sigma/\mu(\%)$	$\sigma/\mu(\%)$
20	14.77±0.15	12.47±0.22
50	9.96±0.14	9.03±0.16
80	9.65±0.14	7.97±0.16
100	8.74±0.12	6.91±0.14
150	7.76±0.17	6.67±0.14
180	7.85±0.10	6.10±0.14
300	7.67±0.09	5.86±0.16
400	7.75±0.09	5.81±0.15
η=-0.45	Test Beam data	MC simulation
N. E. (GeV)	$\sigma/\mu(\%)$	$\sigma/\mu(\%)$
20	13.81±0.13	12.07±0.35
50	9.40±0.12	8.70±0.24
80	8.44±0.11	7.90±0.25
100	7.92±0.12	7.60±0.22
150	6.82±0.16	6.90±0.23
180	6.58±0.08	6.60±0.20
300	6.43±0.09	6.70±0.23
400	6.13±0.09	6.10±0.18
η=-0.55	Test Beam data	MC simulation
N. E. (GeV)	$\sigma/\mu(\%)$	$\sigma/\mu(\%)$
20	12.89±0.29	11.64±0.29
50	9.24±0.12	8.46±0.17
80	7.98±0.10	7.50±0.15
100	7.09±0.10	6.83±0.17
150	6.34±0.13	5.71±0.12
180	6.60±0.09	5.69±0.12
300	6.00±0.08	5.41±0.13
400	5.43±0.05	5.39±0.14

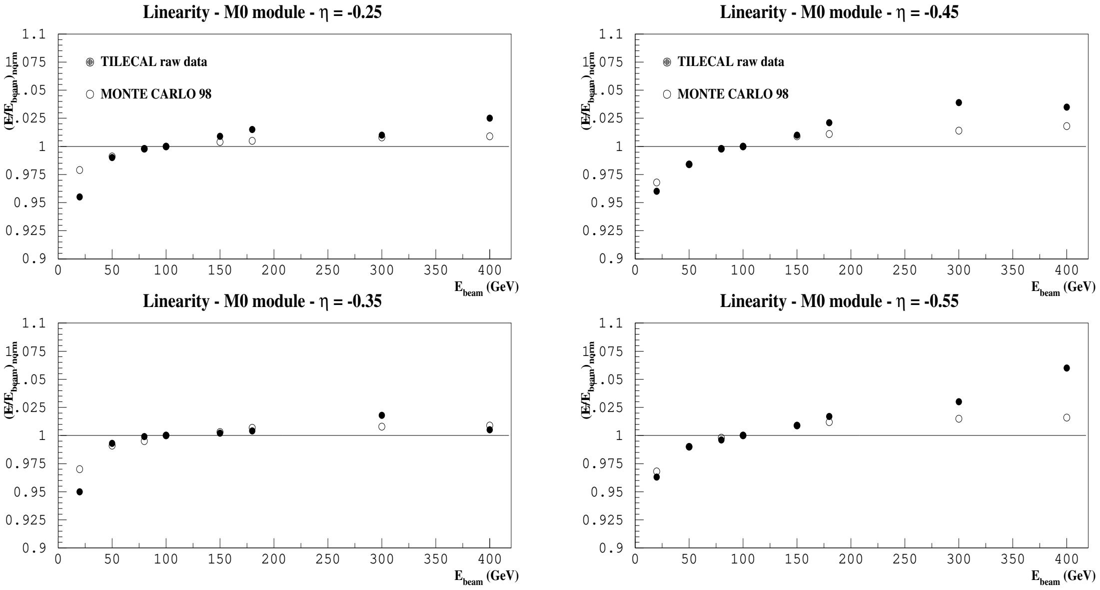

Figure 4.34: *Linearity of raw data for the test beam data and the Monte Carlo simulation. Left: for η=-0.25 (top) and η=-0.35 (bottom). Right: for η=-0.45 (top) and η=-0.55 (bottom).*

Table 4.17: *Statistical (a), constant (b), and noise (c) terms at four different η for test beam pion data and Monte Carlo simulation obtained from raw data.*

η	Test Beam data			MC simulation		
	a (%)	b (%)	c	a (%)	b (%)	c
-0.25	59.10	5.40	0.06	48.30	6.10	0.06
-0.35	56.30	6.88	0.06	56.30	6.88	0.06
-0.45	56.50	5.35	0.06	47.30	5.75	0.06
-0.55	55.20	5.10	0.06	48.80	5.20	0.06

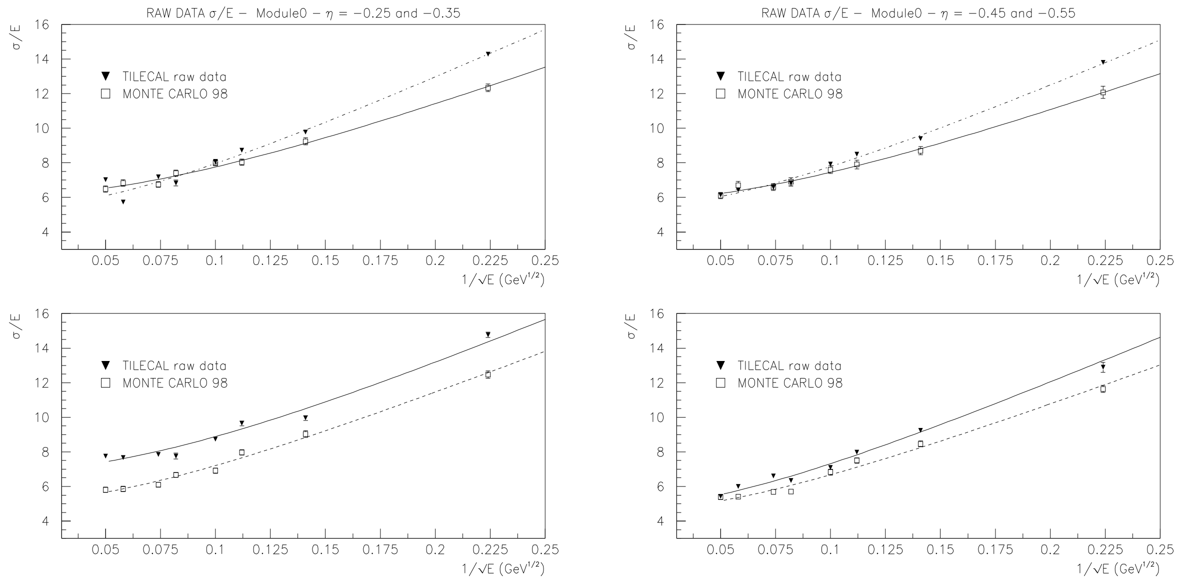

Figure 4.35: *Energy resolution of raw data for the test beam data and the Monte Carlo simulation. Left: for η=-0.25 (top) and η=-0.35 (bottom). Right: for η=-0.45 (top) and η=-0.55 (bottom).*

4.5.2 H1 Method

The linearity and the resolution are two characteristics which can be improved via software offline. Instead of correcting *upwards* the response of cells with relatively small signals, this method pretends to equalize their responses to the one of the cells with large (tipically electromagnetic) deposited energies (see section 4.2.3).

The energy in each cell, E_{cell}, is corrected multiplying its value by a parameter a_i [9] which depends on the energy of the cell (see formula 4.9).

The technical details of the method have been described in the section 4.2.3. As first step, for each beam energy, the cell energy spectrum is divided into n intervals [13] and a correction parameter a_i is calculated for each interval. Several sets of parameters are calculated for all the η values and for test beam data and Monte Carlo simulation.

The set of correction parameters a_i is determined from the data by minimizing the expression 4.13.

The corrected total energy spectra were fitted with Gaussian distributions over a $\pm 2\sigma$ range. From the mean values of the fits we obtain plots of the deviation from a linear response. Such linearity plots, are shown in figure 4.36, left η=-0.25 ,-0.35 and right η=-0.45, -0.55, respectively. The improvement when including the *energy conservation* constraint is very clear; with this constraint the *rms* deviation from linearity is 0.46% and 0.48% for the test beam data and Monte Carlo simulation, respectively. The two *rms* are very similar because we have reconstructed both energies minimizing the functional with the Lagrange multiplier.

The results of the fits to the reconstructed pion energies are given in table 4.18 and 4.19.

The energy resolution (σ/E *vs.* the beam energy) is given in figure 4.37. The resolution obtained here can be parametrized for the test beam data and Monte Carlo simulation as shows the table 4.20.

We obtain similar resolution in the simulation than in the real data because both functional have been minimized with the Lagrange multiplier.

4.5.2.1 Parametrizing the a_i

A total of 112 parameters are used to reconstruct the pion energy. To reduce the number of parameters we proceed as has been described in the section 4.2.3.2.

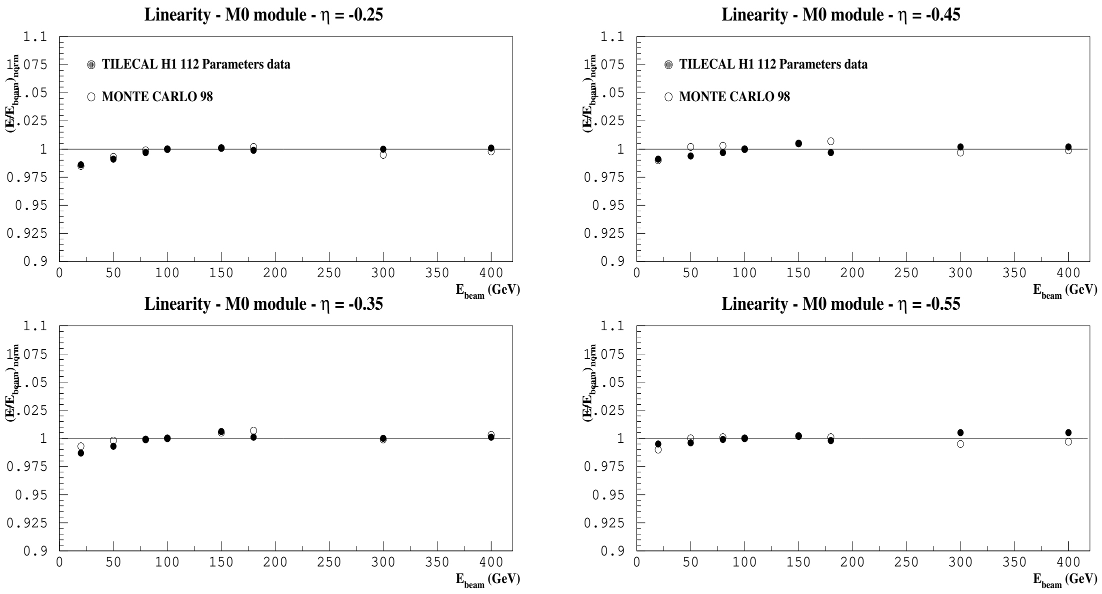

Figure 4.36: *Linearity plot minimizing the functional with the Lagrange multiplier for the test beam data and the Monte Carlo simulation. Left: for η=-0.25 (top) and η=-0.35 (bottom). Right: for η=-0.45 and η=-0.55. The points are obtained normalizing the mean reconstructed energy values from the Gaussian fits to the value of 100 GeV.*

Table 4.18: *Nominal energy, mean reconstructed energy and σ at various beam energies at η=-0.35 for test beam data and Monte Carlo simulation obtained with the constraint to the beam energy.*

η=-0.35	Test Beam data		MC simulation	
N. E. (GeV)	μ (GeV)	σ (GeV)	μ (GeV)	σ (GeV)
20	19.87±0.05	2.11±0.05	20.10±0.04	1.98±0.03
50	50.02±0.09	3.95±0.08	50.53 ±0.08	3.77±0.07
80	80.47±0.11	5.60±0.09	80.90±0.12	5.43±0.09
100	100.7±0.1	6.80±0.10	101.2±0.1	6.24±0.12
150	152.1±0.3	9.30±0.25	153.0±0.2	9.09±0.18
180	181.4±0.2	11.10±0.16	184.2±0.3	10.75±0.22
300	302.1±0.3	18.40±0.29	303.2±0.4	16.08±0.39
400	403.1±0.4	27.40±0.45	406.0±0.7	20.80±0.48

Table 4.19: *Nominal energy and resolution at various beam energies at four different η for test beam data and Monte Carlo simulation obtained with the constraint to the beam energy.*

η=-0.25	Test Beam data	MC simulation
N. E. (GeV)	$\sigma/\mu(\%)$	$\sigma/\mu(\%)$
20	10.63±0.27	10.10±0.29
50	7.95±0.17	7.76±0.17
80	7.39±0.13	7.51±0.16
100	6.99±0.13	7.35±0.16
150	6.98±0.18	7.09±0.15
180	6.92±0.11	6.78±0.16
300	5.93±0.11	5.98±0.15
400	7.40±0.11	5.59±0.15
η=-0.35	Test Beam data	MC simulation
N. E. (GeV)	$\sigma/\mu(\%)$	$\sigma/\mu(\%)$
20	10.62±0.25	9.85±0.27
50	7.90±0.17	7.46±0.15
80	6.95±0.12	6.71±0.12
100	6.75±0.11	6.17±0.13
150	6.11±0.17	5.94±0.13
180	6.12±0.10	5.83±0.13
300	6.09±0.09	5.30±0.13
400	6.69±0.12	5.12±0.12
η=-0.45	Test Beam data	MC simulation
N. E. (GeV)	$\sigma/\mu(\%)$	$\sigma/\mu(\%)$
20	10.41±0.28	10.40±0.27
50	7.52±0.15	7.85±0.28
80	7.00±0.11	7.31±0.29
100	6.56±0.09	6.81±0.27
150	5.85±0.17	6.70±0.24
180	5.86±0.09	6.50±0.19
300	5.36±0.07	5.92±0.25
400	5.75±0.10	5.16±0.14
η=-0.55	Test Beam data	MC simulation
N. E. (GeV)	$\sigma/\mu(\%)$	$\sigma/\mu(\%)$
20	8.85±0.49	9.70±0.15
50	7.55±0.15	7.70±0.17
80	6.81±0.11	7.06±0.19
100	6.14±0.09	6.81±0.18
150	6.08±0.19	6.78±0.19
180	6.03±0.09	6.63±0.18
300	5.58±0.09	5.42±0.16
400	5.40±0.07	5.25±0.17

Table 4.20: *Statistical (a), constant (b), and noise (c) terms at four different η for test beam data and Monte Carlo simulation obtained with the constraint to the beam energy.*

η	Test Beam data			MC simu lation		
	a (%)	b (%)	c	a (%)	b (%)	c
-0.25	35.10	6.30	0.06	39.30	5.10	0.06
-0.35	38.40	5.60	0.06	38.90	4.90	0.06
-0.45	41.30	5.00	0.06	41.70	5.30	0.06
-0.55	37.20	5.10	0.06	37.50	5.55	0.06

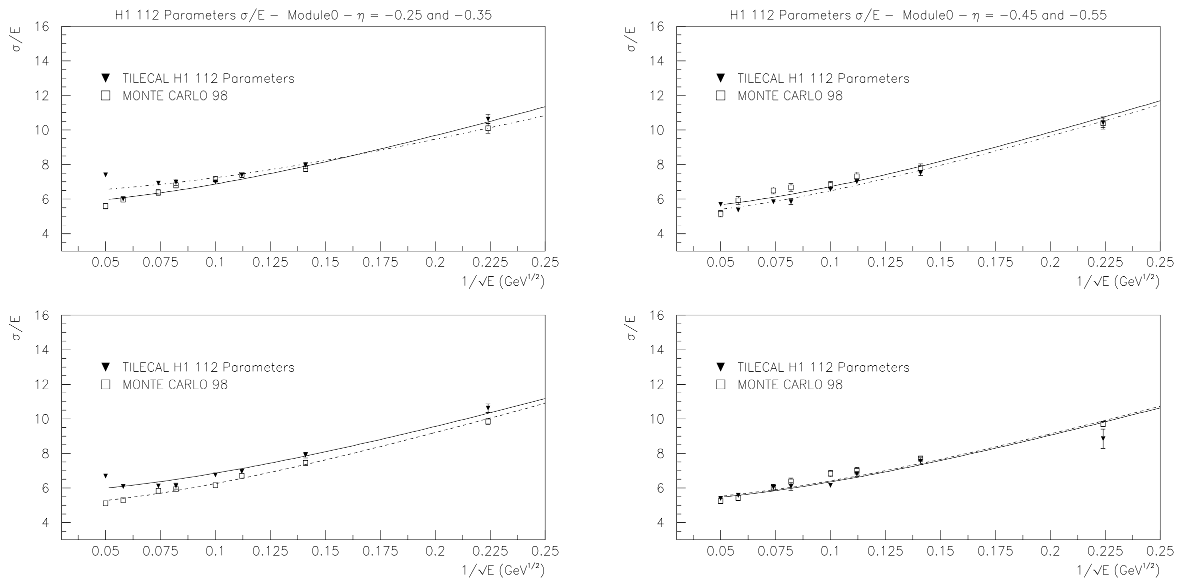

Figure 4.37: *Resolution plot minimizing the functional with the Lagrange multiplier for the test beam data and Monte Carlo simulation. Left: η =-0.25, (top) and η = -0.35 (bottom). Right: η =-0.45, (top) and η =-0.55(bottom) .*

The different values p_1, p_2 for the test beam data and Monte Carlo simulation are shown in figure 4.38 for test beam data and 4.39 for Monte Carlo simulation for various beam energies and η=-0.45. Applying the same parametrization similar results for the other η values have been obtained.

The parameters p_1, p_2 and B (the old modules parameter) are expressed as a function of the beam energy using two parameters dependence (i.e., $p_1' + p_2' \times E_{beam}$). This is shown in figures 4.40 and 4.41; for the test beam data and Monte Carlo simulation at η=-0.45. The same behaviour has been obtained for other η values.

Following theses parametrizations, we have expressed the entire set of corrections by two sets of simple functions, containing a total of only six parameters. The aim now is to check whether the energies reconstructed with 6 rather than 112 parameters are less precise. The mean, σ for η=-0.35 and resolution values for four η obtained from this a_i parametrization are given in the table 4.21 and 4.22; the linearity and resolution plots are given in figure 4.42 and 4.43. Comparing to the results previously obtained with 112 parameters one can see that despite the dramatic reduction of correction parameters the resolution is negligibly worse.

The linearity has degraded because the energy reconstruction is not good enough. This is due to the fact that the errors on the a_i, p_1, p_2 and B (the old modules parameter) are big, therefore the fit is worse than in 1997 test beam. Quantitatively, the *rms* deviation from linearity is now $\sigma = 1.19\%$ and 0.95% for the test beam data and Monte Carlo simulation, respectively, instead of 0.46% and 0.48%.

Table 4.21: *Nominal energy, mean reconstructed energy and σ at various beam energies at η=-0.35 for test beam data and Monte Carlo simulation obtained after the parametrization.*

η=-0.35	Test Beam data		MC simulation	
N. E. (GeV)	μ (GeV)	σ (GeV)	μ (GeV)	σ (GeV)
20	19.56±0.06	2.27±0.06	20.71±0.05	2.09±0.04
50	50.23±0.09	3.95±0.08	51.22 ±0.09	3.82±0.07
80	81.50±0.11	5.68±0.09	80.10±0.12	5.19±0.09
100	101.3±0.1	6.83±0.11	98.62±0.14	5.99±0.12
150	154.5±0.3	9.19±0.24	148.3±0.2	8.21±0.16
180	185.1±0.2	10.94±0.17	178.6±0.2	9.08±0.18
300	310.4±0.3	17.74±0.28	298.2±0.6	14.08±0.49
400	405.4±0.5	26.18±0.44	396.7±0.9	16.91±0.65

The resolution is now parametrized for the test beam data and Monte Carlo simulation as shows the table 4.23.

The *rms* obtained for the Monte Carlo simulation is less than for the test beam data.

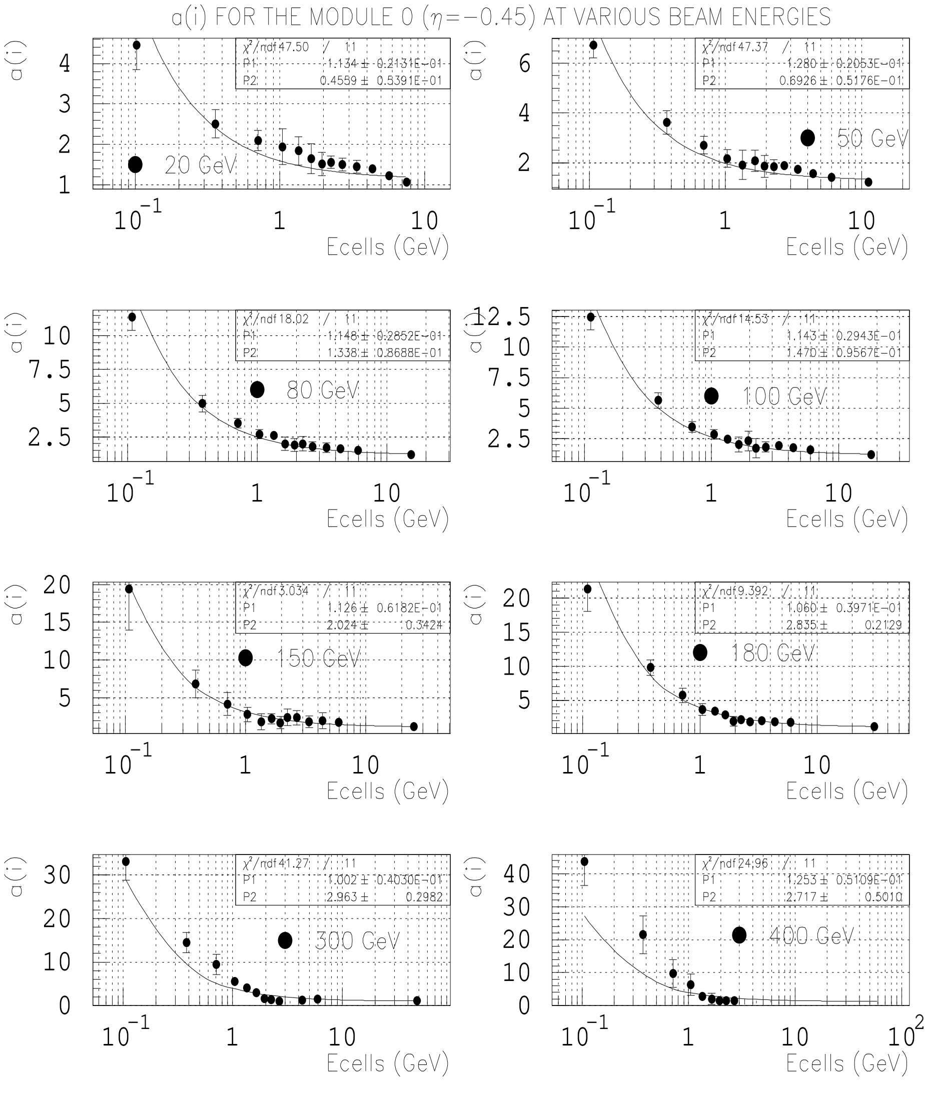

Figure 4.38: *Fits for the a_i parameters at various beam energies and η=-0.45 for the test beam data. The parameters p_1 and p_2 obtained are also shown on the plots.*

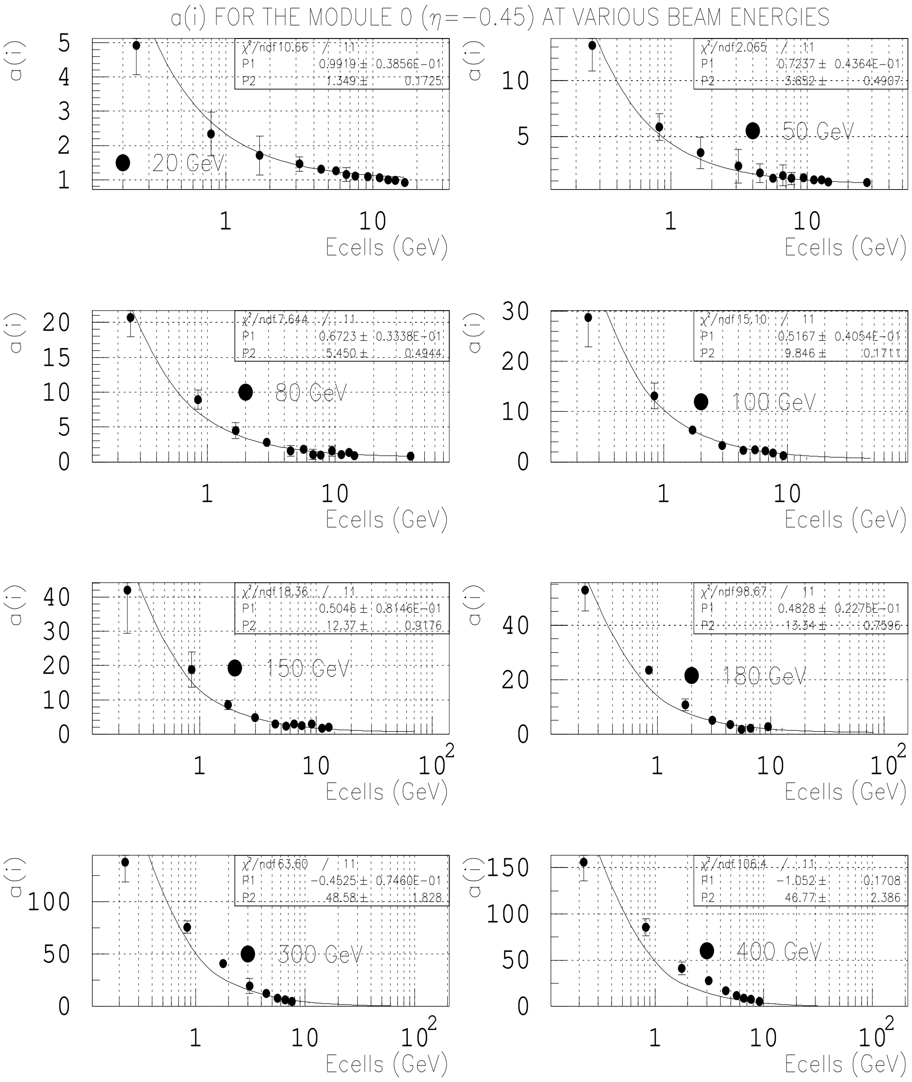

Figure 4.39: *Fits for the a_i parameters at various beam energies and η=-0.45 for the Monte Carlo simulation. The parameters p_1 and p_2 obtained are also shown on the plots.*

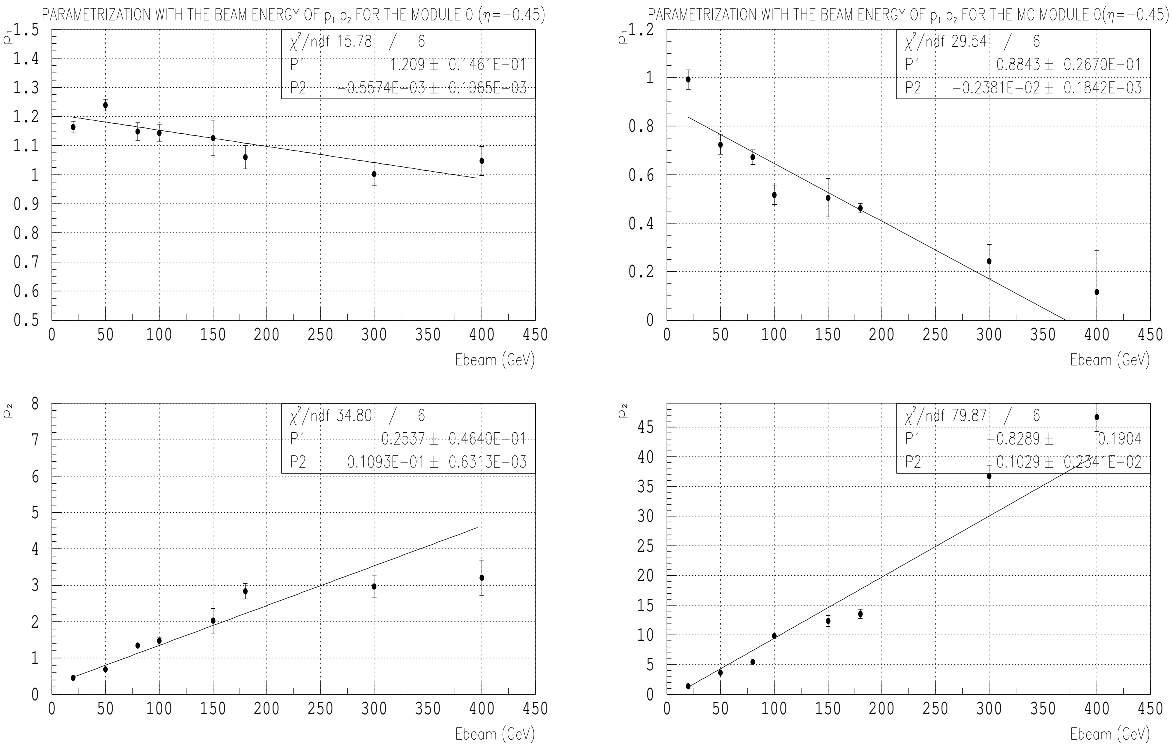

Figure 4.40: *For η=-0.45, the top plots show the parametrization with the beam energy of p_1 for the test beam data (left) and Monte Carlo simulation (right) modules; the bottom plots shown the same for p_2. The values of the parameters p_1' and p_2' from the fits are also presented on the plots.*

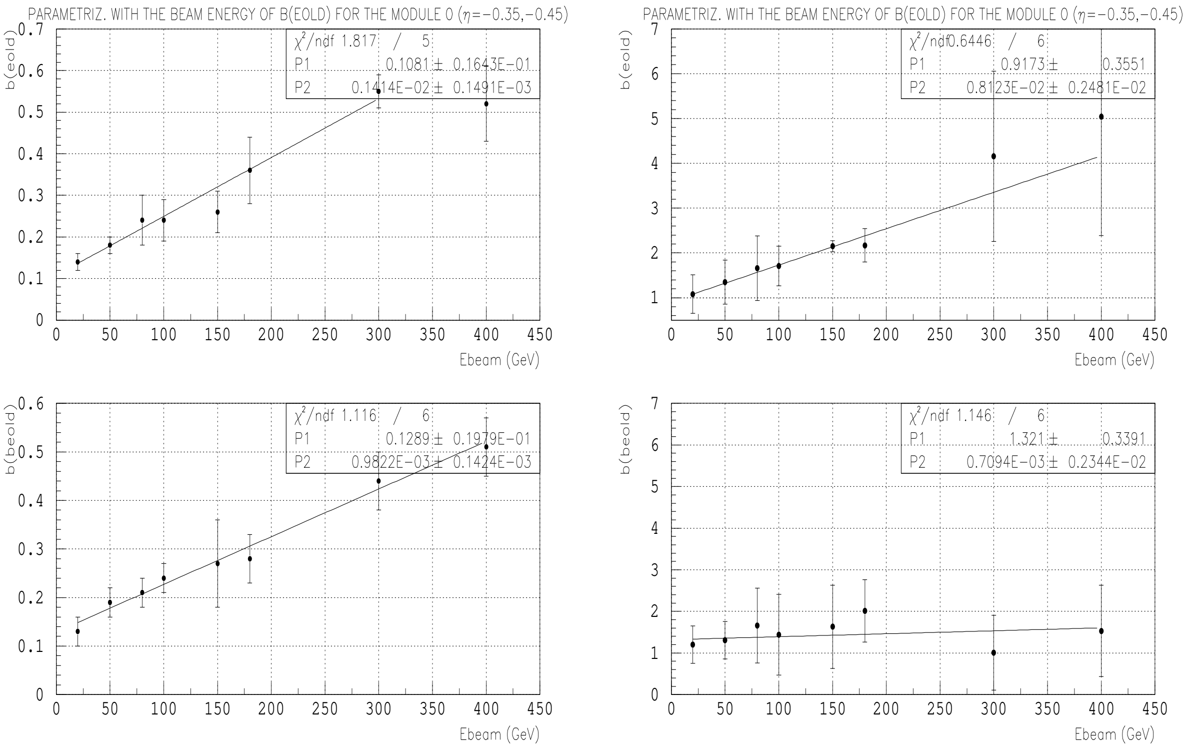

Figure 4.41: *The top plots show the parametrization with the beam energy of B for η=-0.35; the bottom plots show the same for η=-0.45. On the left test beam data and on the right Monte Carlo simulation. The values of the parameters p_1' and p_2' from the fits are also presented on the plots.*

Table 4.22: *Nominal energy and resolution at various beam energies at four different η for test beam data and Monte Carlo simulation obtained after the parametrization.*

η=-0.25	Test Beam data	MC simulation
N. E. (GeV)	$\sigma/\mu(\%)$	$\sigma/\mu(\%)$
20	11.44±0.34	10.32±0.19
50	8.11±0.16	8.00±0.15
80	7.20±0.12	6.84±0.13
100	6.65±0.11	6.81±0.13
150	6.40±0.16	6.73±0.13
180	6.73±0.09	6.23±0.12
300	5.64±0.10	6.01±0.20
400	6.13±0.08	5.16±0.40
η=-0.35	Test Beam data	MC simulation
N. E. (GeV)	$\sigma/\mu(\%)$	$\sigma/\mu(\%)$
20	11.54±0.35	10.00±0.14
50	7.86±0.17	7.41±0.13
80	6.97±0.11	6.47±0.12
100	6.75±0.12	5.95±0.11
150	5.95±0.15	5.55±0.10
180	5.92±0.10	5.08±0.13
300	5.71±0.09	4.72±0.16
400	6.45±0.11	4.26±0.18
η=-0.45	Test Beam data	MC simulation
N. E. (GeV)	$\sigma/\mu(\%)$	$\sigma/\mu(\%)$
20	11.93±0.38	10.32±0.29
50	7.80±0.17	7.98±0.25
80	6.86±0.11	7.33±0.31
100	6.27±0.09	6.47±0.47
150	5.25±0.13	6.40±0.59
180	5.33±0.08	6.36±0.29
300	4.86±0.08	5.14±0.30
400	5.36±0.13	4.79±0.25
η=-0.55	Test Beam data	MC simulation
N. E. (GeV)	$\sigma/\mu(\%)$	$\sigma/\mu(\%)$
20	11.59±0.72	9.81±0.15
50	7.82±0.18	7.36±0.34
80	6.89±0.10	7.23±0.20
100	6.26±0.09	7.21±0.24
150	6.50±0.20	6.52±0.40
180	5.79±0.09	6.17±0.25
300	5.55±0.10	5.48±0.21
400	5.11±0.08	5.29±0.22

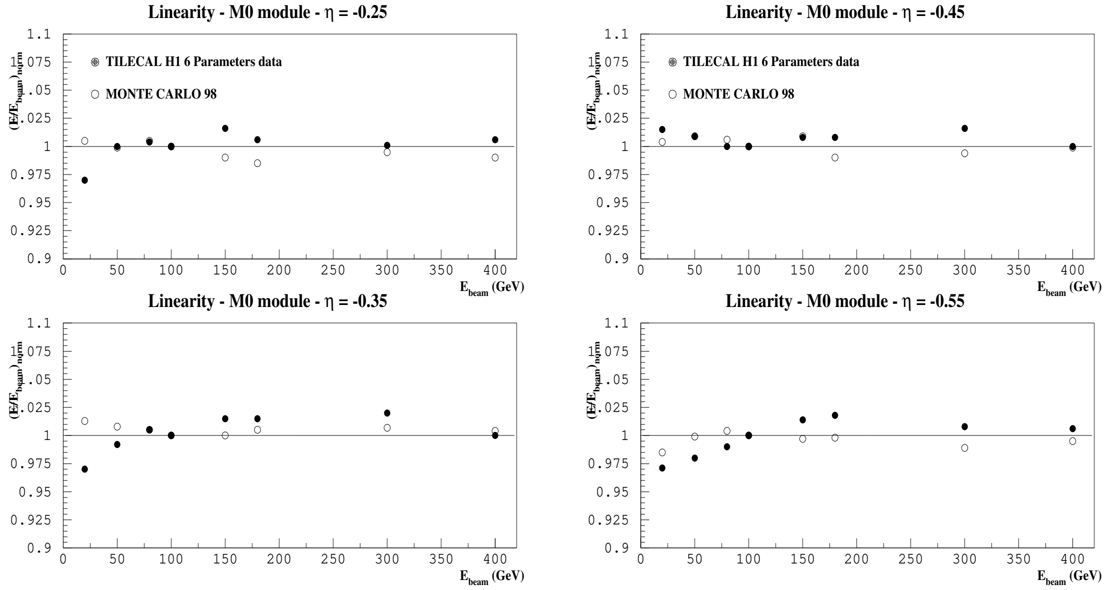

Figure 4.42: *Linearity after the parametrization with the beam energy for test beam data and Monte Carlo simulation. Left: For η=-0.25 (Top) and η=-0.35 (Bottom). Right: For η=-0.45 (Top) and η=-0.55 (Bottom).*

Table 4.23: *Statistical (a), constant (b), and noise (c) terms at four different η for test beam data and Monte Carlo simulation obtained after the parametrization.*

η	Test Beam data			MC simulation		
	a (%)	b (%)	c	a (%)	b (%)	c
-0.25	41.30	5.60	0.06	37.80	5.50	0.06
-0.35	41.10	5.30	0.06	42.20	3.90	0.06
-0.45	45.10	4.10	0.06	43.00	4.60	0.06
-0.55	43.40	4.70	0.06	37.70	5.10	0.06

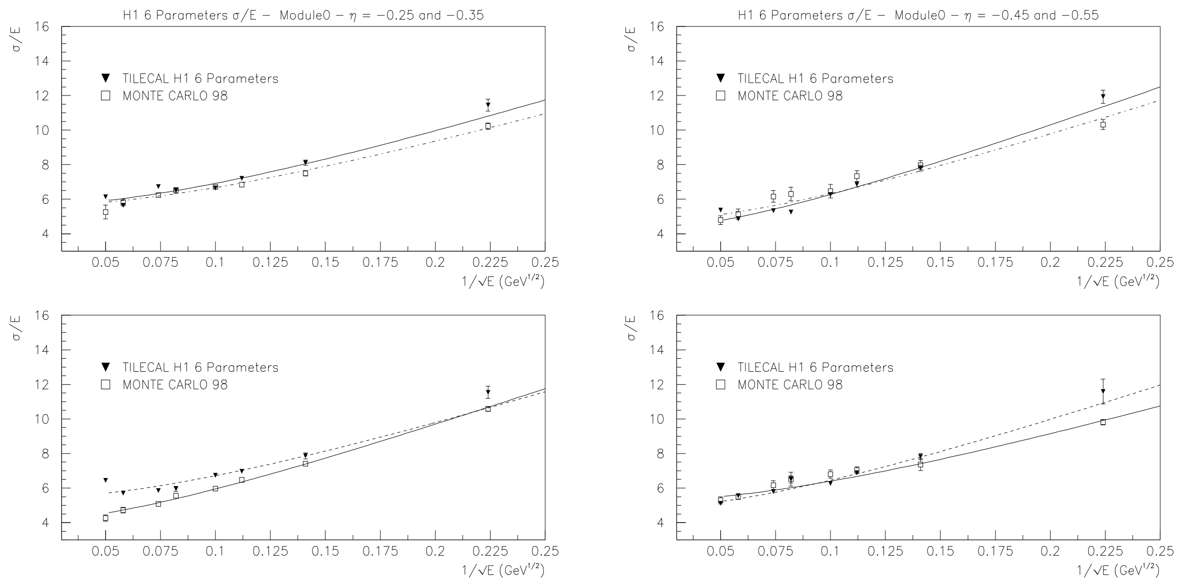

Figure 4.43: *Resolution after the parametrization with the beam energy for test beam data and Monte Carlo simulation. Left: For η=-0.25 (Top) and η=-0.35 (Bottom). Right: For η=-0.45 (Top) and η=-0.55 (Bottom).*

The drastic reduction from 112 to 6 parameters only represents an increase of 0.2 in the *rms*, both for Monte Carlo simulation and real data. For the resolution the statistical term from the fit is less in the Monte Carlo simulation than in the test beam data, this is because the resolution at low energy, where this term dominates, is better for the simulation than for the data.

4.5.2.2 Realistic energy reconstruction assuming no knowledge of the beam energy

The goal of this section is to reconstruct the pion energy in a real life experiment. The procedure was described in the section 4.2.3.3 [27].

We can reconstruct the energy using only 6 parameters and assuming no knowledge of the beam energy. This is shown in Figure 4.44

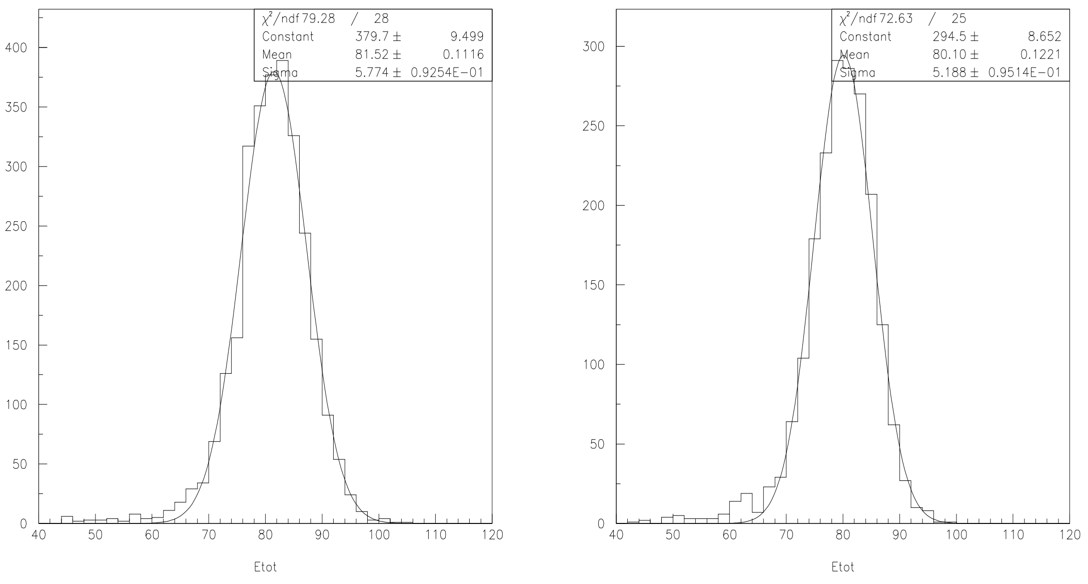

Figure 4.44: *Reconstructed energy using only 6 parameters and assuming no knowledge of the beam energy for pions at 80 GeV and η=-0.35. Left: test beam data. Right: Monte Carlo simulation.*

The mean, σ for η=-0.35 and resolution on the reconstructed energies are presented in tables 4.24 and 4.25. In figure 4.45 the linearity obtained by the *realistic* method is shown; the linearity remains as good as before. For test beam data the non-linearity ranges from 1.19% to 1.37% and from 0.48% to 0.85% for Monte Carlo simulation. The linearity given by the *realistic* method is compared with the linearity obtained using the known beam energy. Also the *rms* for the Monte Carlo simulation is less than for the test beam data.

Table 4.24: *Nominal energy, mean reconstructed energy and σ at various beam energies at η=-0.35 for test beam data and Monte Carlo simulation obtained assuming no knowledge of the beam energy.*

η=-0.35	Test Beam data		MC simulation	
N. E. (GeV)	μ (GeV)	σ (GeV)	μ (GeV)	σ (GeV)
20	19.51±0.06	2.22±0.06	20.58±0.05	2.16±0.04
50	50.22±0.09	3.93±0.07	50.87 ±0.07	3.82±0.07
80	81.79±0.11	5.69±0.09	79.44±0.09	5.16±0.09
100	101.5±0.1	6.86±0.10	98.80±0.11	5.92±0.11
150	154.7±0.3	9.27±0.22	149.9±0.2	8.07±0.16
180	186.8±0.2	11.07±0.16	177.2±0.2	9.19±0.22
300	311.7±0.4	18.01±0.27	297.2±0.5	13.13±0.49
400	406.7±0.5	26.45±0.45	395.7±0.6	15.72±0.60

The resolutions obtained with the realistic algorithm, as we can see in figure 4.46 present a slight degradation with respect to the values given in the previous parametrization that uses the nominal beam energy. This result is unavoidable due to event-to-event fluctuations of hadronic showers. The figure shows that the degradation of the resolution is more pronounced at low energy, as expected from the energy dependence of σ/E. At high energy, the resolution for the test beam data is greater than for the Monte Carlo simulation.

The final results for the test beam data and for the Monte Carlo simulation are shown in the table 4.26.

In this study we have proved that the linearity and resolution of the Barrel Module 0 improve using the H1 method. Also the good agreement between the Monte Carlo simulation and the Test beam data after applying H1 weighting technique for the four different values of η has been seen.

Respect to the linearity, using Lagrange multipliers we found a very good linear response over the range of studied energies, because 112 weights have been used for each module. With the parametrization of these weights using a total of 6 constants and assuming no knowledge of the particle energy the linearity is degraded but the average *rms* is around 1.5% and therefore inside the requirements. The linearity for the Monte Carlo simulation is better than for the test beam data but at high energies the hadronic shower simulation is insufficient and the shower description became quite far away from reality.

Table 4.25: *Nominal energy and resolution at various beam energies at four different η for test beam data and Monte Carlo simulation obtained assuming no knowledge of the beam energy.*

η=-0.25	Test Beam data	MC simulation
N. E. (GeV)	$\sigma/\mu(\%)$	$\sigma/\mu(\%)$
20	11.72±0.34	11.08±0.19
50	8.05±0.16	8.12±0.15
80	7.25±0.12	6.92±0.12
100	6.69±0.11	6.90±0.13
150	6.44±0.16	6.67±0.13
180	6.75±0.09	6.17±0.12
300	5.65±0.10	5.78±0.20
400	6.17±0.08	5.10±0.20
η=-0.35	Test Beam data	MC simulation
N. E. (GeV)	$\sigma/\mu(\%)$	$\sigma/\mu(\%)$
20	11.39±0.34	10.49±0.19
50	7.84±0.15	7.50±0.13
80	6.95±0.12	6.50±0.11
100	6.75±0.11	5.97±0.11
150	5.99±0.15	5.34±0.10
180	5.92±0.09	5.08±0.13
300	5.77±0.09	4.41±0.16
400	6.55±0.12	3.97±0.15
η=-0.45	Test Beam data	MC simulation
N. E. (GeV)	$\sigma/\mu(\%)$	$\sigma/\mu(\%)$
20	11.89±0.38	9.62±0.28
50	7.58±0.15	8.30±0.32
80	6.89±0.12	7.69±0.33
100	6.27±0.10	7.50±0.35
150	5.28±0.14	6.57±0.36
180	5.30±0.08	6.37±0.35
300	4.86±0.08	5.21±0.26
400	5.35±0.10	4.83±0.22
η=-0.55	Test Beam data	MC simulation
N. E. (GeV)	$\sigma/\mu(\%)$	$\sigma/\mu(\%)$
20	11.30±0.72	9.83±0.17
50	7.60±0.18	7.70±0.19
80	6.97±0.10	7.86±0.22
100	6.25±0.09	7.21±0.25
150	6.36±0.20	6.86±0.23
180	5.85±0.09	6.24±0.21
300	5.70±0.10	5.26±0.22
400	5.48±0.08	5.06±0.19

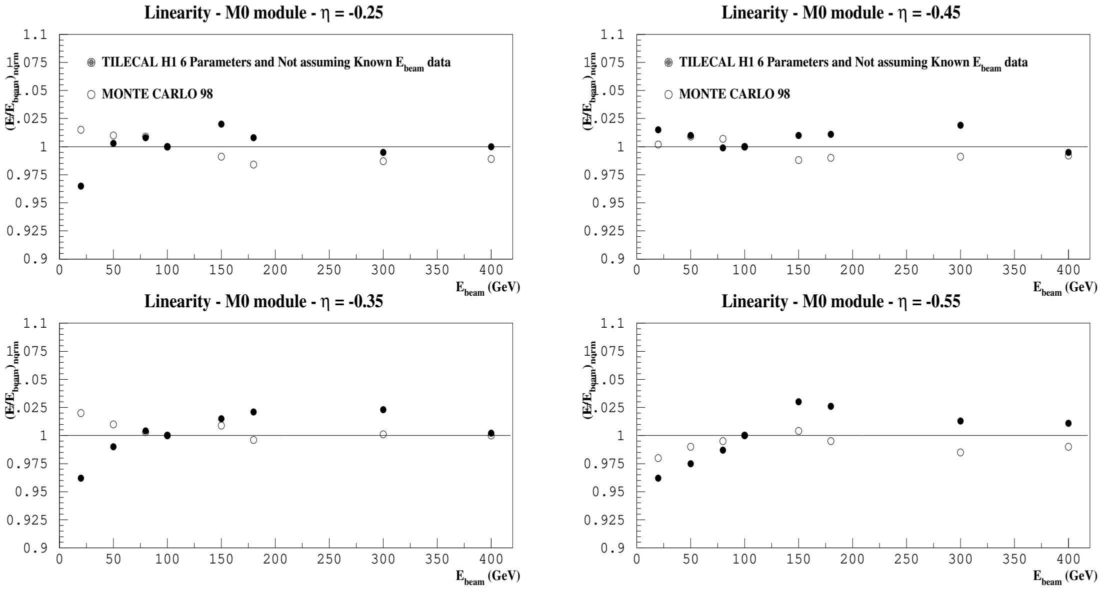

Figure 4.45: *Linearity plots without the beam energy knowledge for test beam data and Monte Carlo simulation. Left: For* η*=-0.25 (Top) and* η*=-0.35 (Bottom). Right: For* η*=-0.45 (Top) and* η*=-0.55 (Bottom).*

Table 4.26: *Statistical (a), constant (b), and noise (c) terms at four different* η *for test beam data and Monte Carlo simulation obtained assuming no knowledge of the beam energy.*

η	Test Beam data			MC simulation		
	a (%)	b (%)	c	a (%)	b (%)	c
-0.25	41.10	5.70	0.06	42.80	5.20	0.06
-0.35	40.80	5.30	0.06	45.70	3.70	0.06
-0.45	45.90	4.20	0.06	42.60	5.00	0.06
-0.55	43.20	4.80	0.06	39.00	5.10	0.06

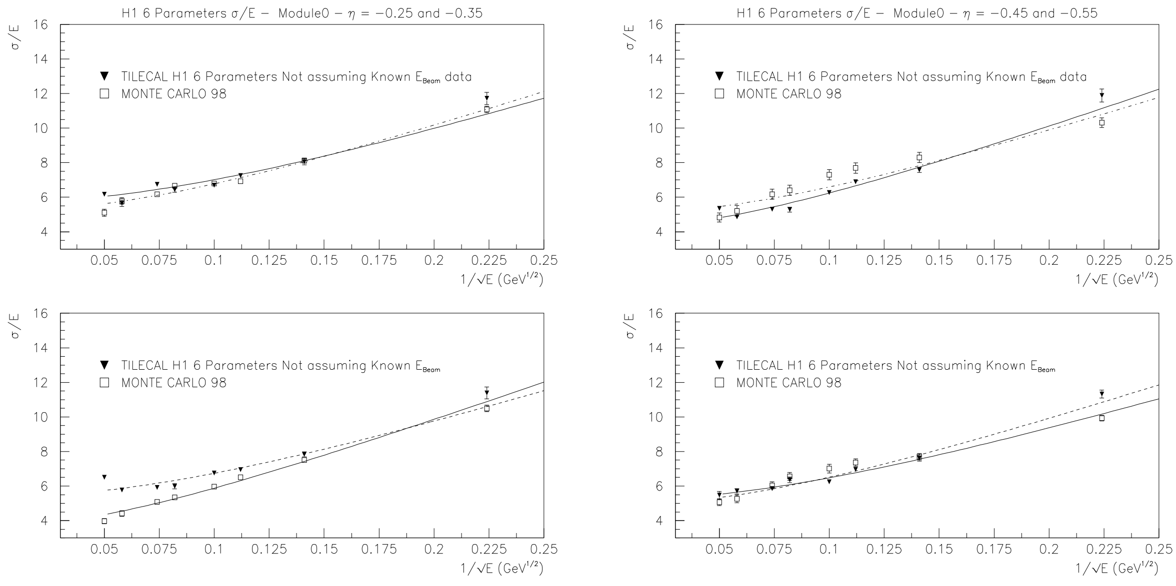

Figure 4.46: *Resolution plots without the beam energy knowledge for test beam data and Monte Carlo simulation. Left: For η=-0.25 (Top) and η=-0.35 (Bottom). Right: For η=-0.45 (Top) and η=-0.55 (Bottom).*

For the resolution, the use of all those weights improves significantly the resolution with respect to the raw data algorithm. As expected, the resolution degrades somewhat when no knowledge of the particle energy is assumed, been better than the obtained with the other methods. The statistical and the constant terms are very similar for the Monte Carlo simulation and test beam data having a mean value around 43% and 5%, respectively.

4.5.3 Leakages parametrization

The aim of this section is to parametrize the Module 0 leakages in order to improve the resolution. A prove that leakages exist is that in the Muon Wall located behind it there is signal.

A first idea was to apply cuts on the variable *MuBackHit* which represents the number of cells inside Back Muon Wall with signal greater than 0.7 mip. The figure 4.47 shows this variable for pion calibration beams with energies 20, 100 and 400 GeV at η=-0.45.

At high energies the *MubackHit* variable can reach values up to 10, 12 and, 14, while at low energies only 1 or 2. This is because at high energies the leakage in the Barrel Module 0 is greater than at low energies. We can make a cut on this variable to obtain better results in the resolution, reducing the leakages contribution.

For this pourpose we have reconstructed the raw energy detected in the Barrel Module 0 for η=-0.45 and pion beam energy 400 GeV without and with cut in *MubackHit* (*Mubackhit* < 3). This is shown in Figure 4.48. The resolution is better (evidently) when the cut is applied (from 5.7% to 5.0% for 400 GeV) but the number of entries has been strongly reduced (about 60% for 400 GeV) and also there is a clear reduction of the low energy tails. For this reason we decided to avoid the use of this cut.

Two alternatives have been tried to parametrize the leakages: with a gaussian or with an exponential. For the case where the main assumption is that the leakage is characterized by an exponential, the energy response of the ideal calorimeter (ideal resolution and correct energy scale) would have the shape:

$$R_0(e; E_0, \langle E_{leak} \rangle) = e^{-(E_0 - e)/\langle E_{leak} \rangle} \tag{4.18}$$

where E_0 is the nominal energy and $\langle E_{leak} \rangle$ is the mean value of the energy leaked out of the calorimeter. The formula is valid for $e \leq E_0$ and R_0 is equal to 0 otherwise.

Due to the e/h factor it becomes:

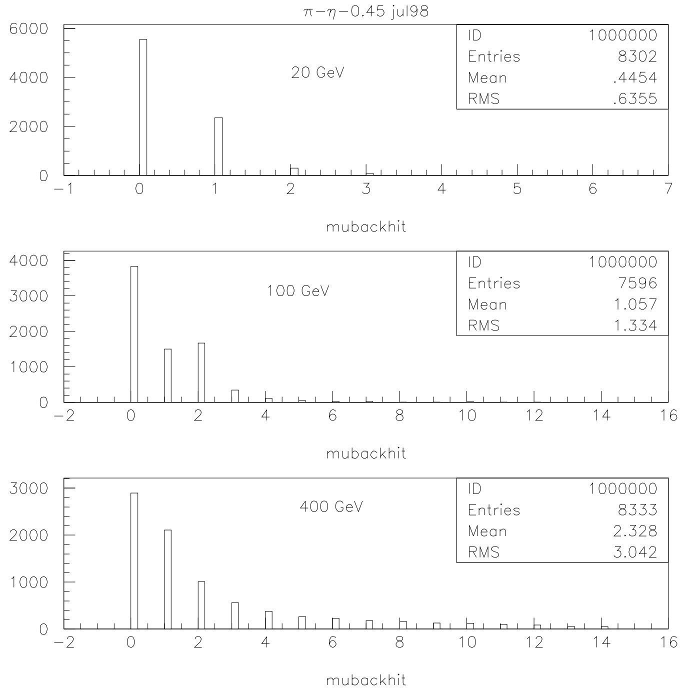

Figure 4.47: *Values of the MuBackHit variable for pion calibration beams at* η*=-0.45 and for three different energies.*

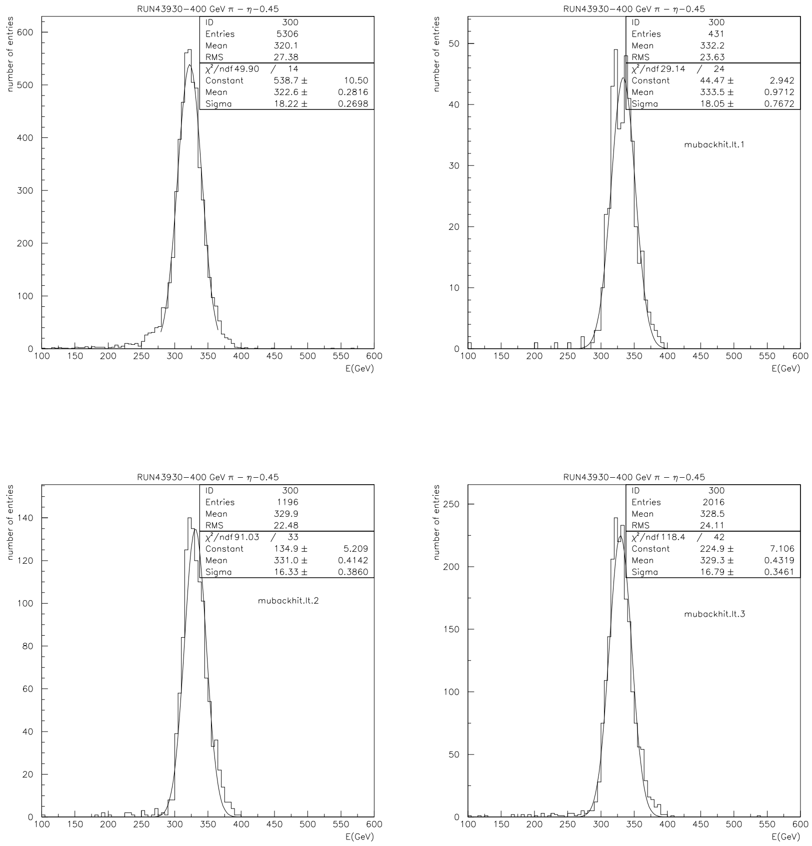

Figure 4.48: *Raw energy in the Barrel Module 0 for pions at 400 GeV and* η*=-0.45. Top left: without cut in MubackHit. Top right: with cut in MubackHit < 1. Bottom left: with cut in MubackHit < 2. Bottom right: with cut in MubackHit < 3.*

$$R_m(e; E_0, \langle E_{leak} \rangle) = e^{-(E_m - e)/\langle E_{leak} \rangle} \tag{4.19}$$

where E_m is a measured energy in the electromagnetic scale (it is lower that the nominal value E_0).

Because of the calorimeter resolution, each value e is smeared by the Gaussian distribution:

$$G(\epsilon; E_0, \sigma(e)) = e^{-(\epsilon - e)^2/(2\sigma^2(e))} \tag{4.20}$$

and consequently the measured response of the TileCal modules is (up to normalization factors):

$$\begin{aligned} R_{measured}(\epsilon) &= \int_0^{E_m} G(\epsilon; E_0, \sigma(e)) \times R_m(e; E_0, \langle E_{leak} \rangle) de \\ &= \int_0^{E_m} e^{-(\epsilon - e)^2/(2\sigma^2(e))} \times e^{-(E_m - e)/\langle E_{leak} \rangle} de \end{aligned} \tag{4.21}$$

and it contains three parameters:

1. The calorimeter response in the case of no leakage E_m.

2. The calorimeter resolution $\sigma(e)$. It might be constant ($\sigma(e) = \sigma(E_m)$) or energy-dependent according to the formula: $\sigma(e) = \sigma(E_m) \times \sqrt{e/E_m}$.

3. The mean energy leaked out of the calorimeter $\langle E_{leak} \rangle$.

In the case of no leakage ($\langle E_{leak} \rangle = 0$), the formula for $R_{measured}(\epsilon)$ contains an exponential function, with infinity large slope, which is equal to the $\delta(e - E_m)$ function and it becomes equal to the Gaussian distribution:

$$\begin{aligned} R_{measured}(\epsilon) &= \int_0^{E_m} G(\epsilon; E_0, \sigma(e)) \times \delta(e - E_m) de \\ &= e^{-(\epsilon - E_m)^2/(2\sigma^2)} \end{aligned} \tag{4.22}$$

Figure 4.49 shows the raw energy detected in the Barrel Module 0 for pion beam energy 400 GeV with cut in the *MubackHit* variable and parametrizing the leakages (low energy tails) with a gaussian and with an exponential. In the three cases the resolution is 5.2% but if we fit the whole distribution with two gaussians (signal and leakage) or

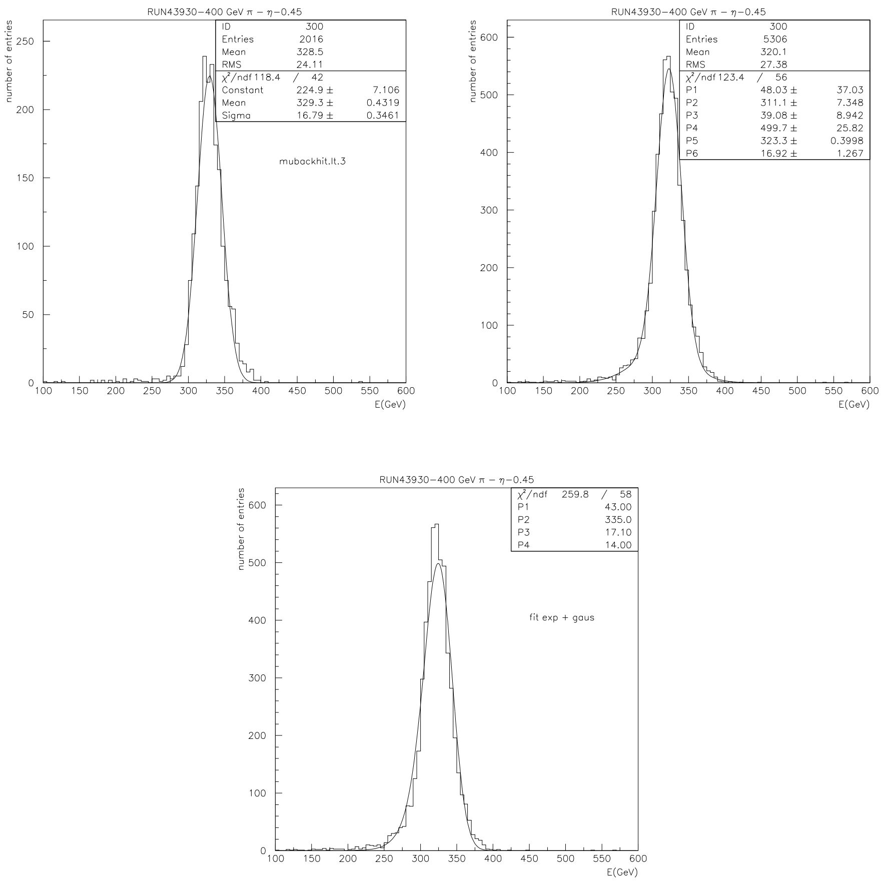

Figure 4.49: *Raw energy in the Barrel Module 0 for pions at 400 GeV and η=-0.45. a) With cut in MubackHit, b) parametrizing the leakages with a gaussian and c) characterizing the leakages with an exponential.*

with the convolution of the exponential and the gaussian, all the physical entries are used.

According with the expresion (4.17) we present in table 4.27 the results of μ, σ and σ/μ for $\eta = -0.45$ obtained from raw data and fitted with two gaussians; in table 4.28 the same results but using the convolution between the exponential and the gaussian are shown. Also the plots of linearity and energy resolution without to parametrize the leakage (top) and parametrizing the leakage with a gaussian (bottom) can be seen in figures 4.50 and 4.51, respectively. Figure 4.52 represents the energy resolution fitting with the convolution between the exponential and the gaussian.

Table 4.27: *Nominal energy, mean reconstructed energy , σ and resolution at various beam energies at $\eta = -0.45$ obtained from raw data and doing the fit with two gaussians.*

η=-0.45 N. E. (GeV)	μ (GeV)	σ (GeV)	σ/μ (%)
20	14.91 ± 0.02	2.06 ± 0.02	13.85 ± 0.13
50	38.62 ± 0.07	3.64 ± 0.05	9.42 ± 0.12
80	60.80 ± 0.46	4.63 ± 0.14	7.61 ± 0.23
100	77.98 ± 0.13	5.87 ± 0.37	7.52 ± 0.40
150	115.2 ± 0.7	6.73 ± 0.71	5.87 ± 0.60
180	143.4 ± 0.2	8.39 ± 0.22	5.85 ± 0.15
300	244.3 ± 0.3	14.83 ± 0.31	6.07 ± 0.13
400	323.3 ± 0.3	16.92 ± 0.90	5.23 ± 0.30

Table 4.28: *Nominal energy, mean reconstructed energy , σ and resolution at various beam energies at $\eta = -0.45$ obtained from raw data and doing the fit with the convolution between the exponential and the gaussian.*

η=-0.45 N. E. (GeV)	μ (GeV)	σ (GeV)	σ/μ (%)
20	14.91 ± 0.02	2.06 ± 0.03	13.85 ± 0.12
50	38.62 ± 0.06	3.64 ± 0.04	9.42 ± 0.15
80	63.20 ± 0.22	4.75 ± 0.17	7.81 ± 0.25
100	80.13 ± 0.15	6.01 ± 0.27	7.52 ± 0.33
150	119.17 ± 0.6	6.88 ± 0.75	5.91 ± 0.55
180	145.3 ± 0.3	8.87 ± 0.19	6.01 ± 0.17
300	248.3 ± 0.2	14.92 ± 0.34	6.02 ± 0.11
400	335.3 ± 0.2	17.10 ± 0.87	5.10 ± 0.33

The *rms* for the linearity is 2.5% when only one gaussian is used in the fit and 2.8% when two gaussians are fitted. The *rms* are quite similar because the two procedures

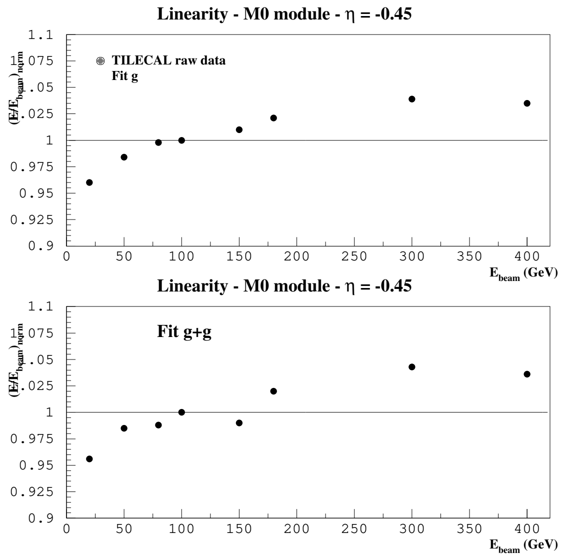

Figure 4.50: *Linearity of raw data doing the fit without to parametrize the leakage (top) and parametrizing the leakage with a gaussian (bottom) for* $\eta = -0.45$.

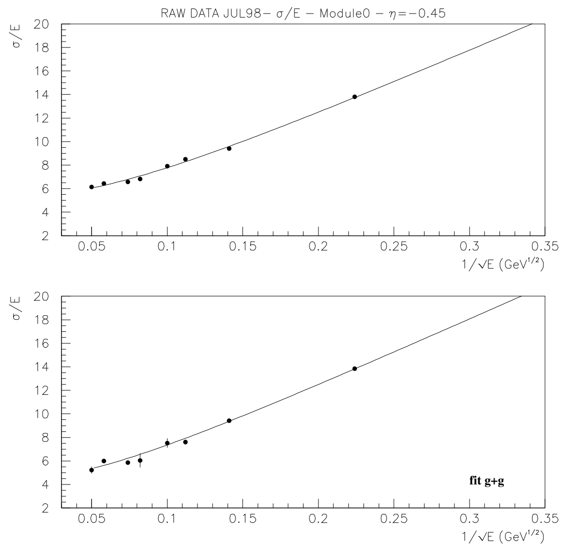

Figure 4.51: *Energy resolution of raw data doing the fit without to parametrize the leakage (top) and parametrizing the leakage with a gaussian (bottom) for* $\eta = -0.45$.

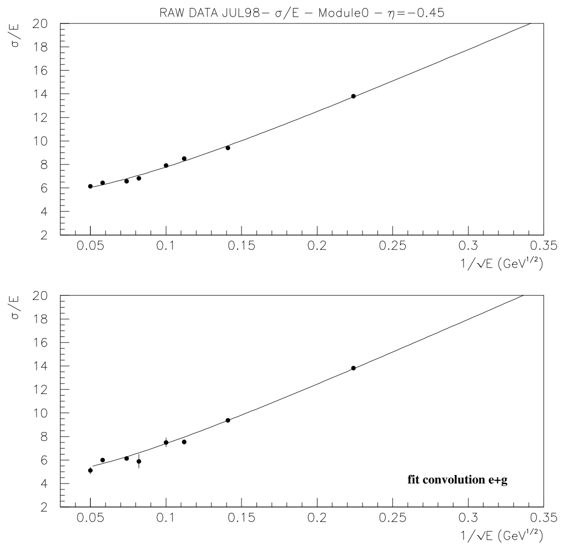

Figure 4.52: *Energy resolution of raw data doing the fit without parametrize the leakage (top) and parametrizing the leakage with an exponential (bottom) for $\eta = -0.45$.*

give practically the same value for the μ parameter.

For the resolution the fit results are presented in table 4.29, for the fit using one gaussian, two gaussians, the convolution between the exponential and the gaussian and the H1 method.

The statistical term is similar in the three cases (for the three fits) but the constant term is better when we parametrize the leakage with a gaussian or and exponential. This is because the resolution has been calculated with the gaussian distribution. And besides, the constant term for the H1 method and for the two leakage parametrization is similar due to the fact that the weighting itself already provides a reduction of the low energy tails (see figure 4.44).

Table 4.29: *Statistical (a) and constant (b) terms for $\eta = -0.45$ doing the fit with a gaussian , two gaussians, the convolution between the exponential and the gaussian and applying the H1 method. The noise (c) term have been fixed at 0.06 GeV.*

η	Fit (1 gaussian)		Fit (2 gaussians)		Fit (Conv. Exp. g.)		H1	
	a (%)	b (%)	a (%)	b (%)	a (%)	b (%)	a (%)	b (%)
-0.45	56.50	5.35	58.30	4.49	57.9	4.62	45.10	4.15

The figure 4.53 shows the comparison between the mean energy leaked out of the calorimeter $\langle E_{leak} \rangle$ when we parametrize the leakage with a gaussian (peak1-peak2) or with an exponential (slope of the exponent) and the energy dependence of the leakage.

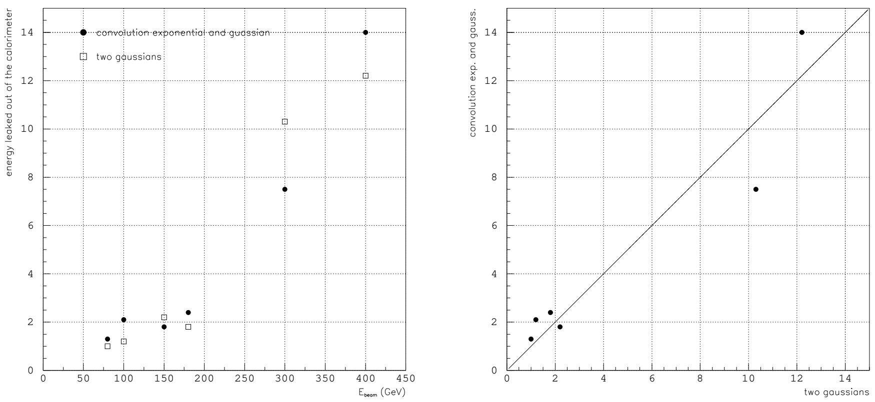

Figure 4.53: *Comparison between the mean energy leaked out of the calorimeter* $\langle E_{leak} \rangle$ *when we parametrize the leakage with a gaussian or with an exponential. a) Energy dependence. b) Correlation between both methods.*

In summary the two methods applied to parametrize the leakage give the same resolution and they provide the mean value of the energy leaked out of the calorimeter. The weighting technique already provides by itself a reduction of the low energy tails.

4.5.4 The e/h and the e/π ratios

The responses obtained for e and π give the possibility to determine the e/h ratio, an intrinsic characteristic of a non-compensated calorimeter. In our case the electron - pion ratios reveal complicated structures $e/\pi = f(E, \eta)$. Figure 4.54 shows the e/π ratios for Module-0 for $E = 20$, 50 100, 180 and 300 GeV at $\eta = -0.35$, -0.45 and -0.55 and for Monte Carlo simulation at $\eta = -0.45$. The errors include statistical error and a systematic error of 1% (the error is due to the uncertainties on the value of the beam energy and on the leakage), added in quadrature. For extracting the e/h we have used the standard e/π method. The data have been fitted using equation (4.16) and a comparison with the Monte Carlo simulation at $\eta = -0.45$ has been done.

The e/h ratio of a sampling calorimeter with an iron-scintillator structure is expected to be > 1 for the conventional orientation of tiles perpendicular to incident hadrons. The results are presented in table 4.30. The e/h value is greater for η = -0.35 than for other $\eta' s$. That could be explained because the shower is better contained for η = -0.55

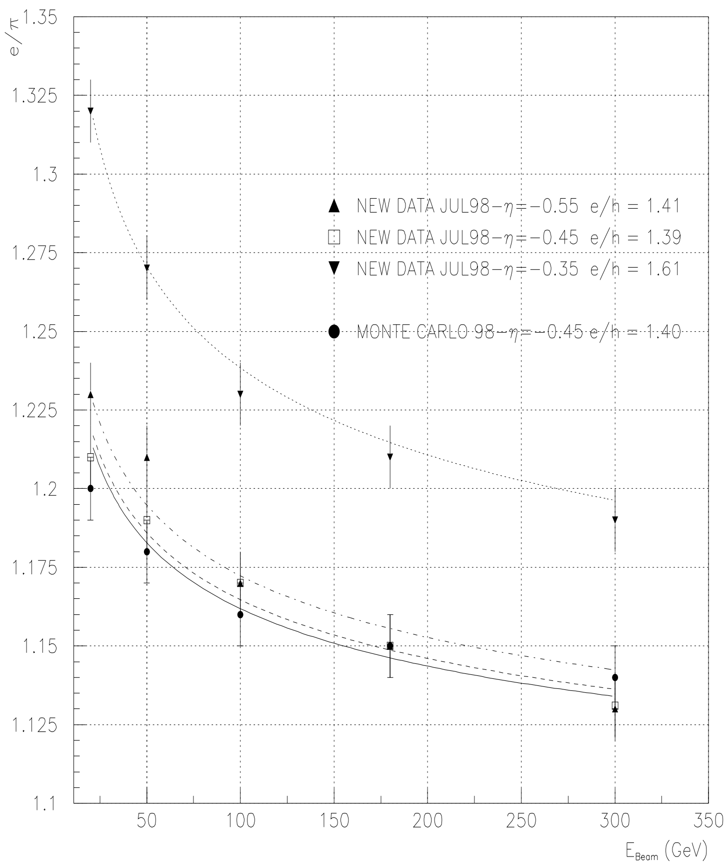

Figure 4.54: *The e/π ratio as a function of the beam energy for the Barrel Module 0 tested in the 1998 test beam at three different η's.The lines are the fits of the equation (4.16). The comparison for Monte Carlo data at η=-0.45 is also plotted.*

than for η = -0.35. Deviations from $e/h = 1$ contribute to the constant term in the energy resolution (see equation 4.7). This constant term is about 5.33 for η = -0.35 and 4.87 for η = -0.55.

The value $e/h = 1.39$ corresponding to η = -0.45 is in good agreement with the 1.36 obtained from previous precise studies and reported in the TDR [17].

Table 4.30: *The values of the e/h ratio for the Barrel module 0 at three differents η's using the equation (4.16). Also the Monte Carlo simulation, at η=-0.45 is given in the table.*

Module	η	e/h
M0	-0.35	1.61 $\pm$0.015
M0	-0.45	1.39 $\pm$0.012
M0	-0.55	1.41 $\pm$0.012
M. C.	-0.45	1.40 $\pm$0.013

4.6 Comparison between Extended Barrel and Barrel Module 0

Two Extended Barrel Modules 0 were exposed in 1997 to the calibration beams, the first was built in Barcelona (BCN), Spain, and the other at Argonne, USA. One Barrel Module 0 was exposed in 1998 to the calibrations beams.

The H1 weighting technique has been studied for both test beams. The table 4.31 shows the results obtained for the energy resolution after applying the H1 weighting technique to 1997 and 1998 test beam.

The average resolution for Extended Barrel is $\frac{\sigma}{E} = \frac{45.6\%}{\sqrt{E}} \oplus 3.0\% \oplus \frac{0.06}{E}$ and for the Barrel is $\frac{\sigma}{E} = \frac{42.7\%}{\sqrt{E}} \oplus 5.0\% \oplus \frac{0.06}{E}$. The statistical term is similar in the two cases and it is less than 50% (Hadronic calorimeter requirements [28]). The constant term is less in the Extedend Barrel than in the Barrel. As this term is related with the leakage, we can say that the Barrel Module 0 has more leakage than the Extended Barrel Modules 0 because the η values are higher than in the Barrel. For the Extended Barrel this term has a value around 3% (inside of the requirements) and for the barrel 5% (outside of the requirements).

The tables 4.32 and 4.33 show the *rms* for both Extended Barrel modules and for the Barrel Module 0 after applying the H1 weighting technique.

Table 4.31: *The statistical and constant term from the resolution curves for the two Extended Barrel modules (1997 test beam) and for the Barrel module 0 (1998 test beam) at differents η's .*

MODULE	η	a %	b %
BCN	-1.1	45.6 $\pm$ 0.7	2.71 $\pm$ 0.07
ANL	-1.1	47.8 $\pm$ 0.6	2.25 $\pm$ 0.06
BCN	-1.2	45.2 $\pm$ 0.7	3.10 $\pm$ 0.07
ANL	-1.2	43.7 $\pm$ 1.0	3.91 $\pm$ 0.07
M0	-0.25	41.1 $\pm$ 1.3	5.68 $\pm$ 0.08
M0	-0.35	40.7 $\pm$ 1.2	5.33 $\pm$ 0.08
M0	-0.45	45.9 $\pm$ 1.0	4.22 $\pm$ 0.08
M0	-0.55	43.2 $\pm$ 1.0	4.87 $\pm$ 0.10

Table 4.32: *The rms for both Extended Barrel modules and two values of η.*

η	-1.1	-1.2
BCN RMS (%)	1.2	3.0
ANL RMS (%)	1.8	2.9

The average *rms* for Extended Barrel modules is 2.2% and for the Barrel module is 1.5%. The linearity requirements for the hadronic calorimeter come from the study of quark compositness where the jet energy scale has to be linear within 2% up to a transverse energy of 4 TeV. The *rms* from the Barrel is less than this value.

The *e/h* ratio is very similar for both calorimeter prototipes (around 1.4) and there is a good agreement with previous precise studies and the Monte Carlo simulation. In the BCN extended barrel module, the *e/h* value increases when the shower is worse contained, and for the Barrel Module 0 we obtain the same behaviour [29].

Table 4.33: *The rms for the Barrel Module 0 at four different η's.*

η	-0.25	-0.35	-0.45	-0.55
RMS (%)	1.4	1.8	0.8	2.0

Bibliography

[1] R. Brun and F. Carminati, GEANT Detector Description and Simulation Tool, CERN Program Library, Long Writeup W5013, September 1993.

[2] C. Zeitnitz et al., The GEANT-CALOR Interface user's guide, CERN, AUG. 1995.

[3] S. Agnvall et al., Evaluation of FERMI Read-out of the ATLAS Tilecal Prototype, Nucl. Instr. and Meth. A403 (1998) 98-114.

[4] http://evalu20.ific.uv.es/sgonzale/cuts.html. Private comunication with B. Di Girolamo.

[5] N. Del Prete, F. Spanò, Cross-talk coefficients from muon data analysis, November 1997 AW; S. Burdin, Cross-talk coefficients determination from muon data analysis, March 1998 AW; S. Bravo, Cs data analysis, November 1997 AW; S. Nemecek, Cross-talk coeffcients from electrons data analysis, November 1997 and March 1998 AW.

[6] M. Cobal et al., Analysis of the first combined test of the LArgon and TILECAL barrel calorimeter prototypes, ATLAS Internal Note, TILECAL-No-67 (1995).

[7] H. Abramowicz et al., Nucl. Inst. and Meth. A180 (1981) 429.

[8] Private comunication with J. Kerstin.

[9] H1 Calorimeter Group, W. Braunschweig et al., DESY Internal report, DESY 89-022 (1989).

[10] F. Ariztizabal et al., Nucl. Inst. and Meth. A349 (1994) 384.

[11] A. E. Kiryunin, Study of the Hadron Energy Resolution of a Liquid Argon Calorimeter by Applying the H1 weighting technique, ATLAS Internal Note CAL-NO-016 (1993).

[12] H1 Calorimeter Group, B. Andrieu et al., Results from Pion Calibration Runs for the H1 Liquid Argon Calorimeter and Comparisons with Simulations, DESY internal report, DESY 93-047 (1993).

[13] M. P. Casado et al., ATLAS Internal Note TILECAL-NO-75 (1996).

[14] J. A. Budagov et al., Electron Response and e/h Ratio of ATLAS Iron-Scintillator Hadron Prototype Calorimeter with longitudinal Tile Configuration, Atlas Internal Note 02-02-1996.

[15] R. Wigmans, Nucl. Instr. and Meth. A265 (1988) 273.

[16] R. Wigmans, Nucl. Instr. and Meth. A259 (1987) 273.

[17] Tile Hadronic Calorimeter TDR, CERN/LHCC 96-42 (1996).

[18] DICE manual Version 0.10, CERN, Switzerland, Feb. 1995.

[19] M. Nessi et al., ATLAS Internal Note SOFT-NO-16 (1994).

[20] Comparison between the ATLAS/TileCal hadron barrel calorimeter prototype test beam data and Hadronic Simulation packge. I. Efthymiopoulos, 28-10-1996.

[21] M. Metcalf, Effective FORTRAN 77, CERN, Geneva, Switzerland

[22] J. Shiers et al., ZEBRA System, CERN Program Library, Long Writeup Q100/Q101, February 1995

[23] T. Sjostrand, High-Energy-Physics Event Generation with PYTHIA 5.7 and JETSET 7.4, CERN preprint CERN-TH.7111/93 and CERN-TH.7112/93.

[24] G. Marchesini et al., Comput. Phys. Commnu. 67 (1992) 465.

[25] F. E. Paige and S. D. Protopopescu, Manual ISAJET 7.13.

[26] C. W. Fabjan, CERN-PPE-94-61 (1994).

[27] F. Camarena et al., ATLAS Internal Note TILECAL-NO-99-001 (1999); F. Camarena, Estudios sobre el "Módulo 0" del TILECAL de ATLAS, tesis de licenciatura, Enero 1999.

[28] Calorimeter Performance, CERN/LHCC 96-40 (1997).

[29] Y. A. Kulchitsky et al., ATLAS Internal Note TILECAL-99-002 (1999).

[30] V. Castillo and S. González, ATLAS Internal Note TILECAL-99-020 (1999).

Chapter 5

Higgs decay to top quarks at hadron colliders

In this chapter we consider a Higgs boson search, with zero or suppressed coupling to the weak vector bosons, via its decay to $t\bar{t}$ in a possible extension of the Standard Model (SM), the Minimal Supersymmetric Standard Model (MSSM). The Higgs particle is copiously produced at hadron colliders through gluon-gluon collisions, via virtual top-quark loop [1], as shown in figure 5.1(a). However, at a hadron collider there is a large irreducible background from the QCD production of top quarks, shown in figure 5.1(b). The signal, $gg \to H \to t\bar{t}$, and the background $gg \to t\bar{t}$ interfere, generically resulting in a peak-dip structure at the Higgs mass [2]. In some cases the dip dominates, such that the signal for the presence of the Higgs boson is a small *deficit* in the production of $t\bar{t}$ pairs of invariant mass near the Higgs mass.

The MSSM model necessarily needs two Higgs doublets [3], one which couples to fermions with $T_{3L} = +1/2$ and the other which couples to fermions with $T_{3L} = -1/2$. At the tree level, all Higgs boson masses and couplings can be expressed in terms of only two parameters, for example m_A, the mass of the CP-odd boson, and tanβ, the ratio of the vacuum expectation values of the Higgs doublets. A complete study is therefore more complicated than in the SM, where the only free parameter in the Higgs sector is the Higgs mass. In addition, when considering production and decay of Higgs bosons, the whole particle spectrum of the model has to be taken into account, since the R-odd particles (squarks, sleptons, gauginos, higgsinos) can also play an important role. The production or decay processes that correspond to the tree-level diagrams can be obtained from the corresponding formulae for the SM Higgs boson by simply multiplying the various amplitudes by the appropriate supersymmetric correction factors.

QCD corrections are partially taken into account by including running quark masses

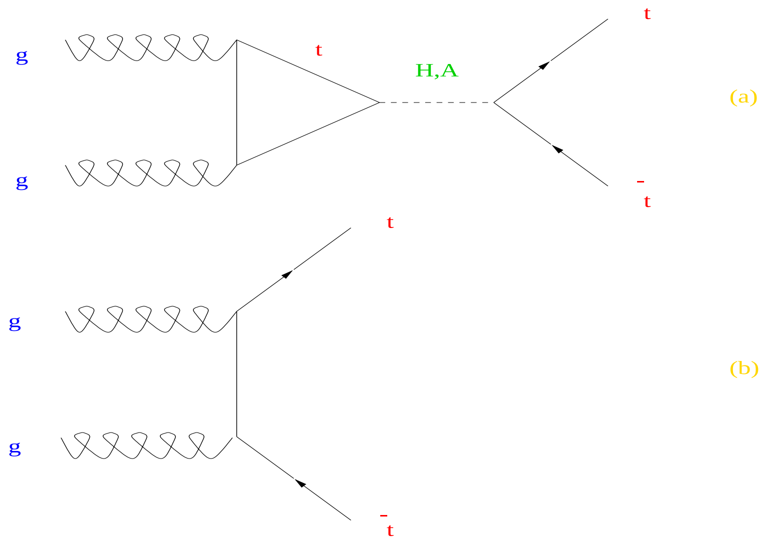

Figure 5.1: *Feynman diagrams for $gg \to t\bar{t}$: (a) s-channel Higgs scalar (H) or pseudoscalar (A) exchange via top-quark loop, (b) leading-order QCD (u- channel and s-channel diagrams not shown).*

in the calculations of branching ratios, and it is assumed that all supersymmetric particles are heavy enough not to play an important role in the phenomenology of MSSM Higgs boson decays. In addition, negligible mixing in the stop and sbottom mass matrices is assumed, and the higgsino mass parameter $|\mu|$ is assumed to be negligible in comparison with the SUSY scale.

In contrast to the SM case, the MSSM Higgs sector is quite sensitive to the value of m_t. The main uncertainty in the predictions for the MSSM Higgs sector arises from the present experimental uncertainty of $\sim \pm$ 15 GeV [4] on the top-quark mass m_t. For a consistent comparison with studies performed for LEP2 [5], a central value of $m_t = 175$ GeV is used throughout this chapter.

Because of the strong coupling of the SM Higgs boson to gauge boson pairs, (see figure 5.2), the $H \to t\bar{t}$ branching ratio for this channel is too small to be observable in the SM case. In The MSSM case, the pseudoscalar Higgs boson does not couple to the weak vector bosons. If this pseudoscalar is relatively heavy, the heavier Higgs scalar couples only weakly to the weak vector bosons. This is true regard less of the ratio of vacuum-expectation values of the two Higgs doublets. The $H \to t\bar{t}$ and $A \to t\bar{t}$ branching ratios are close to 100% for m_H, $m_A > 2m_t$ and for tan$\beta \sim 1$ (see figure 5.3).

The results considered in this chapter are generic to the scenario where the dominant decay of the Higgs boson is to top quarks. If the ratio of vacuum-expectation values is much larger than unity, the coupling of H to top quark is suppressed and its coupling to the bottom quark enhanced (see figure 5.3), such that the production of the Higgs

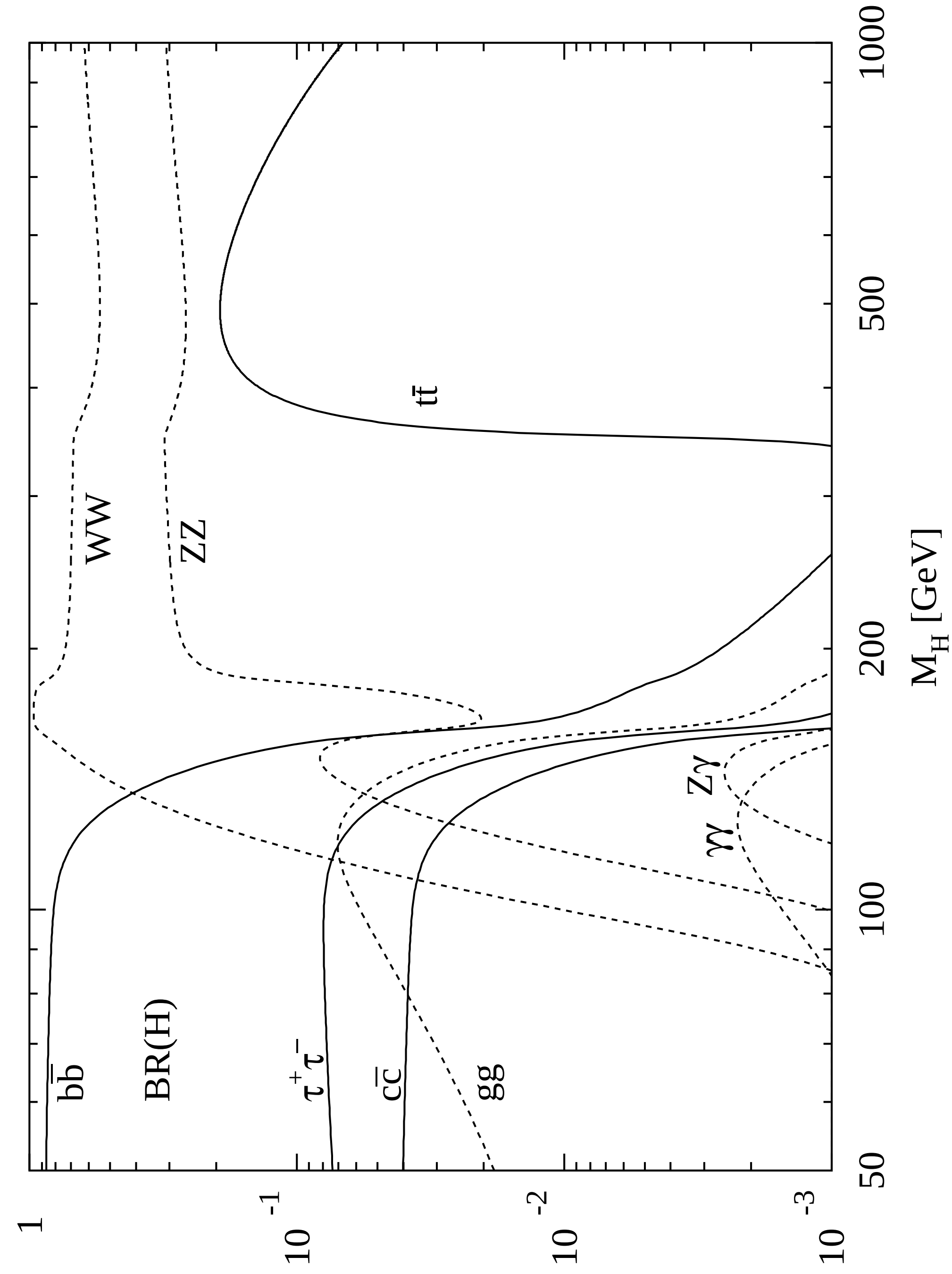

Figure 5.2: *Branching ratios of the dominant decay modes of the SM Higgs particle. All relevant higher-order corrections are taken into account.*

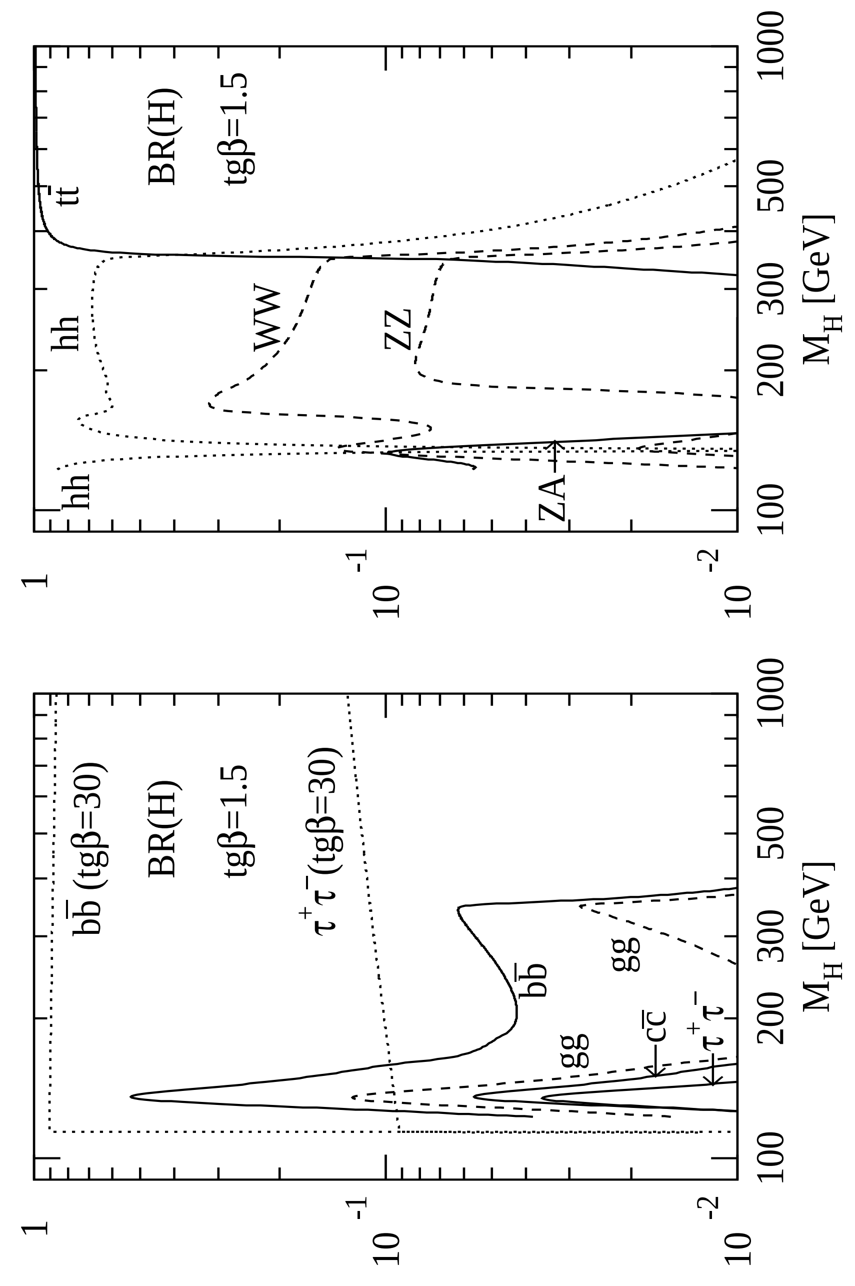

Figure 5.3: *Branching ratios of the MSSM Higgs boson H for non-SUSY decay modes as a function of the mass for two values of tgβ = 1.5, 30 and vanishing mixing. The common squark mass has been chosen as M_s = 1 TeV.*

via a bottom-quark loop, and its decay to $b\bar{b}$, become non-neglibible.

The differential cross section for $gg \to t\bar{t}$, including the squares of the scalar-Higgs amplitude and the continuum QCD amplitude, as well as the interference of the two amplitudes, is [6]:

$$\frac{d\sigma}{dz} = \frac{\alpha_s^2 G_F^2 m^2 s^2}{1536\pi^3} \times \beta^3 \left|\frac{N(s/m^2)}{s - m_H^2 + i m_H \Gamma_H(s)}\right|^2 \tag{5.1}$$
$$-\frac{\alpha_s^2 G_F^2 m^2 s \beta^3}{384\pi\sqrt{2}} \times \left(\frac{1}{p_1 \cdot p_3} + \frac{1}{p_2 \cdot p_3}\right)$$
$$\times Re\left[\frac{N(s/m^2)}{s - m_H^2 + i m_H \Gamma_H(s)}\right]$$
$$+\frac{d\sigma_{QCD}}{dz}$$

where $p_{1,2}$ are the momenta of the incoming gluons, $p_{3,4}$ are the outgoing top-quark and top-antiquark momenta, z is the cosine of the scattering angle between an incoming gluon and the top quark, m is the top-quark mass and β is the velocity of the top quark and top antiquark in the center-of-momentum frame. The *dot* products of the four momenta are:

$$p_1 \cdot p_2 = \frac{1}{4} s(1 - \beta z) \tag{5.2}$$
$$p_2 \cdot p_3 = \frac{1}{4} s(1 + \beta z).$$

The function associated with the virtual top-quark loop is:

$$N(s/m^2) = \frac{3}{2}\frac{m^2}{s}\left[4 - \left(1 - \frac{4m^2}{s}\right) I(s/m^2)\right] \tag{5.3}$$

where

$$I(s/m^2) = \left[ln\frac{1+\beta}{1-\beta} - i\pi\right]^2 \qquad (s > 4m^2). \tag{5.4}$$

The energy-dependent Higgs width is:

$$m_H \Gamma_H(s) = \frac{3 G_F m^2 s}{4\pi\sqrt{2}} \beta^3 \tag{5.5}$$

The cross-section for the continuum QCD production of $gg \to t\bar{t}$ is [7]:

$$\frac{d\sigma_{QCD}}{dz} = \frac{\pi\alpha_s^2}{12s}\beta(\frac{s^2}{p1\cdot p3\ p2\cdot p3} - 9) \tag{5.6}$$
$$\times[\frac{(p_1\cdot p_3)^2}{s^2} + \frac{(p_2\cdot p_3)^2}{s^2} + \frac{m^2}{s} - \frac{m^4}{4p_1\cdot p_3\ p_2\cdot p_3}].$$

Figure 5.4 shows the cross-section for $gg \to t\bar{t}$ as a function of the $t\bar{t}$ invariant mass, for $m_t = 170$ GeV and $m_H = 400$, 500, 600, 700, and 800 GeV. For $m_H = 400$ GeV, the presence of the Higgs boson produces a peak, followed by a dip, near the Higgs mass. For larger Higgs masses the peak is absent, and the Higgs reveals itself as a dip in the $t\bar{t}$ invariant-mass spectrum. For $m_H = 500$ GeV, the total top-quark cross-section differs little from the cross-section with no Higgs present, due to the cancellation between the peak and the dip. For larger Higgs masses, the presence of the Higgs results in a small decrease in the total top-quark cross-section.

The effect of the pseudoscalar Higgs boson A on the $t\bar{t}$ invariant-mass spectrum is also considered. The $H \to t\bar{t}$ and $A \to t\bar{t}$ decays cannot be distinguished experimentally from each other, since the H- and A-bosons are almost degenerated in mass in the relevant region of parameter space (m_A, tanβ). This particle does not couple to the weak vector bosons, and couples to the top quark (see figure 5.5) with standard-model strength if the ratio of the vacuum-expectation values of the two Higgs doublets is close to unity. For larger values of this ratio, the pseudoscalar Higgs coupling to top quarks is suppressed (see figure 5.5), so its width is narrower. The production of the pseudoscalar Higgs via a bottom-quark loop and the decay to $b\bar{b}$ may also become significant, reducing the branching ratio to $t\bar{t}$ and the effect of the Higgs on top-quark production. However, the pseudoscalar Higgs does not couple to weak vector bosons in a generic two-Higgs-doublet model, so there is no competition from the decay to weak vector bosons.

The cross sections, given in figure 5.4 are qualitatively similar to the cross sections for the pseudoscalar Higgs. The energy dependent Higgs width is :

$$m_A\Gamma_A(s) = \frac{3G_F m^2 s}{4\pi\sqrt{2}}\beta. \tag{5.7}$$

The pseudoscalar-Higgs width is suppressed by β, rather than β^3 as is the scalar-Higgs width, so the pseudoscalar Higgs boson is noticeably wider than the scalar Higgs boson for $m_{H/A} = 400$ and 500 GeV.

The peak-dip structure in the $t\bar{t}$ invariant-mass spectrum due to the scalar or pseudoscalar Higgs bosons can be viewed as due to a final-state interaction of the $t\bar{t}$ [8], [9].

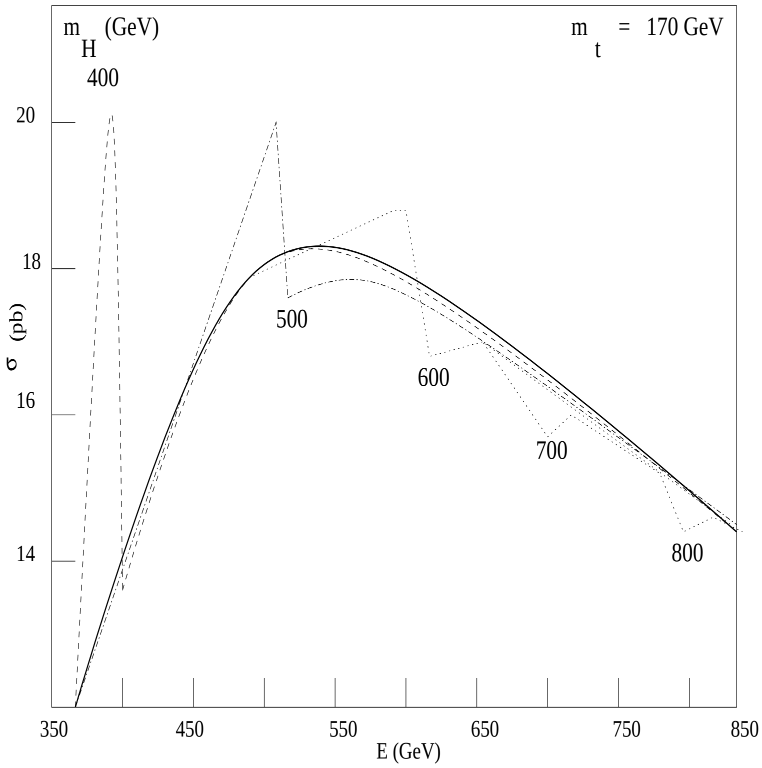

Figure 5.4: *Total cross-section for $g \to t\bar{t}$, for m_t = 170 GeV, as a fuction of the $t\bar{t}$ invariant mass. The calculation includes the effects of the heavy Higgs scalar (H) of the minimal supersymetric model (with the ratio of the vacuum-expectation values of the two Higgs doublets close to unity), as well as the continuum QCD production of $t\bar{t}$, for m_H = 400, 500, 600, 700, and 800 GeV.*

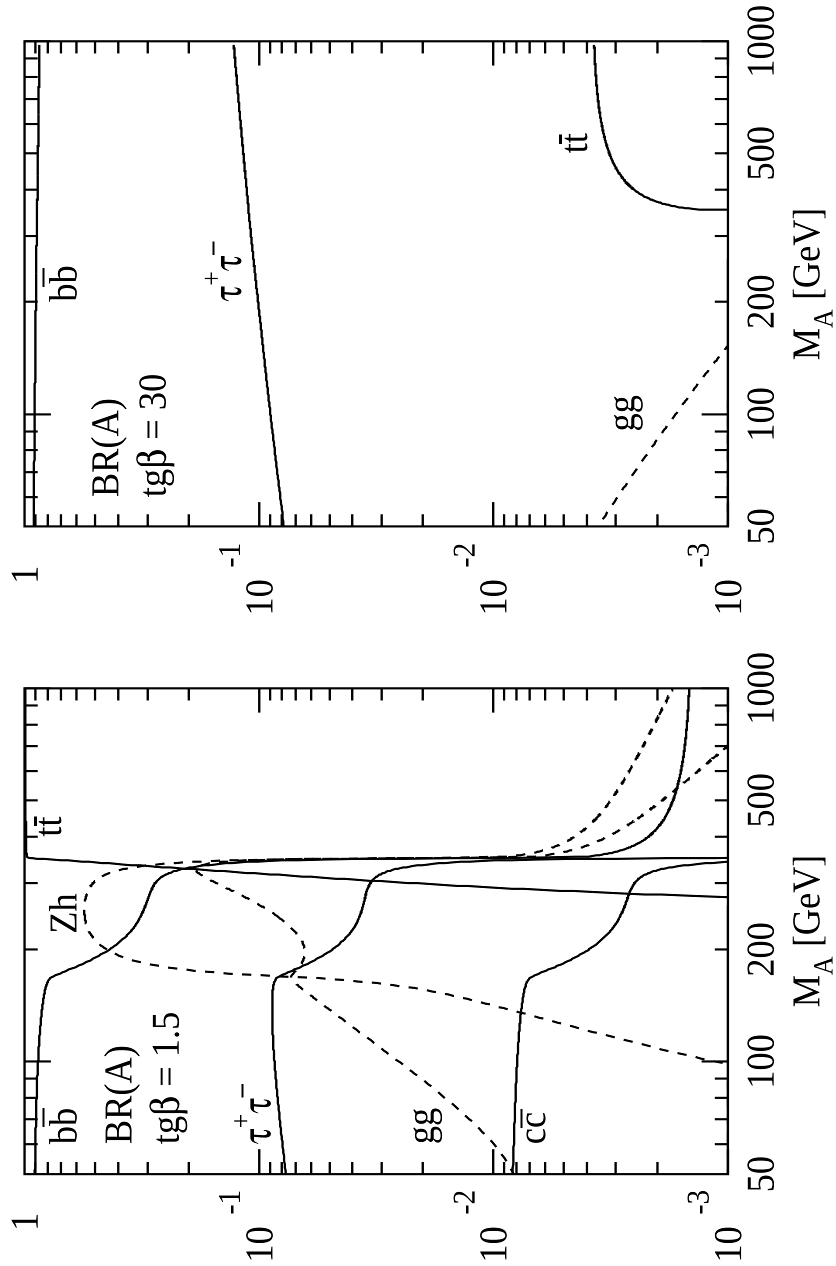

Figure 5.5: *Branching ratios of the MSSM Higgs boson A for non-SUSY decay modes as a function of the mass for two values of tgβ = 1.5, 30 and vanishing mixing. The common squark mass has been chosen as M_s = 1 TeV.*

Physics processes, including initial- and final-state radiation, hadronisation, and decays, were simulated using PYTHIA 5.7 [10] at $\sqrt{s} = 14$ TeV and with its default set of structure function parametrisations. However, large uncertainties in the signal and background cross-sections production remain, due to higher-order corrections, structure function parametrisations, as well as the models used for full event generation. In addition, despite the existence of many higher-order QCD correction (K-factor) calculations, not all processes of interest at the Large Hadron Collider (LHC) have benefited from this theoretical effort. Therefore, the present chapter has consistently and conservatively avoided the use of K-factors, resorting to lowest-order predictions for both signal and backgrounds.

The results presented here come predominantly from ATLFAST [11] simulation, such as the mass resolutions, reconstruction/identification efficiencies and signal and background rates. Also a comparison with a full simulation of ATLAS detector has been done in order to check in detail the detector performances. The systematic studies presented in this chapter allow definite conclusions to be drawn concerning the ATLAS discovery potential over the whole (m_A, tanβ) parameter space in the channel $H/A \to t\bar{t}$.

Theoretical and experimental uncertainties may change the positions of discovery curves in a significant way; the dominant theoretical ones are:

- the top-quark mass m_t,
- the MSSM parameters,
- the mass spectrum of SUSY particles,
- the K-factor corrections to signal and background production,
- the structure function parametrisations,
- the higher-order radiative corrections to the MSSM Higgs boson masses and couplings.

This chapter is organised as follows: subsections 5.1 and 5.2 quantify the general properties of the MSSM model; in particular, the relations between the Higgs boson masses, coupling, widths, production cross-sections and branching ratios are discussed as well as the expected rates at LHC for the interesting channel. SM predictions are also shown, in order to shed light on the differences or similarities between the two models. Subsection 5.3 describes the automatic procedure used to produce the physics events. Subsection 5.4 discusses the observability of the decay channel, summarising in a systematic way the signal and background rates as well as the expected significances at low and high luminosities. Numbers are quoted for a few mass values. The 5σ-discovery contour curves are presented for the decay channel in the (m_A, tanβ) plane, for the value of $m_t = 175$ GeV and for the low integrated luminosity. Subsection 5.5

documents the performed comparison between full simulation and a fast simulation of the ATLAS detector for complete physics events with Higgs bosons production. Finally a review of the discovery potential of the ATLAS detector for SM and MSSM Higgs boson is done in subsection 5.6.

5.1 Masses, couplings and widths

At the tree level, all Higgs boson masses and couplings can be expressed in terms of only two parameters, for example m_A and tanβ. The following relations can be used:

$$m_{H,h}^2 = \frac{1}{2}[m_A^2 + m_Z^2 \pm \sqrt{(m_A^2 + m_Z^2)^2 - 4m_A^2 m_Z^2 cos^2 2\beta}] \tag{5.8}$$

$$m_{H^\pm}^2 = m_W^2 + m_A^2 \tag{5.9}$$

The mixing angle α ($-\frac{\pi}{2} < \alpha < 0$) required to diagonalise the Higgs mass matrix is given by the following expression:

$$cos2\alpha = -cos2\beta \, \frac{m_A^2 - m_Z^2}{m_H^2 - m_h^2}. \tag{5.10}$$

These tree-level formulae for the Higgs-boson masses and couplings are however subject to large radiative corrections, dominated by the exchange of virtual top and bottom quarks and squarks in the loop diagrams. They introduce a dependence on the top and squark masses and on the mixing in the stop-sbottom mass matrices into the formulae for the Higgs masses and couplings (see e.g. [12]).

When considering MSSM Higgs boson production and decay, the most important part of these radiative corrections is taken into account by using corrected formulae for the mass matrix and then determining α from the input parameters. Coupling to fermions/gauge bosons can still be expressed in terms of the fermion/gauge boson masses and of the angles β and α. In this chapter one always assumes that all SUSY particles masses are at 1 TeV, therefore the mixing in the stop and sbottom mass matrices is negligible and the value of the Higgsino-mass term $|\mu|$ is much smaller than M_{SUSY}.

The consequence of these radiative corrections is that the expressions for m_h and m_H now depend on m_t. In particular, the maximum allowed value of m_h is shifted upwards by a factor proportional to the fourth power of m_t. This explains why the tree-level predictions for m_h are considerably affected by the radiative corrections for large values of m_t. In Tables 5.1 and 5.2 the two-loop numerical values of the MSSM Higgs-bosons masses are given for m_t = 150, 175 and 200 GeV and tanβ = 3 and 30 as a function of m_A.

Table 5.1: Dependence of m_H on m_A for tanβ = 3 and m_t = 150, 175, and 200 GeV.

m_A (GeV)	m_H (GeV)		
	m_t = 150 GeV	m_t = 175 GeV	m_t = 200 GeV
80.0	115.8	123.5	135.5
100.0	125.9	131.6	141.3
160.0	172.5	174.4	177.8
200.0	209.0	210.3	212.3
280.0	286.0	286.6	287.5
320.0	325.2	325.6	326.4
360.0	364.5	364.9	365.5
400.0	404.0	404.3	404.8
500.0	503.2	503.4	503.8

Table 5.2: Dependence of m_H on m_A for tanβ = 30 and m_t = 150, 175, and 200 GeV

m_A (GeV)	m_H (GeV)		
	m_t = 150 GeV	m_t = 175 GeV	m_t = 200 GeV
80.0	103.0	113.1	126.7
100.0	104.6	113.5	126.9
160.0	160.2	160.2	160.3
200.0	200.1	200.1	200.2
280.0	280.1	280.1	280.1
320.0	320.1	320.1	320.1
360.0	360.1	360.1	360.1
400.0	400.0	400.0	400.0
500.0	500.0	500.0	500.0

The dependence of m_H on m_t is very weak and limited to small values of m_A (m_A < 200 GeV).

Figure 5.6 presents the correction factors to the MSSM *H*-boson couplings relative to the SM couplings to fermions and massive gauge bosons as a function of m_A (left side) and of m_H (right side), for m_t = 175 GeV and for different values of tanβ.

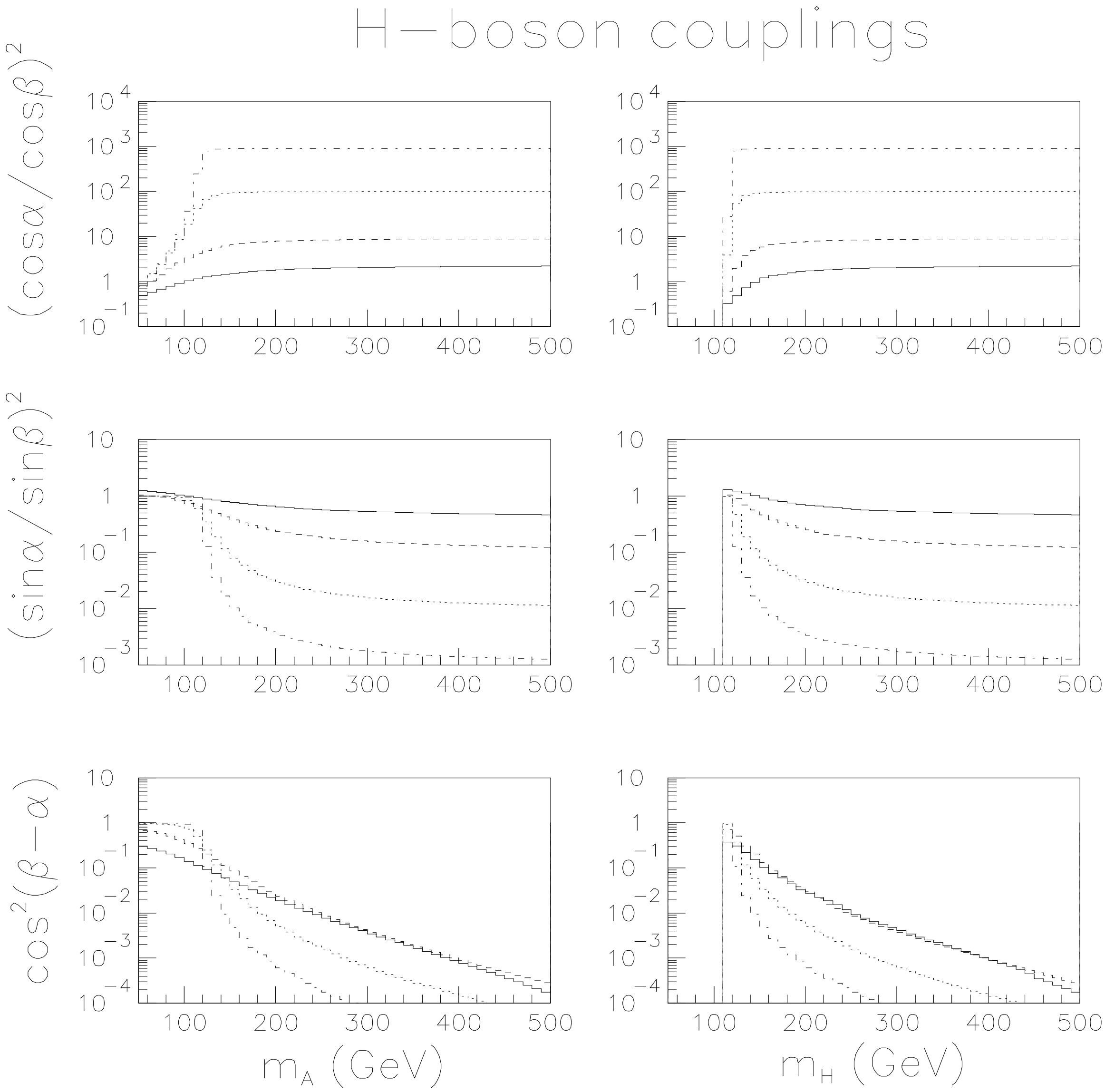

Figure 5.6: *The two-loop predictions for the MSSM correction factors to the H-boson coupling to fermions and massive gauge bosons as a function of m_A (left side) and of m_H (right side) for m_t = 175 GeV and for different values of tanβ. The solid lines are for tanβ = 1.5, the dashed lines for tanβ = 3.0, the dotted lines for tanβ = 10.0 and the dot-dashed lines for tanβ = 30.0.*

The couplings of the MSSM H-boson to down-type quarks and leptons are strongly enhanced with respect to the SM couplings over a large region of the parameter space (tanβ > 10 and m_A > 100 GeV). Over this region, the couplings of the H-boson to up-type quarks are strongly suppressed; those to massive gauge bosons are even more strongly suppressed, for all values of tanβ and for almost all values of m_A (m_A > 120 GeV).

The total decay widths of the MSSM Higgs bosons all differ significantly from that of a SM Higgs boson of the same mass. Tables 5.3 and 5.4 show how these widths vary as a function of mass and of tanβ, for m_t = 175 GeV and for H and A respectively. For comparison, the corresponding width of a SM Higgs boson of the same mass is also given [13].

Table 5.3: Total decay width of the H-boson for m_t = 175 GeV.

m_H	Γ_H^{tot} (GeV) SM Higgs	Γ_H^{tot} (GeV) tanβ=3	Γ_H^{tot} (GeV) tanβ=10.0	Γ_H^{tot} (GeV) tanβ = 30.0	Γ_H^{tot} (GeV) tanβ = 50.0
120.0	0.004	0.005	0.126	2.291	6.84
130.0	0.004	0.010	0.232	2.690	7.90
150.0	0.02	0.073	0.392	3.594	10.00
200.0	1.37	0.249	0.508	4.451	12.37
250.0	4.10	0.268	0.615	5.298	14.71
300.0	8.42	0.255	0.705	6.122	17.00
350.0	15.6	0.400	0.807	6.915	19.20
400.0	27.8	0.845	0.933	7.698	21.36
450.0	45.2	1.335	1.061	8.472	23.50
500.0	63.6	1.594	1.128	8.873	24.61

Table 5.4: Total decay width of the A-boson for m_t = 175 GeV.

m_A	Γ_A^{tot} (GeV) SM Higgs	Γ_A^{tot} (GeV) tanβ=3	Γ_A^{tot} (GeV) tanβ=10.0	Γ_A^{tot} (GeV) tanβ = 30.0	Γ_A^{tot} (GeV) tanβ = 50.0
100.0	0.004	0.023	0.252	2.270	6.305
150.0	0.02	0.032	0.353	3.179	8.831
200.0	1.37	0.043	0.450	4.050	11.24
250.0	4.10	0.062	0.545	4.890	13.58
300.0	8.42	0.072	0.637	5.711	15.86
350.0	15.6	0.084	0.726	6.516	18.10
400.0	27.8	1.402	0.932	7.321	20.30
450.0	45.2	2.012	1.073	8.108	22.47
500.0	63.6	2.520	1.204	8.883	24.62

The decay widths of the H-boson and A-boson are very similar for $m_H = m_A$. They become large, 3 to 25 GeV, for large values of m_H, m_A and of tanβ, and will have to be taken into account when studying the accessible channels in this region of parameter space. For small values of tanβ, the H-boson width is much smaller than the corresponding one to the SM Higgs boson mass.

5.2 Branching ratios, cross-sections and rates

5.2.1 H-boson

The H-boson is the heavier of the CP-even MSSM neutral Higgs bosons: the mass range of interest goes from 110 to 500 GeV. Over this mass range, the SM Higgs boson can be discovered mainly through $H \to ZZ^{(*)} \to 4l$ decays, but also through $H \to \gamma\gamma$ decays at the lower end of the mass spectrum. However, in the case of the MSSM H-boson, the spectrum of decay channel is richer and varies rapidly with m_A and with tanβ. This is due to the strong suppression of the HZZ coupling, which enhances the branching ratios to other decay channels, such as $H \to \tau\tau$ and $H \to t\bar{t}$.

As shown in figure 5.7, the $H \to t\bar{t}$ channel is the dominant one for low values of tanβ and for $m_H > 2m_t$. This arises again from the strongly suppressed H-boson coupling to gauge bosons. As tanβ increases, the $H \to t\bar{t}$ channel competes with the $H \to b\bar{b}$ decay channel, and its branching ratio is reduced to less than 10% for tan$\beta = 10$.

As discussed in previous section, several processes contribute to the Higgs boson production at the LHC. The H-boson production cross-section is usually calculated as the sum of contributions from the following subprocesses: $gg \to H$, $qq \to qqH$ (W W_{fus}, ZZ_{fus}) and $b\bar{b}H$. Figure 5.8 shows this sum for four values of tanβ and for three values of m_t. The contribution from the $b\bar{b}H$ channel is strongly enhanced for large values of tanβ (note the differences in vertical scale).

Table 5.5 shows the expected rates for the $H \to t\bar{t}$ channel, which is enhanced with respect to the SM case for low values of tanβ. However, the rapid increase of the $H \to b\bar{b}$ branching ratio as tanβ increases, strongly suppresses the discovery potential for this channel for values of tanβ larger than ~ 3.

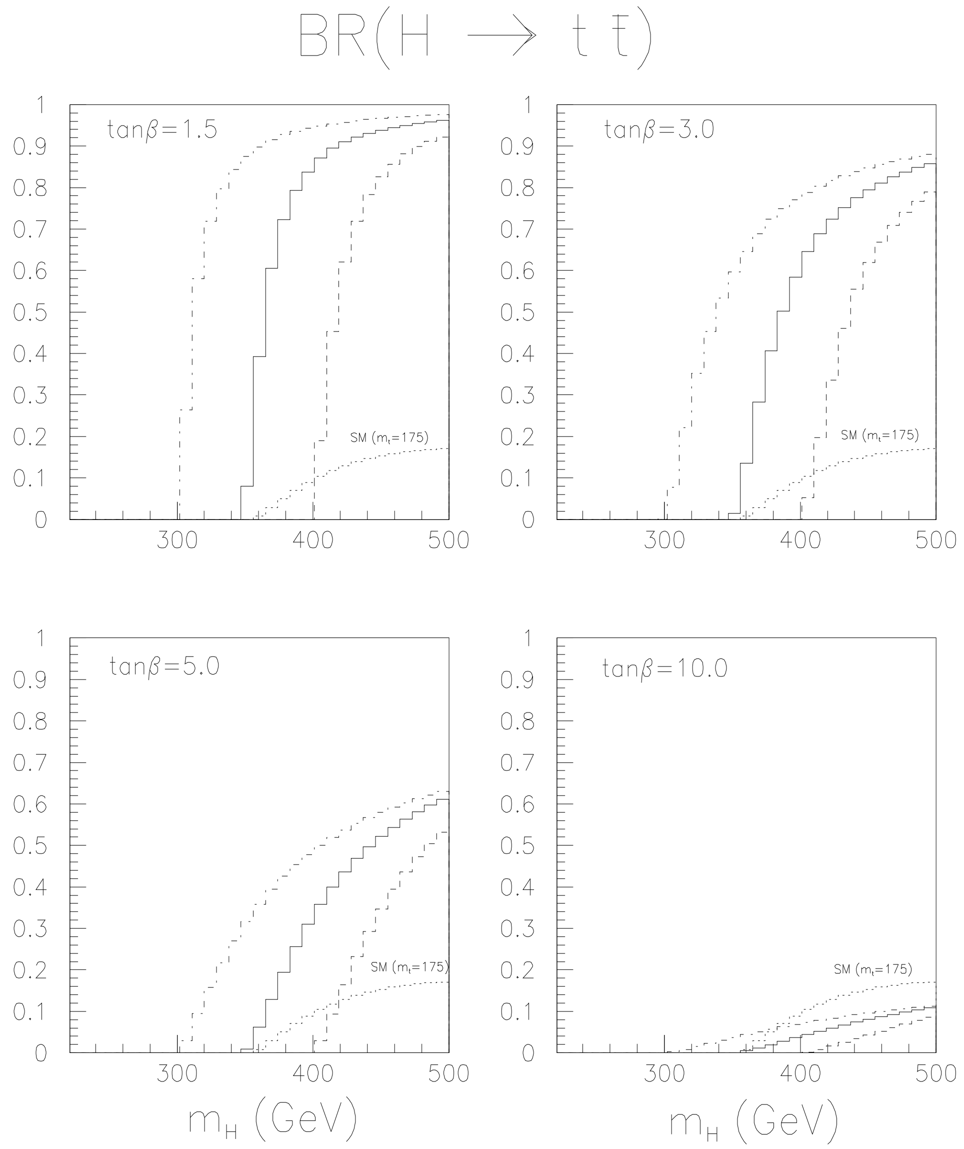

Figure 5.7: *$H \to t\bar{t}$ branching ratio as a function of m_H for four values of tanβ. The solid line is for m_t = 175 GeV, the dashed one for m_t = 200 GeV and the dot-dashed one for m_t = 150 GeV. The figures also show the SM predictions for m_t = 175 GeV (dotted lines).*

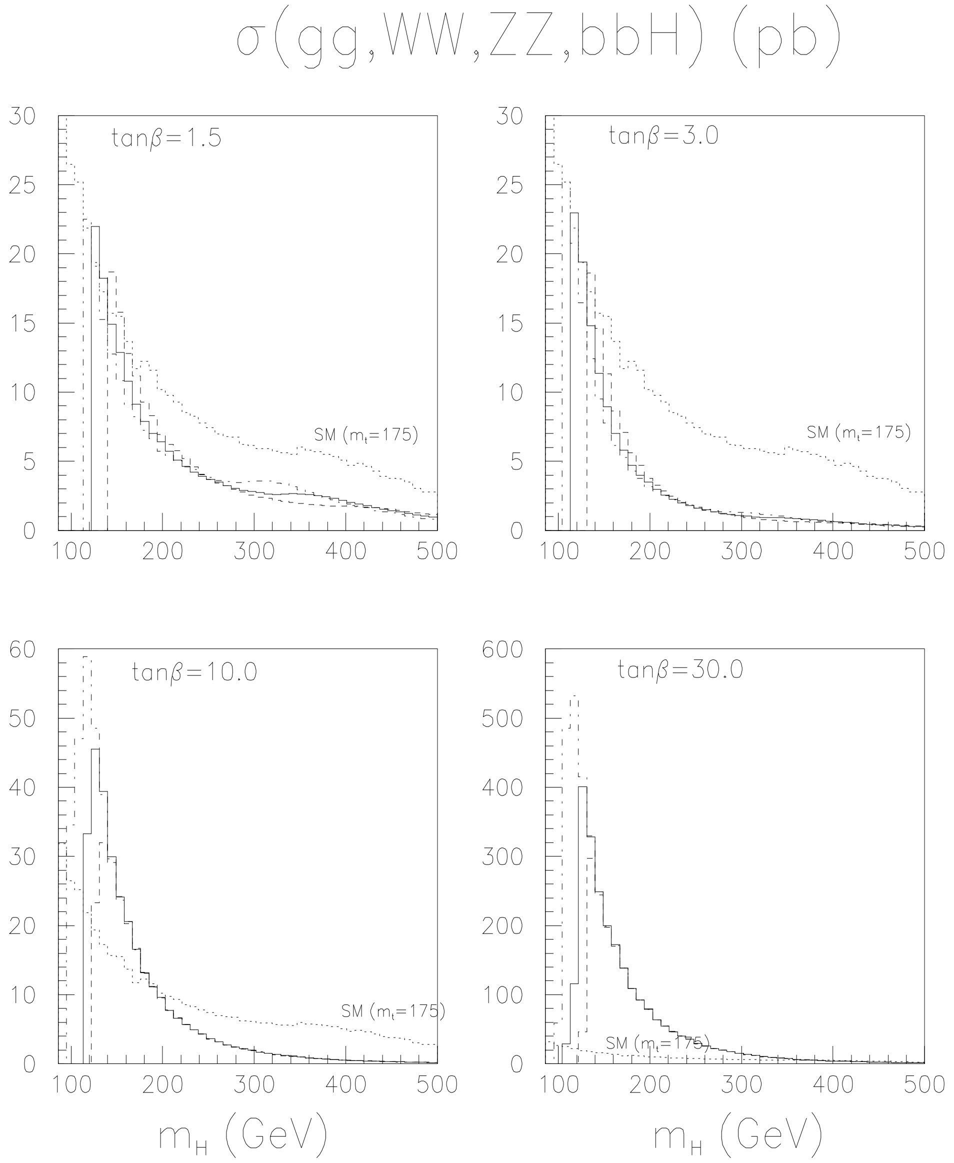

Figure 5.8: *Production cross-section for an H-boson ($gg \to H$, $qq \to qqH$ ($W W_{fus}$, ZZ_{fus}) and $b\bar{b}H$) as a function of m_H for four values of tanβ. The solid line is for m_t = 175 GeV, the dashed one for m_t = 200 GeV and the dot-dashed one for m_t = 150 GeV. The figures also show the SM predictions for m_t = 175 GeV (dotted lines).*

Table 5.5: *Expected rates ($\sigma \times BR$) for $H \rightarrow t\bar{t}$ decays as a function of m_H for m_t = 175 GeV and four different values of tanβ. The corresponding rates in the SM case are also shown.*

m_H (GeV)	$\sigma \times BR(pb)$				
	SM Higgs	MSSM H-boson			
		tan$\beta = 1.5$	tan$\beta = 3.0$	tan$\beta = 5.0$	tan$\beta = 10.0$
370.0	0.10	1.90	0.31	0.03	0.01
400.0	0.23	1.87	0.43	0.06	0.01
450.0	0.26	1.42	0.37	0.05	0.01
500.0	0.21	0.90	0.27	0.04	0.01

5.2.2 A-boson

The CP-odd neutral Higgs boson, or A-boson, is degenerate in mass with the *H*-boson over a large fraction of the (m_A, tanβ) plane. Many of the interesting final states ($t\bar{t}$, $\tau^+\tau^-$, $\mu^+\mu^-$) would therefore be observable for the *H*- and *A*-boson together. The absence of tree-level couplings of the *A*-boson to gauge-boson pairs [13] has an important impact on the predictions discussed below.

As shown in figure 5.9, the $A \rightarrow t\bar{t}$ channel is the dominant one for low values of tanβ and for $m_A > 2m_t$. As tanβ increases, the $A \rightarrow t\bar{t}$ channel competes with $A \rightarrow b\bar{b}$ decay channel, and its branching ratio is reduced to less than 20% for tan$\beta = 10$, where it is close to the SM one.

Due to the absence of *WWA* and *ZZA* couplings, the *A*-boson is produced only through the gg fusion and $b\bar{b}A$ subprocesses. As shown in figure 5.10, the addition of the production cross-sections is larger than the corresponding SM one in most cases. This effect is most visible for values of tanβ larger than ~ 10, where the $b\bar{b}A$ subprocess is dominant. For lower values of tanβ, the $b\bar{b}A$ contribution disappears quickly and the production cross-section decreases quite fast to values well below the SM Higgs cross-sections. The dependence on m_t is weak, but for the lowest values of tanβ, the gg cross-section is enhanced and clear peaks in the production cross-section appear around $2m_t$.

Table 5.6 shows that the expected rates for the $A \rightarrow t\bar{t}$ channel have the same properties as in the case of the *H*-boson. The only noticeable difference is for low values of tanβ, where the larger production cross-section, and to a lesser extent the larger branching ratios, result in larger expected rates.

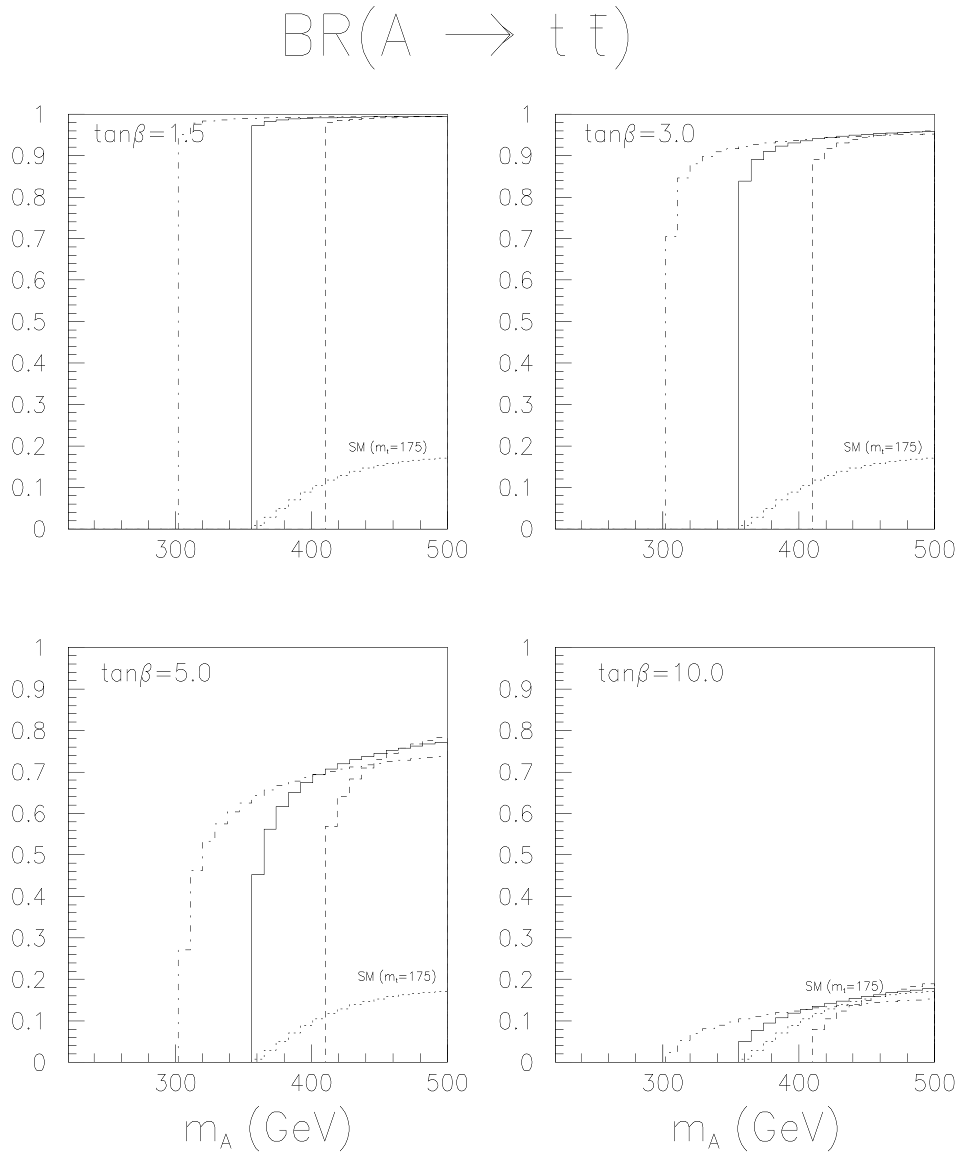

Figure 5.9: *$A \to t\bar{t}$ branching ratio as a function of m_A for four values of tanβ. The solid line is for m_t = 175 GeV, the dashed one for m_t = 200 GeV and the dot-dashed one for m_t = 150 GeV. The figures also show the SM predictions (dotted lines).*

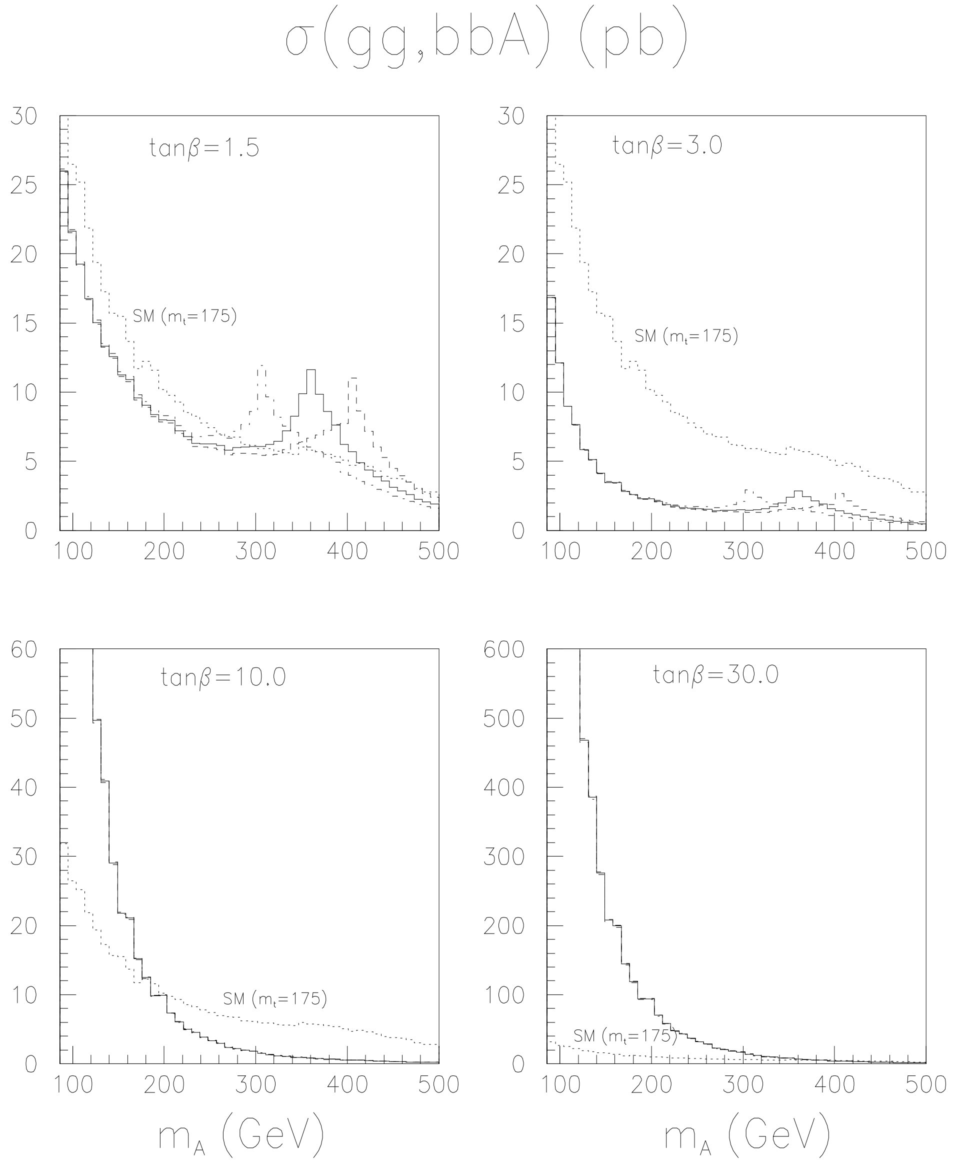

Figure 5.10: *Production cross-section for an A-boson ($gg \to A$, $b\bar{b}A$) as a function of m_A for four values of tanβ. The solid line is for m_t = 175 GeV, the dashed one for m_t = 200 GeV and the dot-dashed one for m_t = 150 GeV. The figures also show the SM predictions for m_t = 175 GeV (dotted lines).*

Table 5.6: *Expected rates ($\sigma \times BR$) for $A \to t\bar{t}$ decays as a function of m_A for m_t = 175 GeV and four different values of tanβ. The corresponding rates in the SM case are also shown.*

m_H (GeV)	$\sigma \times BR(pb)$				
	SM Higgs	MSSM A-boson			
		tan$\beta = 1.5$	tan$\beta = 3.0$	tan$\beta = 5.0$	tan$\beta = 10.0$
370.0	0.10	9.90	2.16	0.55	0.03
400.0	0.23	6.53	1.51	0.45	0.03
450.0	0.26	3.38	0.80	0.27	0.02
500.0	0.21	2.00	0.25	0.15	0.02

5.3 A fast simulation package for ATLAS

Particle-level simulation (ATLFAST [11]) is a kind of intermediate step between simple parton-level analysis of the event topology and very sophisticated and CPU-consuming full detector simulation. It can be done in a more or less complex way but is *never* meant to replace the full simulation of the detector response. However, this kind of simulation is needed for quick and approximate estimates of signal and background rates for specific channels. In addition, fast simulation is the only practical tool for long-statistics studies of complex background processes at the LHC.

This package attempts to reproduce as well as possible the expected ATLAS detector mass resolution for important physics signals, as obtained from full simulation. It does not attempt at present to reproduce accurately the expected efficiencies for lepton and photon isolation, but does attempt to do so for any jet reconstruction efficiency, especially for b-jets, and for the missing E_T resolution. However, for any specific channel, the ATLAS predictions in terms of resolution and reconstruction efficiency, should always be confirmed with full-simulation results.

Not all detector effects can be readily parametrised in fast simulation and only the basic information of the detector geometry is used by the package. This basic information is for example: the η-coverage for precision physics and for the calorimetry, the size of the barrel/endcap transition region for the electromagnetic calorimeter, and the granularity of the calorimeters. No effects related with the detailed shapes of particle showers in the calorimeters and with the charged track multiplicity in jets, etc. are taken into account.

The main goal of the ATLFAST package is to simulate and analyse fully generated events and select isolated leptons and photons, reconstruct jets, label b-jets, c-jets and τ-jets and estimate the missing transverse energy. A more or less accurate parametrisation of photon, electron and muon momentum resolution is included, as well as a parametrisation of the hadronic calorimeter energy resolution and the effect of the ATLAS magnetic field on jet reconstruction. The reconstruction of helix track parameters in the Inner Detector is also provided assuming separate parametrisations of the resolutions for muon, electron and pion tracks.

From the point of view of convenience, it turns out that some properties of the detector are better simulated/analysed at the level of the ntuples created by ATLFAST. For this purpose ATLFAST-B was created, with routines randomly simulating b-, c- and τ-tagging and providing jet-energy recalibration. Therefore, the proposed procedure is to simulate events with ATLFAST and to analyse the results using the ATLFAST-B utilities whenever needed.

The ATLFAST package was used for systematics studies of MSSM Higgs discovery. The package developed for the MSSM Higgs sector consists of three main parts:

- the PYTHIA 5.707 [10] event generator, interfaced to a routine [14], which calculates the MSSM Higgs boson masses and couplings in the two-loop equivalent approximation;

- a set of semi-analytical routines, which calculate the MSSM correction factors to the production cross-sections and the MSSM branching ratios. This part uses the code from [15];

- a set of semi-analytical routines, used to interpolate the expected experimental significances in the (m_A, tanβ) and (m_h, tanβ) planes, and a semi-automatic derivation of the expected 5σ-discovery contour curves.

The generated events were run through a fast simulation of the ATLAS detector in the following way:

- Jets are reconstructed by default for $p_T > 15$ GeV (before rescaling to the original parton energy) and $|\eta| < 5.0$, and isolated leptons are reconstructed for $p_T > 6$ GeV and $|\eta| < 2.5$. Hadronic jets are labelled as true c-jets or b-jets if they are within the b-tagging acceptance of the Inner Detector, $|\eta| < 2.5$, and if they are associated to a parent c-quark or b-quark;

- the overall ATLAS b-tagging performance is emulated in a crude manner by randomly tagging true b-jets as such with a probability of 60% (resp. 50%) at low (resp. high) luminosity, by randomly mis-tagging true c-jets as b-jets with a probability of 10%, and by randomly mis-tagging all other jets as b-jets with a probability of 1%;

- jet energies are re-scaled on average to the original parton energies using the p_T-dependent scaling factors described in [11], separately for b-jets and non-b-jets;

- if necessary, a lepton veto is applied, requiring that no isolated lepton (electron or muon) with $p_T > 10$ GeV and $|\eta| < 2.5$ is reconstructed in the event;

• if necessary, a jet veto is applied, requiring no additional jet with $p_T > 15$ GeV (resp. 40 GeV) within $|\eta| < 5.0$ at low (resp. high) luminosity;

• finally, in some rare cases, a τ-lepton veto is applied to events for which a hadronic jet from τ-decay was reconstructed with $p_T > 15$ GeV and $|\eta| < 2.5$.

The version of ATLFAST used for the work reported here did not yet allow to account for the degradation of the jet energy resolution at high luminosity due to pile-up effects.

Whereas this package provides the means to change m_t in a flexible way, at the moment there is almost no flexibility as far as the MSSM parameters (other than m_A and tanβ) are concerned. In practice, the simulation assumes that mixing is minimal in the SUSY sector and that all SUSY particles (stops, sbottoms, charginos, neutralinos, etc.) have a mass of ~ 1 TeV.

This package does not presently treat in a consistent way QCD corrections when evolving quark masses, the strong coupling constant α_s and decay widths, since the treatment of these issues is different in PYTHIA, [14] and [15]. The uncertainties arising from these inconsistencies are however believed to be smaller than the dominant experimental and theoretical uncertainties (higher-order corrections, m_t, structure functions).

5.4 Search for MSSM Higgs in the top quark decay mode

The strategy used to identify $\mathrm{t\bar{t}}$ events from H/A decays consists in a search for $\mathrm{WWb\bar{b}}$ final states. One top decay ($\mathrm{t \to Wb}$) has to be followed by the semileptonic decay of the W-boson ($\mathrm{W} \to l\nu$) in order to provide a trigger for this channel. The second W-boson is required to decay hadronically ($\mathrm{W \to jj}$). In this way we obtain a final state topology with one isolated lepton and four reconstructed jets originated from b-quarks and from the W hadronic decay ($\mathrm{W \to jj}$). The Higgs signal should appear in the invariant $\mathrm{t\bar{t}}$ mass distribution as a peak on top of the continuum background.

The background processes can be classified into two categories:

• the irreducible background, consisting of $\mathrm{t\bar{t}} \to bl\nu bjj$ events in the continuum,

• the reducible background from W + jets containing multi-jet events.

In this section, we discuss the observability of the H/A $\rightarrow$ t$\bar{\text{t}}$ channel with two b-tagged jets. The efficiency for b-jet identification is assumed to be ε_b = 60% (50%) at low (high) luminosity. The corresponding efficiencies for c-jets and u-jets are ε_c = 10% and ε_j = 1%, respectively [16]. Leptons are selected using the following cuts: $|\eta| < 2.5$ and $p_T >$ 20 GeV for electrons and muons. Jets from W $\rightarrow jj$ decays and b-jets are selected with p_T above 40 GeV inside the rapidity region $|\eta| < 2.5$. It is assumed that the experiment can trigger on such events (using the single lepton trigger) and efficiently reconstruct all leptons and jets at low and high luminosities. At high luminosity the threshold for electrons is raised to 30 GeV, whereas the 20 GeV threshold is maintained for muons [17].

The cross-sections for signal and background are presented in subsection 5.4.1. Two reconstruction procedures in order to obtain the invariant mass of H/A decaying to t$\bar{\text{t}}$ are introduced in subsection 5.4.2. The difference between both procedures is discussed in subsection 5.4.3. Finally, the signal and background fit procedures are described in subsection 5.4.4.

5.4.1 Cross-section for the process H/A $\rightarrow t\bar{t}$ channel with two b-tagged jets

Higgs boson (H/A) signal production at LHC is dominated by the gg fusion processes [2]. The expected rates ($\sigma \times BR$) for $m_{H/A}$ = 370, 400 and 450 GeV, with m_{top} = 175 GeV and CTEQ2L structure functions, are shown in Table 5.7.

Table 5.7: *H/A $\rightarrow t\bar{t} \rightarrow bl\nu bjj$ cross sections for $m_{H/A}$ = 370, 400 and 450 GeV and m_{top} = 175 GeV.*

Process	$m_{H/A}$=370 GeV	$m_{H/A}$=400 GeV	$m_{H/A}$=450 GeV
gg $\rightarrow$ H	1.9 pb	1.9 pb	1.4 pb
gg $\rightarrow$ A	9.9 pb	6.5 pb	3.4 pb
Total	11.8 pb	8.4 pb	4.8 pb

The main background come from t$\bar{\text{t}}$ $\rightarrow bl\nu bjj$ events produced in the continuum. At LHC, top quark production in the continuum is due to gg fusion and $q\bar{q}$ annihilation and has a large cross-section as it is shown in Table 5.8.

Another background source is (W $\rightarrow l\nu$) + jets production. This background has a relatively large cross section dominated by $qg \rightarrow Wq$ and $q\bar{q} \rightarrow Wg$ processes (see Table 5.9).

Table 5.8: *$t\bar{t} \to bl\nu bjj$ cross sections for m_{top} = 175 GeV.*

Process	$\sigma \times BR$
gg→t$\bar{t}$	228 pb
q$\bar{q}$→t$\bar{t}$	31 pb
Total	259 pb

Table 5.9: *$(W \to l\nu)$ + jets cross sections with default p_T^{hard} cut ($p_T^{hard} > 1$ GeV).*

Process	σ (mb)
qg	2.8×10^{-5}
q$\bar{q}$	3.7×10^{-5}
Total	6.5×10^{-5}

After the selection cuts are applied, the background from t$\bar{t}$ continuum dominates. This background is also much larger than the signal. As already discussed in reference [13], after requiring top-pair reconstruction the background from non-t$\bar{t}$ sources (QCD jets, W+jets, etc) can be neglected. The total number of events generated for each channel and the acceptance after applying the intial selection cuts are shown in Table 5.10.

Table 5.10: *Statistics generated in each channel and acceptances of the inital selection cuts for low and high thresholds.*

Channel	# generated events	Statistical weight	Acceptances (without pile-up) low threshold	Acceptances (with pile-up) high threshold
H/A 370 (GeV)	200k	0.6	12.8 %	11.3 %
H/A 400 (GeV)	200k	0.4	12.1%	10.6%
H/A 450 (GeV)	200k	0.25	11.5%	10.1%
t$\bar{t}$	200k	12.5	17.5%	15.1%

5.4.2 Extraction of the t$\bar{t}$ signal with perfect b-tagging

This subsection discusses the single and double top-quark reconstruction, as expected with ATLAS detector for inclusive t$\bar{t}$ events.

The initial selection requires at least 4 reconstructed jets with p_T> 40 GeV and $|\eta| <$ 2.5, two of them being labelled as b-jets and at least one reconstructed isolated lepton with p_T> 20 (20) GeV for muons and p_T> 20 (30) GeV for electrons and $|\eta| < 2.5$ at low (high) luminosity. The total acceptance of this selection cuts for inclusive $t\bar{t}$ and for signal events with $m_{H/A}$ = 370, 400 and 450 GeV is specified in Table 5.10.

Several algorithms for reconstructing the invariant mass of the $t\bar{t}$ pair have been studied in order to minimise the combinatorial background. In the following, we compare two algorithms [18], [19]:

• All possible combinations of b-jets with reconstructed decays $W \rightarrow l\nu$ and $W \rightarrow jj$ contribute to the m_{tt} mass distribution.

• Only the combination with the best χ^2 is taken into account. The χ^2 is defined as $\chi^2 = (m_{bl\nu} - m_t)^2 + (m_{jjb} - m_t)^2$.

5.4.2.1 First Algorithm

Single top-quark reconstruction in the hadronic channel

In this case all possible jj combinations are examined. The invariant mass distribution m_{jj} is shown in Figure 5.11 using four different Monte Carlo generation conditions (only hard scattering, initial state radiation, final state radiation and hadronisation decays). The signal from W $\rightarrow$ jj decays is clearly visible above the combinatorial background and the expected mass resolution degrades from σ_m = 5.5 GeV (only hard scattering process) to σ_m = 10 GeV (initial and final state radiation and hadronisation/decays included). The distributions for the signal and background are shown in Figure 5.12. All jj combinations with $m_{jj} = m_W \pm 20$ GeV ($\pm\ 2\sigma_m$ mass window) are retained for further analysis. In 70% of the events, at least one of such combination is found. To estimate the combinatorial background events from the side-bands around m_W (m_W=40-60 GeV, and m_W=100-120 GeV) are used:

• for each accepted jj pair, the two possible jjb combinations are considered (two b-tagged jets required),

• for the jj combinations chosen, the 4-momenta are rescaled to impose the constraint $m_{jj} = m_W$,

• finally, m_{jjb} is computed for each of the top-quark candidates.

If jjb combination satisfy the cut $m_{jjb} = m_{top} \pm 30$ GeV, the event is accepted for further analysis.

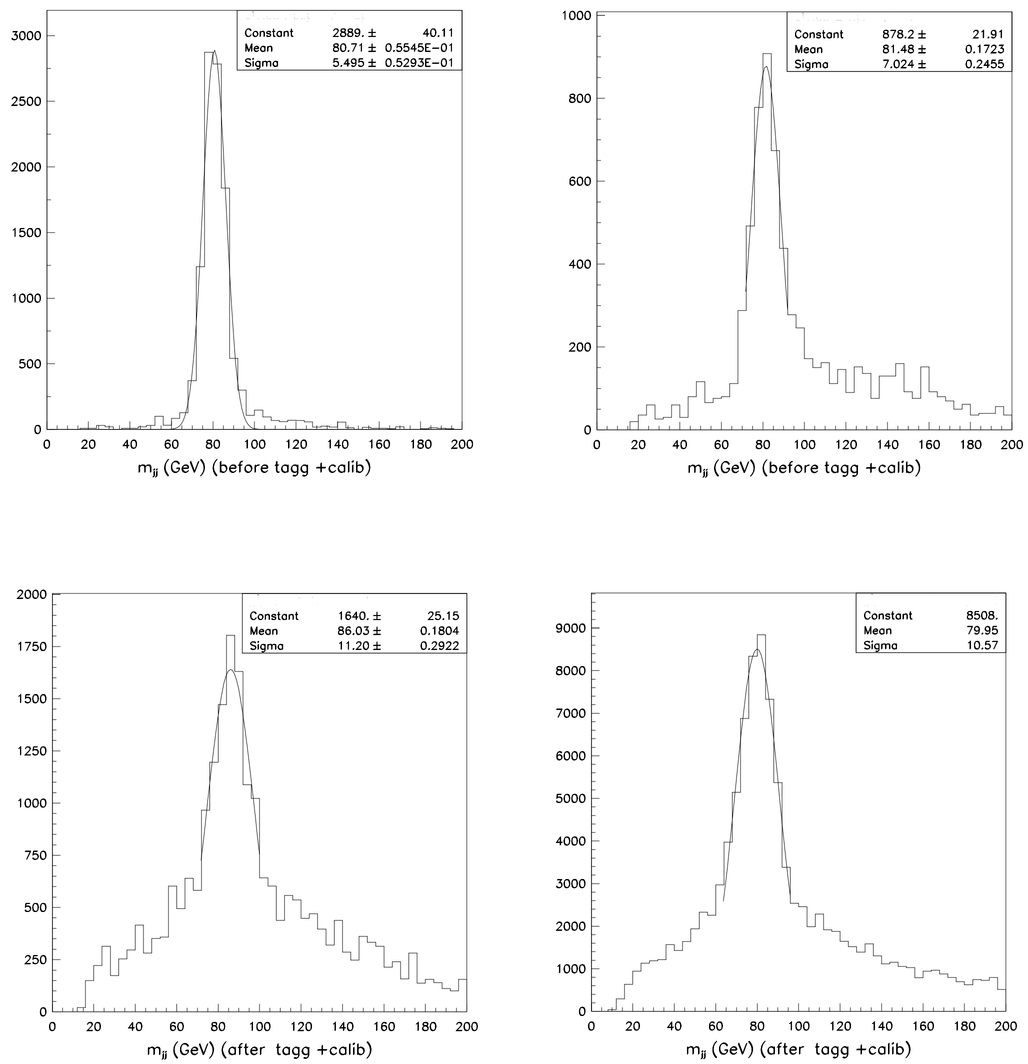

Figure 5.11: *Distribution of reconstructed invariant mass for jet pairs, m_{jj}, as a function of the ingredients used in the event generation: hard scattering process (top left), + initial state radiation (top right), + final state radiation (bottom left) and + hadronisation/decays (bottom right).*

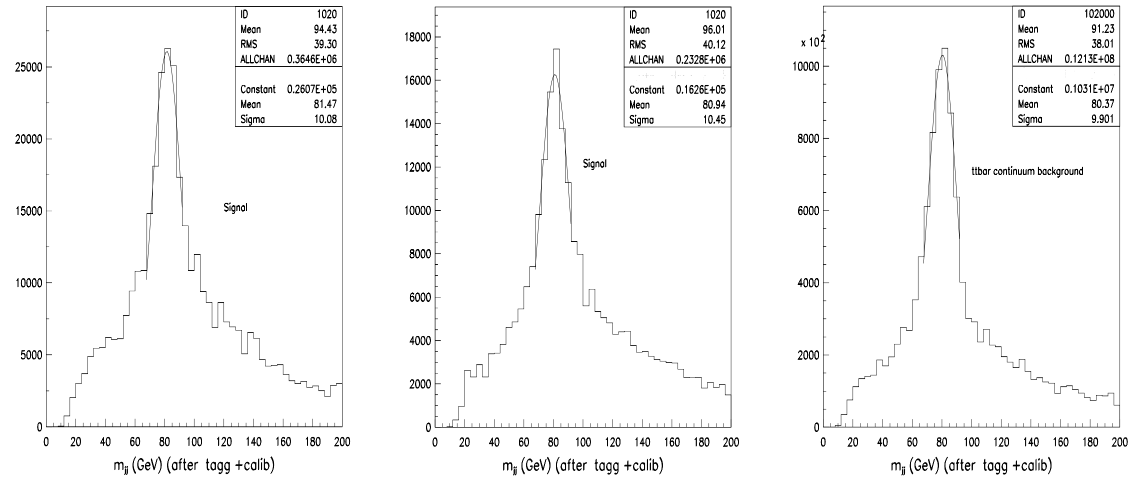

Figure 5.12: *Reconstructed distribution of m_{jj} for: a) 400 GeV signal, b) 450 GeV signal and c) $t\bar{t}$ continuum background events passing the selection cuts described in the introduction, for an integrated luminosity of 3 10^4 pb^{-1}. Hadronisation/decays in the event generation has been used.*

The resulting invariant mass distributions for all valid jjb combinations are shown in Figure 5.13. The peak is well centered around m_{top} and the side-bands background reproduce the shape and magnitude of the combinatorial background.

Figure 5.14 shows the jjb invariant-mass peak after background subtraction, both for 400 and 450 GeV signal and $t\bar{t}$ continuum background events, and for an integrated luminosity of 3 10^4 pb^{-1}. The expected resolution is $\sigma_m = 9$ GeV (initial and final state radiation and hadronisation/decays included) with 13% of the events falling outside the $\pm 2\sigma$ mass window. The peak is almost Gaussian and centered around m_{top}. The distribution of m_{jj} for all combinations (solid) and combinations selected as optimal ones for the t $\rightarrow$ jjb reconstruction (dashed) are shown on Figure 5.15.

Single top-quark reconstruction in the semileptonic channel

The reconstruction of W $\rightarrow l\nu$ decays is limited by the difficulty of reconstructing the neutrino four-momentum. The transverse components of the neutrino momentum (p_x^ν, p_y^ν) can be computed from the components of the missing energy in the event (p_x^{miss}, p_y^{miss}), but the information on the longitudinal component (p_z^ν) is missing because of the large amount of energy escaping in the beampipe. The component p_z^ν can be extracted solving equation (5.11):

$$m_W^2 = (E^\nu + E^l)^2 - (p_x^\nu + p_x^l)^2 - (p_y^\nu + p_y^l)^2 - (p_z^\nu + p_z^l)^2 \tag{5.11}$$

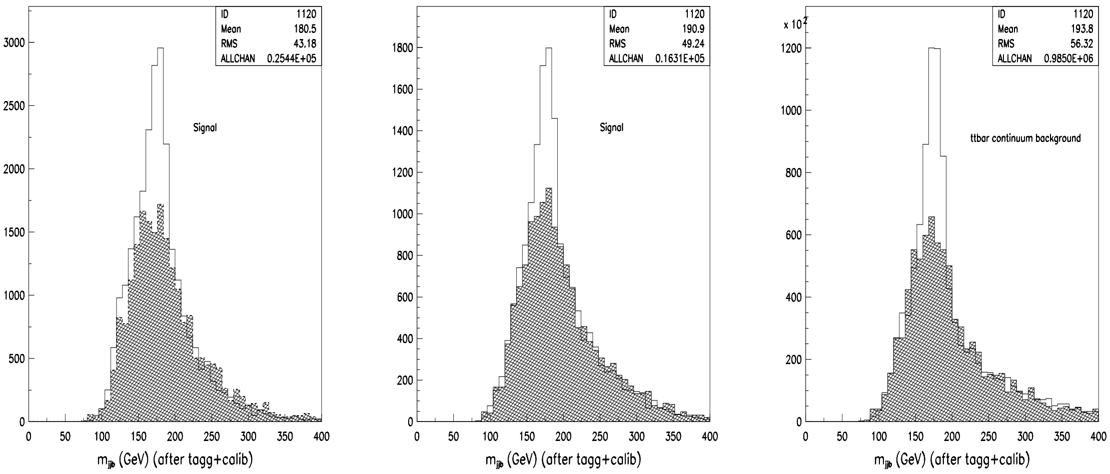

Figure 5.13: *Reconstructed distribution of m_{jjb} for: a) 400 GeV signal, b) 450 GeV signal and c) $t\bar{t}$ continuum background events, passing the selection cuts described in the introduction using the constraint $m_{jj} = m_W$ (solide line), for an integrated luminosity of 3 10^4 pb^{-1}. The light shaded area represents the level of combinatorial background estimated using events from the side-bands around m_W.*

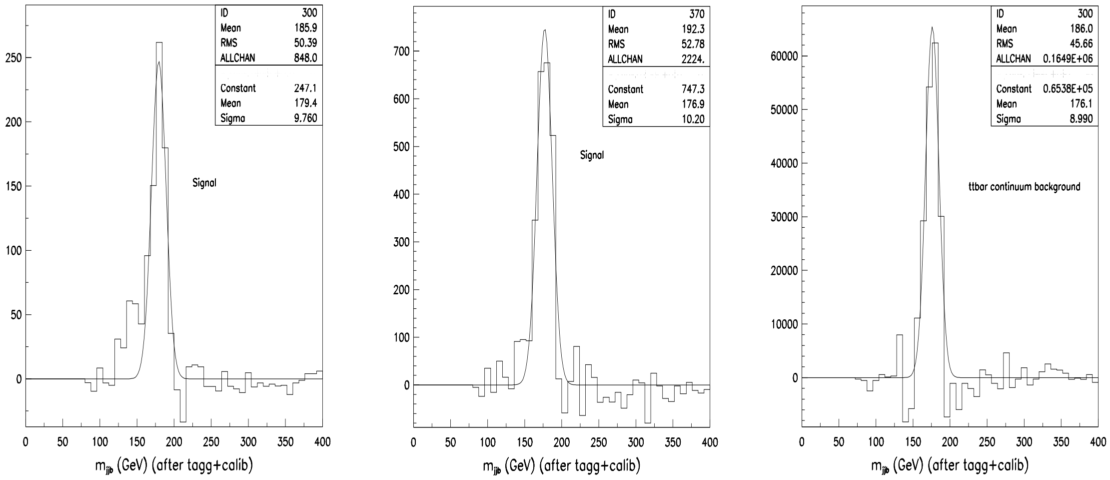

Figure 5.14: *Reconstructed distribution of m_{jjb} for: a) 400 GeV signal, b) 450 GeV signal and c) $t\bar{t}$ continuum background events from Figure 5.13 after subtracting the combinatorial background events.*

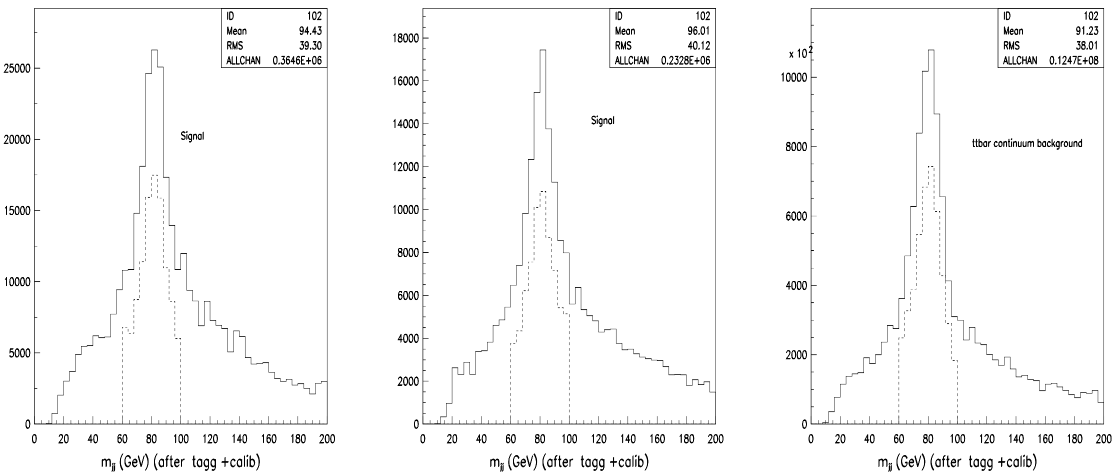

Figure 5.15: *Distribution of reconstructed invariant mass m_{jj} for all combinations (solid) and combinations chosen for the $t \to jjb$ reconstruction (dashed) in the mass window $m_{jj} = 80 \pm 20$ GeV for the 400 and 450 GeV signal and $t\bar{t}$ continuum background.*

where $p_x^\nu = p_x^{miss}$, $p_y^\nu = p_y^{miss}$. The neutrino is assumed to be massless. The $m_{l\nu}$ distribution is a delta-type peak and the effect of the natural width of the W-boson is ignored in this approach. The W-mass equation can have one or two solutions. In case two solutions exist, both are accepted for further analysis.

Finally, we compute two possible $m_{bl\nu}$ combinations. If a b$l\nu$ combination satisfying the cut $m_{bl\nu} = m_{top} \pm 30$ GeV exists, the event is accepted for further analysis.

The resulting invariant mass distributions for all valid b$l\nu$ combinations are shown in Figure 5.16. The peaks are well centered around m_{top} and the shape and magnitude of the j$l\nu$ (where j is a light jet) background is well reproduced.

Figure 5.17 shows the b$l\nu$ invariant-mass peak after background subtraction, both for the 400 and 450 GeV signal and t$\bar{\text{t}}$ background events, for an integrated luminosity of 3 10^4 pb^{-1}. The expected resolution is $\sigma_m = 16$ GeV with 12% of the events falling outside the $\pm 2\sigma_m$ mass window. The mass resolution is worse for the $t \to l\nu b$ decays ($\sim$ 16 GeV) than for the $t \to bjj$ decays ($\sim$ 10 GeV), because of the large uncertainty in the longitudinal momentum of the neutrino.

Reconstruction of top-quark pairs

The W $\to l\nu$ and W $\to$ jj decays are reconstructed as described before. In order to reconstruct t $\to bl\nu$ and t$\to jjb$ decays simultaneously, all possible pairs of b$l\nu$ and jjb

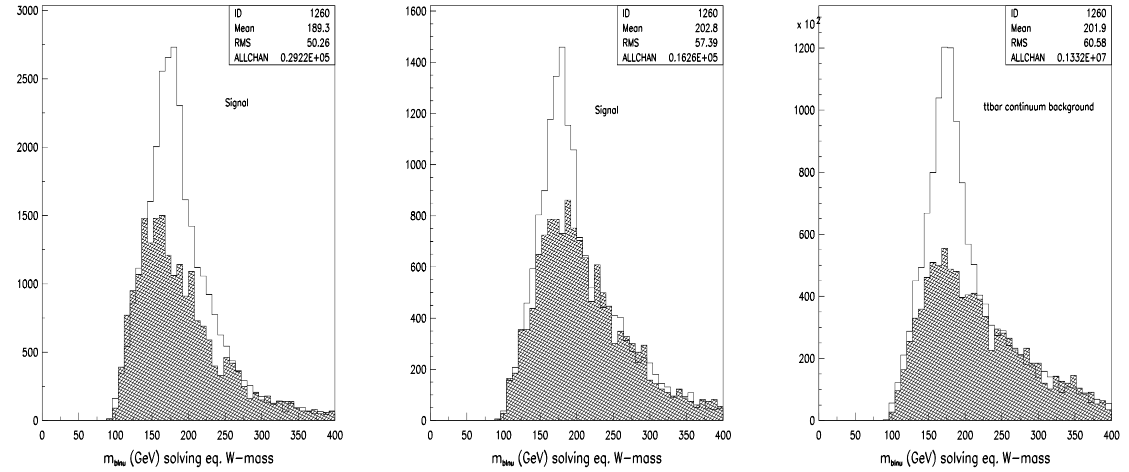

Figure 5.16: *Reconstructed distribution of $m_{bl\nu}$ for: a) 400 GeV signal, b) 450 GeV signal and c) $t\bar{t}$ continuum background events passing the selection cuts, for an integrated luminosity of 3 10^4 pb^{-1}. The light shaded area represents the $jl\nu$ background (where j is a light jet).*

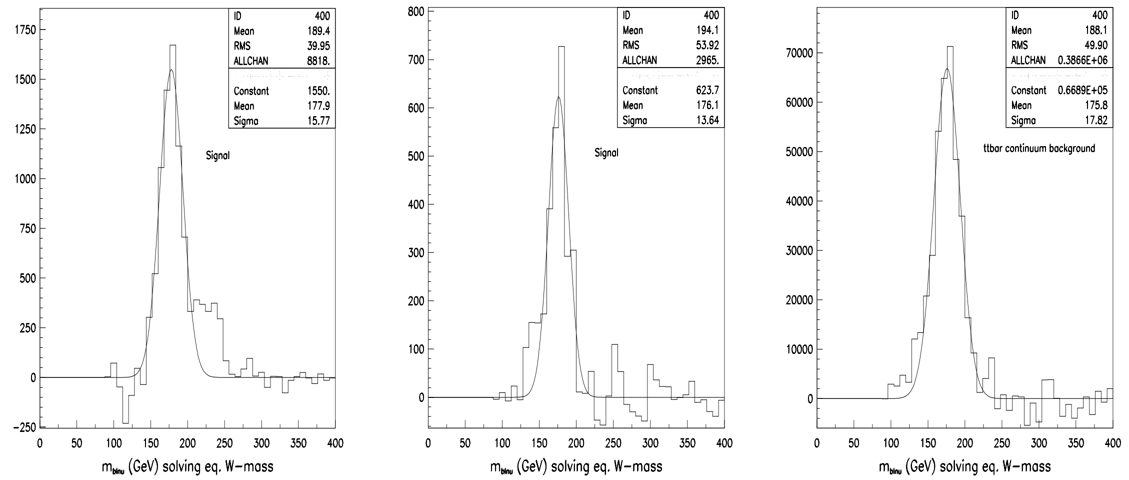

Figure 5.17: *Reconstructed distribution of $m_{bl\nu}$ for: a) 400 GeV signal, b) 450 GeV signal and c) $t\bar{t}$ continuum background events from Figure 5.16 after subtracting the combinatorial background events.*

combinations are considered and then m_{tt} is computed, for each combination satisfaying the cut $m_{(jjb)(bl\nu)} = m_{top} \pm 30$ GeV. The distributions of $m_{bl\nu}$ and m_{jjb} selected for top-quark pairs reconstruction are shown in Figure 5.18.

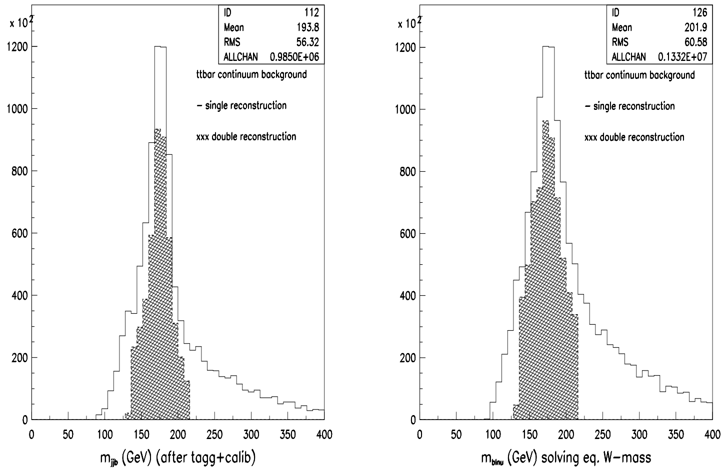

Figure 5.18: *Expected m_{jjb}, $m_{bl\nu}$ distributions for an integrated luminosity of 3 10^4 pb^{-1}. The shaded histograms denote events for which both top-quarks are reconstructed inside the chosen mass window.*

The 4-momenta of the reconstructed top-quarks are rescaled in order to obtain the expected top mass. Figure 5.19 shows the distributions for the reconstructed invariant mass of the $t\bar{t}$ pair, obtained from H $\rightarrow t\bar{t}$ decays with $m_H = 370$, 400 and 450 GeV and for the $t\bar{t}$ continuum. The resolution degrades from $\sigma_m = 36$ GeV (with 33 % of the events falling outside the $\pm 2\sigma$ mass window) to $\sigma_m = 59$ GeV (with 10 % of the events outside the mass window) when $m_{H/A}$ increases from 370 to 450 GeV.

Tables 5.11 and 5.12 show the efficiencies for single top and full $t\bar{t}$ reconstruction and the overall acceptances for the signal and background and for $m_{H/A} = 370$, 400 and 450 GeV and for $m_t = 175$ GeV. These acceptances assume a lepton reconstruction efficiency of 90%, and a b-tagging efficiency of 60%.

Table 5.13 shows the expected number of events for the signal and the $t\bar{t}$ continuum background and the significance (signal/$\sqrt{background}$) for an integrated luminosity of 3 10^4 pb^{-1} and 10^5 pb^{-1} . The background from continuum $t\bar{t}$ production is much larger than the signal. The signal-to-background ratio varies between 3.0 % and 6.4 % in the range of Higgs-boson masses 370-400 GeV. Given the large m_{tt} mass window needed to extract the signal (see Table 5.12), the signal can only be observed above the continuum background as an excess of events. This is illustrated in Figure 5.20 for (a) $m_{H/A} =$ 370 GeV, (b) $m_{H/A} = 400$ GeV and (c) $m_{H/A} = 450$ GeV for events with both top decays reconstructed inside the mass window. The solid line in the histogram shows

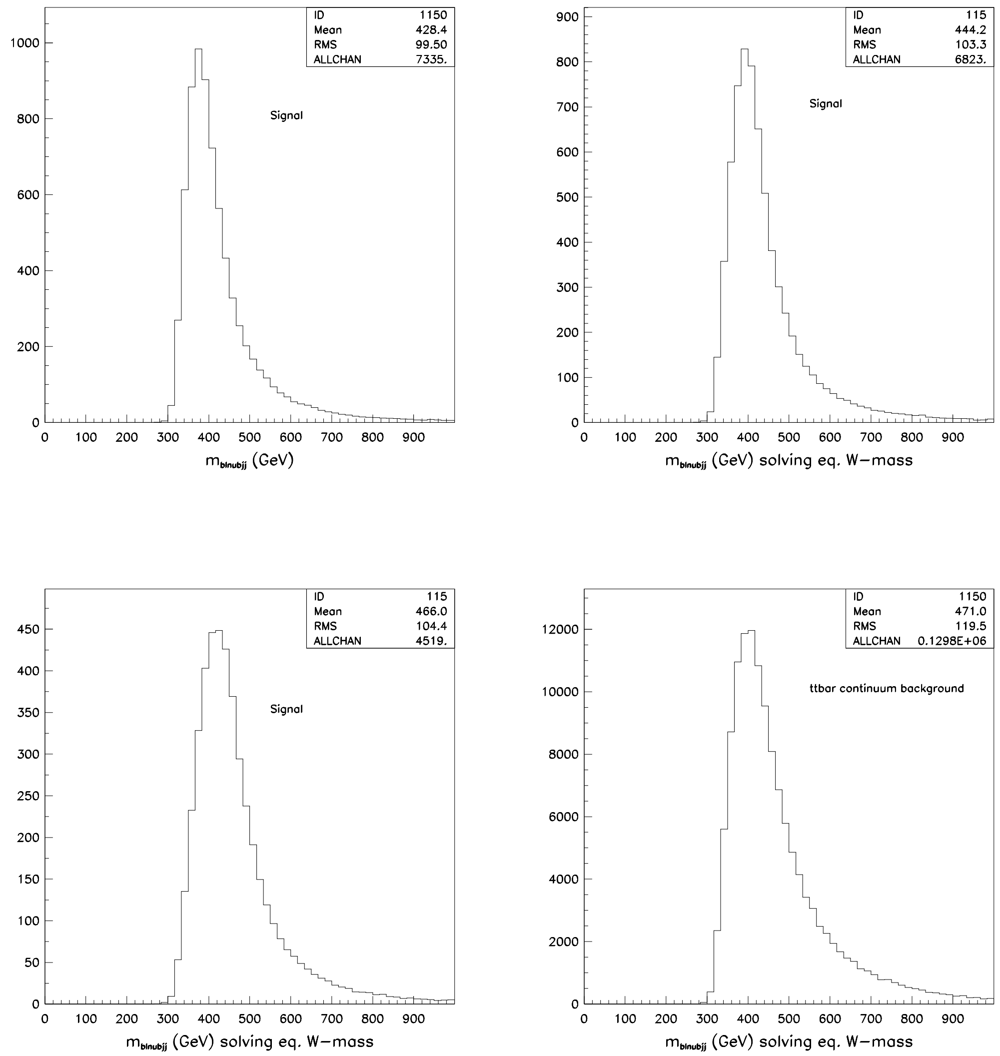

Figure 5.19: *Reconstructed invariant mass distribution of the $t\bar{t}$ pair, $m_{bjjbl\nu}$, for $H \to t\bar{t}$ decays with: a) m_H = 370 GeV, b) m_H = 400 GeV, c) m_H = 450 GeV and d) for the $t\bar{t}$ continuum background.*

Table 5.11: *Efficiencies for single top and full $t\bar{t}$ reconstruction and for perfect b-tagging performance.*

m_A, m_H (GeV)	Selection	Acceptance $m_t \pm 2\sigma$	σ_m (GeV)
370	Single t $\rightarrow b l \nu$	0.82	15.5
	Single t $\rightarrow$ jjb		
	($m_{jj} = m_W \pm 20$ GeV)	0.75	9.0
	Both top quarks	0.50	
	t $\rightarrow b l \nu$		16.0
	t $\rightarrow$ jjb		9.8
400	Single t $\rightarrow b l \nu$	0.81	16.0
	Single t $\rightarrow$ jjb		
	($m_{jj} = m_W \pm 20$ GeV)	0.73	9.0
	Both top quarks	0.51	
	t $\rightarrow b l \nu$		15.7
	t $\rightarrow$ jjb		10.5
450	Single t $\rightarrow b l \nu$	0.80	14.0
	Single t $\rightarrow$ jjb		
	($m_{jj} = m_W \pm 20$ GeV)	0.70	10.0
	Both top quarks	0.48	
	t $\rightarrow b l \nu$		14.5
	t $\rightarrow$ jjb		10.2

Table 5.12: *Acceptances of all selection cuts for the $H/A \rightarrow$ signal and for the $t\bar{t}$ background. The numbers include the lepton reconstruction and b-tagging efficiencies.*

m_A, m_H (GeV)	Mass bin (GeV)	Signal acceptance	Background acceptance
370	390 $\pm$ 72	3.8 %	2.8 %
400	415 $\pm$ 78	4.76 %	3.5 %
450	440 $\pm$ 118	6.9 %	4.4 %

the signal+background distribution, the dashed line shows only the background events, the dark region shows the contribution from H/A $\rightarrow$ t$\bar{\text{t}}$.

The previous results are compatible with those presented in [13].

Table 5.13: *Expected number of events for signal and background at low and high luminosities for combined H/A $\rightarrow t\bar{t}$ decays and tanβ=1.5.*

	Low luminosity			High luminosity		
m_A, m_H (GeV)	Signal	Background	Signif.	Signal	Background	Signif.
370	4400	68700	16.8	10200	159000	25.5
400	4050	85700	13.8	9370	198400	21.0
450	3250	107200	9.9	7520	248200	15.1

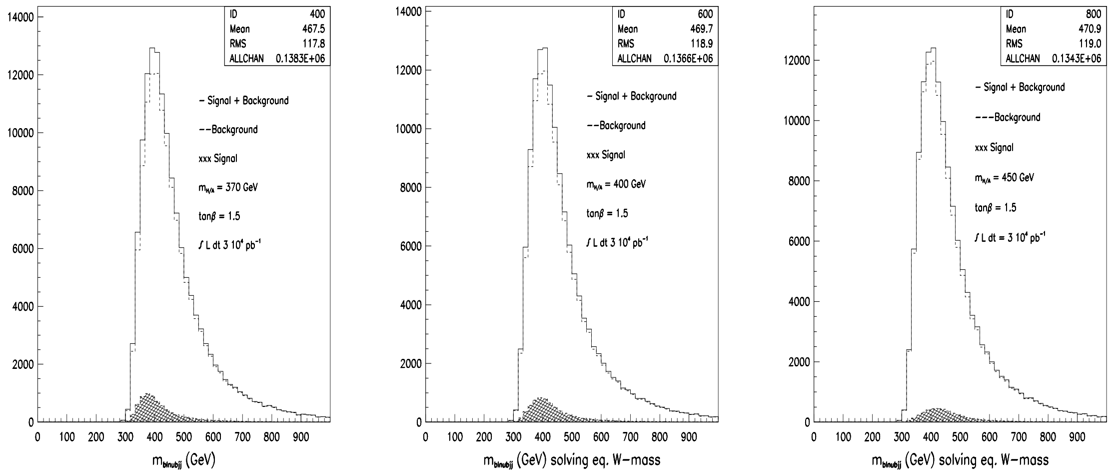

Figure 5.20: *Reconstructed distribution of $t\bar{t}$ mass, $m_{bjjbl\nu}$, for the combined H/A $\rightarrow t\bar{t}$ signal with (a) $m_{H/A}$ = 370 GeV, (b) $m_{H/A}$ = 400 GeV and (c) $m_{H/A}$ = 450 GeV (shaded histogram). The continuum $t\bar{t}$ background (dashed histogram) and signal+background (solid histogram) are also shown. Results are presented for an integrated luminosity of 3 10^4 pb^{-1} and for tanβ=1.5.*

5.4.2.2 Second Reconstruction Algorithm

Single top-quark reconstruction in the hadronic channel

In the second algorithm, the W $\rightarrow$ jj candidates are reconstructed as described before (5.4.2.1). For each candidate with $m_{jj} = 80 \pm 20$ the jj four-momenta are rescaled to obtain the expected m_W mass ($m_{jj} = m_w$). The jjb combination which minimises the value of $\chi^2 = (m_{jjb} - m_t)^2$ is selected. Figure 5.21 shows the reconstructed invariant mass using different approaches at the generation level with initial and final state radiation and hadronisation/decays in the event generation. The resolution is $\sigma = 11.7$ GeV for the best *jjb* combination (with 20% of the events falling outside the $\pm 2\sigma$ mass window). The peak is almost Gaussian and centered around m_{top}. Once the W-mass constraint is applied, the top mass resolution (t $\rightarrow$ *jjb*) is dominated by the quality of the b-jet reconstruction.

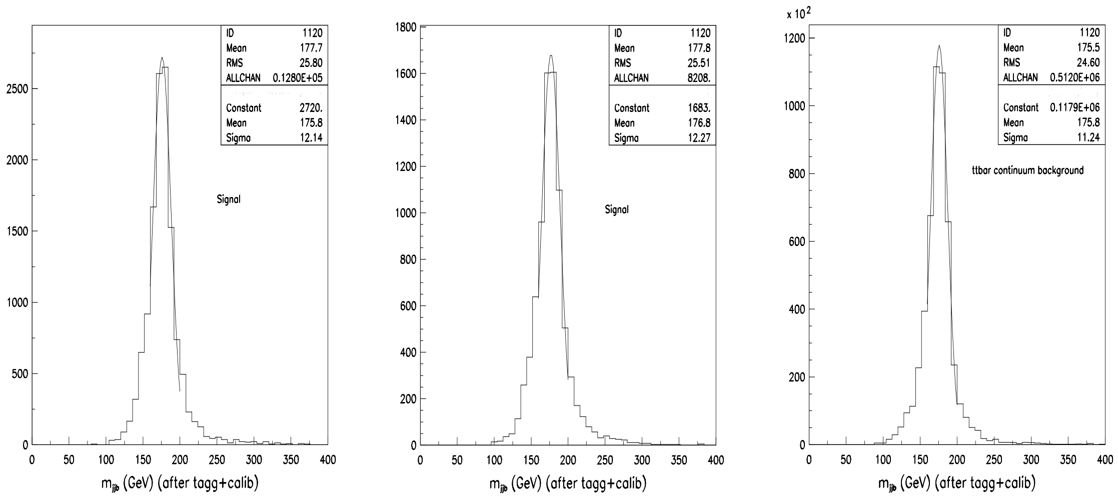

Figure 5.21: *Distribution of reconstructed invariant mass of t $\rightarrow$ jjb, for the best combination of jjb, for: a) 400 GeV signal, b) 450 GeV signal and c) $t\bar{t}$ continuum background with initial and final state radiation and hadronisation/decays in the event generation.*

Single top-quark reconstruction in the semileptonic channel

The W $\rightarrow l\nu$ candidates are reconstructed as described in subsection 5.4.2.1. For events containing a reconstructed candidate, all four possible b$l\nu$ combinations are considered and the combination with best $\chi^2 = (m_{bl\nu} - m_t)^2$ is selected. Figure 5.22 shows the $m_{bl\nu}$ distributions. A resolution of $\sigma_m = 9.6$ GeV is obtained with 18% of the events falling outside the $\pm 2\sigma$ mass window.

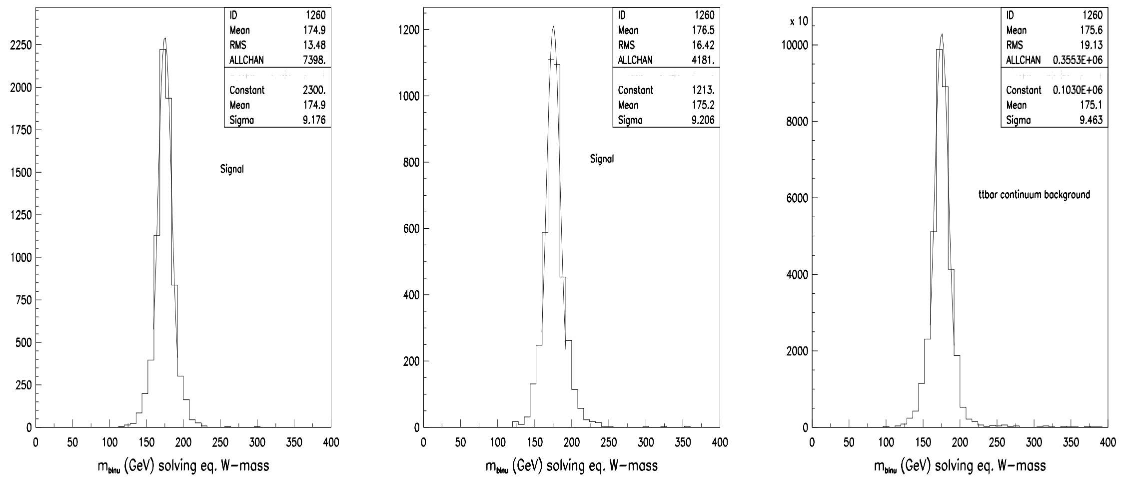

Figure 5.22: *Distribution of reconstructed invariant mass of $t \rightarrow bl\nu$ decays in inclusive $t\bar{t}$ events, for the best combination of $bl\nu$, for: a) 400 GeV signal, b) 450 GeV signal and c) $t\bar{t}$ continuum background.*

Reconstruction of top-quark pairs

In order to reconstruct top-quark pairs, all jj combinations are considered. Then all possible $l\nu$ + 2 b-quarks are considered. Finally, all possible (jjb, $bl\nu$) combinations are analysed. The combination with the best χ^2 given by equation (5.12) is selected.

$$\chi^2 = (m_{jjb} - m_t)^2/\sigma_{jjb} + (m_{bl\nu} - m_t)^2/\sigma_{bl\nu} \tag{5.12}$$

Figure 5.23 shows the mass distributions of $m_{bl\nu}$ and m_{jjb}, assuming the b-tagging performance expected at low luminosity.

After reconstructing the top-quark momenta, the m_t mass constraint is imposed in order to obtain $m_{H/A}$. Figure 5.24 shows the mass distribution for H/A $\rightarrow$ $\mathrm{t\bar{t}}$ with $m_{H/A}$ = 370, 400 and 450 GeV and for the $\mathrm{t\bar{t}}$ continuum background. The expected resolution degrades from σ_m = 13 GeV (with 29.1% of the events falling outside the $\pm 2\sigma$ mass window) to σ_m = 20 GeV with (6.3% of the events outside the mass window) when $m_{H/A}$ varies from 370 to 450 GeV.

Tables 5.14 and 5.15 show the efficiencies for single t and $\mathrm{t\bar{t}}$ pairs reconstruction and the overall signal and background acceptances for a $m_{H/A}$ = 370, 400 and 450 GeV, $\tan\beta$ = 1.5 and m_{top} = 175 GeV.

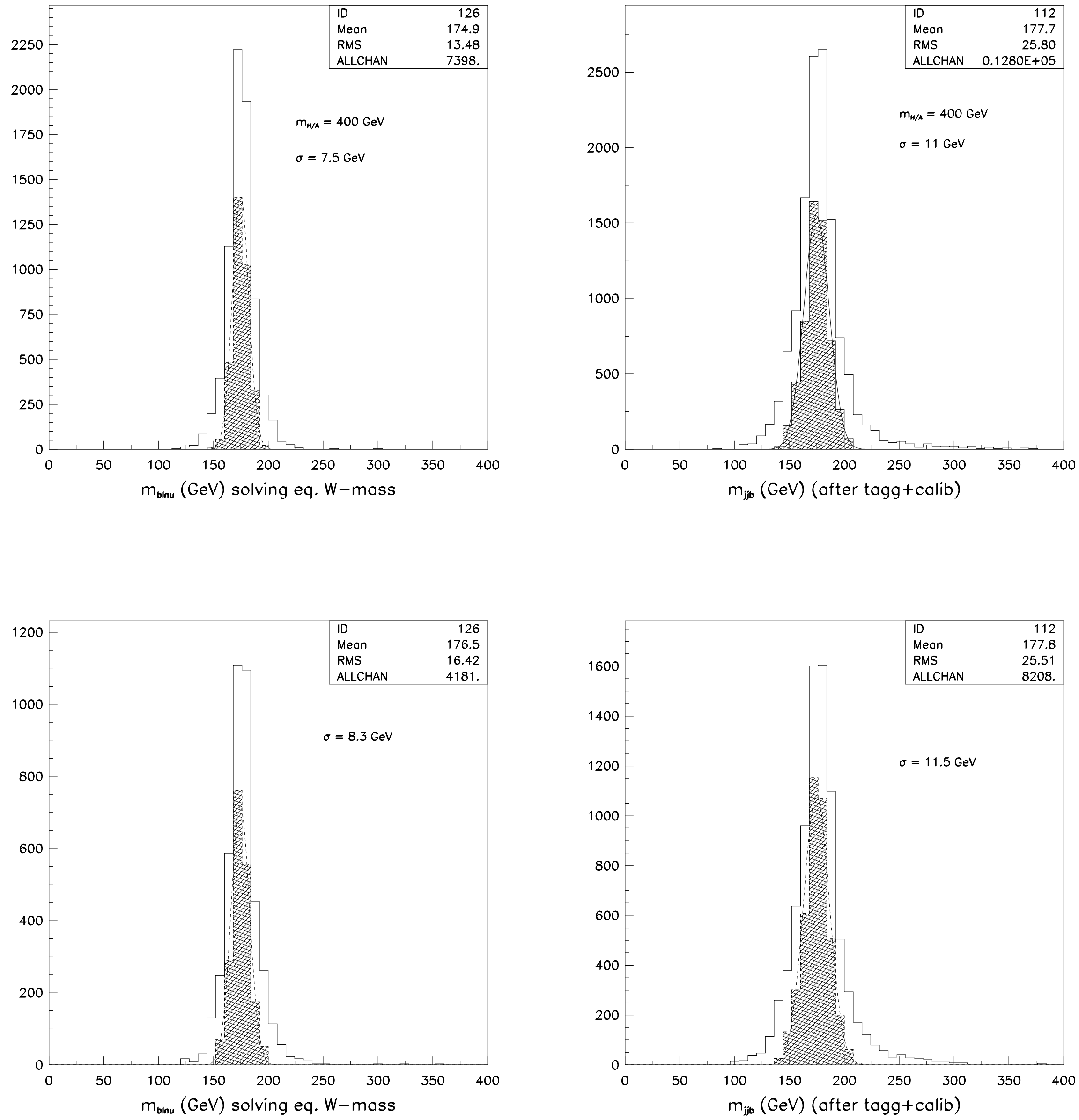

Figure 5.23: *Expected $m_{bl\nu}$ (left), m_{jjb} (right) distributions for the signal events 400 GeV (top) and 450 GeV (bottom) and for an integrated luminosity of 3 10^4 pb^{-1}. The shaded histogram denotes events for which both top-quarks are reconstructed inside the chosen mass window.*

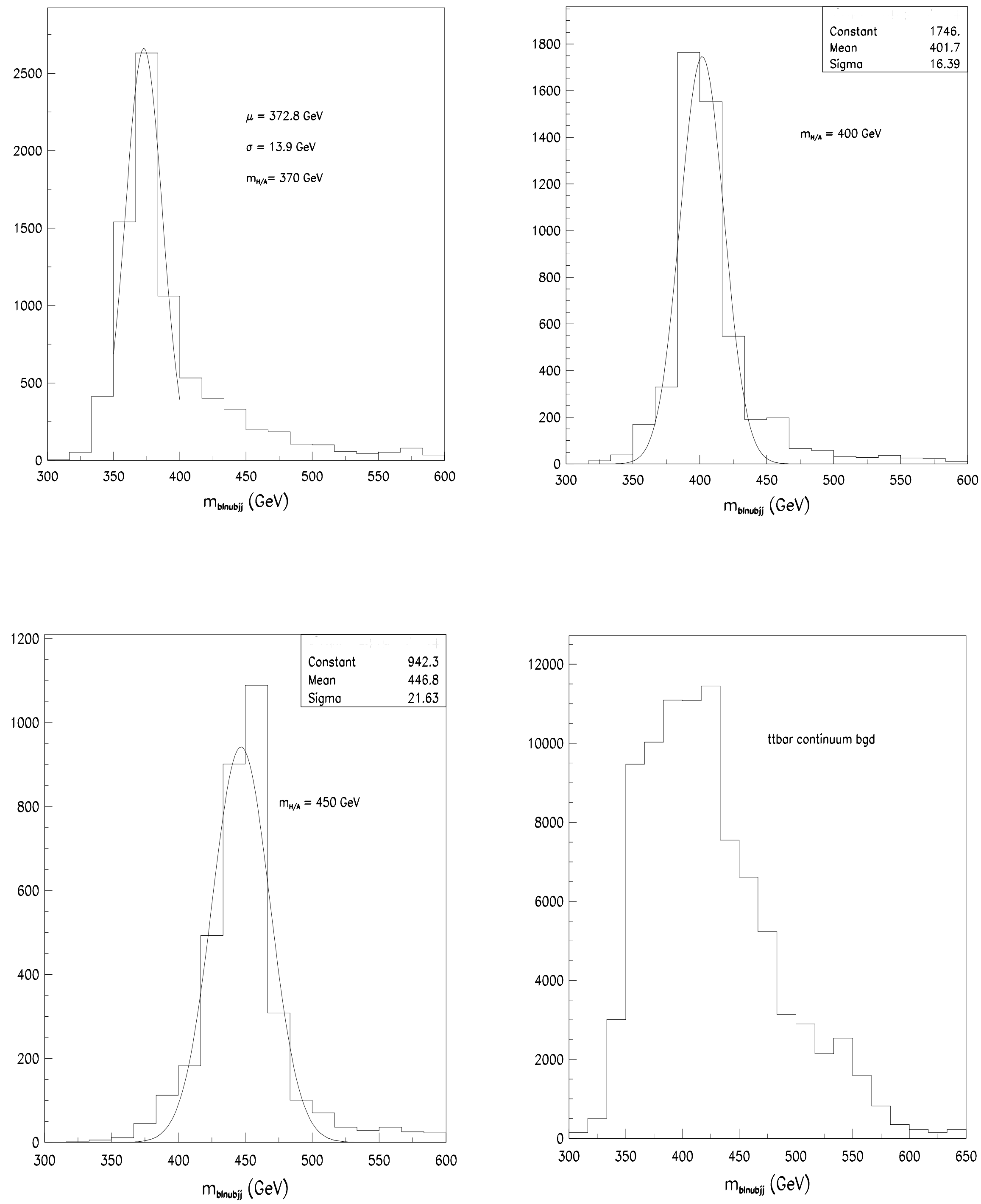

Figure 5.24: *Reconstructed invariant mass distribution of the $t\bar{t}$ pair, $m_{bjjbl\nu}$, for $H/A \to t\bar{t}$ decays with a) $m_{H/A}$ = 370 GeV b) $m_{H/A}$ = 400 GeV c) $m_{H/A}$ = 450 GeV and d) for the $t\bar{t}$ continuum background.*

Table 5.14: *Efficiencies for single top and full $t\bar{t}$ reconstruction and for b-tagging performance.*

m_A, m_H (GeV)	Selection	Acceptance $m_t \pm 2\sigma$	σ_m (GeV)
370	Single t $\rightarrow bl\nu$	0.82	9.2
	Single t $\rightarrow$ jjb		
	($m_{jj} = m_W \pm 20$ GeV)	0.75	11.6
	Both top quarks	0.46	
	t $\rightarrow bl\nu$		7.4
	t $\rightarrow$ jjb		10.9
400	Single t $\rightarrow bl\nu$	0.81	9.6
	Single t $\rightarrow$ jjb		
	($m_{jj} = m_W \pm 20$ GeV)	0.73	11.7
	Both top quarks	0.48	
	t $\rightarrow bl\nu$		7.5
	t $\rightarrow$ jjb		11.0
450	Single t $\rightarrow bl\nu$	0.80	9.7
	Single t $\rightarrow$ jjb		
	($m_{jj} = m_W \pm 20$ GeV)	0.70	11.8
	Both top quarks	0.44	
	t $\rightarrow bl\nu$		8.5
	t $\rightarrow$ jjb		11.5

Table 5.15: *Acceptances of all selection cuts for the H/A $\rightarrow$ signal and for the $t\bar{t}$ background. The numbers include the lepton reconstruction and b-tagging efficiencies.*

m_A, m_H (GeV)	Mass bin (GeV)	Signal acceptance	Background acceptance
370	373 ± 26	3.86 %	1.3 %
400	402 ± 30	4.75 %	1.7 %
450	448 ± 40	6.8 %	2.3 %

The expected number of events for the signal and $t\bar{t}$ continuum background, assuming integrated luminosites of 3 10^4 $pb^{-1}$and 10^5 pb^{-1} are reported in Table 5.16. The expected background from $t\bar{t}$ continuum is smaller than the background observed with the previous algorithm because a smaller mass window can be used due to the improved invariant mass resolution. The signal-to-background ratio varies between 6.3% and 13.4% in the Higgs-boson mass range considered in the present analysis.

Table 5.16: *Expected number of events for signal and background for combined $H/A \to t\bar{t}$ decays at low and high luminosities and $\tan\beta$=1.5.*

	Low luminosity			High luminosity		
m_A, m_H (GeV)	Signal	Background	Signif.	Signal	Background	Signif.
370	4500	34200	24.3	10500	79100	37.3
400	4200	39500	21.1	9800	91400	32.4
450	3200	52900	14.2	7550	122400	21.6

5.4.3 Comparison of algorithms

The second algorithm improves substantially the signal resolution with respect to the first one (from 36 to 13 GeV for $m_{H/A}$ = 370 GeV and from 60 to 20 GeV for $m_{H/A}$ = 450 GeV), and as a consequence the signal-to-background ratio (from 3.0% and 6.4% to 6.3% and 13.4% respectively) and the statistical significance (from 16.8 and 9.9 to 24.3 and 14.2). On the other side, the first algorithm provides a useful check because it can reproduce in a more unbiased way the shape and magnitude of the combinatorial background to the t $\to$ jjb hadronic channel, and the jlν background to blν semileptonic channel.

Table 5.17 shows the results obtained for the two algorithms studied in the present analysis.

5.4.4 Fitting procedure

Figure 5.25 illustrates the expected signal+background m_{tt} distribution, for H/A $\to$ $t\bar{t}$ with $m_{H/A}$ = 370, 400 and 450 GeV, above the smooth continuum background for an integrated luminosity of 3 10^4 pb^{-1} and in the Higgs mass range 300-650 GeV. The full line corresponds to a polynomial fit of the $t\bar{t}$ continuum background in the range

Table 5.17: *Similarities and differences between algorithms.*

First Algorithm	**Second Algorithm**
1) *Hadronic channel*	1) *Hadronic channel*
All jj combinations examined	All jj combinations examined
$m_{jj} = m_W \pm 20$ GeV retained	$m_{jj} = m_W \pm 20$ GeV retained
Constraint $m_{jj} = m_W$	Constraint $m_{jj} = m_W$
Two possible jjb combinations $\sigma_{jjb} = 10$ GeV	
2) *Semileptonic channel*	2) *Semileptonic channel*
p_z^ν extracted (1)	p_z^ν extracted (1)
All possible blν combinations examined $\sigma_{bl\nu} = 16$ GeV	
3) *Top-quark pairs*	3) *Top-quark pairs*
All jjb and blν pairs examined	All jjb and blν pairs examined Best $\chi^2 = (m_{jjb} - m_t)^2/\sigma_{jjb} + (m_{bl\nu} - m_t)^2/\sigma_{bl\nu}$ retained $\sigma_{jjb} = 11$ GeV $\sigma_{bl\nu} = 9$ GeV
Events with $m_{jjb(bl\nu)} = m_{top} \pm 30$ GeV retained	Events with $m_{jjb(bl\nu)} = m_{top} \pm 30$ GeV retained
m_{jjb} and $m_{bl\nu}$ rescaled to m_t	m_{jjb} and $m_{bl\nu}$ rescaled to m_t
m_{tt} reconstructed $\sigma_{tt} = 39$ to 59 GeV	m_{tt} reconstructed $\sigma_{tt} =$ 15-20 GeV for m_H=370-450 GeV

300-400 GeV for $m_{H/A} = 370$ GeV and in the range 400-650 GeV for $m_{H/A} = 400$ and 450 GeV . The peak has been extracted (bottom plots) taking into account just the statistical error.

Table 5.18 shows the fit results after background subtraction.

Table 5.18: *Mean and σ obtained after background subtraction.*

Channel	Mean (GeV)	σ (GeV)
H/A 370 (GeV)	371.9	15.7
H/A 400 (GeV)	403.7	16.6
H/A 450 (GeV)	446.6	21.2

The systematic error from overall normalisation can be estimated by varying the background between 1 and 3%. There is in additional error due to the background shape. This error has been estimated by fitting the background shape below and above the signal peak. For $m_{H/A} = 370$ GeV the background is taken below 345 GeV and above 395 GeV (the signal resolution is $\sim$ 13 GeV). For $m_{H/A} = 450$ GeV the background is taken below 410 GeV and above 490 GeV (the signal resolution is $\sim$ 20 GeV). In the $m_{H/A} = 400$ GeV case, the background is peaked in the same region as the signal. Therefore only an excess of events can be quotted.

Figure 5.26 shows the polynomial background fit outside the mass window for $m_{H/A} = 370$ GeV and $m_{H/A} = 450$ GeV.

Figure 5.27 shows the signal+background fit for H/A $\rightarrow$ t$\bar{\text{t}}$ with $m_{H/A} = 370$ and 450 GeV using the polynomial obtained previously and a gaussian distribution on top of it.

In order to check that the signal does not disappear when the shape of the background changes, the t$\bar{\text{t}}$ background is reconstructed with only one b-tagged jet but assuming the same normalisation outside mass window. With this procedure the background changes by about 9% in a few bins below mass peak. Figure 5.28 shows the new background shape (top). In this figure the line represents the expected theoretical background (polynomial obtained previously). The signal+background fit (bottom) is performed using the previously obtained polynomial and a gaussian distribution.

When the background shape changes around 9% in few bins below the mass peak, the mean value obtained from the fit changes by about 2% (from 447 GeV to 454 GeV), therefore the signal does not disappear. However, the width decreases by about 23% (from 21 GeV to 16 GeV) because the new background is more broad in the range 380-440 GeV and so the signal peak is better defined.

Table 5.19 shows results of the fit. The first column shows the details of the fitting procedure, the second and third columns show the parameters resulting from the fit, R

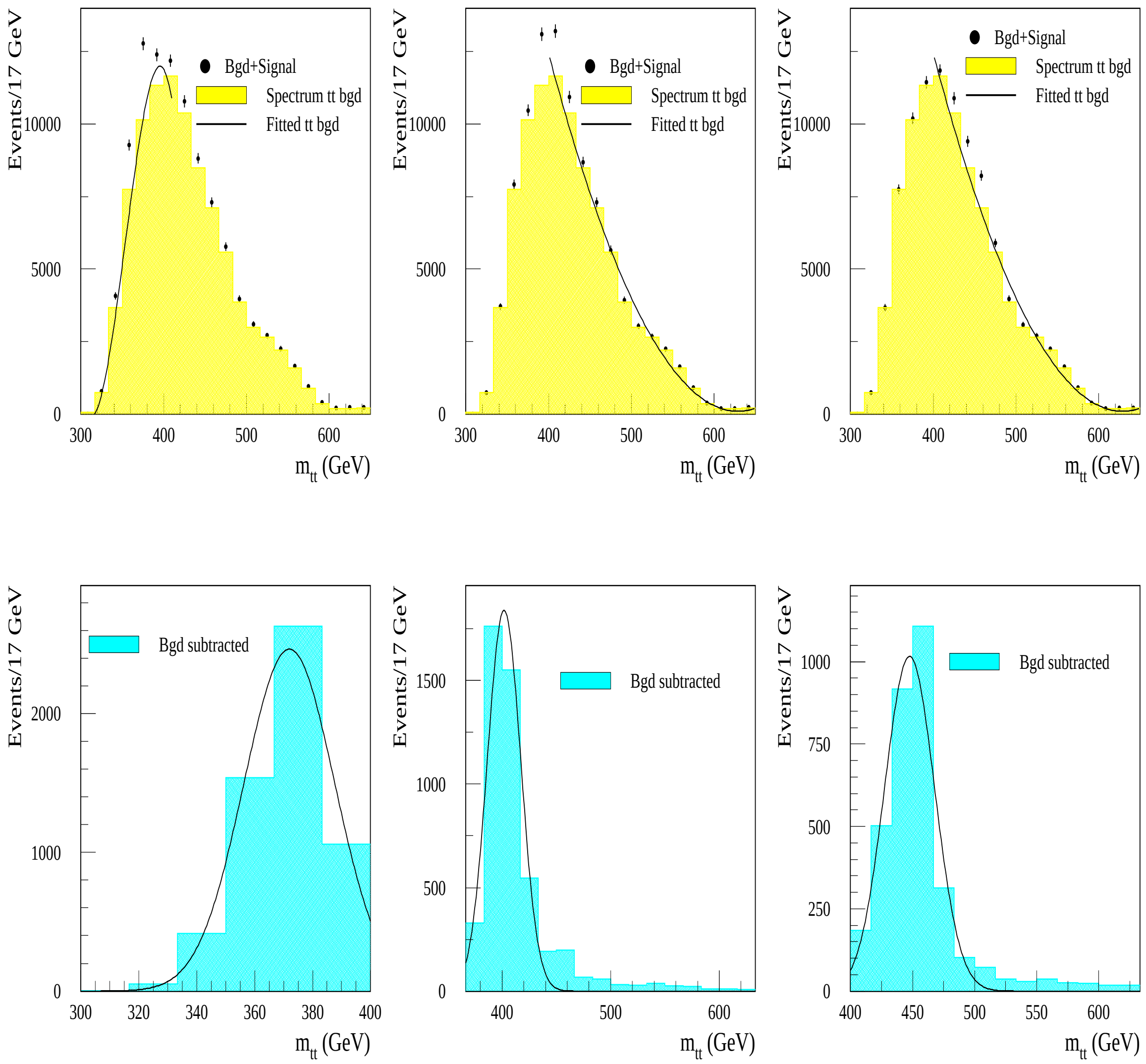

Figure 5.25: *Expected background+signal for: (a) Signal with $m_{H/A}$ = 370 GeV, (b) Signal with $m_{H/A}$= 400 GeV and (c) Signal with $m_{H/A}$ = 450 GeV above continuum background. The line corresponds to a fit of the background spectrum, errors are statistical only. (d) Signal $m_{H/A}$ = 370 GeV, (e) Signal $m_{H/A}$ = 400 GeV, and (f) Signal $m_{H/A}$ = 450 GeV, after background subtraction.*

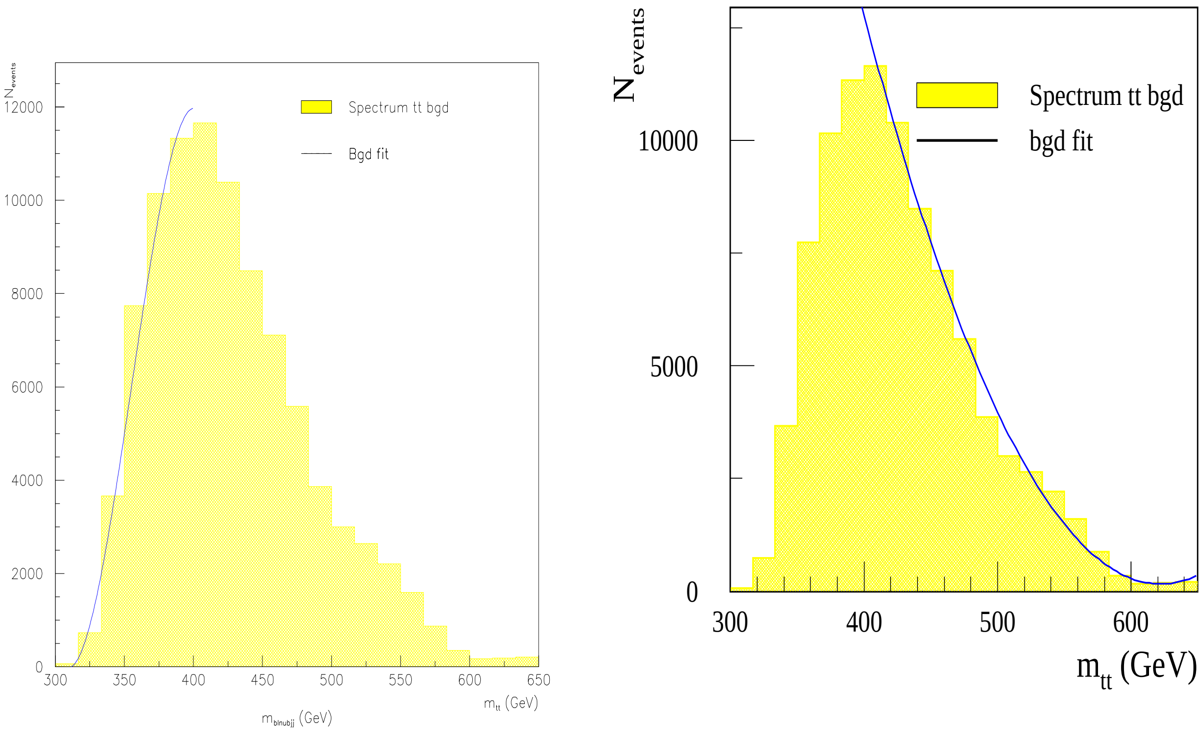

Figure 5.26: *The polynomial fit of the $t\bar{t}$ continuum spectrum outside the signal window with: a) $m_{H/A}$ = 370 GeV and b) $m_{H/A}$ = 450 GeV.*

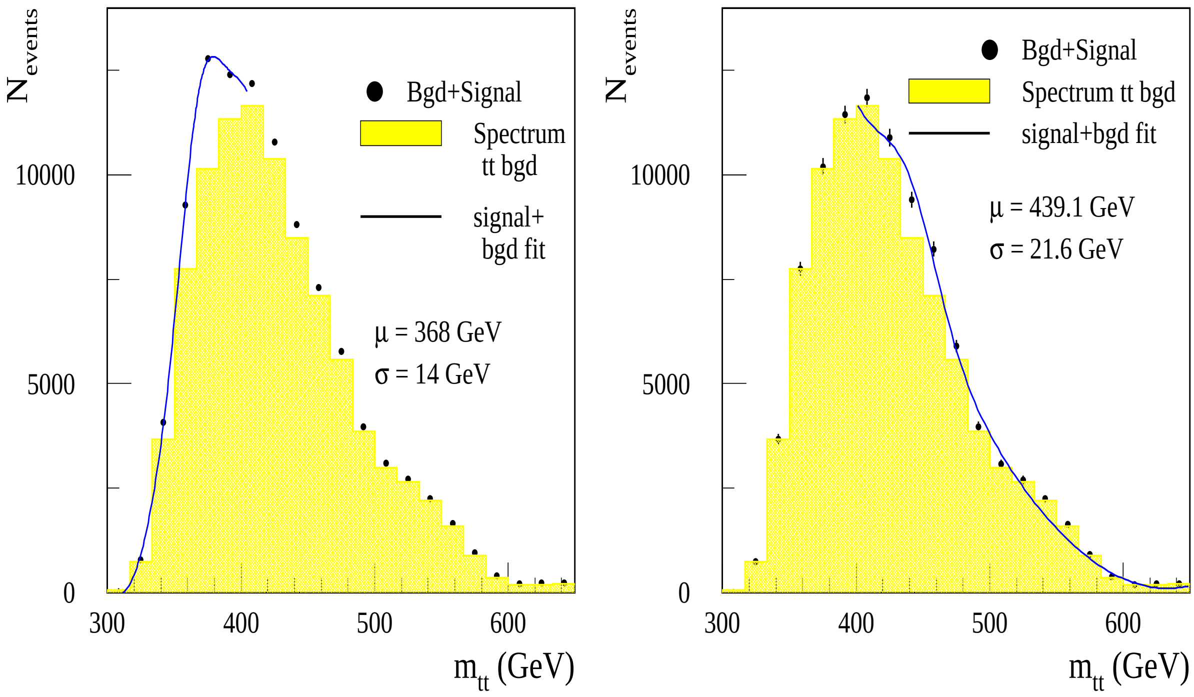

Figure 5.27: *Expected spectrum for background. The lines denote fitted spectrum outside the window for the signal with: a)* $m_{H/A}$ *= 370 GeV and b)* $m_{H/A}$ *= 450 GeV.*

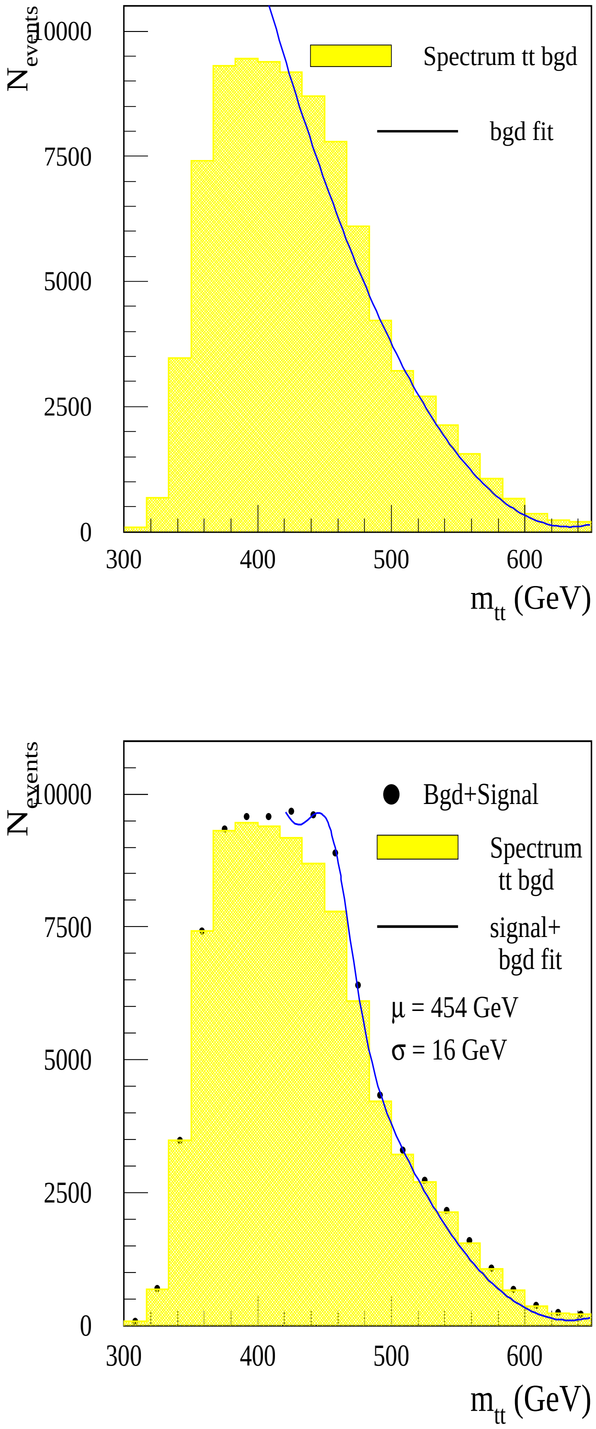

Figure 5.28: *New background shape (top) with only one b-tagging but assuming the same normalisation outside mass window and the signal+background fit (bottom) using the theoretical background plus a gaussian.*

is the expected number of events in the signal, and the χ^2 of the fit is given as well. The parameters obtained after performing the background+signal fit (Figure 5.27) are consistent with the parameters obtained by fitting the signal alone (Figure 5.24). The difference in the R values are due to the different ways of performing the fit.

Table 5.19: *Mean, σ, expected number of events for signal (R) and χ^2 obtained from the fitting procedure for different distributions as specified in Table.*

Fit	Mean (GeV)	σ (GeV)	R	χ^2
ATLFAST ($m_{H/A}$= 450)	447.0	21.6	3200	26
Gaussian after bgd subtraction	447.0	20.0	3100	29
Gaussian + polyn. on signal+bgd	439.1	21.6	2400	36
Gaussian + polyn. on signal+bgd (changed shape)	454.0	16.0	2700	47
ATLFAST ($m_{H/A}$= 370)	372.8	13.8	4500	13
Gaussian after bgd subtraction	371.9	15.7	4270	17
Gaussian + polyn. on signal+bgd	368.1	13.9	3550	32

5.4.5 Interference effects with the pure QCD process gg $\rightarrow$ Q$\bar{\text{Q}}$

As discussed in references [2], [20], a signal from H/A$\rightarrow$ t$\bar{\text{t}}$ decays appears as a peak in the t$\bar{\text{t}}$ invariant mass spectrum above the t$\bar{\text{t}}$ continuum background for values of m_H smaller than 500 GeV. There is however an interference between the signal and background amplitudes which causes an oscillating structure in the differential cross-section around s=m_H^2. This effect leads to a strong suppression of the signal at higher masses. For m_H = 500 GeV the total cross-section differs only slightly from the cross-section with no Higgs present. This interference effect is much stronger for the A than for the H boson. According to the results presented in [2], [20] this suppression is estimated to be 30% for m_H = 370 GeV, 50% for m_H = 400 GeV and 70% for m_H = 450 GeV.

Table 5.20 shows the results obtained for the H/A $\rightarrow$ t$\bar{\text{t}}$ channel including the effect of the negative interference with continuum production.

These numbers show a significant suppresion for a Higgs mass of 450 GeV, which becomes even stronger for 500 GeV. A significant signal (5σ level) can be extracted only below 400 GeV. For masses larger than 450 GeV, the Higgs yield is strongly suppressed and a significant signal can not longer be extracted. For masses around 400 GeV, the signal and background peaks coincide, and the sensitivity can only be estimated by a ratio of the type $\frac{signal}{0.01 \times background}$, where a 1% uncertaintity on the background is assumed.

Table 5.20: *Observability of the $H/A \to t\bar{t}$ channel for an integrated luminosity of 30 fb^{-1} and 100 fb^{-1}, for tanβ = 1.5. The rough estimation of the effect of the negative interference with continuum production has been included.*

m_H (GeV)	370	400	450
$\sigma \times$ BR (pb) (no supression)	11.8	8.4	4.8
$\sigma \times$ BR (pb) (with supression)	8.3	4.2	1.4
Signal #			
(Low. Lum.)	3190	2120	980
(Hig. Lum.)	7380	4900	2270
Backgr. #			
(Low. Lum.)	34200	39500	52900
(Hig. Lum.)	79100	91400	122400
Significan.			
(Low. Lum.)			
=S/$\sqrt{B}$	17.3		4.3
=S/0.01B		5.4	
(Hig. Lum.)			
=S/$\sqrt{B}$	26.2		6.5
=S/0.01B		5.4	

The leptonic mode (two W→ lν decays) is not discussed in the present analysis. This channel would contribute by an additional 10% contribution to both the signal and the background and only slightly improve the expected significance [21].

5.4.6 Discovery curves in the relevant region of parameter space

The signal-to-background ratio varies between 9% and 1% over the mass range from 370 to 450 GeV. For an integrated luminosity of 30 fb^{-1} and tanβ = 1.5, about 2120 signal events and 4×10^4 background events are expected inside a mass windows of $\pm2\sigma_m$ around m_A = 400 GeV. For high luminosity operation and an integrated luminosaity of 100 fb^{-1} one expects for Higgs mass of 400 GeV about 4900 signal and 9×10^4 background events.

The mass resolution quoted above imply that the width of a typical mass window for observing most of the signal would be between ±30 GeV and ±40 GeV. The extraction of the signal would only be possible for Higgs masses above the kinematic peak of the background distribution, which is around m_{tt} = 400 GeV. Such extraction assumes that the uncertainty on the shape of the continuum background is small and that it can be fitted from events outside the assumed Higgs mass window.

For masses close to 400 GeV only an excees of events above the continuum background would be observed. This excess would be statiscally significant, as shown in Table 5.20 and Figure 5.27, but this significance would only be meaningful if the theoretical uncertainties on the continuum background shape were not larger than about a percent. Although the theoretical uncertainties on the continumm t$\bar{t}$ production are much larger today, it is hoped that they would be reduced with time, and that the experimental data at the LHC would also contribute to a better understanding of heavy-flavour continuum production.

For the optimimistic scenario assuming that the differential spectrum of m_{tt} would be known to better than 1% from a contribution of theory and experimental data, the signal significances including this systematic uncertainty for masses close to 400 GeV are shown in Table 5.20, and the 5σ-discovery contour curves in the (m_A, tanβ) plane for H/A → t$\bar{t}$ decays are shown in Figure 5.29. These curves cover at best a limited region in parameter space, namely that corresponding to $2m_t < m_A <$ 470 GeV. In conclusion this channel will be only of very limited use as a discovery channel.

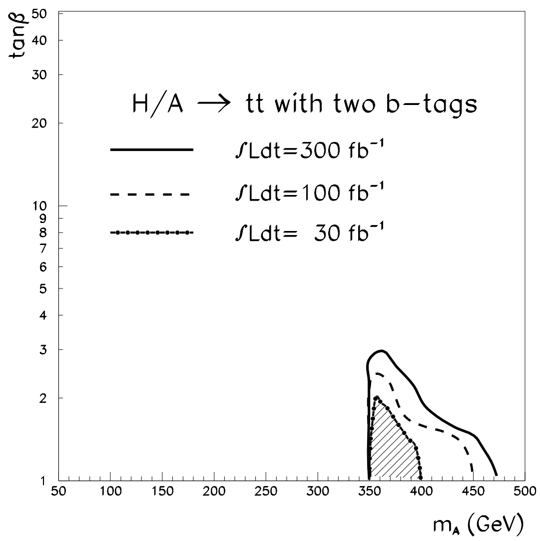

Figure 5.29: *For integrated luminosities of 30* fb^{-1}, *100* fb^{-1} *and 300* fb^{-1}, *5*σ*-discovery contour curves for the* $H/A \to t\bar{t}$ *channel in the* (m_A, *tan*β) *plane.*

5.5 Comparison between full and fast simulation of ATLAS detector

The decay channel H/A $\rightarrow$ t$\bar{\text{t}}$ $\rightarrow$ $bl\nu\bar{b}jj$ has been already studied in the previous subsection using a fast detector simulation. It was shown that for a 400 GeV Higgs boson mass, background and signal peak coincide in the same invariant mass region and the signal extraction is therefore difficult to perform but for $m_H = 370$ GeV a clear signal can be extracted. However the analysis presented below is useful as a benchmark for the ATLAS detector performances in the reconstruction of quantities used in the physics events.

The full simulation is always needed to study effects due to noise, calibration and intercalibration of calorimeters, detailed showers development, pile-up, cracks, and to provide parametrisation for fast simulation. The GEANT package has been used to simulate in detail the detector characteristics and performances. The simulation program framework is provided by a package called SLUG (Simulation for LHC Using GEANT [22]), which gives the basic infrastructure for handling ZEBRA banks. It also provides a set of facilities for dealing with event generation, detector geometry and simulation, event merging for pile-up studies, together with stubs for user-defined routines to gain acces to every step in the simulation process and tools for managing histograms and n-tuples.

However the full simulation is largely time consuming, therefore in some cases it is necessary to dispose of a detector fast simulation.

Fast simulation is an intermediate step between a simple parton-level analysis of the event topology, which in general yields to too much optimistic results for physics processes at hadron colliders, and a very sophisticated and high CPU-time intensive full detector simulation and reconstruction. This kind of approach is needed for quick and approximate estimates of signal and background rates for specific channels. In addition, fast simulation and reconstruction is the only practical tool for a high-statistics studies of complex background processes. A complete package for fast detector simulation of ATLAS and physics analysis has been implemented: ATLFAST. It can be used for fast simulation of signal and background processes, including the most crucial detector aspects: jet reconstruction in the calorimeters, momentum/energy smearing for leptons and photons, magnetic field effects and missing transverse energy evaluation.

Signal events were generated with PYTHIA 5.7 and fully simulated on the CERN PCSF in 1998-99. The comparison between full simulation and ATLFAST has been done for one mass point: m_A=400 GeV.

The statistics used for full and fast simulation consists in the same sample of signal events (20000 events, Run Numbers 65801-66000), generated with PYTHIA and using the same datacard file for both simulations. The events were simulated with electronic noise but not taking into account the effect from minimum bias. The leptons and missing energy are reconstructed with the fast simulation only.

With the objective of improve the simulation efficiency the events were filtered on:

- one electron with $p_T > 17$ GeV and $|\eta| < 2.7$,
- two b-quarks with $p_T > 15$ GeV and $|\eta| < 2.7$.

This Monte Carlo generation filter was not applied on the study done in section 5.4.

The acceptances and the quantities involved in kinematic cuts for full and fast simulation are presented in subsection 5.5.1. The subsection 5.5.2 describes and compares three proposed methods to correct reconstructed quantities for physics effects related with the parton fragmentation. Finally, the comparison of the resolution and Higgs mass reconstruction between full and fast simulation in the case of low luminosity performance ($3\ 10^4\ pb^{-1}$) are discussed in subsection 5.5.3.

5.5.1 Comparison of the acceptances and quantities involved in kinematic cuts

In both cases the events were only analysed (after MC generation) if they passed the following filter cuts:

• Two reconstructed jets labelled as b-jets with p_T> 40 GeV and $|\eta|$ < 2.5 (from t $\rightarrow$ Wb). The expected efficiency for b-jets identification is ε_b = 60% (50%) at low (high) luminosity with ε_c = 10% and ε_j = 1% respectively.

• Isolated lepton within $|\eta|$ < 2.5 and p_T> 20 GeV for electrons and muons at low luminosity.

• Two reconstructed jets with $|\eta|$ < 2.5 and p_T> 40 GeV (from W $\rightarrow$ jj).

Figure 5.30 shows the isolated lepton multiplicity from full and fast simulation without any other cuts and with $|\eta|$ < 2.5 and p_T > 20 GeV cuts.

Figure 5.31 shows jets multiplicity from full and fast simulation without cuts and with $|\eta|$ < 2.5 and p_T > 40 GeV cuts. Figure 5.32 shows the same plots but for b-labelled jets.

The table 5.21 shows the acceptances of each cut selections separately (leptons, jets, bjets). The lepton acceptance is very similar because in both cases we have taken the lepton from fast simulation. This is due to the fact that isolated electrons are treated as jets in ATRECON and some jets in full simulation are just electrons. The same procedure is followed in ATLFAST, but these jets are remove and replaced by electrons.

Acc.	electrons	muons	leptons	jets	bjets
Fast	0.90	0.77	0.88	0.41	0.62
Full	0.89	0.74	0.85	0.49	0.59

Table 5.21: *Acceptances for each cut selections (leptons, jets, bjets).*

Figure 5.33 shows the comparison between the acceptances for different topologies after kinematic cuts (mentioned above) applied sequentially using full simulation and ATLFAST for m_A = 400 GeV. Each categorie is defined as:

• light jets: $|\eta|$ < 2.5 and p_T > 40 GeV;

• leptons: $|\eta|$ < 2.5 and p_T > 20 GeV for electrons and muons;

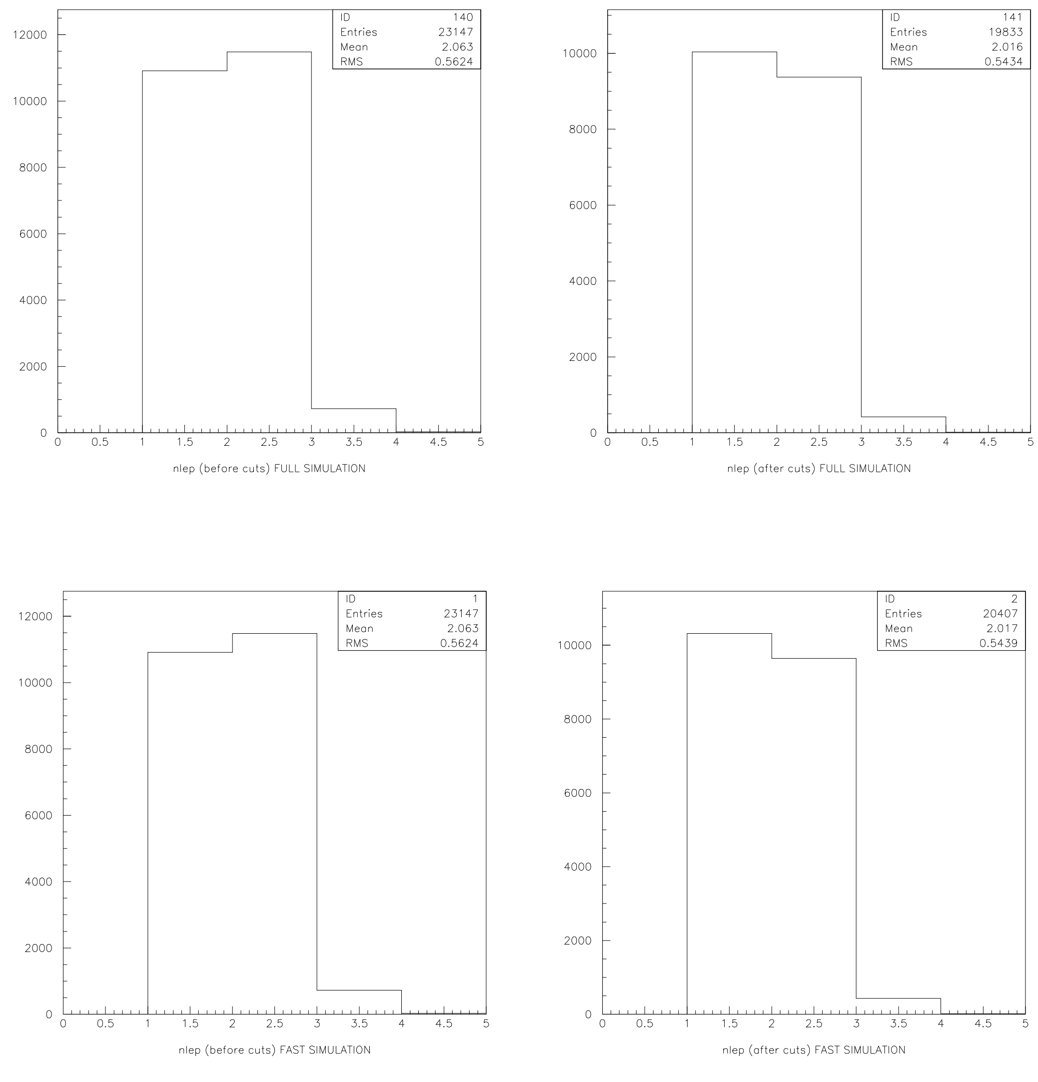

Figure 5.30: *Isolated lepton multiplicity from full (top) and fast (bottom) simulation without cuts (left) and with cuts (right), $m_{H/A} = 400$ GeV.*

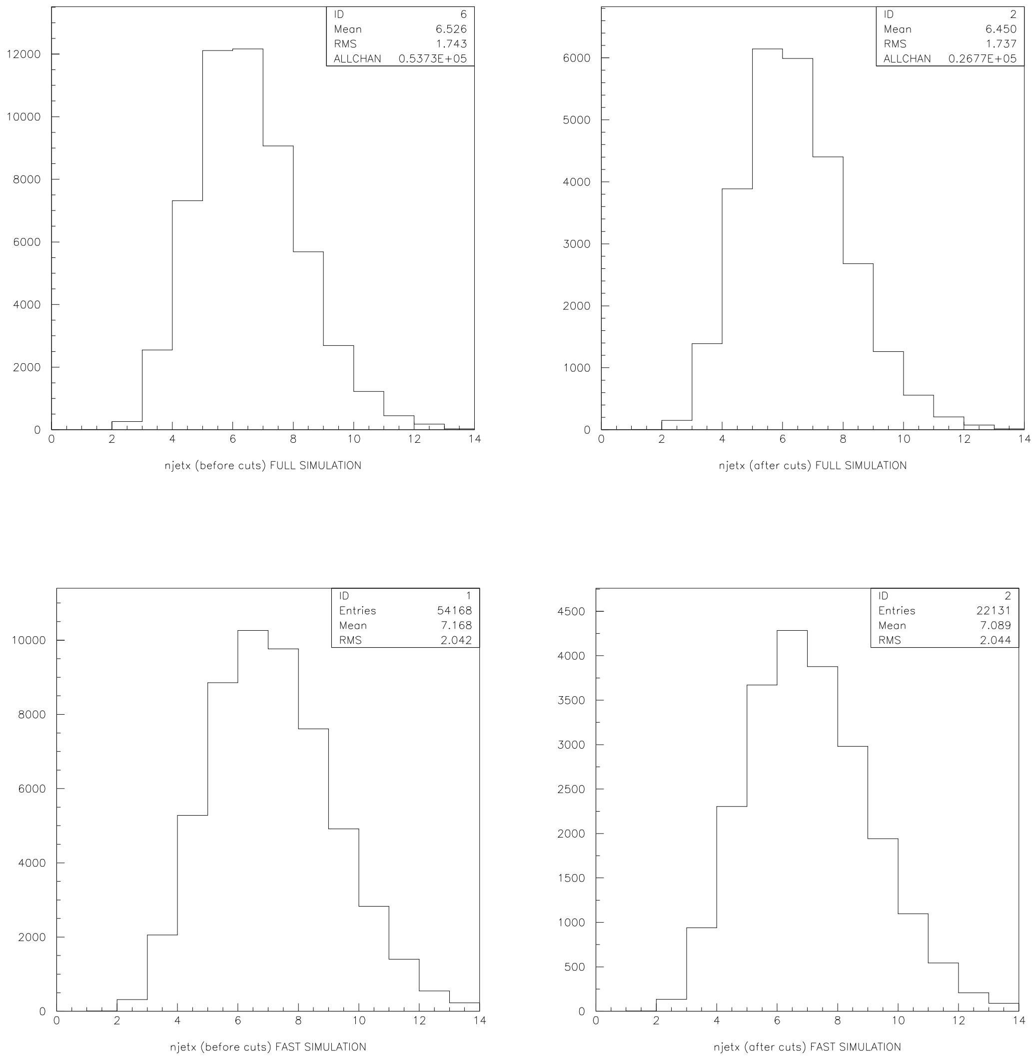

Figure 5.31: *Jets multiplicity from full (top) and fast (bottom) simulation without cuts (left) and with cuts (right), $m_{H/A} = 400$ GeV.*

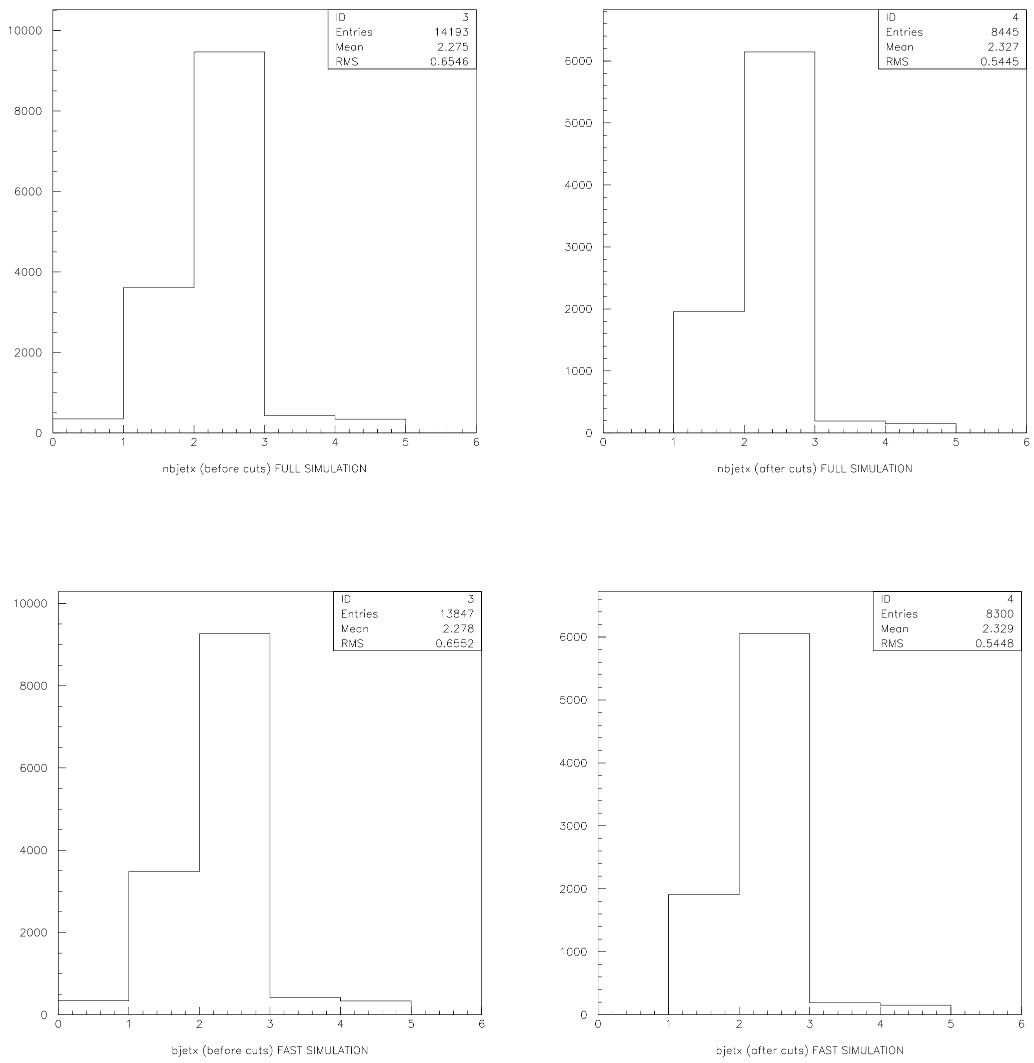

Figure 5.32: *b-labelled jets multiplicity from full (top) and fast (bottom) simulation without cuts (left) and with cuts (right),* $m_{H/A} = 400$ *GeV.*

- b-jets: $|\eta| < 2.5$ and $p_T > 40$ GeV.

The acceptances of each cut are comparable for the two types of simulation. The larger discrepancy is observed for multiplicity of light jets. This is partially due to the implementation of the jets energy threshold in both simulations [23].

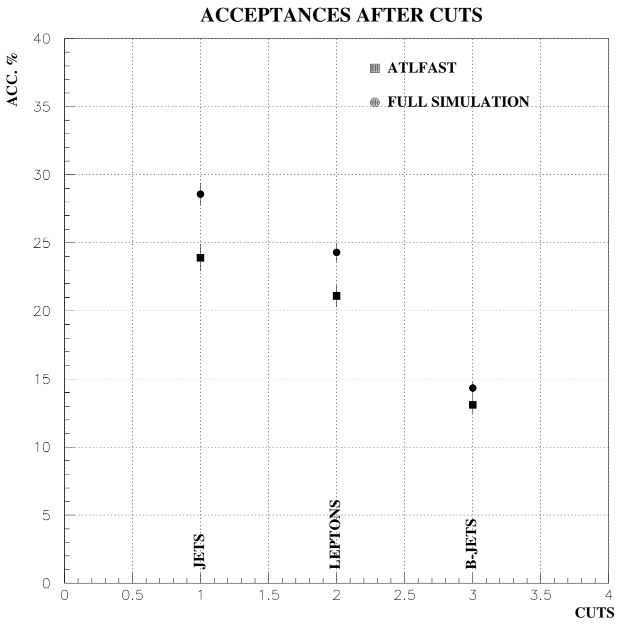

Figure 5.33: *Comparison between the acceptances for different topologies after kinematic cuts using full simulation and ATLFAST for A events, $m_A = 400$ GeV.*

In ATLFAST the transverse energies of all undecayed particles, except neutrinos, muons and SUSY LSP, are added up in the calorimeter cells with granularity 0.1×0.1 for $|\eta| < 3$ and 0.2×0.2 for $3 < |\eta| < 5$. All calorimeter cells with transverse energy greater than the chosen seed energy (1.5 GeV) are taken as possible initiators of a cluster, in order of decreasing E_T, to verify if the total E_T summed over all cells in a cone of a chosen radius (ΔR=0.4) exceeds the minimum required threshold for a reconstructed cluster (10 GeV). Only after that, clusters with transverse energy above the threshold (15 GeV) are accepted as jets (see [24] for more details).

In full simulation the cone algorithm for the A/H $\rightarrow t\bar{t}$ events has been used (starting from the combined calorimeter matrix, where the energies of calorimeter towers with granularity 0.1×0.1 are stored) with a seed = 1 GeV and a cone radius of 0.4. A sliding-window algorithm is used, looking for local energy maxima in a 3×3 cell window, by scanning the whole combined calorimeter matrix. If a window contains a local maximum and its total energy is above a 2 GeV threshold such 3×3 cell cluster is used to define a jet candidate. Only clusters with transverse energy above 12-15 GeV are accepted as jets. For each candidate the kinematic variables are calculated using information from a 9×9 cell window with the same center as the selected cluster (see [25] for more details).

After all the above cuts have been applied the final acceptances are in agreement within 2σ.

The most relevant detector effects come from the non-compesanting [25] ATLAS calorimeter and the energy loss in the dead material. These effects are η dependent because the amount and position of dead material along the shower depends on η and because different calorimeters have different levels of non-compensation. To correct these effects we have used a calorimetric jet calibration [26]. The calibration method is what we called in the TDR [25] the *Benchmark approach* which provides the *hadronic scale* and also improves the energy resolution. But this method is not providing the ultimate performace. In the future also other methods, like for example the H1 weighting [27] will be available and fully parameterised in the full η range. Such calibration however does not corrects the physics effects involved in the parton fragmentation and final state radiation.

In figures 5.34 and 5.35 the distributions of the main quantities involved in the kinematic cuts (p_T and $|\eta|$) as obtained from the full and fast simulations are shown for signal events with $m_{H/A} = 400$ GeV. In the case of full simmulation reconstructed jets are calibrated with the calorimetric calibration [26]. The mean and RMS values of the distributions are in good agreement for the two simulation packages. The transverse momentum mean value is greater in the full than in the fast simulation case. This is due to the fact that in full simulation the reconstructed momentum of the jets is slightly overstimated due to calibration problems and also because of the addition of the electronic noise; in the fast simulation the jets are not recalibrated. Consistently in both cases calibration for the physics effects is done in a separate step.

The relative difference in pseudorapidity, $\Delta\eta/\eta$, and in transverse momenta, $\Delta p_T/p_T$, for quantities reconstructed with the fast and full simulations are shown in figure 5.36 for light quarks and b-jets. The accuracy of the comparison is good, showing much larger tails and worse resolution for p_T than for η. It is also resonable because there is better agreement between light jets than between b-jets.

5.5.2 Three proposed recalibration methods

The recalibration factors, that are provided in this subsection, are corrections for the physics effects involved in the parton fragmentation, Final State Radiation (FSR), etc, as is explained below.

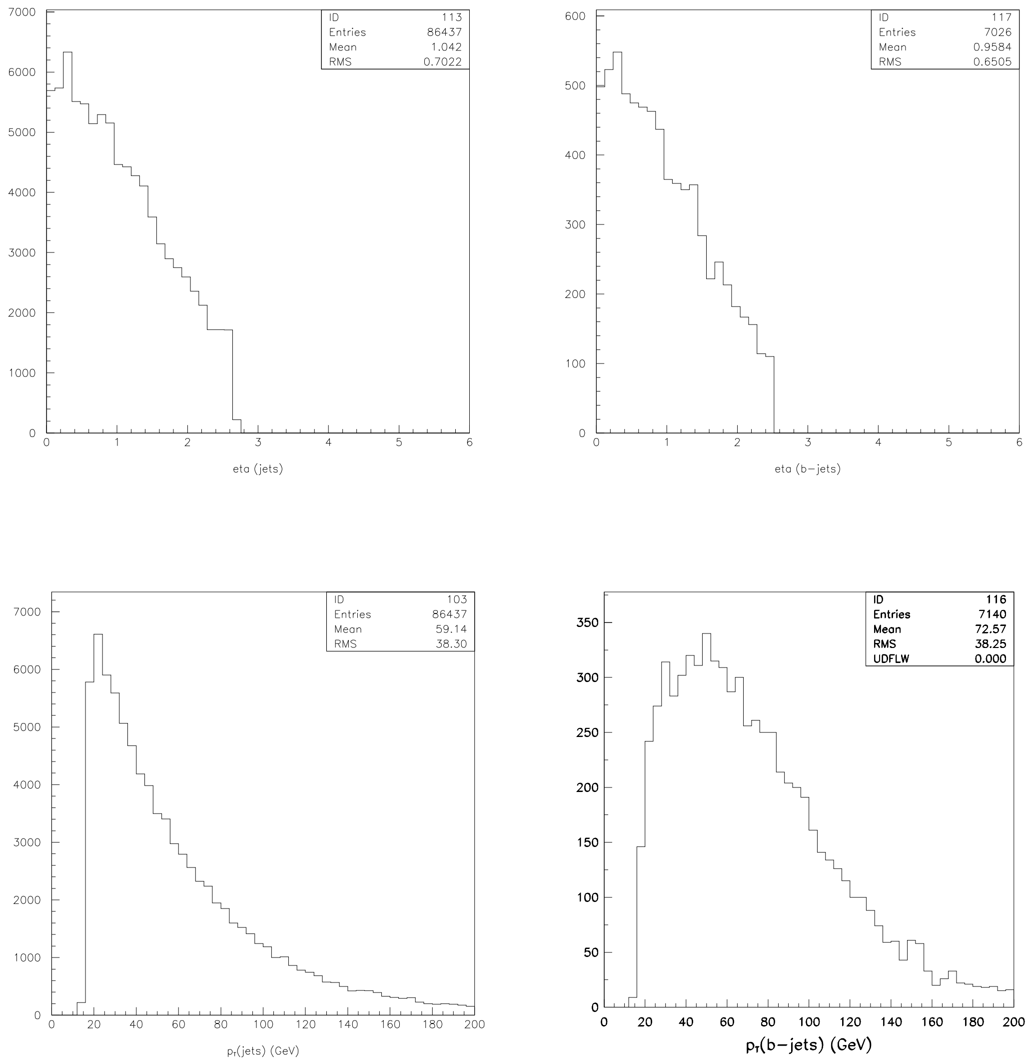

Figure 5.34: *Distributions from full simulation of the quantities involved in kinematic cuts for H/A events, $m_{H/A}$ = 400 GeV. a) $|\eta|$ distribution for light jets, b) $|\eta|$ distribution for b-jets, c) p_T^{jets} distribution for light jets and d) p_T^{b-jets} distribution for b-jets.*

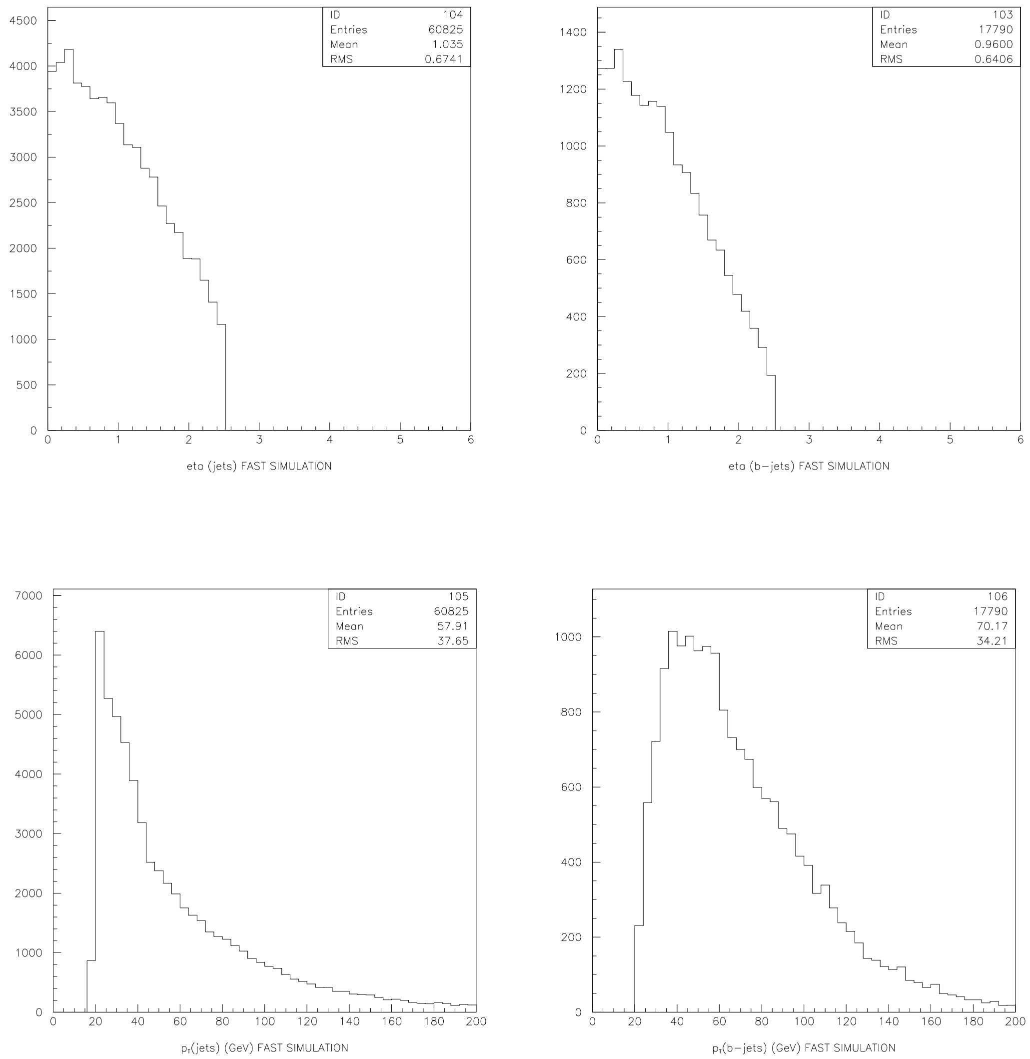

Figure 5.35: *Distributions from ATLFAST of the quantities involved in kinematic cuts for H/A events,* $m_{H/A} = 400$ *GeV. a)* $|\eta|$ *distribution for light jets, b)* $|\eta|$ *distribution for b-jets, c)*p_T^{jets} *distribution for light jets and d)* p_T^{b-jets} *distribution for b-jets.*

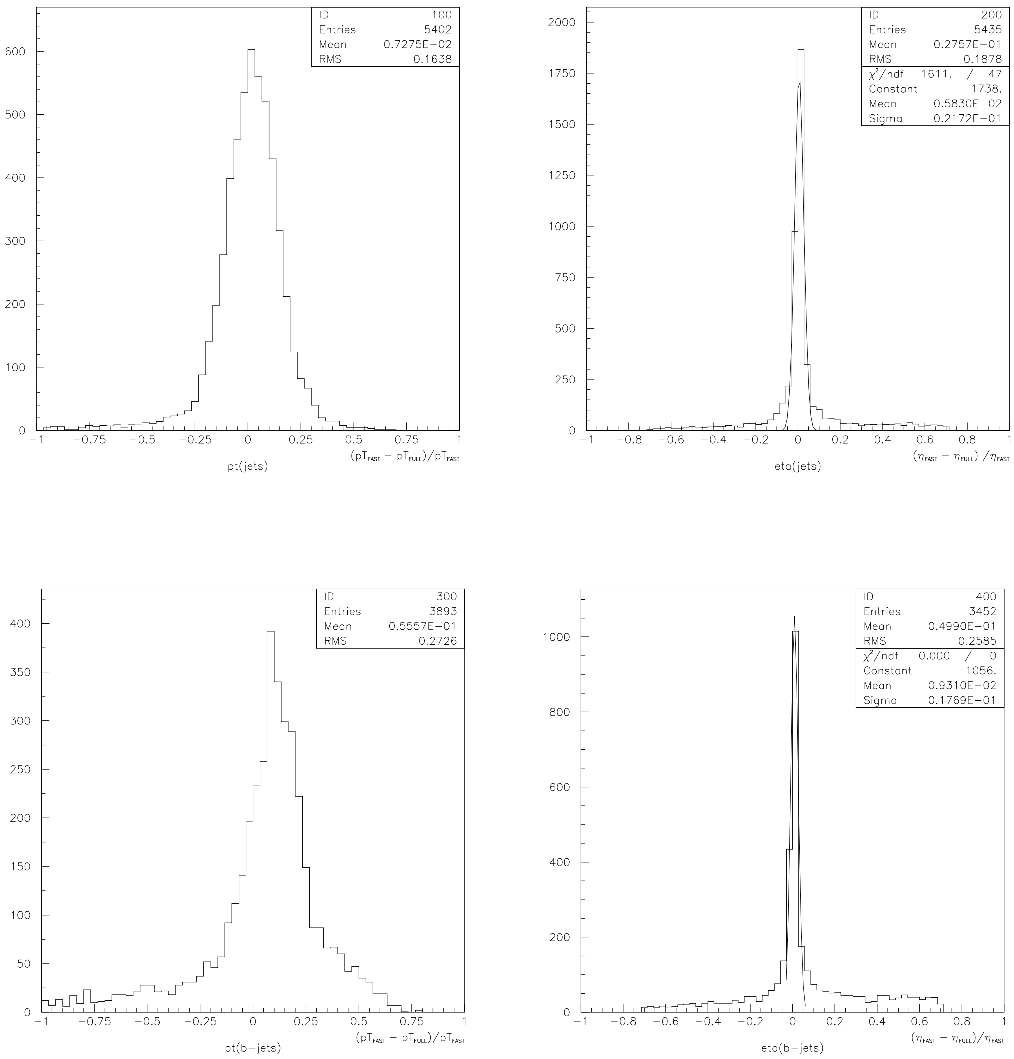

Figure 5.36: *The $\Delta p_T/p_T$ (left) and $\Delta\eta/\eta$ (right) distributions for quantities reconstructed with the fast and full simulations for light jets (top) and b-jets (bottom), $m_{H/A}$ = 400 GeV.*

A jet is reconstructed as the deposited measurable energy resulting from a parton produced in the hard interaction. When a jet is reconstructed, not all particles produced in the fragmentation can be collected. The magnetic field sweeps out the low p_T particles, but the area of the calorimeter where the energy is collected can not be arbitrarily large for various reasons: optimisation of signal to noise (electronic noise or minimum bias), another jet closed-by. So usually the reconstructed jet is restricted to a *cone*. To go back to the initial parton energy one has to correct for the fragmentation effects and out of cone losses. This correction depends on the physics processes under consideration: the amount of Final State Radiation or the type of the initiating parton (light quark, b-quark).

The following three methods were used to correct these effects: *Z+jet (average)*, *recalibration with neighbour jet* and *Z+jet (mean)*. The comparison between the different physics calibration methods is shown after the jets reconstructed with full simulation are corrected with the calorimetric calibration [26].

5.5.2.1 Z+jet (average) method

The jet momenta are recalibrated by a calibration factor $K_{jet} = < p_T^{parton}/p_T^{jet} >$. Where, p_T^{parton} denotes the transverse momentum of the parton initiating the jet (before FSR). Figure 5.37 shows these calibration factors as a function of p_T^{jet} for the b-jets and light quarks and for fast and full simulation, respectively. We make a fit to the histogram and use fitted function to recalibrate. The recalibration histograms for light quarks are more similar than for b-jets. This is because the shape of the p_T^{jet} distribution for b-jets is more different between the fast and the full simulations than for light quarks (see figures 5.34 and 5.35).

The recalibration coefficient values should be larger than 1.0. At high-p_T ($>$ 80 GeV) unphysical values of recalibration coefficients ($<$ 1) are seen. This is because the high-p_T jets come from high-p_T W's and as a consequence of the boost the two jets tend to pile-up. Using the jet algorithm, the jet with higher p_T is first reconstructed and the cells used in the reconstruction cone can have energies belonging to the other jet.

5.5.2.2 Recalibration with neighbour jets method

The recalibration coefficient (figure 5.37) is quite high for low-p_T jets. That is because the out-of-cone energy losses are higher for low-p_T events and the associated jets usually

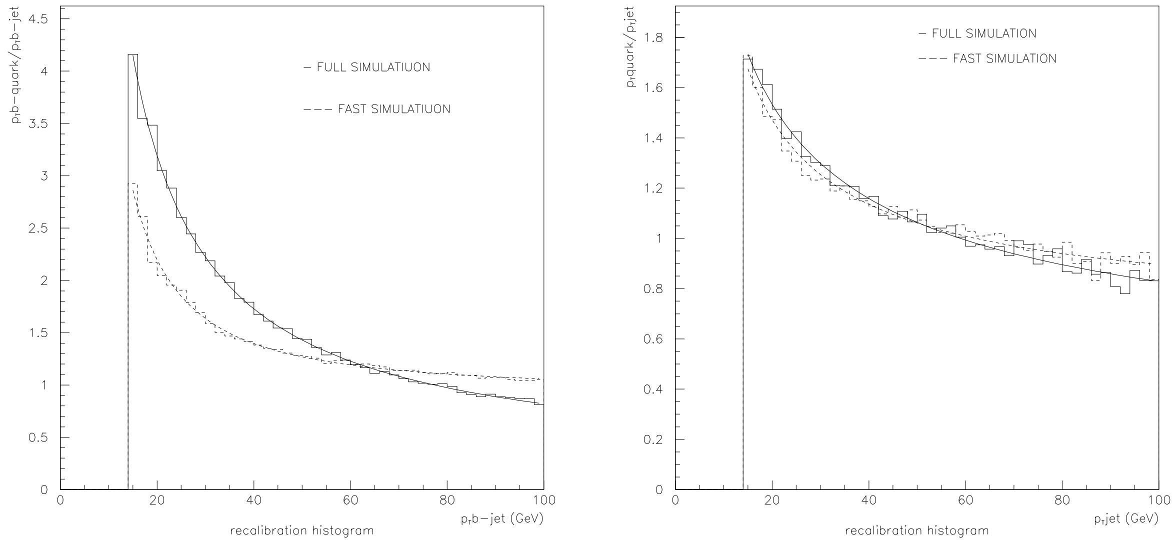

Figure 5.37: *Recalibration histograms. Calibration factor* $K_{jet} = < p_T^{parton}/p_T^{jet} >$ *as a function of* p_T^{b-jet}*, a) for b-jets, b) for light quarks; both for fast and full simulations.*

loos a lot of energy in FSR. An idea to improve the recalibration coefficients could be to add neighbour jets. The FSR process is depicted on figure 5.38.

Considering events with low-p_T b-jets one can observe that those b-jets come from b-quarks which loosed about half of their energies on FSR. Usually most of this energy is taken by one or few gluons; so one should expect a gluon jet to be close to the b-jet. The method consists in taking a group of jets (usually one!) in a larger cone around b-jets and treat them as a single jet. One should add their energies but also correct their direction.

Figure 5.39 compares the calibration factors for *Z+jet (average)* method after the above mentioned procedure has been applied as a function of p_T^{jet} for the b-jet, for fast and full simulation. The fitted function is used to recalibrate jets.

5.5.2.3 Z+jet (mean) method

This method is in fact similar to the Z+jet (average) method but instead of taking the average value of the P_T^{quark}/P_T^{jet} distribution, the mean of the fit peak position is used to extract the calibration factors. The main objection against the previous

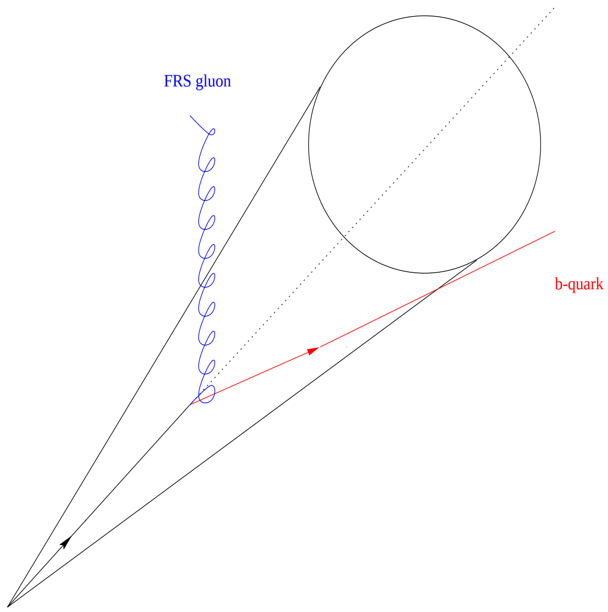

Figure 5.38: *Final State Radiation diagram (FSR) process.*

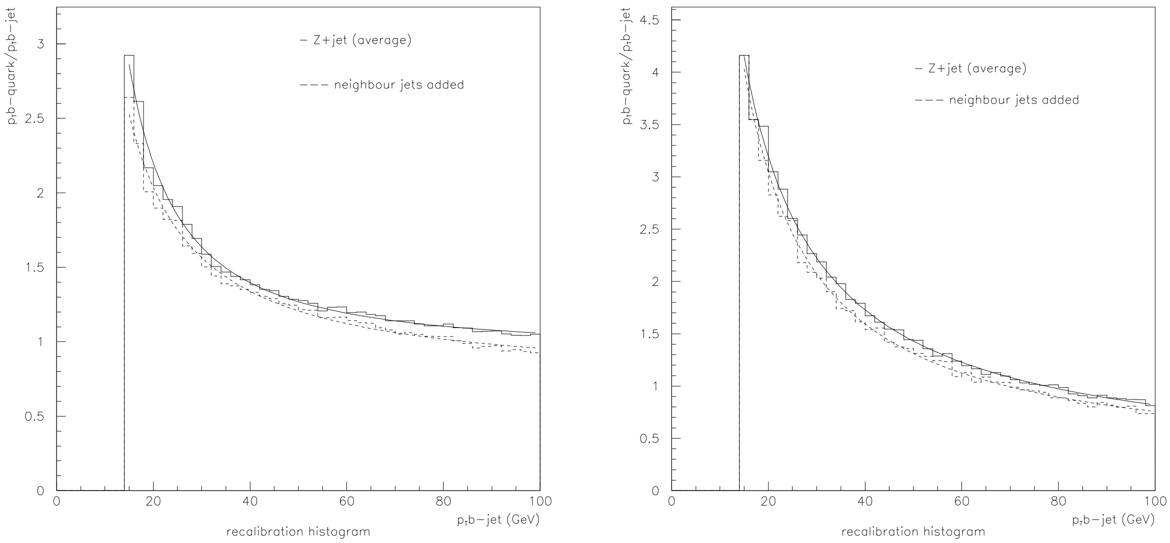

Figure 5.39: *Calibration factor,* $K_{b-jet} = < p_T^{b-quark}/p_T^{b-jet} >$ *as a function of* p_T^{b-jet}. *Comparison of recalibration histograms for fast simulation (left) and for the full one (right plot) obtained in both methods: Z+jet (average) and with addition of neighbour jets.*

recalibration is that the P_T^{jet}/P_T^{quark} distribution was not peaked at 1 after jet detector effect calibrations.

Figure 5.40 shows the P_T^{jet}/P_T^{quark} distributions for the b-jets and light quarks for several P_T^{jet} ranges and using the Z+jet (average) method. The distributions for the (0-200 GeV) range are peaked around of 0.95.

So the first step is to obtain the P_T^{jet}/P_T^{quark} distribution (after calorimetric calibration) being peaked at 1 (with some tails). This corresponds to what is described in TDR [28] as the Z+jet (mean) method.

Figure 5.41 shows these calibration factors as a function of p_T^{jet} for the b-jets and for the light jets using the Z+jet (mean) method. We recalibrate the energy of all the jets using the parametrization shown in this figure.

Figure 5.42 shows the P_T^{jet}/P_T^{quark} distributions for the b-jets and light jets for several P_T^{jet} ranges and using the Z+jet (mean) method. The distributions for the (0-200 GeV) range are peaked around of 0.99. Now the P_T^{jet}/P_T^{quark} is peaked around 1 with an accuracy about 1% (ATLAS precision on the mass scale [9]). In the (50-70 GeV) and (70-90 GeV) ranges, the distributions show tails on the right side. It means that P_T^{jet} is greater than P_T^{quark}, this is because the high-p_T jets come from high-p_T W's. As a consequence of the boost the two jets tend to pile-up and the cells used in the reconstruction cone can have energies belogin to the other jet.

Figure 5.43 shows the P_T^{jet}/P_T^{quark} distribution for the b-jets after calorimetric jet calibration and after calorimetric and Z+jet (mean) calibrations. In figure 5.44 the equivalent plots for light quarks are shown. We can observe the jet calibration related with the detector and physics effects. So, to go to back to the intial parton energy, one has to correct the physics (Z+jet method) and the detector effects (calorimetric calibration).

5.5.3 Reconstruction of the H/A $\rightarrow$ t$\bar{\text{t}}$

Several algorithms for reconstruction of the invariant mass of the t$\bar{\text{t}}$ pairs have been studied. The detailed description of the algorithms used for the reconstruction have been presented in previous subsection 5.4.2.2.

The procedure for the reconstruction of top-quark pairs consists in taking all jjb and blν pairs. Events with both $m_{jjb(bl\nu)} = m_{top} \pm 30$ GeV are retained, and the $m_{jjb}(bl\nu)$ are rescaled to m_{top}. For each event only one combination (jjb)(blν), giving the best value of $\chi^2 = (m_{bl\nu} - m_t)^2/\sigma_{bl\nu} + (m_{jjb} - m_t)^2/\sigma_{jjb}$ is selected.

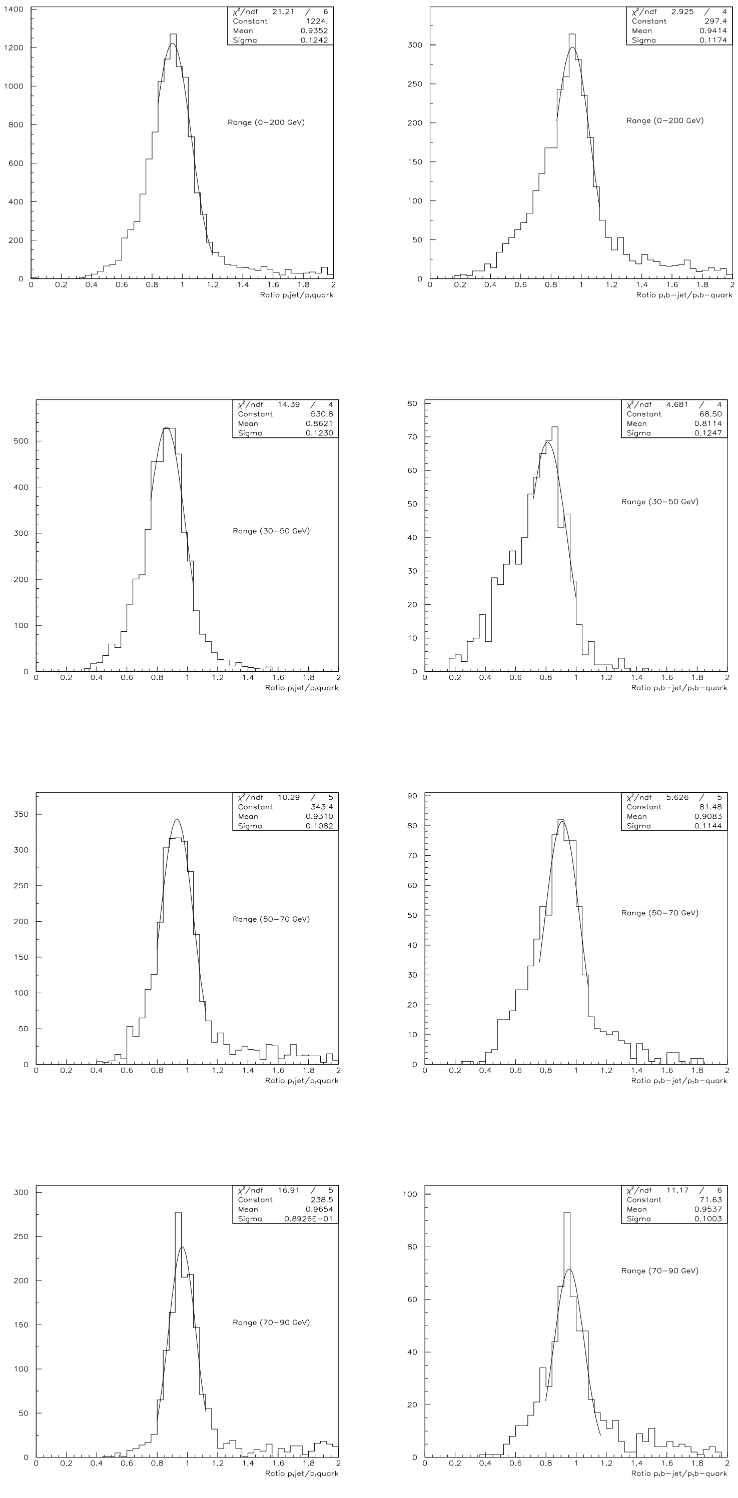

Figure 5.40: P_T^{jet}/P_T^{quark} *distributions for light quarks (left) and for b-jets (right plot) for several* P_T^{jet} *ranges and using the Z+jet(average) method.*

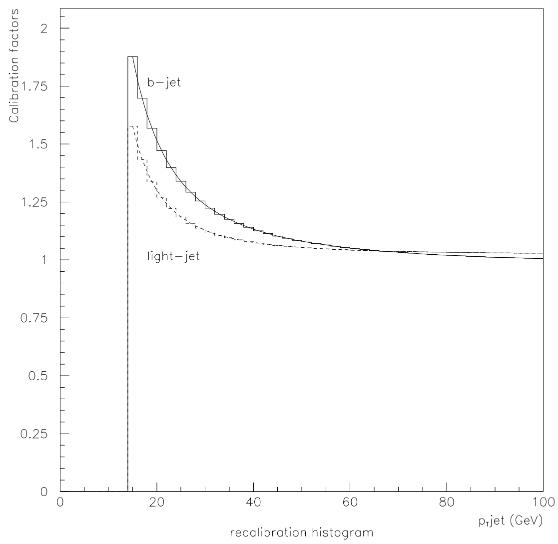

Figure 5.41: *Recalibration histograms using the Z+jet (mean) method. Calibration factor,* $K_{jet} = < p_T^{parton}/p_T^{jet} >$ *as a function of* p_T^{jet}.

5.5.3.1 Z+jet (average) method

For the single top-quark reconstruction in the hadronic channel, all possible jj combinations are examined; the distribution of their invariant mass m_{jj} is shown in figure 5.45 for the fast and full simulation. The mass peak is around 80 GeV (p_T>40 GeV) and u-jets with this energy may not need to be recalibrated (the recalibration coefficient is close to 1 for energy greater than 40 GeV). A more pronounced peak is observed in the fast than in the full simulation case, this is because the resolution is worse in the full than in the fast simulation and the combinatorial background is larger for the full simulation. For each candidate with m_{jj} = 80 ± 20 GeV the jj four momentum is rescaled to impose the constraint $m_{jj} = m_W$; the two possible jjb combinations are considered. Out of all possible jjb combinations the one which minimises the value of $\chi^2 = (m_{jjb} - m_t)^2$ is chosen. Figure 5.46 shows the reconstructed invariant mass under the last condition for fast and full simulation. The resulting m_W resolutions were 18.4 and 21.7 GeV for fast and full simulation, respectively. In the full simulation case, the resolution for the m_W has been obtained selecting the candidates with m_{jj} = 80 ± 20 GeV and then doing the fit. The m_{jjb} invariant mass resolutions were σ = 18.7 GeV and σ = 22.7 GeV for fast and full simulation, respectively.

The reconstruction of the semileptonic channel W $\rightarrow l\nu$ is limited by the impossibility

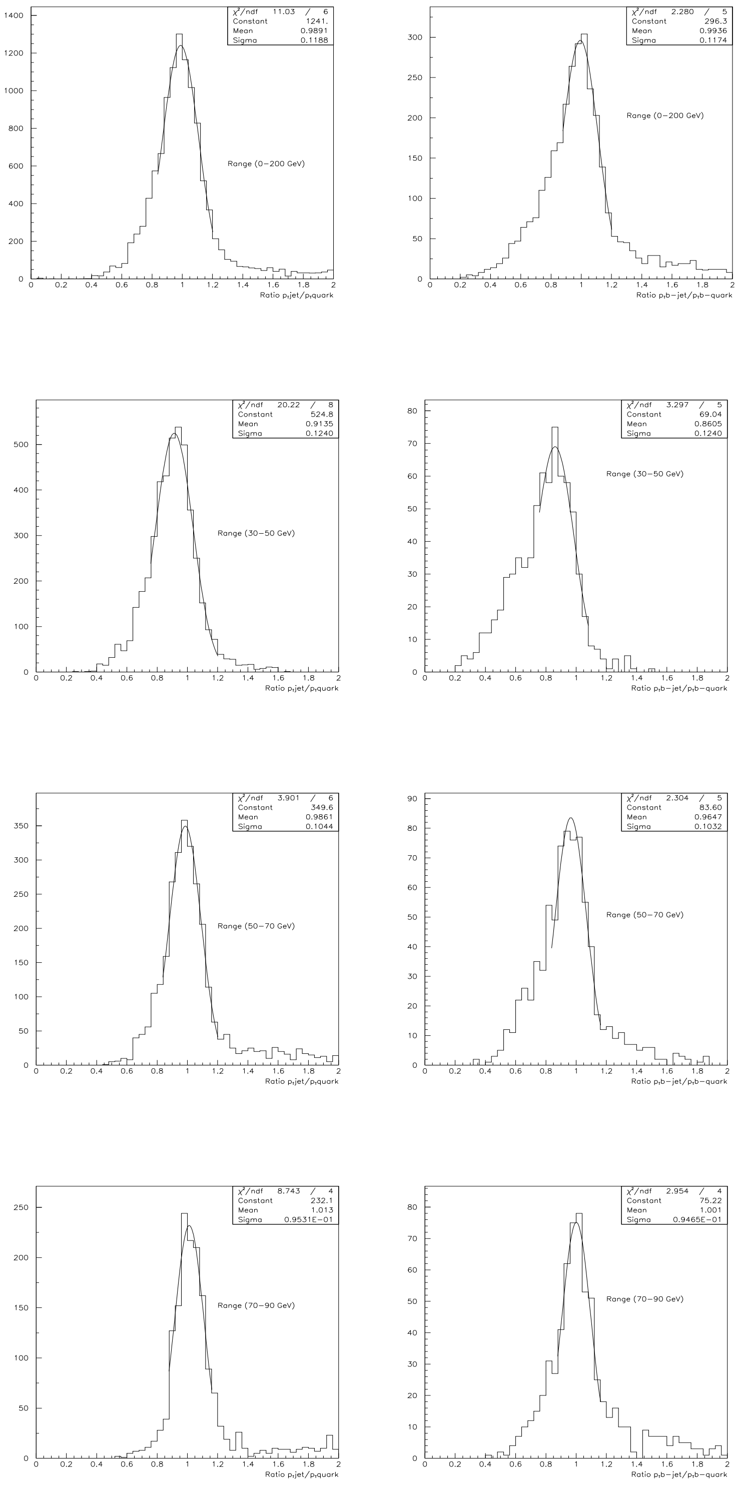

Figure 5.42: P_T^{jet}/P_T^{quark} *distributions for light quarks (left) and for b-jets (right plot) for several* P_T^{jet} *ranges and using the Z+jet (mean) method.*

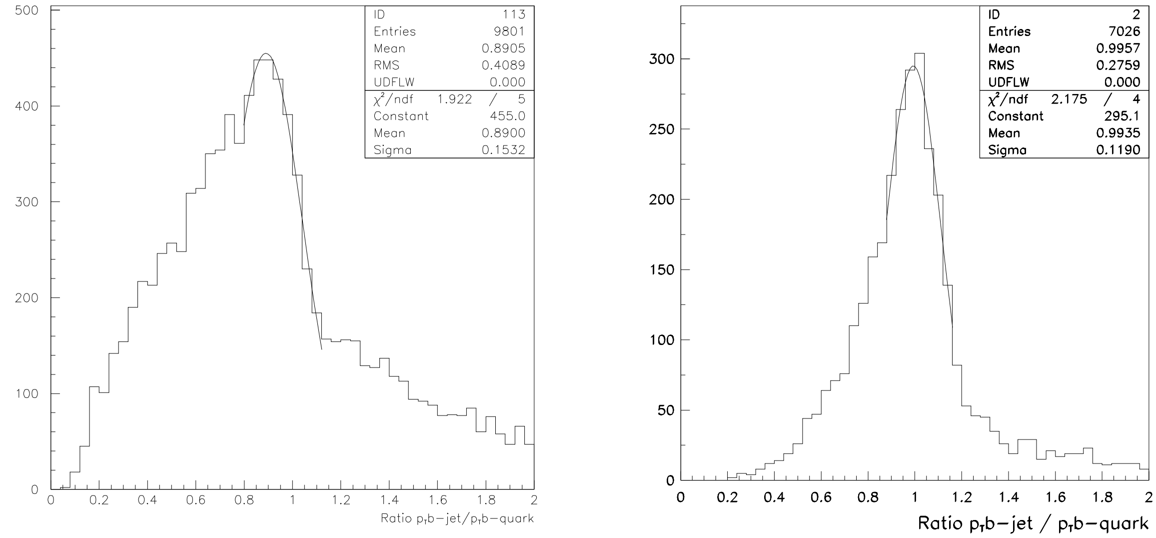

Figure 5.43: $P_T^{b-jet}/P_T^{b-quark}$ *distributions for b-jets after calorimetric jet calibration (left) and after calorimetric and Z+jet (mean) calibrations (right plot).*

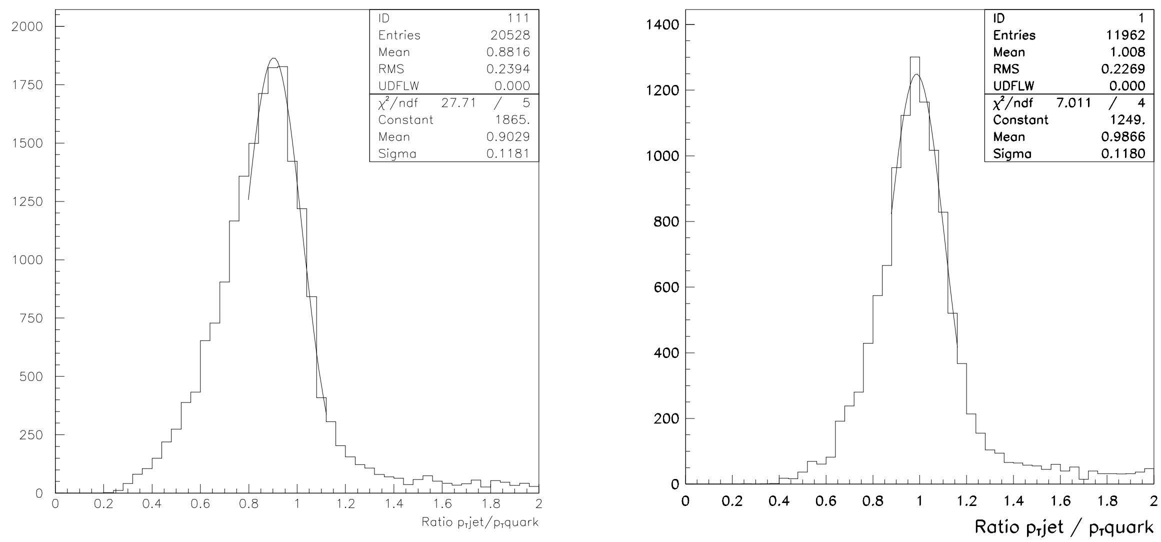

Figure 5.44: P_T^{jet}/P_T^{quark} *distributions for light-jets after calorimetric jet calibration (left) and after calorimetric and Z+jet (mean) calibrations (right plot).*

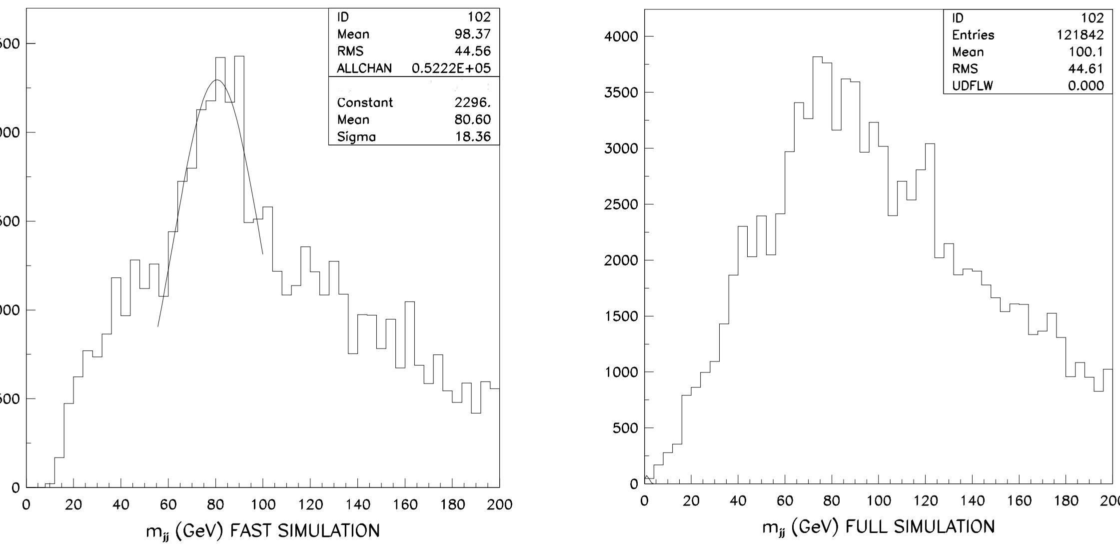

Figure 5.45: *Distribution of reconstructed invariant mass for jet pairs, m_{jj} in fast (left) and full (right) simulation.*

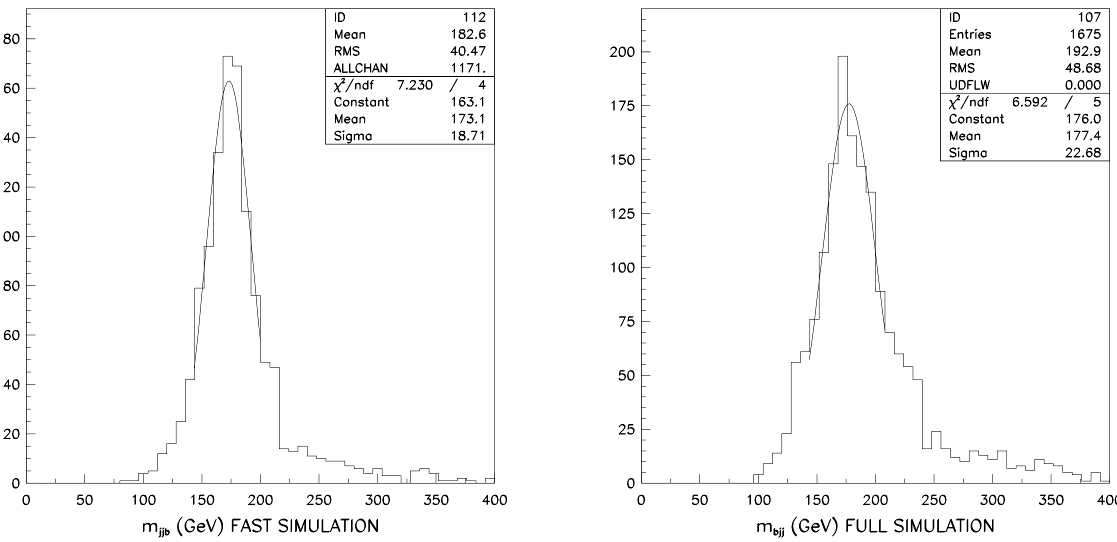

Figure 5.46: *Distribution of reconstructed $t \to jjb$ invariant mass, for the best combination of jjb for fast (left) and full (right) simulation.*

of reconstructing the neutrino four-momentum. The transverse components of the neutrino momentum (p_x^ν, p_y^ν) are recovered from the components of the missing energy (p_x^{miss}, p_y^{miss}) in the event, while the information on the longitudinal component (p_z^ν) is lost because of the large amount of energy escaping down the beampipe. The component p_z^ν can be extracted solving the equation (5.13) for the W-boson mass, which requires the reconstructed neutrino and lepton system to form the W-mass.

$$m_W^2 = (E^\nu + E^l)^2 - (p_x^\nu + p_x^l)^2 - (p_y^\nu + p_y^l)^2 - (p_z^\nu + p_z^l)^2 \tag{5.13}$$

where $p_x^\nu = p_x^{miss}$, $p_y^\nu = p_y^{miss}$ and the neutrino is assumed to be massless.

For events containing a reconstructed $W \to l\nu$ candidate, each of the four possible b$l\nu$ combinations is considered and the one which best reconstructs the top-quark mass, i.e. which minimises the value $\chi^2 = (m_{bl\nu} - m_t)^2$, is chosen as the top-quark candidate. Figure 5.47 shows the resulting $m_{bl\nu}$ distributions for fast and full simulation. In both cases we have taken the lepton and neutrino from fast simulation. Resolutions of $\sigma =$ 11.9 and 13.0 GeV are obtained for fast and full simulation, respectively.

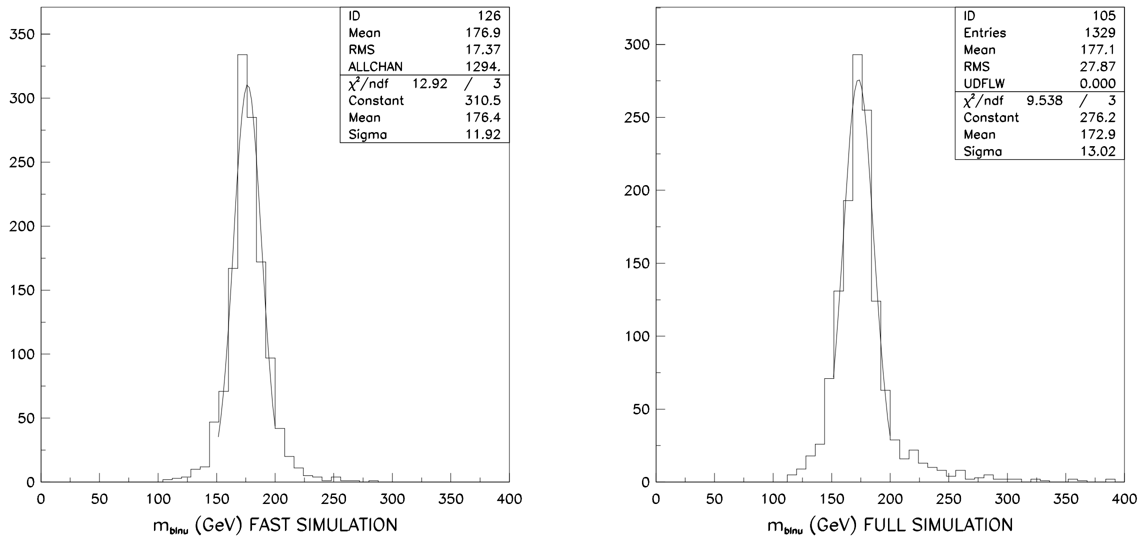

Figure 5.47: *Distribution of reconstructed $t \to bl\nu$ invariant mass, for the best combination of $bl\nu$ for fast (left) and full (right) simulation. In both cases the $W \to l\nu$ has been reconstructed with fast simulation.*

The procedure for the reconstruction of top-quark pairs consists in taking all posible jj combinations and applying the W-mass constraint, then all possible $l\nu$ combinations plus two b-jets are considered and a loop over (jjb, $bl\nu$) pairs is performed. After, the best combinations, which minimise the value of the equation (5.14) are taken into account.

$$\chi^2 = (m_{jjb} - m_t)^2/\sigma_{jjb} + (m_{bl\nu} - m_t)^2/\sigma_{bl\nu} \tag{5.14}$$

Figure 5.48 shows the distributions of $m_{bl\nu}$ and m_{jjb} for full and fast simulation selected as optimal for the top quark pairs reconstruction inside the chosen mass window and for the low-luminosity b-tagging performance.

Once both top-quarks are reconstructed, their 4-vectors can be rescaled by applying a constraint on m_t before reconstructing $m_{H/A}$. Figure 5.49 shows the m_{tt} mass distribution for fast and full simulation and for $m_A = 400$ GeV. The expected resolution is $\sigma = 16.7$ and 24.0 GeV for fast and full simulation, respectively.

In summary, the two simulation packages are in good agreement for the cuts acceptance. The m_W, m_{jjb} and m_{tt} resolutions are in reasonable agreement (in comparison with other similar studies [28]), with the full simulation predicting resolutions which are 10-25% worse than those from the fast simulation. In the case $m_{bl\nu}$ this agreement is too optimistic because both $W \to l\nu$ have been reconstructed with the fast simulation.

5.5.3.2 Neighbour jets method

We can reconstruct the invariant mass distributions and to see the difference in the distribution shape for the Z+jet (average) method and for the method which adds the neighbour jets.

After reconstructing the W $\to$ jj candidates, as described in the previous sections, the obtained distributions are the same due to the fact that only the recalibration factors of b-jets have been used. Figure 5.50 shows the reconstructed t $\to$ jjb invariant mass with neighbour jets added for fast and full simulation. The m_{jjb} invariant mass resolutions are 16.9 GeV and 21.7 GeV for fast and full simulation, respectively.

Figure 5.51 shows the resulting $m_{bl\nu}$ distributions for fast and full simulation with neighbour jets added. The resolution is $\sigma = 11.2$ GeV and 13.9 GeV for fast and full simulation, respectively. The reconstructed lepton and the missing energy (neutrino) have been taken from fast simulation in both cases.

On figure 5.52 one can see the m_{tt} distribution for the method with neighbour jets added for fast and full simulation. The m_{tt} invariant mass resolutions are 19.3 GeV and 21.2 GeV for fast and full simulation, respectively.

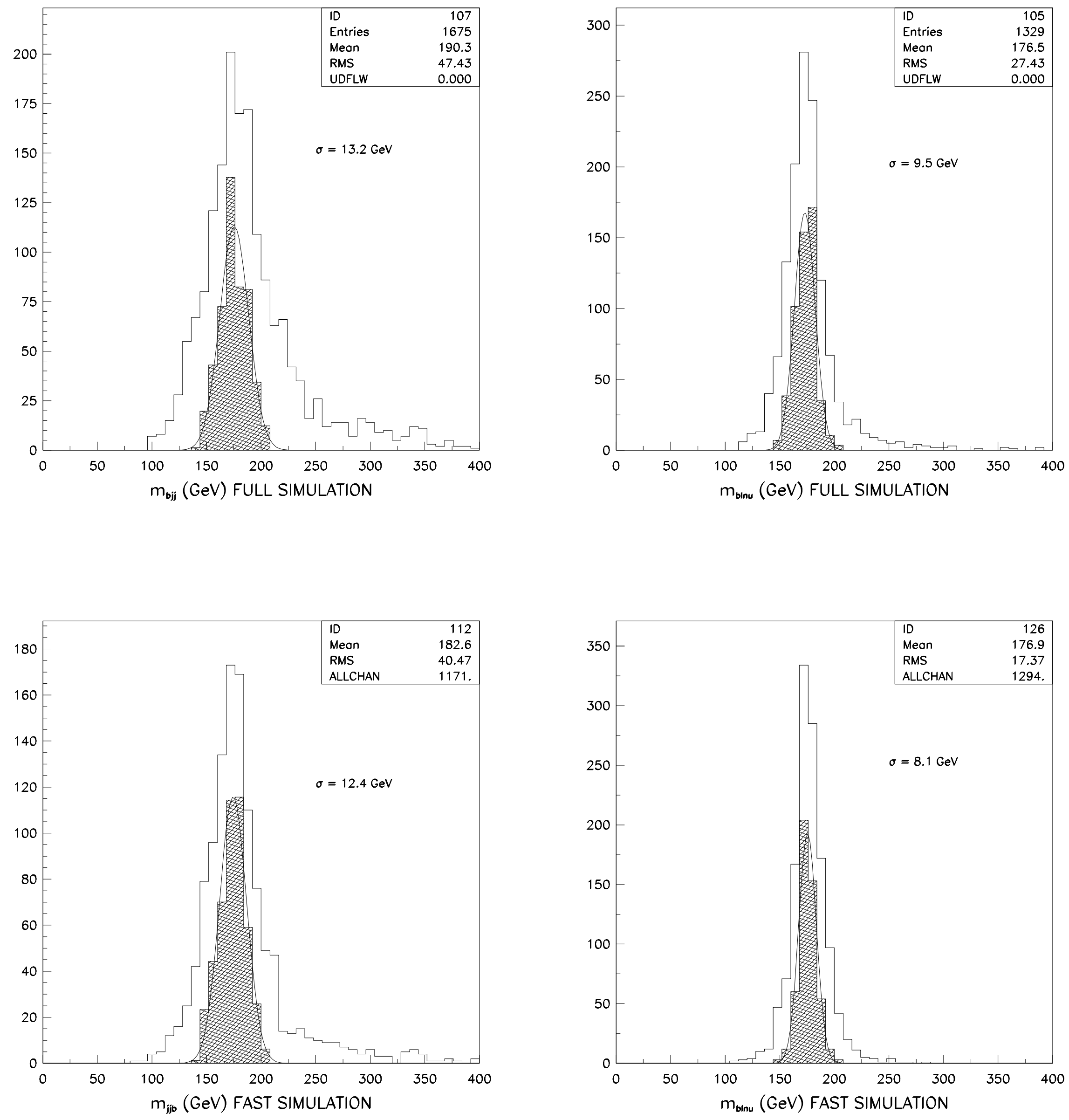

Figure 5.48: *Expected* $m_{bl\nu}$ *(right)* , m_{jjb} *(left) distributions for full (top) and fast (bottom) simulation and for an integrated luminosity of 3* 10^4 pb^{-1}. *The shaded histogram denotes events for which both top-quarks are reconstructed inside the chosen mass window.*

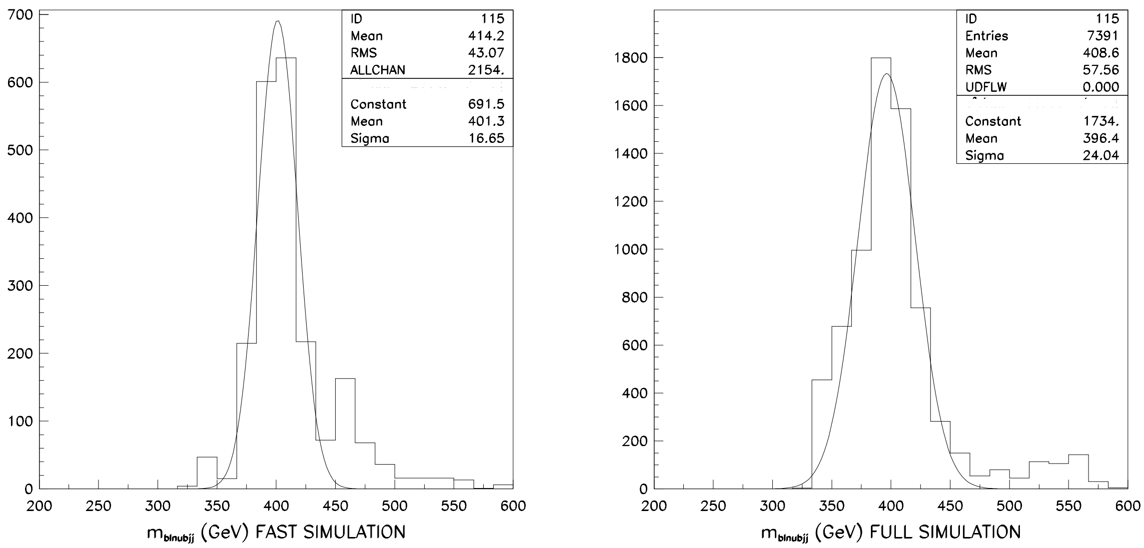

Figure 5.49: *Reconstructed invariant mass distribution of the $t\bar{t}$ pairs, for $m_A = 400$ GeV and for fast (left) and full (right) simulation.*

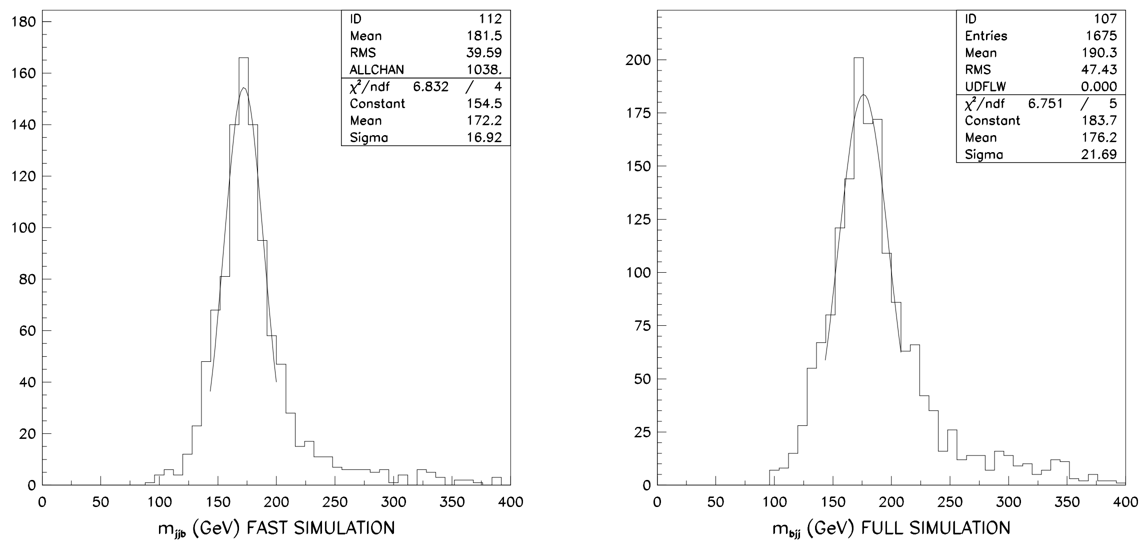

Figure 5.50: *Distribution of the reconstructed $t \to jjb$ invariant mass, for the best combination of jjb for fast (left) and full (right) simulation using the neighbour jets method.*

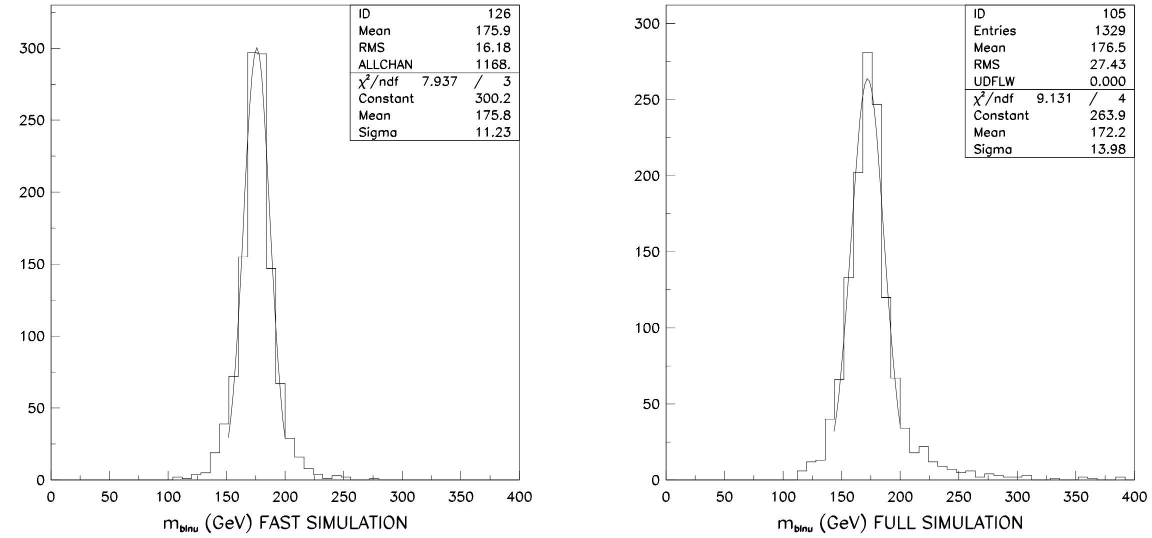

Figure 5.51: *Distribution of the reconstructed $t \to bl\nu$ invariant mass, for the best combination of $bl\nu$ for fast (left) and full (right) simulation with addition of neighbour jets. In both cases the $W \to l\nu$ is reconstructed from fast simulation.*

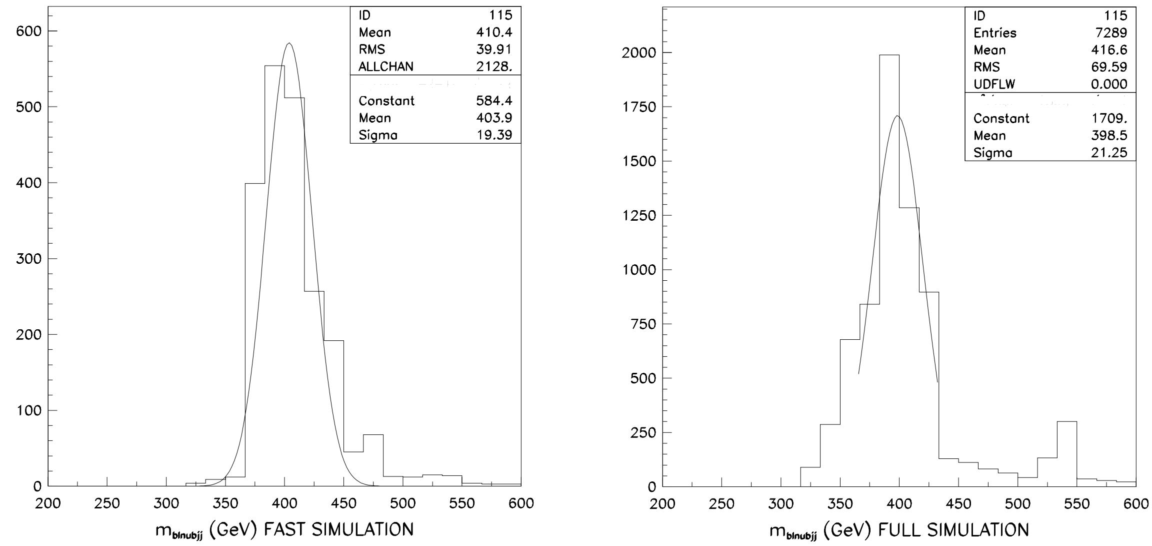

Figure 5.52: *Reconstructed invariant mass distribution of the $t\bar{t}$ pairs, for $m_A = 400$ GeV, for fast (left) and full (right) simulation and with addition of neighbour jets.*

The same behaviour is observed in the mass resolution, the m_{jjb} and m_{tt} mass resolutions are in reasonable agreement [28], with the full simulation predicting resolutions which are 10-20% worse than those from the fast simulation.

The resolution improves adding the neighbour jets (see Table 5.22). For example, the m_{tt} invariant mass resolution is 21.2 GeV for the neighbour jets added and 24.0 GeV for the traditional method in the full simulation case.

Table 5.22: *Invariant mass resolution obtained with the recalibration neighbour jets and the Z+jet (average) method for the fast and full simulation, respectively.*

Resolution	Fast simulation		Full simulation	
	Z+jet (average) σ (GeV)	Neighbour σ (GeV)	Z+jet (average) σ (GeV)	Neighbour σ (GeV)
$t \to bjj$	18.71	16.92	22.68	21.69
$t \to bl\nu$	11.92	11.23	13.02	13.98
m_{tt}	19.39	16.65	24.04	21.25

5.5.3.3 Z+jet (mean) method

We can reconstruct the invariant mass distributions and to see the differences in the distribution shapes for the Z+jet (average) and the Z+jet (mean) method.

The procedure is:

- for fast simulation we use the parametrization obtained with Z+jet (mean) method;

- for full simulation we use the calorimetric jet calibration provided by the ATLAS calorimeter and then we apply Z+jet (mean) parametrization (the same as above).

The algorithm for reconstructing the invariant masses is the same that in the previous sections. Figure 5.53 shows the reconstructed invariant mass for the hadronic channel W $\to$ jj. The resulting m_W resolutions were 13.7 and 15.2 GeV for fast and full simulation, respectively. In the full simulation case, the resolution for the m_W has been obtained selecting the candidates with $m_{jj} = 80 \pm 20$ GeV and then doing the fit.

Figure 5.54 shows the reconstructed t $\to$ jjb invariant mass using the parametrization obtained with Z+jet (mean) method for fast and full simulation. The m_{jjb} invariant mass resolutions are 13.9 GeV and 21.1 GeV for fast and full simulation, respectively.

Figure 5.55 shows the resulting $m_{bl\nu}$ distributions for fast and full simulations. The resolutions are 11.5 GeV and 12.7 GeV for fast and full simulation, respectively.

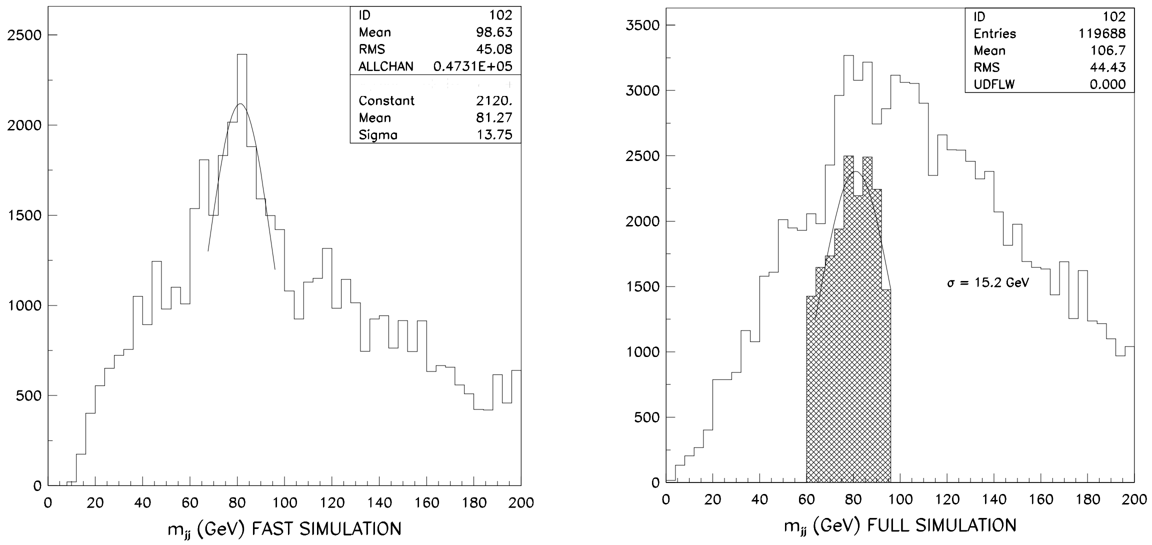

Figure 5.53: *Distribution of reconstructed invariant mass for jet pairs, m_{jj} in fast (left) and full (right) simulation using the Z+jet (mean) method. The shaded histogram denotes events chosen as optimal ones for the $t \to jjb$ reconstruction.*

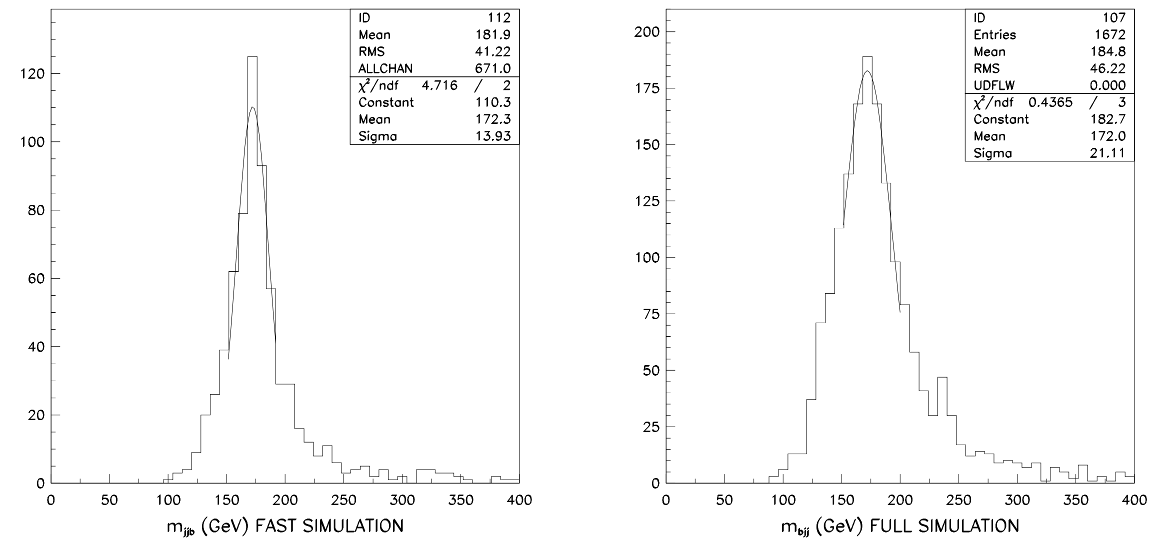

Figure 5.54: *Distribution of the reconstructed $t \to jjb$ invariant mass, for the best combination of jjb for fast (left) and full (right) simulation using the Z+jet (mean) method.*

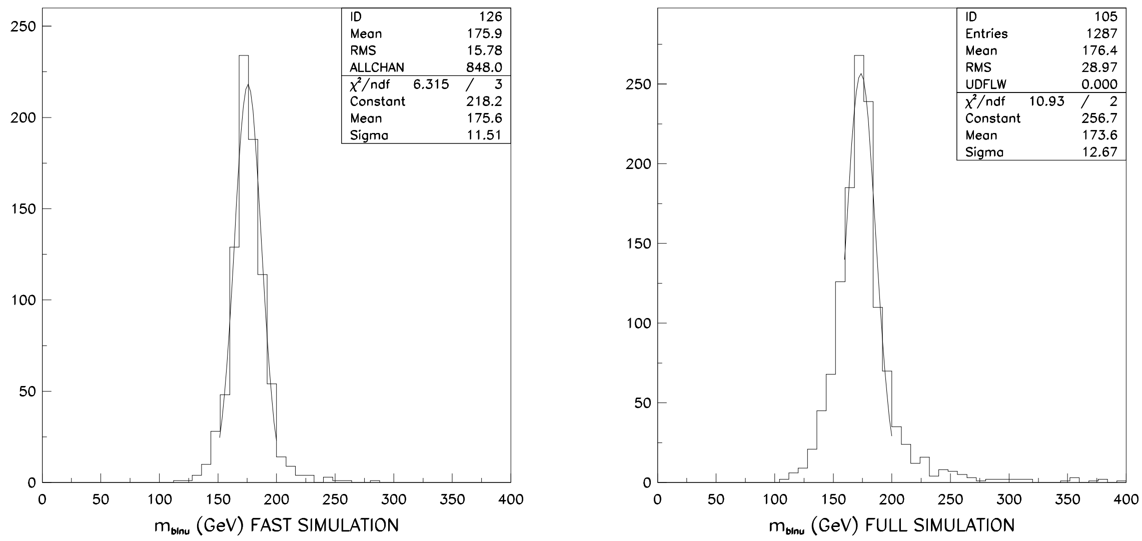

Figure 5.55: *Distribution of the reconstructed $t \to bl\nu$ invariant mass, for the best combination of $bl\nu$ for fast (left) and full (right) simulation using the Z+jet (mean) method.*

Figure 5.56 shows the m_{tt} mass distribution for fast and full simulation. The expected resolution is 17.2 GeV and 17.5 GeV for fast and full simulation, respectively.

The m_W, m_{jjb} and m_{tt} resolutions are in reasonable agreement (in comparison with other similar studies), with the full simulation predicting resolutions which are 10-20% worse than those from the fast simulation.

In summary, the Z+jet (mean) method provides the distribution of P_T^{jet}/P_T^{quark} peaked at 1. The invariant mass resolutions improves (see Table 5.23), given that before to apply the method the invariant mass distribution for $bl\nu$ channel was not well centered around m_{top} (175 GeV) in the full simulation case. Using Z+jet (mean) method we are getting 1% (accuracy of our jet energy scale for ATLAS) agreement on the position of the mass peak.

The main conclusion of the present study is that the predictions from the two simulation packages are in good agreement for the kinematic cuts acceptance and the quantities involved in the analysis. The m_W, m_{jjb} and m_{tt} mass resolutions are in reasonable agreement, with the full simulation predicting resolutions which are 10-20% worse than those from the fast simulation.

Taking a group of jets (usually one!) in a cone around b-jets an treating them as single jets, the obtained recalibration coefficients are better than using the Z+jet

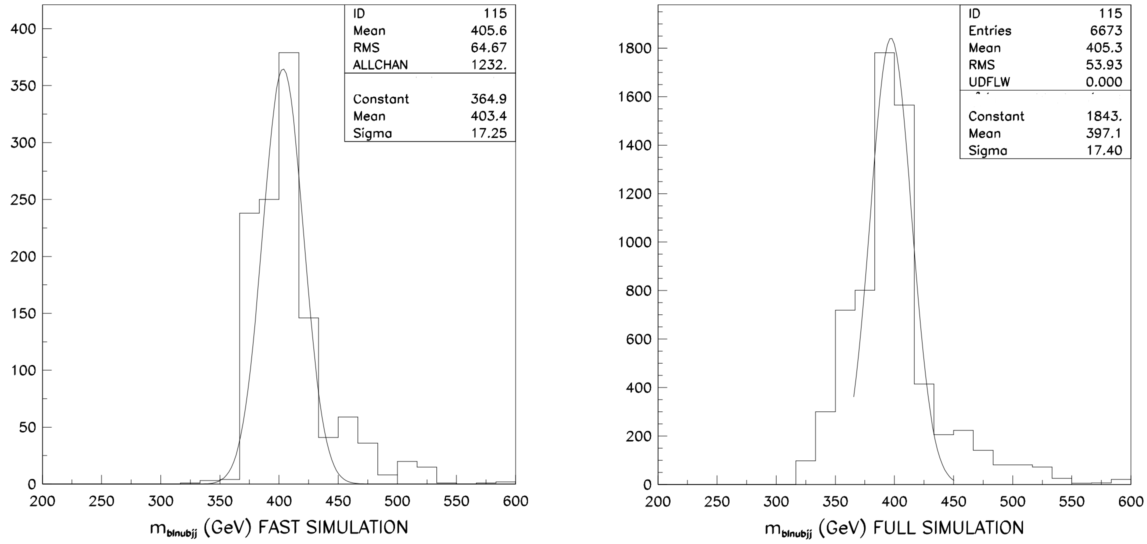

Figure 5.56: *Reconstructed invariant mass distribution of the $t\bar{t}$ pairs, for $m_A = 400$ GeV, for fast (left) and full (right) simulation and using the parametrization obtained with Z+jet (mean) method.*

Table 5.23: *Invariant mass resolution obtained with: the Z+jet (average), the recalibration neighbour jets and Z+jet (mean) methods for the fast and full simulation.*

Resolution	Fast simulation			Full simulation		
	(average) σ (GeV)	Neighbour σ (GeV)	(mean) σ (GeV)	(average) σ (GeV)	Neighbour σ (GeV)	(mean) σ (GeV)
$t \to bjj$	18.71	16.92	13.93	22.68	21.69	21.11
$t \to bl\nu$	11.92	11.23	11.51	13.02	13.98	12.67
m_{tt}	19.39	16.65	17.25	24.04	21.25	17.5

(average) method. However, the P_T^{jet}/P_T^{quark} distribution are not peaked at 1 after calibration and consequently the invariant mass distribution for $bl\nu$ is not well centered around top mass.

Using the method called calibration with Z+jet (mean) events we obtain the P_T^{jet}/P_T^{quark} distribution (after calorimetric calibration) peaked at 1 (with some tails), the 1% agreement on the position of the $bl\nu$ mass peak is reached and the invariant mass resolutions have been improved.

The two simulations can be used in a complementary way to study physics channels: full simulation has to be used to check in detail the detector performances (and to provide parametrisation for fast simulation), fast simulation can be used as a croos-check for full simulation reconstruction code and the algorithms used there, and also for the production of large statistics samples of events for the physics analysis.

5.6 Discovery potential of the ATLAS detector for the SM and MSSM Higgs boson

The experimental observation of one or several Higgs bosons [29] will be fundamental for a better understanding of the electroweak symmetry-breaking mechanism. In the Standard Model [30], one doublet of scalar fields is assumed, leading to the existence of one neutral scalar particle *H*. The Higgs-boson mass, m_H, is not theoretically predicted. From the unitarity arguments an upper limit of $\sim$ 1 TeV can be derived [31]. The requirements of the stability of the electroweak vacuum and the perturbative validity of the Standard Model allows to set upper and lower bounds depending on the cutoff value chosen for the energy scale Δ up to which the Standard Model is assumed to be valid [32]. Such analysis exist at the two-loop level for both low [33] and upper [34] Higgs mass bounds. If the cutoff value is chosen at the Planck mass, which means that no new physics appears up to that scale, the Higgs-boson mass is required to be in the range between $130 < m_H < 190$ GeV. This bound becomes weaker if new physics appears at lower mass scales. If the cutoff is chosen to be 1 TeV, the Higgs-boson mass is constrained to be in the range $50 < m_H < 800$ GeV. Experimentally, constraints on the Standard Model Higgs-boson mass are derived directly from searches at LEP2, which presently lead to $m_H > 105$ GeV [35].

In supersymmetric theories, the Higgs sector is extended to contain at least two doublets of scalar fields. In the minimal version, the so-called MSSM mode [36], there are five physical Higgs particles: two CP-even Higgs bosons *h* and *H*, one CP-odd Higgs boson *A*, and two charged Higgs bosons $H^{\pm}$. Two parameters, which are generally chosen to be m_A and tanβ, the ratio between the vacuum expectation values of the two

Higgs doublets, detemine the structure of the Higgs sector at tree level. However, large radiative corrections affect the Higgs masses and couplings. The lightest neutral scalar Higgs-boson mass, m_h, is theoretically constrained to be smaller than $\sim$ 150 GeV [37].

The aim of this subsection is to review and asses the performance of the ATLAS detector in search for a Standard Model Higgs boson, for the various supersymmetric Higgs bosons and for alternative signals of electroweak symmetry breaking. New improvements respect to previous studies has been taken into account as:

• Improvements on theoretical calculations of cross-sections, branching ratios *etc.*, which have appeared since the Technical Proposal [38] was published, are taken into account.

• The study of the MSSM Higgs sector is extended by several channels, which had not been considered in the Technical Proposal. In addition, cases where SUSY particles are light and appear in Higgs decays and cases where Higgs bosons are produced in decays of SUSY particles are considered in some detail here.

The results presented in this section are obtained predominantly from fast detector simulations, where the detector response and resolution functions have been taken into account. Physics processes have been simulated with the PYTHIA Monte Carlo program, including initial-and final-state radiation, hadronisation and decays. The signal and background production cross-sections are affected by uncertainties due to higher-order corrections, structure function parametrisations and event generation. Over the recent years, there has been done considerable progress in the calculation of higher-order QCD corrections to the cross-sections for the Higgs-boson production [39]. However, the higher-order QCD corrections to the production cross-sections are not known for all signal and background processes.

If a SM Higgs boson exists, its discovery over the full mass range, from the LEP200 lower limit to the TeV scale will be possible after a few years of running at low luminosity (see figure 5.57) :

• The most important channels in the intermediate mass region, $m_H < 2m_Z$, for which a mass peak would be reconstructed, are the four-lepton channel, $H \to ZZ^* \to 4l$, the direct two-photon channel, $H \to \gamma\gamma$, as well as the associated production channels, where the Higgs boson is produced in associaton with a vector boson or a $t\bar{t}$ pair. In these channels, both the $\gamma\gamma$ and $b\bar{b}$ decay modes can be discovered at the LHC. For Higgs-boson masses around 170 GeV, for which the ZZ^* branching ratio is suppressed, the discovery potential can be enhanced by searching for the $H \to WW^* \to l\nu l\nu$ decay. In this case, the Higgs-boson signal would only be observed as an excess of events.

• For $m_H > 2m_Z$ the dominant discovery channel is the four-lepton channel.

• In the mass range between 600 GeV and about 1 TeV, a Higgs boson would be discovered through $WW \to l\nu jj$ mode. The sensitivity in this channel can also

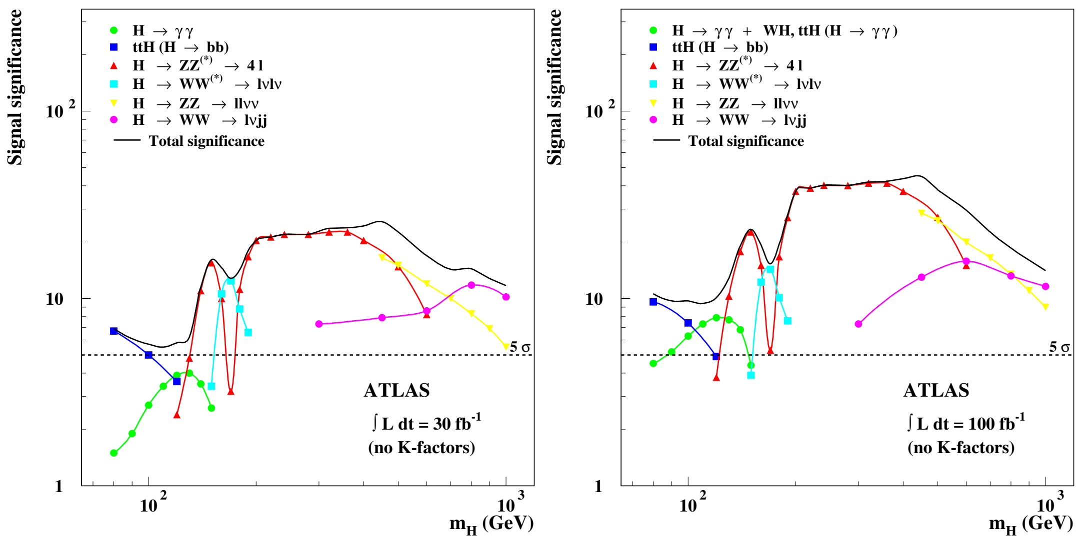

Figure 5.57: *ATLAS sensitivity for the discovey of a Standard Model Higgs boson. The statistical significances are plotted for individual channels, as well as for the combination of all channels, assuming integrated luminosities of 30 fb*$^{-1}$ *(left) and 100 fb*$^{-1}$ *(right). Depending on the numbers of signal and background events, the statistical significance has been computed* $S\sqrt{B}$ *or using Poisson statistics.*

be extended down to lower masses, where it provide independent and complementary information to the four-lepton channel. For $400 < m_H < 900$ GeV the $H \to WW \to l\nu jj$ channel is complemented by the $H \to ZZ \to lljj$ and $H \to ZZ \to ll\nu\nu$ channels, which would provide additional robustness to a Higgs boson discovery in this mass range.

Over a large fraction of the mass range the discovery of a SM Higgs boson will be possible in two or more independent channels. It has also been shown that, if discovered, important Higgs-boson parameters like the mass and the width can be measured. Together with measurements of the production rates and some couplings and branching ratios they will provide useful constraints on the Higgs couplings to ferminons and bosons which in turn can be used to test the Standard Model predictions and to determine the nature of the resonance.

The ATLAS experiment has also a large potential in the investigation of the MSSM Higgs sector (see figure 5.58). If the SUSY mass scale is large and supersymmetric particles do not appear in the Higgs decay products, the full parameter space in the conventional (m_A, tanβ) plane can be covered assuming an integrated luminosity of about 100 fb^{-1}.

• The interest was focused on the discovery potential of various decays modes accesible in the case of the SM Higgs boson: $h \to \gamma\gamma$, $h \to b\bar{b}$, $H \to ZZ \to 4l$, and of

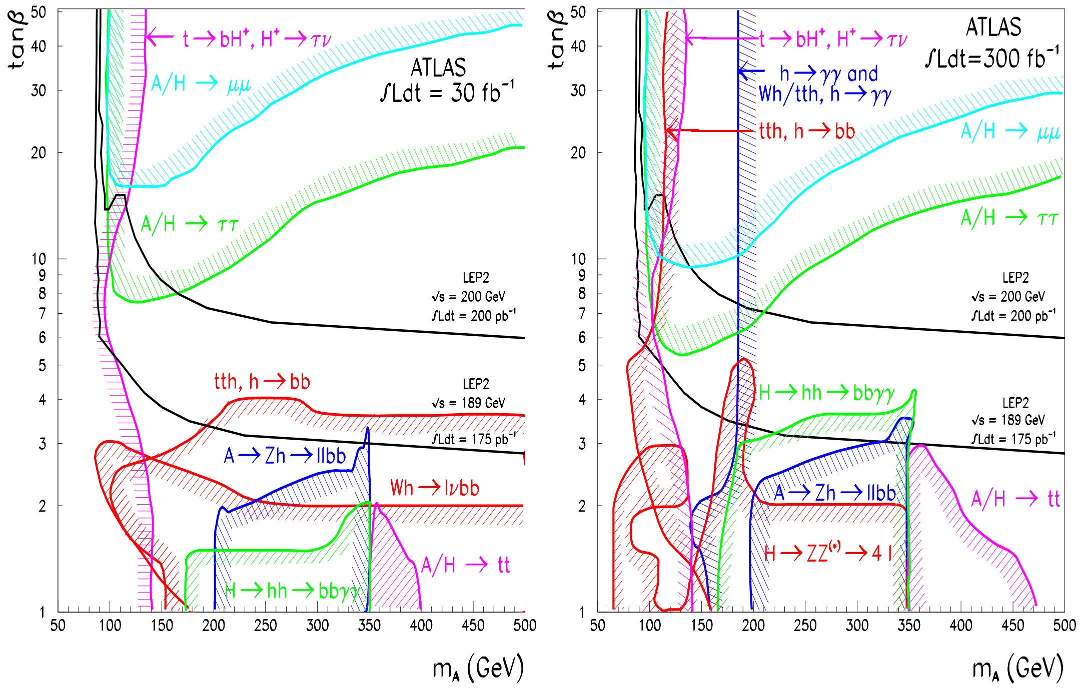

Figure 5.58: *ATLAS sensitivity for the discovey of MSSM Higgs boson (in the case of minimal mixing). The 5σ discovery contour curves are shown in the $(m_A,\ tan\beta)$ plane for individual channels discussed and for integrated luminosities of 30 fb^{-1} (left) and 100 fb^{-1} (right). Also included are the present LEP2 limit (for an integrated luminosity of 175 pb^{-1} per experiment) and the expected ultimate LEP2 limit (for an integrated luminosity of 200 pb^{-1} per experiment at a centre-of-mass energy of 200 GeV).*

modes strongly enhanced at large tanβ: $H/A \to \tau\tau$, $H/A \to \mu\mu$. Much attention was given to other potentially interesting channels such as: $H/A \to t\bar{t}$, $A \to Zh$, $H \to hh$, $H^{\pm} \to tb$.

• The overall discovery potential in the (m_A, tanβ) plane relies heavily on the $H/A \to \tau\tau$ channel, on the $t\bar{t}h$ with $h \to b\bar{b}$ and on the direct and associated $h \to \gamma\gamma$ channels.

• Over a large fraction of this parameter space more than one Higgs boson and/or more than one decay mode would be accessible.

• For almost all cases, the experiment would be able to distinguish between the SM and the MSSM models.

This complete coverage can also be reached independently on the mixing scenario in the stop-sbottom sector. The evidence for Higgs-boson signals would not constitute a direct proof of the existence of supersymmetry, unless supersymmetric particles are discovered themselves.

The interplay between SUSY particles and the Higgs sector has also been addressed. SUSY scenarios have an impact discovery through the opening of Higgs-boson decays to SUSY particles (mostly for H and A) and through the presence of SUSY particles in loops (mostly for production via gg fusion and for $h \to \gamma\gamma$ decays). Scenarios in which SUSY particles are light and appear as Higgs decay products have been studied in the framework of SUGRA models. The discovery potential of the lightest neutral Higgs h in the SM production processes would not be significantly different from what is obtained in the heavy SUSY scenario, since within the model, given present experimental constraints, the decay of h to the lightest SUSY particles is kinematically forbidden. Moreover, over a large fraction of the SUGRA parameter space, the h-boson would appear at the end of the decay cascade of SUSY particles in the channel $\overline{\chi}_2^0 \to \overline{\chi}_1^0 h$ which will be observable with ATLAS detector. The neutral heavy Higgs bosons would be detected in some cases via their decays into neutralinos and charginos, using multi-lepton final states.

In the absence of a scalar Higgs boson, the principal probe for the mechanism of electroweak symmetry breaking will be gauge boson scattering at high energies. It has been shown that ATLAS will be sensitive to the presence of resonances, such as in the WZ system, up to masses around 1.5 TeV. Nonresonant processes, such as in the W^+W^+ production, will require a few years of high luminosity running and a good understanding of the underlying backgrounds.

The important detector requirements in the investigation of electroweak symmetry breaking include: electromagnetic calorimetry, jet-jet mass resolution in the reconstruction of multijet final states, good measurement of missing transverse energy, b-tagging, good electron, muon, tau and photon identification as well as forward jet tagging. The ATLAS detector in its final layout and optimisation is well matched to achieve the necessary requirements. It is also expected that the present design will provide a firm basis for exploring areas of new and unexpected physics.

Bibliography

[1] H. Georgi, S. Glashowd, M. Machacek and D. Nanopoulos, Phys. Rev. Lett. 40 (1978) 692.

[2] D. Dicus, A. Stange, S. Willenbrock, Phys. Letter B 333 (1994) 126-131.

[3] For a review, see J. Gunion, H. Haber, G. Kane and S. Dawson, The Higgs Hunter's Guide (Addison-Wesley, New York, 1990).

[4] F. Abe et al., CDF Collaboration, Phys. Rev. Lett. 73 (1994) 225; Phys. Rev D50 (1994) 2966; Phys. Rev. Lett. 74 (1995) 2626; S. Abachi et al., D0 Collaboration, Phys. Rev. Lett. 74 (1995) 2632.

[5] Interim Report on the Physics Motivations for an Energy Upgrade of LEP2, CERN Preprint CERN-TH/95-151, CERN-PPE/95-78.

[6] K. Gaemers and F. Hoogeveen, Phys. Lett. B 146 (1984) 347.

[7] L. Jones and H.W. Wyld, Phys. Rev. D 17 (1978) 1782; B. Combridge, Nucl. Phys. B 151 (1979) 429; R.K. Ellis and J. Sexton, Nucl. Phys. B 282 (1987) 642.

[8] L. Resnic, Phys. Rev. D 2 (1970) 1975; J. Pumplin, Phys. Rev. D 2 (1970) 1859; T. Bauer, Phys. Rev. Lett. 25 (1970) 485.

[9] J-L. Basdevant, E. Berger, D. Dicus, C. Kao and S. Willenbrock, Phys. Lett. B. 313 (1993) 402.

[10] T. Sȯstrand, "High-Energy-Physics Event Generation with PYTHIA 5.7 and JETSET 7.4", CERN preprints CERN-TH.7111/93 and CERN-TH.7112/93, Comput. Phys. Commun. 82 (1994) 74.

[11] E. Richter-Was et al., ATLFAST 2.0 a fast simulation package for ATLAS, ATLAS Internal Note, PHYS-98-131 (1998)

[12] A. Brignole et al., Phys. Lett B271 (1991) 123; J. Ellis, G. Ridolfi and F. Zwirner, Phys. Lett. B257 (1991) 83; J. Ellis, G. Ridolfi and F. Zwirner, Phys. Lett. B262 (1991) 477.

[13] Elzbieta Richter-Was, et al., ATLAS Internal Note, PHYS-No-074.

[14] M. Carena et al., Phys. Lett. B355 (1995) 209; M. Carena et al., CERN preprint CERN-TH/95-45.

[15] Z. Kunszt and F. Zwirner, Nucl. Phys. B385 (1992) 3.

[16] ATLAS Collaboration, ATLAS Inner Detector TDR, CERN/LHCC/97-16, ATLAS TDR 4, 30 April 1997.

[17] ATLAS Collaboration, ATLAS Trigger Performance, CERN/LHCC 98-15, ATLAS TDR 4, 30 April 1997.

[18] E. Richter-Was et al., ATLAS Internal Note PHYS-NO-108 (1997).

[19] E. Richter-Was and M. Sapinski, ATLAS Internal Note PHY-NO-131 (1998).

[20] K. Gaemers et al., Higgs production and decay into heavy flavours with the gluon fusion mechanism, Physics Letters B 146 (1984) 347.

[21] E. Richter-Was, Private Comunication.

[22] R. Brun et al., GEANT3, CERN/DD/EE/84-1 (1996).

[23] D. Cavalli and S. Resconi, Comparison between full simulation and fast simulation of ATLAS detector, ATLAS Internal Note PHYS-NO-100 (1997).

[24] E. Richter-Was, D. Froidevaux, L. Poggioli, ATLAS Internal Note PHYS-079 (1996).

[25] ATLAS Calorimeter Performance Technical Design Report, CERN/LHCC/96-40 (1996).

[26] /afs/cern.ch/user/b/bosman/public/98-2/testjet.

[27] V. Castillo and S. González, Analysis of the 1998 test of the tilecal barrel prototype, ATLAS Internal Note ATL-TILECAL-99-020 (1999).

[28] ATLAS Detector and Physics Performance Technical Design Report, CERN/LHCC/99-14 (1999).

[29] P. W. Higgs, Phys. Rev. Lett. 12 (1964) 132 and Phys. Rev. 145 (1966) 1156; F. Englert and R. Brout, Phys. Rev. Lett. 13 (1964) 321; G. S. Guralnik, C. R. Hagen and T. W. Kibble, Phys. Rev. Lett. 13 (1964) 585.

[30] S. Glashow, Nuc. Phys. 22 (1961) 579; S. Weinberg, Phys Rev Lett 19 (1967) 1264; A. Salam, in: 'Elementary Particle Theory', W. Svartholm, ed., Almquist and Wiksell, Stockolm, 1968; H. D. Politzer, Phys. Rev. Lett 30 (1973) 1346; D. J. Gross and F. E. Waltzed, Phys. Rev. Lett. 30 (1973) 1343.

[31] B. W. Lee et al., Phys. Rev. Lett. 38 (1977) 883; M. Quiros, 'Constraints on the Higgs boson properties from the effective potential', hep-ph/9703412; A. Ghinculov and T. Binoth, Acta Phys. Polon. B30 (1999) 99.

[32] L. Maiani, G. Parisi and R. Petronzio, Nucl. Phys. B136 (1979) 115; N. Cabibbo et al. Nucl. Phys. B158 (1979) 295; R. Dashen and H. Neunberger, Phys. Rev. Lett. 50 (1983) 1897; D. J. E. Callaway, Nucl. Phys. B233 (1984) 189; M. A. Beg et al., Phys. Rev. Lett. 52 (1984) 883; M. Linder, Z. Phys. C31 (1986) 295.

[33] G. Altarelli and G. Isidori, Phys. Lett B337 (1994) 141; J. A. Casas, J. R. Espinosa and M. Quiros, Phys. Lett. B342 (1995) 171; Phys. Lett. B383 (1986) 374.

[34] B. Grzadkowski and M. Lindder, Phys. Lett. B178 (1986) 81; T. Hambye and K. Riesselmann, Phys. Rev. D55 (1997) 7255.

[35] The presented LEP preliminary limits, presented at the 1999 winter conferences: ALEPH 99-007 CONF-99-003, March 1999; DELPHI 99-8 CONF-208; L3 Notes 2382, 2383, March 1999; OPAL Note PN382, March 1999.

[36] For a review on the MSSM, see H. P. Nilles, Phys. Rep. 110 (1984) 1-, P. Nath, R. Arnowitt and A. Chamseed, Applied N=1 Supergravity, ICTP Series in Theoretical Physics, Vol. I (World Scientific, Singapore, 1984); H. Haber and G. Kane, Phys. Rep. 117 (1985).

[37] *E.g.* see 'Higgs Physics at LEP2', M. Carena, P. M. Zerwas (conv) et al, Proceedings of the LEP2 Workshop, G. Altarelli, T. Sjostrand and F. Zwirner (eds), CERN 1995.

[38] ATLAS
Collaboration, TECHNICAL PROPOSAL, CERN/LHCC/94-43, LHCC/P2, 15 December 1994.

[39] For a review see for example, M. Spira, Fortsch. Phys. 46 (1998) 203 and references therein.

Conclusions

The analyses made and the results obtained in the hadronic calorimeter prototipes of the ATLAS detector carried out with the data taken during 1997 - 1998 with extensive tests with pions and electrons have been presented in this thesis. The search for Higgs boson using the data sample of Monte Carlo simulations for the ATLAS detector at energies $E_{cm} = 14$ TeV have been studied and also presented in this thesis. Total integrated luminosities of 30 fb^{-1} (3 years at low luminosity) and 100 fb^{-1} (1 year at high luminosity) were analysed in this work.

The Tile Calorimeter (Tile - Cal) test beam program was supported by the CERN RD program as RD34. Two calorimeter prototipes were analysed: a full scale barrel sector (Module 0) and two Extended Barrel modules 0. Early measurements were performed in the H8 beam line at the SPS at CERN. Data were taken with pions and electrons between 20 and 400 GeV. A full simulation package has been developed based on the GEANT program which describes in full detail the barrel detector prototipe that was used for the 1998 test beam runs in order to comparate the data and Monte Carlo events.

Before going into the energy reconstruction of the pion and electron data, a crucial phenomenom for understanting of the different techniques used has been discussed. This concept is the so-called *nom-compensation* in hadron calorimetry and is the main physical motivation for the algorithms applied in the reconstruction of the Extended Barrel and Barrel pion data. The energy released by electron with the signal released by pions of equal incident energy has been compared; this ratio is usually named e/π in calorimetry and allows us to introduce the concept of nom-compensation: $e/\pi \neq 1$. In most sampling calorimeter $e/\pi > 1$: this is mostly caused by the energy loss to overcome the binding energy of the excited nucleus in the hadronic shower development. The binding energy to boil off these nucleons is *robbed* from the energy of the cascade ($\sim 20\%$) and in most cases will not contribute to a measurable (*visible*) energy. For hadrons the resolution and linearity of a nom-compensated calorimeter ($e/\pi \neq 1$) are degraded by the different response to the electromagnetic and hadronic components of the hadronic shower.

Nevertheless, it is possible to achieve compensation and improve the linearity and resolution. Two different strategies have been adopted, which may result in $e/\pi \sim 1$:

• designing an intrisically compensated calorimeter (U, Pb, etc...).

• achieving compensation in off-line analysis using different weights for the electromagnetic and hadronic components of the shower.

The approachs applied in this work use just the later method in trying to achieve compensation.

In order to estimate the energy from pions, several reconstruction methods have been studies. A new approach inspired in the H1 collaboration to correct the data has been developed and comparated with previous methods.

The linearity and resolution parameters in the data reconstruction have been studied in three steps, from "Raw data" to "H1" weighting method going through the "benchmark" approach. The "Raw data" analysis has studied the direct data taken in the detector without to apply any weighting method. In the "Benchmark" algorithm the energy of the particles is obtained as the sum of several terms and the involved parameters, constants with the beam energy, are optimized by minimizing the fractional energy resolution and correct the energy losses due to the longitudinal and transversal leakage. The "H1" weighting technique is based in correcting *upwards* the energy of the cells instead of *downwards* improving the linearity and the resolution detector.

The results obtained in the test beam of the Tile - Cal prototipes are the following:

• The linearity and resolution of the Tile Calorimeter prototypes improve using the "H1" method as are summarised in table 5.24 and 5.25. Also these results are compatible for the two prototypes used in the 1997 and 1998 test beam and different values of η. In the ATLAS environment, the game will be to develop an effective jet reconstruction algorithm. This method described here may be flexible and powerful enough to suit this purpose.

Respect to the linearity, the "Benchmark" approach gives aproximately the same results than the "Raw data", improving a little at high energies due to the leakage corrections. Using the "H1" approach we found a good linear response inside of the ATLAS colaboration requirements. The linearity obtained with Monte Carlo simulation is better than for the test beam data but at high energies the hadronic shower simulation is insufficent and the shower descriptions became quite far away from reality.

For the resolution, the "H1" method improves significantly the resolution with respect to the "Raw data" or the "Benchmark" algortihm. The statistical and the constant terms for the resolution are very similar for Monte Carlo simulation and test beam data.

Table 5.24: *Resolution parameters for the different approachs, prototypes and η values.*

Method	MODULE	η	a %	b %
Raw Data	BCN	-1.1	46.7± 0.9	5.34±0.08
	BCN	-1.2	43.7± 1.2	4.80±0.08
	ANL	-1.1	51.7± 0.8	5.09±0.08
	ANL	-1.2	49.9± 1.4	6.04±0.08
	M0	-0.25	59.1± 1.9	5.40±0.08
	M0	-0.35	56.3± 1.5	6.88±0.10
	M0	-0.45	56.5± 1.5	5.35±0.08
	M0	-0.55	55.2± 1.4	5.10±0.11
Benchmark	BCN	-1.1	50.1±1.4	3.10±0.10
	BCN	-1.2	52.2±1.5	4.21±0.12
	ANL	-1.1	51.5±1.5	4.87±0.12
	ANL	-1.2	59.1±1.9	3.71±0.16
H1	BCN	-1.1	45.6± 0.7	2.71±0.07
	BCN	-1.2	47.8± 0.6	2.25±0.06
	ANL	-1.1	45.2± 0.7	3.10±0.07
	ANL	-1.2	43.7± 1.0	3.91±0.07
	M0	-0.25	41.1± 1.3	5.68±0.08
	M0	-0.35	40.7± 1.2	5.33±0.08
	M0	-0.45	45.9± 1.0	4.22±0.08
	M0	-0.55	43.2± 1.0	4.87±0.10

- A scan over η has been made in order to obtain the e/h ratio. The e/h ratio of a sampling calorimeter with an iron-scintillator structure is expected to be > 1 as is shown in table 5.26 and the values are in good agreement with the results obtained from previous precise studies.

- A comparison between the barrel and extended barrel prototypes has been made. The resolution, linearity and e/h ratio for both prototypes are inside of the Hadronic Calorimeter requirements. The statistical resolution term and e/h ratio are very similars in the two cases. However, the constant resolution term is less in the Extended Barrel than in the Barrel. As this term is related with the leakage, we can say that the Barrel Module 0 has more leakage than the Extended Barrel Module 0. Respect to the linearity, the RMS for the Barrel is better than for the Extended Barrel due to the bad quality of data from 1997 test beam.

The search for a Higgs boson via its decay to $t\bar{t}$ in a possible extension of the Standard Model, the MSSM, has been explained in detail. It is assumed that SUSY particle masses are large, so the Higgs-boson decay to SUSY particles are kinematicaly forbidden. The physical states of the Higgs boson are two charged ($H^{\pm}$) and three

Table 5.25: *RMS for the different approachs, prototypes and η values.*

Method	MODULE	η	RMS (%)
Raw Data	BCN	-1.1	4.3
	BCN	-1.2	4.3
	ANL	-1.1	4.3
	ANL	-1.2	4.3
	M0	-0.25	2.0
	M0	-0.35	2.5
	M0	-0.45	2.0
	M0	-0.55	2.5
Benchmark	BCN	-1.1	4.5
	BCN	-1.2	4.5
	ANL	-1.1	4.5
	ANL	-1.2	4.5
H1	BCN	-1.1	1.2
	BCN	-1.2	2.5
	ANL	-1.1	1.8
	ANL	-1.2	2.9
	M0	-0.25	1.4
	M0	-0.35	1.8
	M0	-0.45	0.8
	M0	-0.55	2.0

neutral (h, H, A) physical states. The Higgs particle is copiously produced at hadron collider through gluon-gluon collisions, via virtual top quark loop. However at a hadron collider there is a large irreducible background from the QCD production of top quarks.

Due to the strong coupling of the SM Higgs boson to gauge-boson pairs, the H $\rightarrow$ t$\bar{\text{t}}$ branching ratio is too small ($\sim$ 10%) for this channel to be observable in the SM case. In the MSSM case, however, the H $\rightarrow$ t$\bar{\text{t}}$ and A $\rightarrow$ t$\bar{\text{t}}$ branching ratios are close to 100% for $m_{H,A} > 2m_t$ and for tan$\beta \sim 1$. The signal from H/A $\rightarrow$ t$\bar{\text{t}}$ decays appears as a peak in the t$\bar{\text{t}}$ invariant mass spectrum above the t$\bar{\text{t}}$ continuum background for values of m_H smaller than 500 GeV. There is an interferance between the signal and background amplitudes which causes a strong suppresion of the observability of the signal at higher masses. This suppresion of the total H+A rates is estimated to be roughly 30%, 50% and 70% for m_H = 370 GeV, 400 GeV and 450 GeV. These factors are taken into account in the analysis presented in this thesis.

The study presented has been performed using the data sample of the Monte Carlo simulation for the ATLAS detector at the LHC collider. Two programs has been used, ATLFAST, a fast simulation of signal and background and, SLUG-DICE-ATRECON

Table 5.26: *The values of e/h ratio for different prototypes and η values.*

MODULE	η	e/h
BCN	-1.1	1.38 $\pm$ 0.013
BCN	-1.2	1.48 $\pm$ 0.014
BCN	-1.3	1.52 $\pm$ 0.015
BCN	-1.4	1.60 $\pm$ 0.016
M0	-0.35	1.61 $\pm$ 0.015
M0	-0.45	1.39 $\pm$ 0.012
M0	-0.55	1.41 $\pm$ 0.012

for a sophisticated full detector simulation. In order to be able to cross-check the results obtained with ATLFAST a comparison between fast and full simulation has been performed. Because ATLFAST is an intermidiate step between a simple parton-level analysis and a very sophisticated full detector simulation.

The signal is extracted by searching for WWb$\bar{\text{b}}$ final states, with one W $\rightarrow$ lν and one W $\rightarrow$ jj decay. The lepton is required for the trigger. This final topology consists of one isolated lepton and four reconstructed jets. The lepton was required to have $p_T >$ 20 GeV and $|\eta| < 2.5$. For all jets, those from W-decay and the two b-jets, $p_T >$ 40 GeV and $|\eta| < 2.5$ were required. The assumed efficiency for b-jets identification is ϵ_b = 60% (50%) at low (high) luminosity.

Two algorithms for reconstructing the invariant mass of the t$\bar{\text{t}}$ pair have been studied. The second algorithm improves substantially the signal resolution, the signal-to-background ratio and the statistical significance with respect to the first one. However, the first algorithm is interesting as it reproduces in more unbiases way the shape and magnitude of the combinatorial background to the hadronic (t $\rightarrow$ jjb) and the semileptonic (t $\rightarrow$ blν) channel.

After to reconstruct the invariant mass of the top quarks a study in order to subtract the signal peak from the background has been performed for a m_A = 370, 400 and 450 GeV. The statistical error, the systematic error from overall normalisation and from the shape of the background have been taken into account.

The results obtained are the following:

- The expected mass resolution on m_{tt} mass increases from 14 to 20 GeV as m_H increases from 370 to 450 GeV. This implies that a typical mass window to observe most of the signal would be between 25 and 80 GeV. After both top quark have been reconstructed, the background from continuum t$\bar{\text{t}}$ production is much larger than all other backgrounds (such as W + jets).

• The signal-to-background ratio varies between 9% and 1% over the mass range from 370 to 450 GeV. For an integrated luminosity of 30 fb^{-1} (3 years at low luminosity) and tanβ = 1.5 about 2120 signal events and 40000 background events are expected inside a mass window of $\pm 2\sigma_m$ around m_A = 400 GeV, see table 5.27. For high luminosity operation and an integrated luminosity of 100 fb^{-1} (1 year at high luminosity) one expects for Higgs mass of 400 GeV about 4900 signal and 90000 background events.

Table 5.27: *Observability of the $H/A \to t\bar{t}$ channel for an integrated luminosity of 30 fb^{-1} and 100 fb^{-1}, for tanβ = 1.5. The rough estimation of the effect of the negative interference with continuum production has been included.*

m_H (GeV)	370	400	450
$\sigma \times$ BR (pb) (no supresion)	11.8	8.4	4.8
$\sigma \times$ BR (pb) (with supresion)	8.3	4.2	1.4
Signal #			
(Low Lum.)	3190	2120	980
(Hig. Lum.)	7380	4900	2270
Backgr. #			
(Low Lum.)	34200	39500	52900
(Hig. Lum.)	79100	91400	122400
Significan.			
(Low Lum.)			
=S/$\sqrt{B}$	17.3		4.3
=S/0.01B		5.4	
(Hig. Lum.)			
=S/$\sqrt{B}$	26.2		6.5
=S/0.01B		5.4	

• The extraction of the signal would only possible for Higgs masses above the kinematic peak of the background distribution which is around m_{tt} = 400 GeV. Such an extraction assumes that the uncertainty on the shape of the continuum background is small and that it can be fitted from events outside the assumed Higgs mass window. This leads to the significance levels given in table 5.27.

• For masses close to 400 GeV only an excess of events above the continuum background would be observed. This excess would be statiscally significant, but this significance would only be meaningful if the theoretical uncertainties on the continuum background shape were not larger than about a percent.

• For the optimistic scenario assuming that the differential spectrum of m_{tt} would be known to better than 1% a limited region in parameter space has been found. This limit corresponds to $2m_t < m_A < 470$ GeV for tan$\beta \sim 1$.

• The results obtained for the mass resolution in the H/A $\rightarrow$ t$\bar{\text{t}}$ decay channel for a m_A = 400 GeV and using ATLFAST have been compared with a full detector simulation. The two simulation packages are in good agreement for the kinematic cuts acceptance, the quantities involved in the analysis and the top and Higgs mass resolutions, as is shown in tables 5.28 and 5.29. The two simulations can be used in a complementary way to study physics channels: full simulation has to be used to check in detail the detector performance, fast simulation can be used as a croos-check for full simulation reconstruction code and the algorithms use there and also for the production of large statistics samples of events for the physics analysis.

Table 5.28: *Acceptances for each cut selections (leptons, jets, bjets).*

Ac.	electrons	muons	leptons	*jets*	*bjets*
Fast	0.90	0.77	0.88	0.41	0.62
Full	0.89	0.74	0.85	0.49	0.59

Table 5.29: *Invariant mass resolution obtained for the top and Higgs with a fast and full detector simulation of ATLAS at LHC .*

Resolution	*Fast simulation*	*Full simulation*
	σ (GeV)	σ (GeV)
$t \rightarrow bjj$	13.93	21.11
$t \rightarrow bl\nu$	11.92	12.67
m_{tt}	19.39	17.5

Conclusiones

En este trabajo se ha presentado el análisis realizado y resultados obtenidos en la caracterización de los prototipos del calorímetro hadrónico del detector ATLAS con los datos recogidos durante los años 1997 - 1998 con haces de tests de piones y electrones. También se ha desarrollado un estudio en la búsqueda del bosón de Higgs con los datos simulados por programas Monte Carlo del detector ATLAS a $E_{CM} = 14$ TeV. Las luminosidades totales integradas analizadas en este trabajo fueron 30 fb^{-1} (3 años a baja luminosidad) y 100 fb^{-1} (1 año a baja luminosidad).

El estudio realizado sobre los prototipos del calorímetro hadrónico (Tile - Cal) se enmarcan dentro del programa de test con haces RD34 soportado por el CERN. Se han analizado dos prototipos de calorímetro: un prototipo de la parte del barril ("Barrel Module 0") y otros dos prototipos de sus extensiones ("Extended Barrel Modules 0"). Las medidas se realizaron en la zona de Test H8 del acelerador SPS del CERN utilizando haces de piones y electrones con energías entre 20 y 400 GeV. También se ha hecho un estudio usando un programa de simulación del prototipo del barril central del calorímetro de Tejas basado en el lenguaje GEANT, el cual describe detalladamente el prototipo del detector que fue analizado en test de haces de partículas.

Se ha discutido el concepto de la *no compensación* en calorimetría hadrónica, el cual ha sido la principal motivación física para la aplicación de los algoritmos utilizados en este trabajo en la reconstrucción de la energía procedente de los datos de piones y electrones. Se ha comparado la energía *visible* depositada por los electrones en el calorímetro con la señal dada por los piones a la misma energía; obteniendose el cociente denominado e/π en calorimetría siendo distinto de 1 e introduciendo el conepto de no compensación. Este hecho se debe principalmente a la pérdida de energía *visible* ($\sim 20\%$) de la parte puramente hadrónica de la cascada desarrollada por un hadrón. Esta parte de energía no detectada hace que la respuesta media de los hadrones sea menor que la de los electrones para la misma energía incidente y por lo tanto $e/\pi > 1$. A su vez esta desigualdad implica un empeoramiento en la resolución energética y linealidad del detector.

La resolución y la linealidad pueden ser mejoradas reparando el efecto producido por la no compensación del detector. Hay dos posibles estrategias para resolver el problema:

• diseñar un calorímetro compensado incrementando intrínsicamente la respuesta de la componente hadrónica. Esto se puede hacer utilizando absorbentes pesados (U, Pb, etc...).

• para detectores con una buena granularidad es posible distinguir la componente electromagnética de la cascada hadrónica y aplicar factores de corrección en el análisis *offline* de los datos.

El trabajo presentado en esta tesis ha tenido como objetivo realizar la corrección de los datos y reconstrucción de la energía de los test con haces de partículas utilizando este último método.

Para poder estimar la energía de los piones se han estudiado varios algoritmos de reconstrucción, desarrollándose un nuevo método denominado "H1" para la corrección de los datos y siendo comparado con previos métodos.

En el estudio de la linealidad y resolución del detector se han utilizado tres pasos, desde los "Raw data" hasta el método de pesado "H1" pasando através del método de "Benchmark". El análisis denominado "Raw Data" ha estudiado la linealidad y la resolución en energía del detector analizando los datos obtenidos directamente del detector sin haber sido tratados con ningún método de pesado. El método de "Benchmark" consiste en corregir con determinados parámetros, supuestamente constantes con la energía de la partícula incidente, los efectos producidos por la fuga de energía, tanto longitudinal como tranversal. El método de pesado "H1" corrige los datos aumentando la respuesta de aquellas celdas del calorímetro con señal relativamente pequeña, para equipararla con aquellas celdas donde se ha depositado una gran cantidad de energía (de origen electromagnético), optimizando simultáneamente tanto la linealidad como la resolución del detector.

Los resultados obtenidos en los test con haces de partículas sobre los prototipos del Tile - Cal son los siguientes:

• La resolución y la linealidad de los prototipos del calorímetro de tejas mejoran utilizando el método de pesado "H1" como muestran las tablas 5.30 y 5.31. También los resultados son compatibles para los diferentes prototipos y valores de η. Además el método "H1" ha demostrado ser viable como algoritmo para la reconstrucción de la energía de los "jets" que se producirán en ATLAS.

Respecto a la linealidad, el método de "Benchmark" da los mismos resultados que los "Raw data" mejorandola un poco a altas energías debido a las correcciones efectuadas. Utilizando el método de pesado "H1" encontramos una buena respuesta lineal dentro de los requisitos impuestos por la colaboración ATLAS. La linealidad obtenida con la simulación de Monte Carlo es mejor que para los test con haces, pero hay que tener

Table 5.30: *Parámetros de la resolución para los diferentes métodos, prototipos y valores de η.*

Método	MÓDULO	η	a %	b %
Raw Data	BCN	-1.1	46.7± 0.9	5.34±0.08
	BCN	-1.2	43.7± 1.2	4.80±0.08
	ANL	-1.1	51.7± 0.8	5.09±0.08
	ANL	-1.2	49.9± 1.4	6.04±0.08
	M0	-0.25	59.1± 1.9	5.40±0.08
	M0	-0.35	56.3± 1.5	6.88±0.10
	M0	-0.45	56.5± 1.5	5.35±0.08
	M0	-0.55	55.2± 1.4	5.10±0.11
Benchmark	BCN	-1.1	50.1±1.4	3.10±0.10
	BCN	-1.2	52.2±1.5	4.21±0.12
	ANL	-1.1	51.5±1.5	4.87±0.12
	ANL	-1.2	59.1±1.9	3.71±0.16
H1	BCN	-1.1	45.6± 0.7	2.71±0.07
	BCN	-1.2	47.8± 0.6	2.25±0.06
	ANL	-1.1	45.2± 0.7	3.10±0.07
	ANL	-1.2	43.7± 1.0	3.91±0.07
	M0	-0.25	41.1± 1.3	5.68±0.08
	M0	-0.35	40.7± 1.2	5.33±0.08
	M0	-0.45	45.9± 1.0	4.22±0.08
	M0	-0.55	43.2± 1.0	4.87±0.10

encuenta que no se conoce muy bien el desarrollo de la cascada hadrónica a altas energías y por lo tanto la descripción de esta puede no tener que ver nada con la realidad.

Para la resolución, el método "H1" mejora notablemente la resolución respecto de los "Raw data" y del método de "Benchmark". Además el acuerdo entre los datos y los sucesos Monte Carlo son buenos para los término estadístico y constante de la resolución.

• Se ha llevado a cabo un barrido sobre diferentes valores de η para obtener el valor del factor e/h. Como muestra la tabla 5.32 los resultados obtenidos son mayores que 1 como se espera para el calorímetro de tejas centelleadoras y compatibles con valores encontrados en anteriores test con haces de prototipos previos del detector.

• Se ha hecho un estudio comparativo entre los prototipos del barril y de las extensiones del detector, poniendo de manifiesto que ambos prototipos cumplen con los requisitos exigidos a nivel de resolución, linealidad y e/h por la colaboración ATLAS. Se ha visto que ambos prototipos dan resultados parecidos para el término estadístico en la resolución del detector y para el valor del cociente e/h. Sin embargo, el término

Table 5.31: *RMS para los diferentes métodos, prototipos y valores de η.*

Método	MÓDULO	η	RMS (%)
Raw Data	BCN	-1.1	4.3
	BCN	-1.2	4.3
	ANL	-1.1	4.3
	ANL	-1.2	4.3
	M0	-0.25	2.0
	M0	-0.35	2.5
	M0	-0.45	2.0
	M0	-0.55	2.5
Benchmark	BCN	-1.1	4.5
	BCN	-1.2	4.5
	ANL	-1.1	4.5
	ANL	-1.2	4.5
H1	BCN	-1.1	1.2
	BCN	-1.2	2.5
	ANL	-1.1	1.8
	ANL	-1.2	2.9
	M0	-0.25	1.4
	M0	-0.35	1.8
	M0	-0.45	0.8
	M0	-0.55	2.0

constante en la resolución del detector es menor en los barriles extendidos que en el barril (ver tabla 5.30), pudiendo decir que la pérdida de cascada es mayor en el barril ("barrel module 0") que en las extensiones ("extended barrel modules 0"). Respecto a la linealidad de la respuesta de los piones es mejor en el barril que en las extensiones, lo cual es debido a la baja calidad de los datos del test con haces de 1997.

En este trabajo también se ha estudiado la búsqueda del bosón de Higgs dentro del Modelo Estándar Supersimétrico Mínimo asumiendo que las partículas supersimétricas son suficientemente pesadas para que no tomen un papel importante en las desintegraciones del bosón de Higgs. En este modelo, nos encontramos con cinco estados físicos del bosón de Higgs, dos cargados ($H^{\pm}$) y tres neutros (h, H, A). En esta tesis solo se han considerado las desintegraciones del bosón de Higgs escalar neutro (H) y del pseudoescalar (A) a quarks top. La producción del bosón de Higgs en el LHC se llevará a cabo principalmente por las colisiones entre gluones intercambiando un quark top virtual. Sin embargo, en el LHC tendremos también la producción de quarks top procedentes de las colisiones entre gluones que actuarán como fondo irreducible a nuestra señal.

Table 5.32: *Valores obtenidos para el cociente e/h de los distintos prototipos del detector y para diferentes valores de η.*

MÓDULO	η	e/h
BCN	-1.1	1.38 ± 0.013
BCN	-1.2	1.48 ± 0.014
BCN	-1.3	1.52 ± 0.015
BCN	-1.4	1.60 ± 0.016
M0	-0.35	1.61 ± 0.015
M0	-0.45	1.39 ± 0.012
M0	-0.55	1.41 ± 0.012

En el Model Estándar el bosón de Higgs desintegrándose a quarks top tiene una probabilidad muy baja ($\sim$ 10%), mientras que en el MSSM la probabilidad de desintegración a quarks top es alta ($\sim$ 100%) para masas del Higgs mayores que dos veces la masa del top y valores de tanβ próximos a la unidad. La señal procedente de la desintegración H/A $\rightarrow$ $t\bar{t}$ aparece por encima del fondo irreducible como un pico, cuando obtenemos el espectro de la masa invariante $t\bar{t}$ para valores de la masa del Higgs menores que 500 GeV. Además existe una fuerte supresión en la observabilidad de la señal debido a la interferencia negativa entre las amplitudes del fondo irreducible procedente de QCD y de la señal. Esta supresión es alrededor del 30%, 50% y 70% para masas del Higgs de 370, 400 y 450 GeV. Estos factores han sido tenidos en cuenta en el análisis presentado en esta tesis.

El estudio presentado ha sido realizado utilizando simulaciones de Monte Carlo del detector ATLAS en el colisionador LHC. Concretamente dos programas han sido usados, ATLFAST, para una rápida simulación de la señal y del fondo y, SLUG-DICE-ATRECON, para una sofisticada simulación del detector. También se ha hecho una comparación entre ambos con intención de comprobar los resultados obtenidos con ATLFAST, ya que este es una simulación intermedia entre un análisis a nivel de partones y una simulación completa y sofisticada del detector.

Para poder identificar las desintegraciones del H/A a quarks top, se han elegido estados finales conteniendo $WWb\bar{b}$, con un W $\rightarrow$ lν dando un leptón aisalado utilizado para el "trigger", y el otro W $\rightarrow$ jj. Esto permite tener una topologia final de un leptón aislado y cuatro "jets". Además, se requirió que los "jets" procedentes del bosón W y de los dos "b-jets" tengan un $p_T > 40$ GeV y una $|\eta| < 2.5$ y en el caso del leptón un $p_T >$ 20 GeV y una $|\eta| < 2.5$. También se requirió que ambos "b-jets" fueran identificados con una eficiencia $\epsilon_b = 60\%$ (50%) a baja (alta) luminosidad.

Para reconstruir las desintegraciones de ambos quarks top se han desarrollado dos algoritmos. El segundo de ellos mejora notablemente la resolución de la señal, la relación señal/ruido y la significancia estadística respecto al primero. Sin embargo, el primer algoritmo desarrollado es interesante porque reproduce la forma y la magnitud del fondo combinatorial para el canal hadrónico (t $\rightarrow$ jjb) y el semileptónico (t $\rightarrow$ blν).

Después de realizar la reconstrucción de ambos quarks top, se ha hecho un estudico con intención de extraer la señal respecto del fondo irreducible procedente de QCD, teniendo en cuenta los errores sistemáticos procedentes de la normalización y de la forma del fondo, para el intervalo de masas del Higgs desde 370 a 450 GeV.

Los resultados obtenidos son los siguientes:

• La resolución en masa obtenida para la desintegración del H/A $\rightarrow$ t$\bar{\text{t}}$ aumenta desde 14 GeV hasta 20 GeV para masas del bosón de Higgs entre 370 y 450 GeV respectivamente. Esto implica que será necesario una ventana entre 25 y 80 GeV para poder observar la señal. Además después de la reconstrucción de ambos quarks top, el fondo irreducible (t$\bar{\text{t}}$) procedente de QCD es mucho mayor que el resto de fondos.

• La relación señal/ruido varía entre un 9% y un 1% en el intervalo de masas de 370 a 450 GeV. Para una luminosidad integrada de 30 fb^{-1} (3 años a baja luminosidad), se esperan alrededor de 2120 sucesos de señal y 40000 sucesos de fondo irreducible en una ventana de masas de $\pm 2\sigma_m$ alrededor de la masa del Higgs, para m_A = 400 GeV (ver tabla 5.33). Para una luminosidad integrada de 100 fb^{-1} (1 años a alta luminosidad) se espera para una masa de Higgs de 400 GeV alrededor de 4900 sucesos de señal y 90000 sucesos de fondo irreducible.

• Se ha llevado a cabo un estudio sobre la posible extración de la señal, viendose que solamente seria posible para masas por debajo del pico cinemático formado por la distribución de fondo t$\bar{\text{t}}$, la cual está centrada alrededor de m_{tt} = 400 GeV. La extración realizada asume que las incertitudes sobre la forma del fondo continuo son pequeñas y que este puede ser ajustado utilizando sucesos que esten fuera de la ventana de masas asumida para el Higgs. Esto se encuentra recogido en la tabla 5.33 viendo la significancia estadística.

• Para masas próximas a 400 GeV solamente se podrá observar la señal como un exceso de sucesos por encima del fondo continuo. Este exceso ha de ser significante estadísticamente, pero esta significancia solo será posible si las incertitudes teóricas sobre la forma del fondo continuo no fueran mayores que 1%.

• En un escenario optimista, donde las incertitudes teóricas sobre la producción del fondo continuo t$\bar{\text{t}}$ son alrededor del 1%, se ha establecido un límite en una región del espacio de parámetros. Este límite corresponde a $2m_t < m_A <$ 470 GeV para tan$\beta \sim$ 1.

• Los resultados obtenidos para la resolución en masa de la desintegración del H/A $\rightarrow$ t$\bar{\text{t}}$, para masas del Higgs de 400 GeV utilizando ATLFAST han sido comparadas con una completa y sofisticada simulación del detector. Se ha encontrado un buen acuerdo entre la aceptancia de la selección de los cortes cinemáticos y las resoluciones en la masa

Table 5.33: *Observabilidad del canal $H/A \rightarrow t\bar{t}$ para una luminosidad integrada de 30 fb^{-1} y 100 fb^{-1}, para valores de tanβ = 1.5. Se ha incluido los efectos estimados por la interferencia negativa con el fondo irreducible.*

m_H (GeV)	370	400	450
$\sigma \times$ BR (pb) (sin supresión)	11.8	8.4	4.8
$\sigma \times$ BR (pb) (con supresión)	8.3	4.2	1.4
Señal #			
(Baja Lum.)	3190	2120	980
(Alta Lum.)	7380	4900	2270
Fondo #			
(Baja Lum.)	34200	39500	52900
(Alta Lum.)	79100	91400	122400
Significan.			
(Baja Lum.)			
=S/$\sqrt{B}$	17.3		4.3
=S/0.01B		5.4	
(Alta Lum.)			
=S/$\sqrt{B}$	26.2		6.5
=S/0.01B		5.4	

del top y del bosón de Higgs, como muestran las tablas 5.34 y 5.35. Además ambas simulaciones pueden ser útiles en un camino complementario para estudiar canales físicos: la simulación completa del detector puede ser utilizada para comprobar en detalle las especificaciones del detector y la simulación rápida puede ser usada como una comprobación del código de reconstrucción y algoritmos de la simulación completa y para la producción de un gran número de sucesos para el análisis físico.

Table 5.34: *Aceptancias para cada selección de los cortes (leptones, jets, bjets).*

Ac.	electrones	muones	leptones	*jets*	*bjets*
Fast	0.90	0.77	0.88	0.41	0.62
Full	0.89	0.74	0.85	0.49	0.59

Table 5.35: *Resoluciones en masa del top y del Higgs obtenidas para la simulación rápida y sofisticada del detector ATLAS en el LHC.*

Resolución	*Fast simulation*	*Full simulation*
	σ (GeV)	σ (GeV)
$t \to bjj$	13.93	21.11
$t \to bl\nu$	11.92	12.67
m_{tt}	19.39	17.5